

# Brain Dynamics From Mathematical Perspectives: A Study of Neural Patterning

Sunil Modhara



A thesis submitted to the University of Nottingham for the  
degree of  
DOCTOR OF PHILOSOPHY

MAY 2022

*In loving memory of Beebee and Bob.*

ਬੀਬੀ ਅਤੇ ਮਾਮੇ ਲਈ

*For Mum and Dad.*

## ABSTRACT

The brain is the central hub regulating thought, memory, vision, and many other processes occurring within the body. Neural information transmission occurs through the firing of billions of connected neurons, giving rise to a rich variety of complex patterning. Mathematical models are used alongside direct experimental approaches in understanding the underlying mechanisms at play which drive neural activity, and ultimately, in understanding how the brain works.

This thesis focuses on network and continuum models of neural activity, and computational methods used in understanding the rich patterning that arises due to the interplay between non-local coupling and local dynamics. It advances the understanding of patterning in both cortical and sub-cortical domains by utilising the neural field framework in the modelling and analysis of thalamic tissue – where cellular currents are important in shaping the tissue firing response through the post-inhibitory rebound phenomenon – and of cortical tissue. The rich variety of patterning exhibited by different neural field models is demonstrated through a mixture of direct numerical simulation, as well as via a numerical continuation approach and an analytical study of patterned states such as synchrony, spatially extended periodic orbits, bumps, and travelling waves. Linear instability theory about these patterns is developed and used to predict the points at which solutions destabilise and alternative emergent patterns arise. Models of thalamic tissue often exhibit lurching waves, where activity travels across the domain in a saltatory manner. Here, a direct mechanism, showing the birth of lurching waves at a Neimark-Sacker-type instability of the spatially synchronous periodic orbit, is presented. The construction and stability analyses carried out in this thesis employ techniques from non-smooth dynamical systems (such as saltation methods) to treat the Heaviside nature of models. This

is often coupled with an Evans function approach to determine the linear stability of patterned states.

With the ever-increasing complexity of neural models that are being studied, there is a need to develop ways of systematically studying the non-trivial patterns they exhibit. Computational *continuation* methods are developed, allowing for such a study of periodic solutions and their stability across different parameter regimes, through the use of Newton-Krylov solvers. These techniques are complementary to those outlined above. Using these methods, the relationship between the speed of synaptic transmission and the emergent properties of periodic and travelling periodic patterns such as standing waves and travelling breathers is studied. Many different dynamical systems models of physical phenomena are amenable to analysis using these general computational methods (as long as they have the property that they are sufficiently smooth), and as such, their domain of applicability extends beyond the realm of mathematical neuroscience.

## ACKNOWLEDGEMENTS

It is customary to give thanks to supervisors first, however I'd first like to express my deep gratitude to Yi Ming Lai. For the time you gave me, the work we did together on synchrony in the rebound model, and for diving deep into the nitty gritty of research failures and successes with me. Your impact on me in the early stages of my PhD was nothing but positive. You were a great colleague and friend, and I will remember the time we spent working together fondly. You will be dearly missed.

I must thank my two brilliant supervisors Stephen Coombes and Rüdiger Thul. The past few years have been fun. Thank you both for showing me what academic research looks like, for pushing me, for trusting me to work on what I wanted to work on, and for the opportunities you have both given me. Beyond that though, I am grateful for how much care and support you have both shown me during difficult times these past few years. You are both exceptional academics, but more than this, you are both exceptional *people*.

A very special thank you goes to Daniele Avitabile. For your time, your advice, your expertise, and your humour. Every full day of Zoom meetings with you were truly a pleasure (even the late ones!). Thank you for the confidence and belief you have had in me. You have been fantastic to work with. Berremo insieme un giorno!

Dave Parkin, thank you for setting me up on the servers and keeping an eye on my office Mac. Sudha Cotterill and James Hawkes, thank you for sorting out conference travel and for making demonstrating straightforward for me during the Covid pandemic.

To Gary Mirams, thank you for the enjoyable annual reviews and interesting discussions regarding my work (and that first post-viva drink!). To

Stephen Cox, for giving me the chance to come to Nottingham in 2015, and everything PASS-related, I'll always be grateful.

James Preston, Martin Kurth, and Tom Wicks, a huge thank you to all of you for calming my viva day nerves.

Rachel Nicks, thank you for the very insightful annual reviews and discussions we have had concerning academic careers. Kyle Wedgwood, thank you for the time and advice you gave me at BAMC 2019, the opportunities you have put my way, and for a thought-provoking and very pleasant viva.

I'd like to thank the friends I've made during my time at Nottingham. A special mention needs to go to Sammy for our interesting discussions and for keeping me laughing.

The biggest thank you goes to my family. To Beebee, Mum, Dad, Sunny, and Sunraj, thank you for tolerating me at my worst and for always supporting me (and for letting me commandeering the dining room table for two years!). For everything you have done, are doing, and will do.

## PUBLICATIONS

The following publication has arisen from some of the research carried out during the course of my doctoral studies. It consists of some of the work in Chapter 5.

**Sunil Modhara**, Yi Ming Lai, Rüdiger Thul, and Stephen Coombes. "Neural fields with rebound currents: novel routes to patterning." *SIAM Journal on Applied Dynamical Systems* 20, no. 3 (2021): 1596-1620.

## PUBLICATIONS IN PREPARATION

This publication-in-preparation consists of some of the work in Chapter 3 and the results in Chapters 4 and 5. The complementary GitHub repository containing the relevant code can be found at <https://github.com/danieleavitable/rebound-periodic-orbit-continuation>.

**Sunil Modhara**, Rüdiger Thul, Stephen Coombes, and Daniele Avitabile. "Periodic orbit continuation in spatially extended systems: applications to neuroscience." Expected 2023.

## AWARDS AND PRIZES

The Mathematical Neuroscience and Applications (MNA) Prize for

### **Best Junior Researcher Presentation**

at the workshop "Mathematical Modelling and Statistical Analysis in Neuroscience", Institut Henri Poincaré, Paris, France, February 4th 2022

# PRESENTATIONS

## PRESENTATIONS

- “Neural Fields with Rebound Currents: Novel Routes to Patterning”, Mathematical Modelling and Statistical Analysis in Neuroscience, Institut Henri Poincaré, Paris, 2nd February 2022
- “Neural Fields with Rebound Currents: Novel Routes to Patterning”, Society for Mathematical Biology (SMB) 2021 Online, 14th June 2021
- “Periodic Orbits and Waves in Mathematical Neuroscience”, Department of Mathematics, University of Manchester, Applied Seminar, 4th June 2021
- “Neural Fields with Rebound Currents: Novel Routes to Patterning”, Centre for Systems, Dynamics, and Control, University of Exeter, Dynamics Internal Seminar, 25th March 2021
- “Neural Fields with Rebound Currents: Novel Routes to Patterning”, Mathematical Sciences, University of Nottingham, Post-Graduate Research (PGR) Showcase, 9th November 2020
- “Pattern Formation in Biological Neural Networks with Rebound Currents”, Mathematical Sciences, University of Nottingham, Centre for Mathematical Medicine and Biology (CMMB) Seminar, 21st January 2020

## POSTERS

- “Neural Fields with Rebound Currents: Novel Routes to Patterning”, British Applied Mathematics Colloquium (BAMC) 2021 Online, April 2021

## MINI-SYMPOSIA ORGANISED AND CHAIRED

- “Mathematical neuroscience”, SMB (Society for Mathematical Biology) 2021 Online, with Stephen Coombes, Rüdiger Thul, Daniele Avitabile, June 2021

---

## CONTENTS

---

<b>1</b>	<b>INTRODUCTION</b>	<b>1</b>
1.1	Introduction . . . . .	1
1.2	Thesis Structure . . . . .	3
<b>2</b>	<b>BACKGROUND</b>	<b>7</b>
2.1	Neurons: A Physiological Perspective . . . . .	7
2.2	The Post-Inhibitory Rebound Mechanism . . . . .	12
2.3	Foundations: Single Neuron Models . . . . .	14
2.3.1	The Hodgkin-Huxley Model . . . . .	14
2.3.2	Integrate-and-Fire Models . . . . .	21
2.4	Synapse Modelling . . . . .	23
2.5	From Spiking Models to Rate-based Models . . . . .	27
2.6	From Single Neurons to Networks and Spatial Fields . . . . .	29
2.7	Developments: Networks and Neural Fields . . . . .	32
2.7.1	The Amari Neural Field Model . . . . .	33
2.7.2	A Model of Spike Frequency Adaptation . . . . .	36
2.7.3	Inhibitory Neural Network Models of Thalamic Tissue . . . . .	37
2.8	Stability in Non-Smooth Dynamical Systems . . . . .	43
2.9	Evans Function Stability of Heterogeneous Spatial Patterns . . . . .	47
2.10	Summary . . . . .	49
<b>3</b>	<b>NUMERICAL CONTINUATION METHODOLOGIES</b>	<b>52</b>
3.1	Introduction . . . . .	52
3.1.1	Dynamical Systems . . . . .	52
3.1.2	Space-time Models . . . . .	54
3.1.3	Numerical Continuation . . . . .	55
3.1.4	Continuation Schemes . . . . .	57

3.1.5	The Predictor-Corrector Step . . . . .	58
3.1.6	Summary . . . . .	63
3.2	Equilibria and Travelling Waves . . . . .	64
3.3	Spatially Extended Periodic Orbit Continuation . . . . .	71
3.3.1	A Review of the Problem Formulation . . . . .	71
3.3.2	Numerical Stability Routine . . . . .	75
3.3.3	Computational Implementation . . . . .	76
3.3.4	Convergence Tests . . . . .	77
3.3.5	Results: Breathers in a Neural Field Model . . . . .	80
3.4	Travelling Periodic Orbit Continuation . . . . .	81
3.4.1	Problem Formulation . . . . .	81
3.4.2	Implementation of Shift and Derivative Operators . . .	86
3.4.3	Convergence Tests . . . . .	89
3.4.4	Numerical Stability Routine . . . . .	90
3.5	Summary . . . . .	91
4	NEURAL FIELDS WITH DYNAMIC FIRING THRESHOLDS	95
4.1	Introduction . . . . .	95
4.2	A Semi-Smooth Dynamic Threshold Neural Field Model . . .	98
4.3	Turing Analysis of the Homogeneous Steady State . . . . .	99
4.3.1	Constructing the Homogeneous Steady State . . . . .	99
4.3.2	Linear Stability of the Homogeneous State . . . . .	100
4.3.3	Static Turing and Turing-Hopf Bifurcation Curves . . .	104
4.4	Construction of a Localised Bump Solution . . . . .	112
4.5	Stability of the Localised Bump Solution . . . . .	115
4.6	Equilibria and Travelling Wave Continuation . . . . .	121
4.6.1	Stationary Bump . . . . .	121
4.6.2	Stationary Spatially Periodic Bumps . . . . .	124
4.6.3	Travelling Pulse . . . . .	124
4.7	Translation-Invariance . . . . .	127
4.8	The Inclusion of Localised Spatial Drive . . . . .	127

4.9	Exotic Solutions . . . . .	133
4.10	Continuation of Temporally Periodic Structures . . . . .	135
4.10.1	Standing Waves . . . . .	135
4.10.2	Saltatory Travelling Periodic Waves . . . . .	136
4.10.3	Travelling Breathers . . . . .	139
4.11	Summary . . . . .	142
5	<b>THALAMIC NEURAL FIELDS WITH REBOUND CURRENTS</b>	145
5.1	Introduction . . . . .	145
5.2	The Augmented Neural Field Model . . . . .	152
5.3	Construction of Periodic Spatial Synchrony . . . . .	157
5.4	Linear Stability of Periodic Spatial Synchrony . . . . .	164
5.4.1	Local Saltation Approach . . . . .	164
5.4.2	Non-local Saltation Approach . . . . .	165
5.4.3	Non-smooth Periodic Orbit Stability . . . . .	167
5.4.4	Connectivity-independent Stability . . . . .	171
5.5	Lurching Waves . . . . .	175
5.6	Patterning In Two Dimensions . . . . .	178
5.7	Parameter Continuation . . . . .	183
5.7.1	Synchrony . . . . .	183
5.7.2	Spatially Heterogeneous 2-cycle . . . . .	185
5.8	Construction of Spatially Periodic Travelling Waves . . . . .	189
5.8.1	Synaptic Dynamics . . . . .	189
5.8.2	Rebound Dynamics . . . . .	192
5.8.3	Voltage Dynamics . . . . .	193
5.8.4	The Dispersion Relation . . . . .	194
5.9	Stability of Spatially Periodic Travelling Waves . . . . .	197
5.9.1	Synaptic Dynamics . . . . .	197
5.9.2	Voltage and Rebound Dynamics . . . . .	201
5.9.3	A Reduced Saltation Approach . . . . .	202
5.9.4	The Evans Function . . . . .	204

5.10 Translation Invariance of Spatially Periodic Travelling Waves . . . . .	208
5.11 Summary . . . . .	209
6 DISCUSSION . . . . .	214
6.1 Thesis Recapitulation . . . . .	214
6.2 Future Work . . . . .	216
A APPENDICES: BACKGROUND . . . . .	228
A.1 Green’s Functions for Synaptic Responses . . . . .	228
A.2 Deriving Firing Rates in Integrate-and-Fire Models . . . . .	229
A.2.1 Linear Integrate-and-Fire Model . . . . .	229
A.2.2 Quadratic Integrate-and-Fire Model . . . . .	231
B APPENDICES: NEURAL FIELDS WITH DYNAMIC FIRING THRESH- OLDS . . . . .	232
B.1 First Derivative of Solutions . . . . .	232
C APPENDICES: THALAMIC NEURAL FIELDS WITH REBOUND CUR- RENTS . . . . .	234
C.1 Fourier Transforms of Connectivity Functions . . . . .	234
C.1.1 1D Kernel . . . . .	234
C.1.2 Integral of 1D Kernel . . . . .	236
C.1.3 2D Kernel . . . . .	237
C.2 Derivation of Saltation Matrices . . . . .	240
C.2.1 The Spatially Local Saltation Matrix . . . . .	240
C.2.2 Saltation Matrices in the Co-moving Frame . . . . .	244
C.3 The Fourier Series Representation of $u(\xi)$ . . . . .	246
C.4 Functions for Evans Function Calculation . . . . .	248
References . . . . .	250

---

LIST OF FIGURES

---

Figure 2.1	Basic anatomy of a neuron . . . . .	8
Figure 2.2	Information transmission at the chemical synapse . .	11
Figure 2.3	Hodgkin-Huxley steady state curves and timescales .	19
Figure 2.4	Hodgkin-Huxley action potential . . . . .	20
Figure 2.5	Integrate-and-fire responses . . . . .	22
Figure 2.6	Models of post-synaptic response . . . . .	24
Figure 2.7	Post-synaptic response to a spike-train . . . . .	26
Figure 2.8	Spiking vs. rate-based model illustration . . . . .	29
Figure 2.9	Wizard hat connectivity . . . . .	32
Figure 2.10	Neural field snaking bifurcation diagram . . . . .	34
Figure 2.11	Sigmoidal activation functions in thalamic model [178]	39
Figure 2.12	On-centre and off-centre connectivity . . . . .	40
Figure 2.13	Lurching waves, as discovered by Rinzel et al. [178]. .	41
Figure 2.14	Two-layer thalamic network of TC and RE cells . . . .	42
Figure 2.15	Illustration of the saltation approach . . . . .	45
Figure 2.16	Threshold crossings of an Amari bump . . . . .	48
Figure 2.17	Spatially organised hierarchy of structures in the brain	51
Figure 3.1	Continuation predictor-corrector illustration . . . . .	59
Figure 3.2	Equilibria continuation in a 2-D Hopfield network . .	67
Figure 3.3	Qualitatively distinct periodic orbit instabilities . . . .	75
Figure 3.4	Error and convergence tests in a neural field model .	78
Figure 3.5	Period doubling bifurcation of a breather . . . . .	80
Figure 3.6	Travelling wave periodic orbit illustration . . . . .	84
Figure 3.7	Error in implemented shift and derivative operators .	87
Figure 3.8	Error and convergence for travelling periodic problem	90

---

Figure 3.9	Continuation code structure . . . . .	93
Figure 4.1	A stationary bump solution . . . . .	97
Figure 4.2	Turing and Turing-Hopf bifurcation spectra . . . . .	106
Figure 4.3	Turing and Turing-Hopf curves . . . . .	107
Figure 4.4	Instabilities of the homogeneous steady state: $u(x, t)$ .	109
Figure 4.5	Instabilities of the homogeneous steady state: $h(x, t)$ .	110
Figure 4.6	Tracking the Bogdanov-Takens point . . . . .	111
Figure 4.7	Bump in the smoothed dynamic threshold model . .	113
Figure 4.8	Evans function plots at a drift instability . . . . .	119
Figure 4.9	Simulation demonstration of a drift instability . . . .	119
Figure 4.10	Evans function plots at a dynamic instability . . . . .	120
Figure 4.11	Simulation demonstration of a dynamic instability . .	120
Figure 4.12	Continuation of a stationary bump . . . . .	122
Figure 4.13	Different bumps on the solution branches in Figure 4.12	122
Figure 4.14	Continuation of spatially periodic bumps . . . . .	123
Figure 4.15	Continuation of a travelling pulse solution . . . . .	125
Figure 4.16	Symmetric and asymmetric spatial drive . . . . .	128
Figure 4.17	Evans function plot at instability (symmetric drive) .	129
Figure 4.18	Simulation of a dynamic instability (symmetric drive)	130
Figure 4.19	Evans function plot at instability (asymmetric drive) .	131
Figure 4.20	Simulation of a dynamic instability (asymmetric drive)	132
Figure 4.21	Exotic patterns in the dynamic threshold model . . .	134
Figure 4.22	Continuation of a standing periodic pattern . . . . .	136
Figure 4.23	Bifurcation diagram of a saltatory TWPO solution . .	137
Figure 4.24	Space-time plots and spectra: TWPO saltatory patterns	138
Figure 4.25	Bifurcation diagram of a travelling breather . . . . .	140
Figure 4.26	Space-time plots: TWPO travelling breathers . . . . .	141
Figure 5.1	Action potentials riding the crest of the LTS . . . . .	148
Figure 5.2	Radially symmetric connectivity kernel . . . . .	155
Figure 5.3	Connectivity kernel in 1D . . . . .	159

---

Figure 5.4	$(v, h)$ -phase space of synchrony . . . . .	161
Figure 5.5	Floquet multipliers of synchrony vs. wavenumber . .	169
Figure 5.6	Growth and decay of perturbations . . . . .	170
Figure 5.7	Fourier transforms and $\lambda(\hat{w}(k))$ plots . . . . .	171
Figure 5.8	Emergent pattern and spectrogram: $-1$ instability . .	173
Figure 5.9	Emergent pattern and spectrogram: $+1$ instability . .	174
Figure 5.10	Asymmetric connectivity and Fourier transform . . .	176
Figure 5.11	Neimark-Sacker bifurcation . . . . .	177
Figure 5.12	Emergent pattern and spectrogram: $e^{i\theta}$ instability . .	178
Figure 5.13	Complex spatio-temporal rebound patterning in 2D .	179
Figure 5.14	$-1$ instability of synchrony in 2D . . . . .	180
Figure 5.15	Travelling oscillating hexagons in 2D . . . . .	181
Figure 5.16	Continuation of the synchronous periodic orbit . . . .	184
Figure 5.17	Continuation of the two-cycle pattern . . . . .	186
Figure 5.18	Discontinuities in lurching waves . . . . .	187
Figure 5.19	Periodic travelling waves: solution and phase space .	190
Figure 5.20	Synaptic input to the periodic wavetrain . . . . .	191
Figure 5.21	Periodic travelling waves: dispersion curve . . . . .	195
Figure 5.22	Emergent pattern from an unstable wave . . . . .	196
Figure 5.23	Periodic wavetrain Evans function plots (stable) . . .	206
Figure 5.24	Periodic wavetrain Evans function plots (instability) .	206
Figure 5.25	Periodic wavetrain Evans function plots (unstable) . .	207
Figure 5.26	$v'(\tilde{\zeta})$ at $v = v_{\text{th}}$ . . . . .	209
Figure 6.1	Sigmoidal function and PWL caricatures . . . . .	218
Figure 6.2	Head direction maps on the lattice and continuum . .	221
Figure 6.3	The human connectome . . . . .	226
Figure C.1	Saltation in non-smooth dynamical systems . . . . .	242

---

LIST OF TABLES

---

Table 1	Types of discontinuities in dynamical systems . . . .	44
Table 2	Continuation of various solutions to space-time models	92
Table 3	Parameter values for exotic solutions in Figure 4.21 .	133
Table 4	Standard parameters in the Rebound Model . . . . .	157

## GLOSSARY

---

Acronym	Name
PoSP	Post-Synaptic Potential
EEG	Electroencephalogram
fMRI	Functional Magnetic Resonance Imaging
PIR	Post-Inhibitory Rebound
$I_T$	T-type $\text{Ca}^{2+}$ Current
LTS	Low-Threshold ( $\text{Ca}^{2+}$ ) Spike
TC	Thalamo-cortical
RE	Reticular nucleus
IF	Integrate-and-Fire (model)
LIF	Linear Integrate-and-Fire (model)
QIF	Quadratic Integrate-and-Fire (model)
SFA	Spike Frequency Adaptation
PWL	Piecewise Linear
PWC	Piecewise Constant
PALC	Pseudo-Arclength Continuation
EP	Equilibrium Point
HSS	Homogeneous Steady State
TW	Travelling Wave
PO	Periodic Orbit
TWPO	Travelling Wave Periodic Orbit
NS	Neimark-Sacker (bifurcation)
DTM	Dynamic Threshold (neural field) Model
HDPM	Head Direction Preference Map

---

---

## INTRODUCTION

---

### 1.1 INTRODUCTION

The field of neuroscience has taken great strides forward in the past century in understanding the complex processes that underpin brain function. Two Nobel Prize winning examples are the works by Cajal and Golgi in the early 1900s postulating the existence of and identifying neurons [135, 192, 114], and that of Hodgkin and Huxley in the 1950s identifying the mechanisms behind action potential-generation [100]. Modelling and experimentation have been used hand-in-hand to advance our understanding of the brain and the mechanisms that underlie neural patterning. The work of du Bois-Reymond and others in the mid-1800s culminated in the discovery of the action potential [189]. The early 1900s saw Bernstein hypothesise that the action potential could be explained by potassium ions crossing a cell membrane before Hodgkin and Huxley refined this idea in their modelling study by suggesting sodium ions played an equally important role [101]. The existence of ion channels, through which ions may cross a membrane, was then confirmed experimentally in the 1970s [155], thus substantiating the ideas of Bernstein and Hodgkin and Huxley. Since the 1960s and the advent of modern computing capabilities, there has been a rapid growth in mathematical neuroscience-related research. As such, neuroscience has sprouted into an inherently multi-disciplinary field, combining approaches in biology, scien-

tific computing, and mathematical and statistical modelling to further the understanding of neural processes such as cognition, consciousness, and learning to name just a few [201, 191, 52]. Far from being self-contained within their own field, developments in neuroscience have led to advances in other fields too, such as predictive analytics and artificial intelligence [142, 22]. Artificial neural networks – which pervade the modern world in diverse areas such as facial recognition technology [92], self-driving cars [205], search engine optimisation [112], and financial fraud detection [227] – are computational algorithms inspired by the connectivity and information processing in biological neural networks.

The work in this thesis falls into the domains of mathematical and computational neuroscience. Mathematical models of different brain regions are utilised, developed, and analysed using dynamical systems approaches and computational techniques to shed light on the mechanisms underlying pattern formation in the brain. Much work has been carried out on single-neuron models in the literature [65, 100, 220, 77]. In this thesis, the focus is on networks of connected neurons. The inclusion of network connectivity significantly contributes to the dynamical complexity of models. Current computational limits and analytical techniques often require that simplifying approaches be considered in such cases. One such approach widely used is the continuum limit. This allows for dimension-reduction techniques to be used, with the caveat that instead of considering networks of neurons, a spatial field of neural tissue is considered. Such continuum techniques are more concerned with the overall, coarse-grained activity in a network rather than activity on the scale of individual neurons. Advantageously, field models are favourable for fitting to data obtained from global brain recording methods. The neural field model is an effective description of neural tissue connectivity, and variants of it are used throughout this thesis to understand neural pattern-forming mechanisms. In consultation with colleagues at VU Amsterdam, an opportunity to bring novel continuation techniques into the domain of mathematical neuroscience and develop

these was identified. These allow for the automated computation of invariant dynamical systems solutions such as equilibria and periodic orbits under different parameter regimes. With the ever-growing complexity of neural models, and the desire to find relationships between differences in biophysical parameters and model behaviour, computational tools such as these are a welcome asset.

## 1.2 THESIS STRUCTURE

Below, we set out the structure of this thesis, including what is contained within each chapter. A list of figures, a list of tables, and a glossary are provided for reference in the front matter of this thesis.

### *Chapter 2 – “Background”*

The relevant neural biology is outlined before the major models of single cell neural activity are introduced. A review of synaptic modelling is carried out, comparing and contrasting the benefits of different synaptic models. It is shown how *rate-based* models may be motivated from spiking models, and how network models of connected cells may be constructed from interconnected single cells.

The later parts of this chapter review the main models motivating the work in this thesis before saltation techniques for the analysis of solutions in non-smooth dynamical systems are described and critiqued. The *Evans function approach* for linear stability of patterned states is outlined, and is used extensively along with the saltation method in later chapters of this thesis.

---

### *Chapter 3 – “Numerical Continuation Methodologies”*

This chapter begins with a discussion of techniques from dynamical systems theory relevant to numerical continuation before a review of standard continuation methods is presented. An illustration of equilibria and travelling wave continuation in a neural field model is given before reviewing novel, efficient, matrix-free techniques for carrying out spatially extended periodic orbit continuation. Tests are carried out, ensuring convergence to true periodic orbit solutions and validating the methods, before they are used explicitly to continue a periodic structure in a spatial model.

The final part of this chapter builds on currently existing work to develop novel methodologies allowing the continuation of travelling, periodic solutions in spatio-temporal systems (for clarity, an example of such a pattern is a travelling breather). The methods developed are sufficiently general to cater for models other than neural field-type models and may be used in research areas beyond mathematical neuroscience.

### *Chapter 4 – “Neural Fields with Dynamic Firing Thresholds”*

In contrast to the numerical nature of the previous chapter, the majority of this chapter focuses on analytical techniques in the study of a neural field model incorporating non-trivial, non-constant firing threshold dynamics. A Turing instability analysis is carried out on a model from the literature, characterising patterning that arises upon the instability of a spatially homogeneous steady state. Moreover, it is shown that certain types of instabilities *may not* occur due to the intrinsic nature of the model under consideration.

The existing literature of neural fields with dynamic thresholds is outlined and critiqued, leading to a refined, smoother model, for which a bump solution is characterised and constructed, and its linear stability analysed using Evans function techniques.

---

The chapter concludes with an illustration of the different types of exotic spatially-extended solutions admitted by the model and a spatially-extended periodic orbit continuation of a number of these, using techniques from Chapter 3.

*Chapter 5 – “Thalamic Neural Fields with Rebound Currents”*

The final research chapter of this thesis focuses on a model of sub-cortical, thalamic tissue. A non-standard, modified neural field model incorporating ingredients to effectively describe the dynamics of cells within the thalamus – namely, rebound currents – is studied. The model exhibits characteristic thalamic behaviour through the post-inhibitory rebound phenomenon; we study the pattern forming nature of thalamic tissue by constructing specific patterns and analysing their linear stability in both one- and two-spatial dimensions. We utilise the so-called *saltation* approach to do so, and demonstrate how to extend it in a general way to cater for the study of spatially extended patterns. The dispersion curve for periodic waves, relating the wave-speed to the spatial period, is generated, with stability boundaries found via an Evans function approach.

The literature shows a specific type of solution – lurching waves, with saltatory motion – appearing often in a number of different thalamic models. It is shown that one pathway by which they may arise is via a Neimark-Sacker instability of the synchronous periodic orbit state. A numerical exploration is carried out in two spatial dimensions, hinting at an abundance of rich dynamical behaviour on the plane. Moreover, the planar stability theory developed allows for a systematic study of patterns that arise at bifurcations.

As in Chapter 4, the continuation techniques developed in Chapter 3 are utilised to shed light on the dynamics of highly complex spatio-temporal patterns in the model and illustrate how the time-scales of synaptic activity alter patterning.

---

*Chapter 6 – “Discussion”*

This thesis is concluded with a discussion, summarising the main achievements and placing them within the larger context of the existing literature. This work opens up a number of paths to continue research in a number of different areas of applied mathematics and theoretical biology. This includes numerical continuation methods, analytical methods for stability, and neural models with alternative rebound currents to name just a few. These are all topics for future study and are discussed in greater detail in Chapter 6.

---

## BACKGROUND

---

### 2.1 NEURONS: A PHYSIOLOGICAL PERSPECTIVE

**T**HE brain is a complex organ which regulates the bodily processes of nearly all eukaryotes. The fundamental units, or *cells*, within the brain that are thought to be most important in information transmission are *neurons*, which are supported by glial cells. Figure 2.1 shows the main structure of a typical neuron. The nucleus sits within the cell body, or *soma*, which is surrounded by *dendrites*. These are appendages which allow signals to be received from other cells. The axon is covered in a myelin sheath (though *unmyelinated axons* exist) and connects the soma to the axon terminals. These form junctions with the dendrites of other neurons at locations known as *synapses*.

Electrical signals known as *action potentials* travel down the axon until they reach an axon terminal, often referred to as the *pre-synaptic terminal*. Here, they elicit post-synaptic potentials (PoSP) in the dendrites of connected neurons which travel towards the soma. If enough PoSPs of sufficient strength are elicited in the connected neuron, a *firing event* occurs, in which an action potential is generated at the soma [169]. Each neuron typically forms thousands of synaptic connections with other neurons. There are approximately 100 billion neurons in the human brain, meaning that the total number of synapses is on the order of magnitude of 100 *trillion* [207]. The stagger-

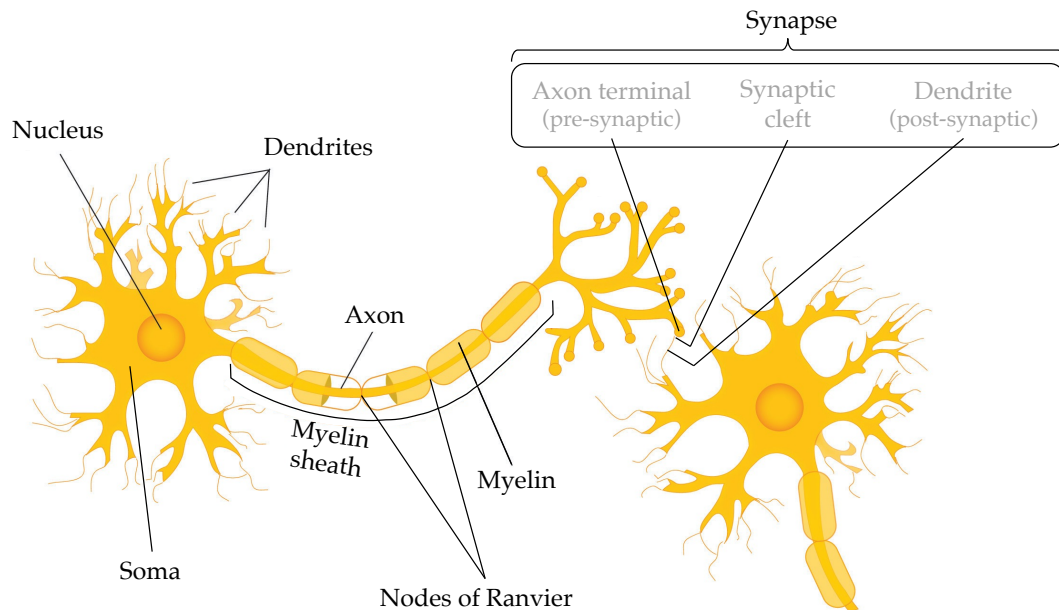


Figure 2.1.: Schematic anatomy of a neuron (left) connected to another neuron (right). The synapse (boxed in the top-right) is shown in more detail in Figure 2.2. This figure (original author Jennifer Walinga) has been modified from Wikimedia Commons and is licensed under the Creative Commons Attribution-ShareAlike 4.0 International License.

ing complexity of the resultant network of neurons requires a robust and efficient communication system of information signalling and processing. Action potentials may be seen as the *language* of neural information processing.

A variety of cells support different types of action potentials including skeletal muscle cells and specialised cardiac cells, however our discussion will focus on *neuronal action potentials* – those occurring in neurons. Action potentials are generated by the movement of sodium ( $\text{Na}^+$ ) and potassium ( $\text{K}^+$ ) ions across the cell membrane through specialised proteins, selectively permeable to ions, known as *ion channels*.

A multitude of different ion channels exist, including voltage-gated [233, 37, 236] – such as the sodium and potassium channels mentioned above; the configuration of voltage-gated channels change in response to membrane

potential – and ligand-gated [103]. Our focus is mainly on voltage-gated ion channels. A channel either allows a flow of ions through it (conducting) or does not (non-conducting). It may consist of activation and inactivation gates which all must be open to ensure the channel is in the conducting state [169, 10, 157]. Inactivation refers to the phenomenon by which an open channel enters a non-conducting conformation (this typically occurs after a change in membrane potential) [173]. Depending on the type of ion channel, inactivating gates may or may not be present [35].

The typical resting membrane potential of a neuron is approximately  $-70\text{mV}$ , meaning that the inside of the cell is more negatively charged than the outside, by  $70\text{mV}$ . At rest, the concentration of  $\text{Na}^+$  ions is higher outside the cell than inside, while the opposite is true for  $\text{K}^+$  ions. In a conventional action potential, a cell fires once the membrane potential reaches a critical value: the firing threshold. This is a consequence of some stimulus applied to the cell, for example synaptic input, noise or some ionic current [171]. The result of this is a large cell depolarisation. The voltage-gated  $\text{Na}^+$  channel opens and  $\text{Na}^+$  ions flow into the cell. The resultant change in polarity causes the  $\text{Na}^+$  channel to close and the voltage-gated  $\text{K}^+$  channel to open, allowing  $\text{K}^+$  ions to leave the cell, resulting in cell repolarisation (typically hyperpolarisation). This repolarisation causes the  $\text{K}^+$  channel to close. This behaviour occurs rapidly and successively down the axon, between myelinated segments of axonal membrane at the *nodes of Ranvier* where a high density of ion channels exist, and characterises a neuronal action potential. For reference, the typical length-scale of an ion channel is  $10\text{nm}$  [200], while for a node of Ranvier, it is  $1\text{-}2\mu\text{m}$  [9]; hundreds of ion channels are able to fit on a one-dimensional cross section of a node. The insulating properties of the myelin sheath increase action potential conduction velocity from  $0.5\text{-}10\text{ms}^{-1}$  in unmyelinated neurons to up to  $150\text{ms}^{-1}$  in myelinated ones [169].

Immediately following an action potential spike, the cell enters its *refractory period* in which the ATP-dependent  $\text{Na}^+/\text{K}^+$  pump returns  $\text{Na}^+$  ions

to the outside and  $K^+$  ions to the inside of the cell. This is an energy-intensive process [17] – the activity of the  $Na^+/K^+$  pump is estimated to account for 20-40% of the brain's total energy consumption [169], indicating its importance in function. The refractory period is composed of the *absolute refractory period*, lasting a few milliseconds [20], in which it is impossible for another action potential to be generated, regardless of the stimulus, and the *relative refractory period*, lasting slightly longer, in which a larger stimulus than usual is required for an action potential to occur. The absolute refractoriness of the membrane in the wake of the action potential is responsible for uni-directional action potential propagation [169]. The refractory period imposes a limit on the number of action potentials that can occur per unit time. That is, it limits the neuronal firing rate [169].

When an action potential generated in a pre-synaptic neuron arrives at a synapse, cell-to-cell communication can occur via electrical synaptic coupling or chemical synaptic coupling. In the former, current flows through specialised membrane channels known as *gap junctions*, while in the latter, an abundance of neurotransmitters, housed in *synaptic vesicles* in the pre-synaptic terminal are released into the *synaptic cleft*, the gap between two neurons connected at a synapse. This induces a PoSP by activating receptor molecules in the post-synaptic neuron [169]. An action potential arriving at the pre-synaptic terminal activates voltage-gated calcium ( $Ca^{2+}$ ) channels, causing an influx of  $Ca^{2+}$  ions. This results in the secretion of neurotransmitters out of their vesicles and into the synaptic cleft. They diffuse through the synaptic cleft and bind to receptors at the post-synaptic neuron. This induces a post-synaptic current, either *excitatory* or *inhibitory* depending upon the neurotransmitter which *increases* or *decreases* the membrane potential of the post-synaptic neuron, respectively. Examples of specific neurotransmitters are acetylcholine (ACh) and glutamate (both excitatory), and gamma-aminobutyric acid (GABA) and glycine (both inhibitory) [169]. This is all summarised in Figure 2.2, which outlines the stages involved in chemical synaptic communication.

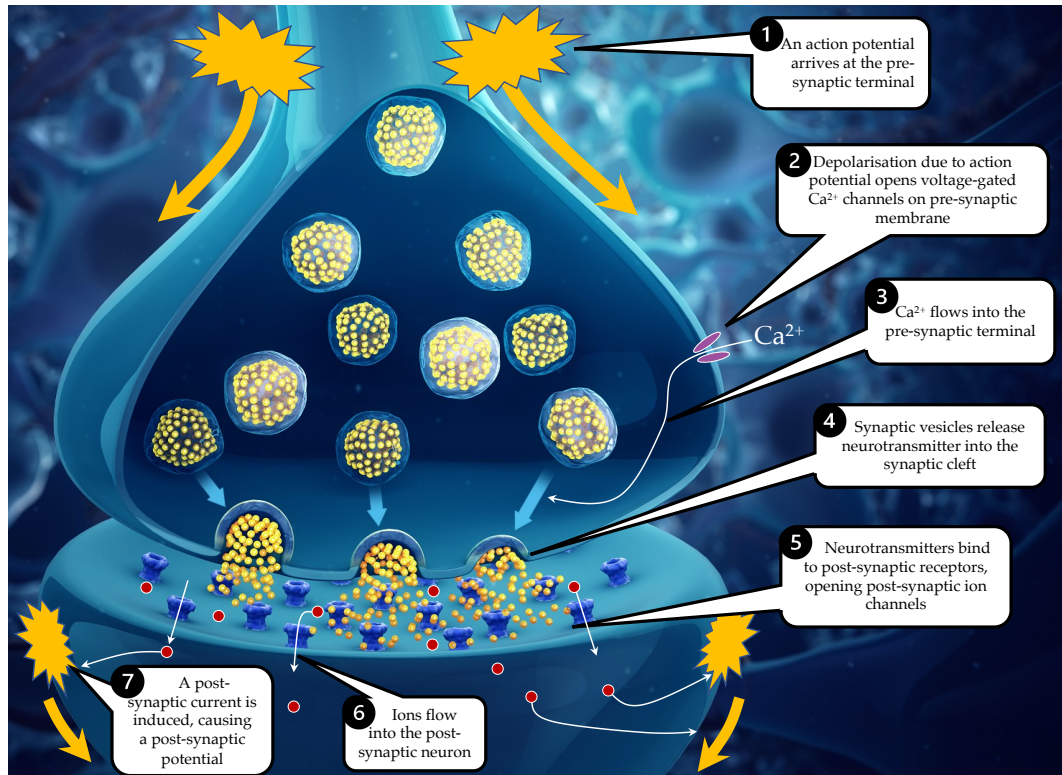


Figure 2.2.: A summary of transmission at a chemical synapse. Ions and neurotransmitters are shown as red and yellow circles, respectively. Neurotransmitters may be either excitatory or inhibitory. This figure (original author <https://www.scientificanimations.com/>) has been modified from Wikimedia Commons and is licensed under the Creative Commons Attribution-ShareAlike 4.0 International License.

A number of methods have been developed to obtain readings of brain activity. Patch clamp experiments allow cellular membrane potential (as well as other cellular properties) to be recorded by an experimentalist, while more macroscopic recording techniques include electroencephalograms (EEG) [161] and functional magnetic resonance imaging (fMRI). EEG detects the activity of large groups of cortical neurons firing together – their synchrony – on a timescale of milliseconds by measuring PoSPs. It has a number of clinical applications including the diagnosis of neuronal disorders such as epilepsy and sleep disorders [162]. fMRI is a relatively new imaging tech-

nique, having been developed in the 1990s. It measures brain activity at the larger spatial scale of the whole-tissue by detecting changes associated with blood oxygen and flow [174]. Areas with higher amounts of blood flow and blood oxygenation are associated with higher levels of neural activity [84]. As such, it is a useful tool in determining how different brain regions are *functionally* related. Due to the measurement of *blood flow*, fMRI is used to evaluate the effects of, and recovery from, stroke [223].

## 2.2 THE POST-INHIBITORY REBOUND MECHANISM

As well as standard neuronal firing via depolarisation, other non-canonical mechanisms exist by which neurons may fire. An example of this is the post-inhibitory rebound (PIR) phenomenon, seen in recordings of thalamic cells, which requires an initial *hyperpolarisation* to cause cells to fire. Characteristically, in cells that exhibit PIR, hyperpolarisation causes de-inactivation of one or more species of ion channels. That is, channels are primed to allow a conductance due to the opening of inactivation gates. Whether or not a flow of ions occurs is then dependent on the state of activation gates of ion channels. Channels allow the flow of ions when their activation and inactivation gates are both open. As the cell recovers from hyperpolarisation, the ion channels' activation gates open, resulting in a large depolarisation as ions rush in and out of the cell.

Typical currents that are important in generating PIR are the T-type  $\text{Ca}^{2+}$  current ( $I_T$ ) and the hyperpolarisation-activated cation current ( $I_h$ ) [8].  $I_T$  arises when there is a non-zero conductance in T-type  $\text{Ca}^{2+}$  channels. These channels are found in thalamic neurons as well as cardiac myocytes, glial cells, and osteoblasts [126, 69] to name just a few cell types. The electrophysiology of T-type channels from different cell types is similar but there are differences in how they inactivate and respond to drugs [164]. This variation can be attributed to the fact that different cell types express different sub-types of ion channels. In the case of the T-type channel, there

are three sub-types, designated  $\text{Ca}_v3.1$ ,  $\text{Ca}_v3.2$ , and  $\text{Ca}_v3.3$ , with all three expressed in various cells throughout the brain [108, 141, 213, 206]. T-type  $\text{Ca}^{2+}$  channels exist on the cell membrane. From a modelling point of view, voltage-gated channels are classically characterised by their steady state curves, which reflect the proportion of activating and inactivating gates that are open as functions of voltage [179]. Hyperpolarising synaptic inhibition leads to a temporary state in which the cell is more excitable than normal (meaning it is more amenable to fire as a result of a smaller stimulus). As the inhibition wears off, the potential of the cell returns towards rest but due to its heightened excitability, it instead fires a low-threshold spike (LTS) resulting in a burst of action potentials as the T-type  $\text{Ca}^{2+}$  conductance grows [221, 165, 113]. T-type  $\text{Ca}^{2+}$  channels are typically only found in high enough densities to be significant in the soma and dendrites of neurons [237], so the LTS itself does not transmit synaptic activity, since to do so, it would need to traverse the axon and reach a pre-synaptic terminal. However other action potentials which *can* transmit synaptic activity ride on the crest of an LTS [136, 180], resulting in a burst response, where a tight cluster of action potentials occurs successively in a short space of time. In this way, the LTS can contribute to information propagation in a network of neurons. Thalamo-cortical relay (TC) neurons are a particular type of cell that exhibit PIR in response to inhibition [7]. The interaction between TC cells and reticular thalamic nucleus (RE) cells in the thalamus through the PIR mechanism generates oscillations that have been recorded in vivo [202] and in vitro [218, 106].

## 2.3 FOUNDATIONS: SINGLE NEURON MODELS

### 2.3.1 *The Hodgkin-Huxley Model*

Most influential in the description of single-cell neural dynamics and the action potential is the Nobel Prize-winning work carried out in 1952 by Alan Hodgkin and Andrew Huxley. Their series of papers [98, 97, 99, 100] culminated in a mathematical model that described various electrical properties in the giant axon of the squid. Compared to modern equipment, the electrodes of the time were large. As such, the *giant axon* of the squid allowed for the insertion of an electrode inside the cell, and for Hodgkin and Huxley to carry out their experiments. Such was the success of their work that the majority of models since have been based on the same formalism.

In essence, their work models the effect of ion movement in and out of the cell on the cell membrane potential. The membrane acts as a capacitor, separating charge inside and outside the cell. It is selectively permeable to ions – that is, ions can cross the membrane only where ion channels exist. Hodgkin and Huxley’s results suggested that ion channels can be modelled as variable resistors in the language of electrical circuitry. The modelling assumes two important currents that contribute towards the dynamics of the action potential: the  $\text{Na}^+$  and  $\text{K}^+$  currents. A third *leak* current is included which models the effects of chloride ( $\text{Cl}^-$ ) and other ions. The first step in their analysis was to divide the total membrane current into a capacitive current and an ionic current. Then the dynamics for the membrane potential,  $V$ , is obtained from Kirchhoff’s current law<sup>1</sup> and is given by the current-balance equation

$$I = C \frac{dV}{dt} + I_{\text{ion}}, \quad (2.1)$$

---

<sup>1</sup> Charge is conserved at a circuit junction, so the total current entering  $I_{\text{in}}$  and leaving  $I_{\text{out}}$  a junction must sum to zero. That is,  $I_{\text{in}} = I_{\text{out}}$ .

where  $I$  is an applied current,  $C$  is the membrane capacitance,  $V$  is the potential difference across the membrane, and  $I_{\text{ion}}$  is the relevant ionic current(s). Given that only three ionic currents are considered, this can be written as

$$I_{\text{ion}} = I_{\text{Na}} + I_{\text{K}} + I_{\text{L}}, \quad (2.2)$$

where the ionic current has been split into components carried by  $\text{Na}^+$  ions ( $I_{\text{Na}}$ ),  $\text{K}^+$  ions ( $I_{\text{K}}$ ), and by other ions ( $I_{\text{L}}$ ). In [97], they showed that each of these currents could be modelled in terms of their conductances and the difference between the membrane potential and the reversal potential for that particular species of ion. That is, they obey Ohm's law (where conductance is the reciprocal of resistance)

$$I_{\text{Na}} = g_{\text{Na}}(V - V_{\text{Na}}), \quad (2.3a)$$

$$I_{\text{K}} = g_{\text{K}}(V - V_{\text{K}}), \quad (2.3b)$$

$$I_{\text{L}} = g_{\text{L}}(V - V_{\text{L}}). \quad (2.3c)$$

where  $V_{\text{Na}}$ ,  $V_{\text{K}}$  and  $V_{\text{L}}$  are the reversal, or *Nernst* potentials for each respective species of ion. At these potentials, there is no net flow of the specific ionic species across the membrane.

For a charged ionic species  $X$ , chemical and electrical gradients act to drive the potential towards the reversal potential, denoted  $V_X$ . The *chemical* gradient

$$\Delta G_{\text{chemical}} = RT \ln \left( \frac{[X]_{\text{out}}}{[X]_{\text{in}}} \right), \quad (2.4)$$

arises from the difference in ion concentration across the membrane. Here,  $R$  is the universal gas constant,  $T$  is the absolute temperature (measured in Kelvin), and  $[X]$  denotes the concentration of species  $X$  with the subscript indicating whether this is outside or inside the cell membrane. The *electrical* gradient

$$\Delta G_{\text{electrical}} = zFV, \quad (2.5)$$

arises due to an unequal amount of charge distribution across the membrane, where  $z$  is the ionic valence (the number of electrons an atom of

species  $X$  uses in bonding [163]),  $F$  is the Faraday constant, and  $V$  is the voltage. These two gradients are together referred to as the electrochemical gradient; this is the quantity that determines the movement of an ion across the membrane [156]. At the reversal potential  $V = V_X$ ,  $\Delta G_{\text{electrical}}$  and  $\Delta G_{\text{chemical}}$  across the membrane are equal [116]. This results in *the Nernst equation*

$$V_X = \frac{RT}{zF} \ln \left( \frac{[X]_{\text{out}}}{[X]_{\text{in}}} \right), \quad (2.6)$$

giving an expression for the reversal potential of an ionic species  $X$ .

Hodgkin and Huxley modelled the conductances  $g_{\text{Na}}$ ,  $g_{\text{K}}$  and  $g_{\text{L}}$  by fitting various conductance models to data. Experimental evidence showed that the end of a recording of potassium conductance could be fitted to a first order equation, but a higher order equation was needed to model the initial phase of conductance response.<sup>2</sup> Their solution was to model potassium conductance as being proportional to the fourth power of some variable,  $n$ , which obeyed a first-order differential equation. That is,

$$g_{\text{K}} = \bar{g}_{\text{K}} n^4, \quad (2.7a)$$

$$\frac{dn}{dt} = \alpha_n(V)(1 - n) - \beta_n(V)n, \quad (2.7b)$$

where  $\bar{g}_{\text{K}}$  is the maximum potassium conductance,  $n$  is the *activating* gating variable which varies in  $[0, 1]$  and  $\alpha_n$  and  $\beta_n$  are rate constants for the fraction of open and closed gates respectively [157]. It is noted that they depend *only* on voltage. Originally, Hodgkin and Huxley stated that the physical basis of this equation is that “ $K^+$  ions can only cross the membrane when four self-similar particles occupy a certain region of the membrane.” The gating charges have since been found [11, 79, 38], confirming their great insight. They showed that potassium conductance is adequately modelled by (2.7). See Figure 2 from [100], showing that the smooth curve obtained from (2.7) is a good fit to experimental recordings. Hodgkin and Huxley acknowledged that a fifth or sixth power of  $n$  may have provided a *better*

---

<sup>2</sup>This is illustrated concretely in Figure 2 of Hodgkin’s and Huxley’s seminal work: [100].

fit, but found their choice of a fourth power of  $n$  to be satisfactory. The steady-state solution of  $n$  satisfies (for a specific value of  $V$ )

$$n_{\infty}(V) = \frac{\alpha_n(V)}{\alpha_n(V) + \beta_n(V)}. \quad (2.8)$$

By fitting to experimental data, expressions were found for the rate constants as

$$\alpha_n(V) = \frac{0.01(V + 10)}{\exp\left(\frac{V+10}{10}\right) - 1}, \quad (2.9a)$$

$$\beta_n(V) = 0.125 \exp\left(\frac{V}{80}\right). \quad (2.9b)$$

By relating  $\alpha_n(V)$  and  $\beta_n(V)$  to  $n_{\infty}(V)$ , and to a new variable  $\tau_n(V)$  describing the voltage-dependent time constant, (2.7b) can be rewritten as

$$\frac{dn}{dt} = \frac{n_{\infty}(V) - n}{\tau_n(V)}, \quad (2.10)$$

which describes the evolution of  $n$  in terms of its steady state curve with respect to  $V$ ,  $n_{\infty}(V)$ , and its time constant,  $\tau_n(V)$ , rather than the rate-based description of  $\alpha_n(V)$  and  $\beta_n(V)$ . The time constant is given by

$$\tau_n(V) = \frac{1}{\alpha_n(V) + \beta_n(V)}. \quad (2.11)$$

In modelling the sodium conductance, Hodgkin and Huxley postulated that

$$g_{\text{Na}} = \bar{g}_{\text{Na}} m^3 h, \quad (2.12)$$

where  $\bar{g}_{\text{Na}}$  is regarded as the maximum sodium conductance, and  $m$  and  $h$  are activating and inactivating gating variables that vary in  $[0, 1]$ . Originally, they stated that this equation “*may be given a physical basis if conductance is assumed to be proportional to the number of sites on the inside of the membrane which are simultaneously occupied by three activating molecules and are not blocked by an inactivating molecule*”. Although modern experimentation [10, 139] has shown that this is not quite the case, the foresight of Hodgkin and Huxley should not be diminished. Indeed, their conductance model does show an excellent fit with empirical data and is remarkable, given the lack of

knowledge of ion channels at the time. The dynamics of the gating variables are given by

$$\frac{dm}{dt} = \alpha_m(V)(1 - m) - \beta_m(V)m, \quad (2.13a)$$

$$\frac{dh}{dt} = \alpha_h(V)(1 - h) - \beta_h(V)h, \quad (2.13b)$$

where  $\alpha_{m,h}$  and  $\beta_{m,h}$  are again rate constants. The variable  $m$  represents the fraction of open activation gates. Therefore, the proportion of activation gates that are open increases as  $m$  gets closer to 1. Similarly, since  $h$  represents the fraction of open inactivation gates, as  $h$  gets closer to 0, the proportion of inactivation gates in the closed state increases. This description of ion channels is deterministic and assumes a large population of independent ion channels and independent binding kinetics, however at the level of *single* – or a small number of – ion channels, a stochastic approach provides a better description; see [42] for an analysis of the Hodgkin-Huxley equations with stochastic channel dynamics. Similarly to the case of the potassium conductance, voltage-dependent expressions for the rate constants are found by fitting to experimental data. They are given by

$$\alpha_m(V) = \frac{0.1(V + 25)}{\exp\left(\frac{V+25}{10}\right) - 1}, \quad (2.14a)$$

$$\beta_m(V) = 4 \exp\left(\frac{V}{18}\right), \quad (2.14b)$$

and

$$\alpha_h(V) = 0.07 \exp\left(\frac{V}{20}\right), \quad (2.15a)$$

$$\beta_h(V) = \frac{1}{\exp\left(\frac{V+30}{10}\right) + 1}. \quad (2.15b)$$

By a similar line of reasoning, the time evolution equations for  $m$  and  $h$  can be written in a similar way to (2.10) (in terms of steady state curves and time constants). The sigmoidal steady state curves  $Y_\infty(V)$  and the time-scales  $\tau_Y(V)$  (as functions of voltage) for the gating variables  $Y \in \{n, m, h\}$  are shown in Figure 2.3. The steady state curves for the activating potassium

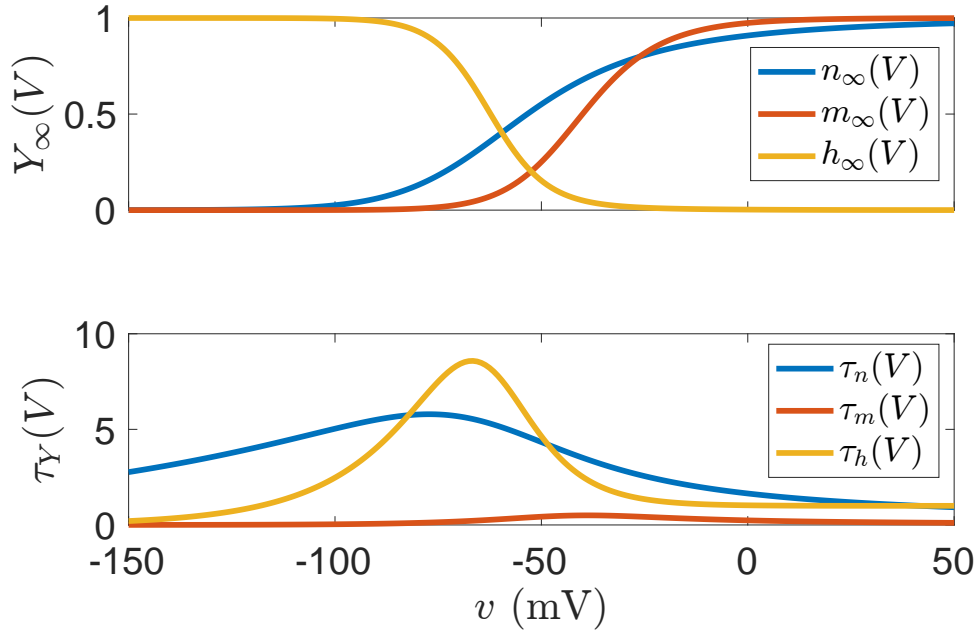


Figure 2.3.: The steady state curves  $Y_\infty(V)$  (upper panel), and the time-scales  $\tau_Y(V)$  (lower panel),  $Y \in \{n, m, h\}$  for the gating variables in the potassium and sodium conductances in the Hodgkin-Huxley model.

and sodium gates  $n_\infty(V)$  and  $m_\infty(V)$  are close to 0 for more negative values of  $V$  and are close to 1 for more positive values of  $V$ . Contrastingly,  $h_\infty(V)$  behaves in the opposite way – it is close to 1 for more negative  $V$  and closer to 0 for more positive values of  $V$ . This is indicative of its *inactivating* gating nature. These descriptions give a good fit of the potassium and sodium conductances.

Obtaining the reversal potential and maximal conductance of the leak current was considered to be difficult due to the current consisting of more than one species of ion. However, once satisfactory values for these were obtained, the complete four-dimensional model could be written as

$$C \frac{dV}{dt} = -\bar{g}_K n^4 (V - V_K) - \bar{g}_{Na} m^3 h (V - V_{Na}) - g_L (V - V_L) + I, \quad (2.16)$$

along with (2.7b), (2.13a), (2.13b), (2.9), (2.14), and (2.15). With this complete model, Hodgkin and Huxley first considered whether the model correctly predicted the total current during a voltage clamp, in which  $dV/dt = 0$ .

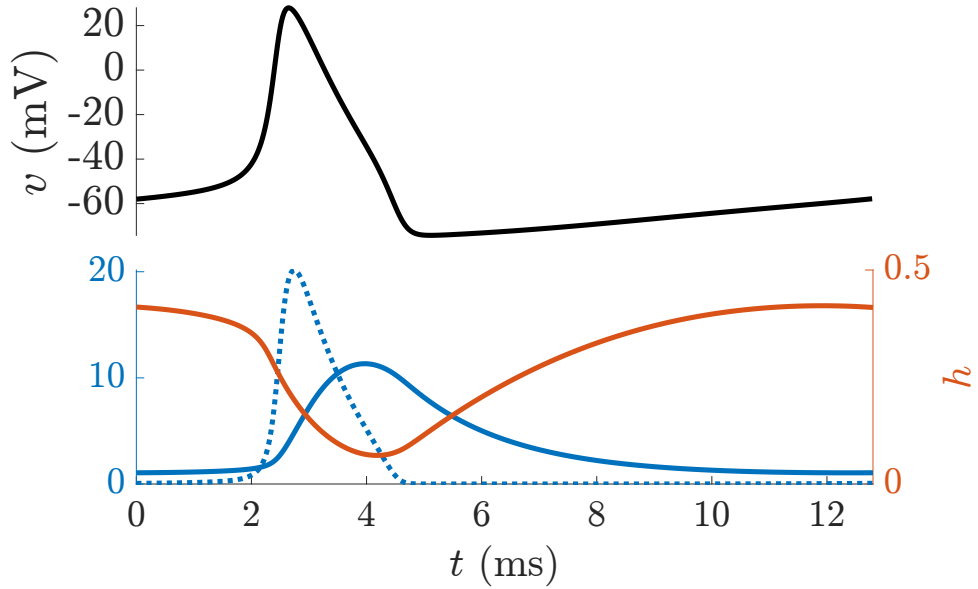


Figure 2.4.: Top: numerical solution of 2.16 showing the temporal evolution of  $V$ . The action potential lasts approximately 3ms, after which the refractory period begins. Bottom: curves showing the time course of  $g_K$  (blue solid) and  $g_{Na}$  (blue dotted) on the left vertical axis, and  $h$  (orange) on the right vertical axis during an action potential and the subsequent refractory period. Initial conditions are  $(v_0, n_0, m_0, h_0) = (-58, 0.4139, 0.1056, 0.4135)$ , with applied current  $I = 15\text{mV}$ . Other parameters are  $\bar{g}_{Na} = 120$ ,  $V_{Na} = 115$ ,  $\bar{g}_K = 36$ ,  $V_K = -12$ ,  $g_L = 0.3$ , and  $V_L = 10.6$ .

In this case, the voltage-dependent rates  $\alpha_{n,m,h}(V)$ ,  $\beta_{n,m,h}(V)$  are constant and a solution for the total current is given by (2.2) as well as expressions for  $n$ ,  $m$ , and  $h$ . The total current was computed for a number of different voltages and showed agreement with experimental curves. Hodgkin and Huxley also considered a partial differential equation (PDE) formulation in which solutions are referred to as *propagated action potentials*. Such depolarisations have a conduction velocity, describing the speed at which the action potential propagates down a nerve fibre. They found a good agreement between the theoretical and the experimental conduction velocity. Solving (2.16) with  $I = 0$  corresponds to a *membrane action potential*. The

shape, duration and amplitude of the action potential were all successfully captured by their model, as well as the absolute and relative refractory periods. The refractory periods arise as a consequence of inactivation, which decays relatively slowly following a depolarisation. This is seen in Figure 2.4 as  $h$  slowly increases back to its steady state value of 1 at the resting voltage following an action potential. For a smaller  $h$ , as is the case during the refractory period, the level that can be reached by the sodium conductance is reduced. In turn, this reduces the maximum depolarisation of the membrane potential.

Hodgkin and Huxley briefly considered the phenomenon known as anode-break excitation, where a neuron fires action potentials in response to the termination of a hyperpolarising current. Upon application of a hyperpolarising current, the membrane potential falls below rest. This is followed by a drop in the membrane potential required for an action potential to occur. They found that upon removal of the hyperpolarising current, an action potential is generated. The mechanism is similar to PIR in that a cell fires after a hyperpolarisation – in fact, Rinzel et al. [178] described PIR as being qualitatively equivalent to anodal break excitation – however unlike in thalamic tissue, burst firing (multiple action potentials) was not seen.

### 2.3.2 *Integrate-and-Fire Models*

Conductance-based models such as the Hodgkin-Huxley model describe the generation of an action potential from a biophysical point of view by considering ion channel dynamics. The integrate-and-fire (IF) model – and variants of it – is a more phenomenological description of a neuron, capable of spike generation, albeit without any underlying biophysical detail such as ion channel dynamics [1, 31]. It is simpler than the Hodgkin-Huxley model in the sense that it is a lower-dimensional description of neural tissue, although this comes at the price of introducing non-smooth dynamics. It is widely used in the study of neural systems. The IF model consists of a

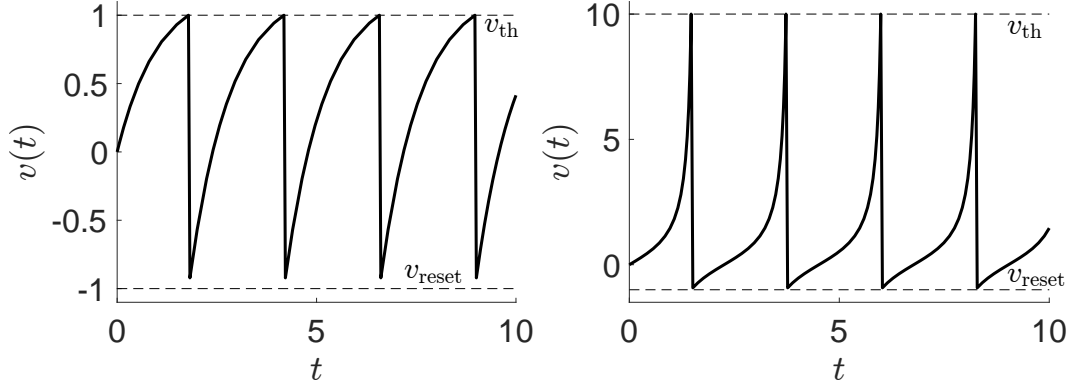


Figure 2.5.: Integrate-and-fire (2.17), (2.18), solutions for the LIF model (left), with  $I = 1.2$ ,  $\tau = 1$ ,  $v_{th} = 1$ , and  $v_{reset} = -1$ , and the QIF model (right), with  $I = 1$ ,  $v_{th} = 10$ , and  $v_{reset} = -1$ .

voltage variable,  $v$ , modelling the neuronal membrane potential of a single neuron, driven by some current  $I$ , as

$$\frac{dv}{dt} = g(v) + I, \quad (2.17)$$

with a firing threshold,  $v_{th}$ , such that once  $v$  reaches  $v_{th}$  from below at some time  $T$ , the voltage is *reset*, to some value  $v_{reset} < v_{th}$ , according to the firing-reset rule

$$v(T^-) = v_{th}, v'(T^-) > 0, \quad \Rightarrow \quad v(T^+) = v_{reset}, \quad (2.18)$$

where  $T^\pm = \lim_{\epsilon \searrow 0} (T \pm \epsilon)$  denote the times immediately after and before the firing time,  $T$  [31]. The function  $g$  defines the type of IF model. Two important models in this class are the linear integrate-and-fire (LIF) model<sup>3</sup>, generated by  $g(v) = -v/\tau$  for some timescale  $\tau$  [130], and the quadratic integrate-and-fire (QIF) model, generated by  $g(v) = v^2$  [195]. See Figure 2.5 for illustrations of the dynamics generated by the LIF and QIF models.

With an initial condition  $v(0) = v_{reset}$ , the general IF model (2.17) qualitatively captures spikes at time  $mT$ ,  $m \in \mathbb{Z}$  if  $I$  is constant, or at the generalised times  $T_m$  if  $I = I(t)$ . There is no underlying biophysical modelling

<sup>3</sup> This is sometimes referred to as the *leaky* IF model in the literature.

here, and there is no attempt to capture the shape of a spike, as the Hodgkin-Huxley model does (see Figure 2.4), but nonetheless, the qualitative spiking features are captured and are consistent with the process being modelled. An IF model with an adaptive threshold has been shown to mostly capture the voltage dynamics of a real neuron, driven by a fluctuating current, where the model is driven by the same current [83]. Thus, even relatively simple models such as the IF model can effectively capture neuronal dynamics.

In the form given here (2.17), the IF model does not account for the signals received from pre-synaptic neurons. We discuss synaptic modelling in the following section.

## 2.4 SYNAPSE MODELLING

Individual neurons are connected to each other at synapses, joining the axons of pre-synaptic neurons to the dendrites of post-synaptic neurons, as illustrated in Figure 2.1. Figure 2.2 outlines the events involved in the generation of a post-synaptic current via a cascade of biochemical reactions causing a change in the post-synaptic membrane potential [219].

The post-synaptic current which arises as a result of synaptic activity can be described by  $I_{\text{syn}} = -g_{\text{syn}}u(v - v_{\text{syn}})$ , where  $g_{\text{syn}}$  is a constant defining the overall strength of synaptic conductance interaction,  $u$  defines the scaled synaptic activity, and  $v$  and  $v_{\text{syn}}$  are the membrane potential and the reversal potential of the post-synaptic neuron respectively. For some action potential arriving at the pre-synaptic terminal at a time  $T > 0$ , the post-synaptic conductance takes the form  $u(t) = \eta(t - T)$ , where  $\eta(t)$  describes the shape of the post-synaptic response to the arrival of a pre-synaptic action potential. Synaptic interactions are assumed to be causal, that is, a pre-synaptic action potential cannot elicit a post-synaptic response occurring in the past. This is captured by the causality condition,  $\eta(t) = 0$  for  $t < 0$ .

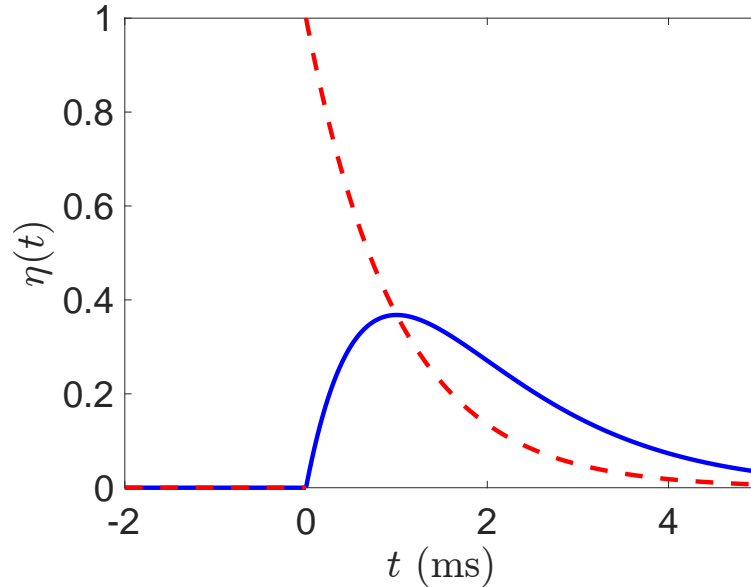


Figure 2.6.: Two different post-synaptic response functions  $\eta(t)$ : exponential decay (red, dashed curve) and the rise and fall  $\alpha$ -function (blue, solid curve), with  $\alpha = 1$  in both cases. The causality condition is captured by  $\eta(t) = 0$  for  $t < 0$ .

The most basic synaptic model assumes *pulsatile coupling*,

$$\eta(t) = \delta(t), \quad (2.19)$$

where  $\delta(\cdot)$  is a Dirac delta function. This captures the transfer of information at a synapse, albeit in a rather crude way in that, here, the post-synaptic response to a pre-synaptic action potential is instantaneous. However, quantities of neurotransmitter traversing the synaptic cleft decay (on the order of milliseconds) after they initially enter the cleft. A modified *exponential decay* model incorporating this behaviour takes the form

$$\eta(t) = \alpha e^{-\alpha t} H(t), \quad (2.20)$$

where  $H(\cdot)$  is a Heaviside function, describing the causality condition, and  $\alpha$  is the rate of decay of the response. As well as the decay of quantities of neurotransmitters over time, it takes a finite amount of time for neurotransmitters to *traverse* the synaptic cleft before arriving at the post-synaptic

terminal. This is adequately described by the *rise and fall* model, given by the  $\alpha$ -function

$$\eta(t) = \alpha^2 t e^{-\alpha t} H(t), \quad (2.21)$$

where  $1/\alpha$  is the finite time-to-peak of the post-synaptic response. The  $\alpha$ -function captures the finite time taken by neurotransmitter particles to cross the synaptic cleft by the small response for small times after  $t = 0$ . The response peaks at some finite time, and subsequently decays. The contrast between the exponential decay and rise and fall responses is shown in Figure 2.6. A point of further model improvement revolves around the immediate rise in the post-synaptic response. A more accurate reflection of the finite time taken for neurotransmitters to arrive at the post-synaptic terminal would require a response function which is held essentially at zero for some *traversal time*,  $\zeta$ , before taking the shape of the rise and fall response. Such a function could be described by  $\eta(t) = \alpha^2 (t - \zeta) e^{-\alpha(t-\zeta)} H(t - \zeta)$ . It should also be noted that a non-zero time is taken for a response to be induced in the post-synaptic neuron. A trade-off must be made between accuracy and convenience. The rise and fall operator is a relatively simple function with convenient properties, and so is an adequate choice for post-synaptic response in the majority of cases.

A neuron typically receives multiple incoming synaptic signals (often from multiple neurons). Assuming a similar post-synaptic response for each signal received, the overall post-synaptic response to a train of  $m$  action potentials, arriving at times  $T^m$ ,  $m \in \mathbb{Z}$ , may be modelled as

$$u(t) = \sum_{m \in \mathbb{Z}} \eta(t - T^m). \quad (2.22)$$

This is illustrated for an incoming train of three spikes in Figure 2.7 for  $\eta(t)$  given by (2.21).

For a function  $\eta$  which is a Green's function of a differential operator  $Q$ , so that  $Q\eta = \delta$ , (2.22) may be rewritten as

$$Qu(t) = \sum_{m \in \mathbb{Z}} \delta(t - T^m). \quad (2.23)$$

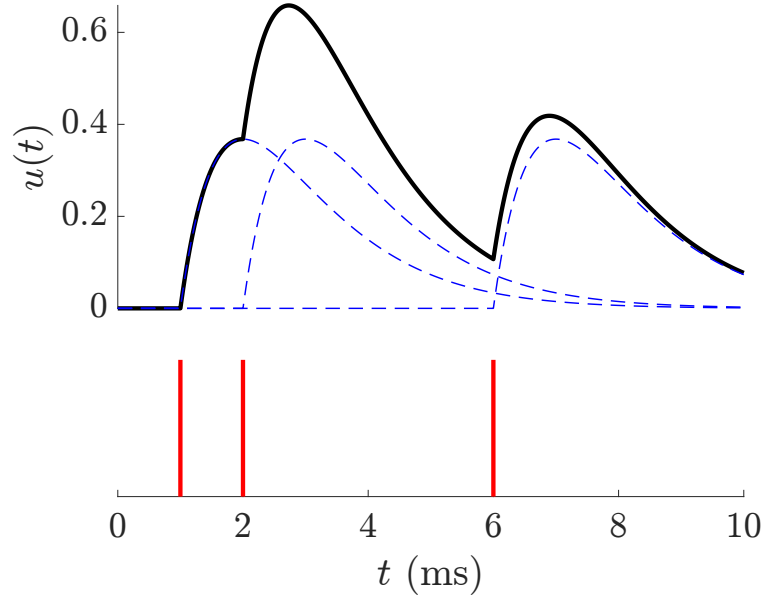


Figure 2.7.: The post-synaptic response  $u(t)$  (black curve) to a train of  $m = 3$  spikes, illustrating how the overall synaptic response sums the conductance changes,  $\eta(t - T_i)$ ,  $i = 1, 2, 3$  (blue dashed curves), arising from individual action potential spikes (illustrated in red) arriving to the pre-synaptic terminal at times  $T_1 = 1$ ,  $T_2 = 2$ ,  $T_3 = 6$ . The rise and fall synaptic response (2.21) for  $\eta$  is used here, with  $\alpha = 1$ .

The three different types of synaptic response considered above are all Green's functions to different linear differential operators. Pulsatile coupling (2.19) corresponds to the zeroth-order operator  $Q = 1$ . Exponential decay (2.20) corresponds to the first-order linear differential operator<sup>4</sup>

$$Q = \left(1 + \frac{1}{\alpha} \frac{d}{dt}\right), \quad (2.24)$$

and the rise and fall  $\alpha$ -function, (2.21), is the Green's function of the second-order linear differential operator

$$Q = \left(1 + \frac{1}{\alpha} \frac{d}{dt}\right)^2. \quad (2.25)$$

---

<sup>4</sup> A calculation showing that the exponential decay function is the Green's function of this first-order differential operator is given in Appendix A.1.

## 2.5 FROM SPIKING MODELS TO RATE-BASED MODELS

A spiking single neuron synapse model given by (2.22) has the equivalent representation

$$u(t) = \int_{-\infty}^{\infty} \eta(s) \sum_{m \in \mathbb{Z}} \delta(s - (t - T^m)) ds, \quad (2.26)$$

so that  $u$  is the temporal convolution of a synaptic response function  $\eta$ , with a spike train  $\sum_{m \in \mathbb{Z}} \delta(t - T^m)$ . To see how a firing rate model may arise, take a short-time average  $\langle \cdot \rangle_{\tau}$  of  $u(t)$  over some time window  $\tau$ , defined as

$$\langle u(t) \rangle_{\tau} = \frac{1}{\tau} \int_t^{t+\tau} u(t') dt', \quad (2.27)$$

Then upon averaging (2.26),

$$\langle u(t) \rangle_{\tau} = \int_{-\infty}^{\infty} \eta(s) \left( \frac{1}{\tau} \int_t^{t+\tau} \sum_{m \in \mathbb{Z}} \delta(s - t' + T^m) dt' \right) ds. \quad (2.28)$$

Now making the assumption that  $u(t)$  varies sufficiently slowly so that  $\langle u(t) \rangle_{\tau} \simeq u(t)$  is constant, (2.28) reduces to

$$u(t) = \int_{-\infty}^{\infty} \eta(s) R(t - s) ds, \quad (2.29)$$

where the rate  $R(t)$  effectively counts the numbers of spikes per unit time  $\tau$ , and is defined as

$$R(t) = \frac{1}{\tau} \int_t^{t+\tau} \sum_{m \in \mathbb{Z}} \delta(T^m - t') dt'. \quad (2.30)$$

Heuristically, the spike train  $\sum_{m \in \mathbb{Z}} \delta(s - t + T^m)$  in (2.26) is replaced by a firing rate  $R(t - s)$ . The exact form of the firing rate is model-dependent. For a linear IF model (2.17, 2.18,  $g(v) = -v/\tau_m$ ) with the addition of a constant synaptic input  $u$  and an absolute refractory period  $\tau_R$ , the firing rate is given by<sup>5</sup>

$$R = \left( \tau_R + \tau_m \log \left( \frac{u - v_{\text{reset}}}{u - v_{\text{th}}} \right) \right)^{-1} H(u - v_{\text{th}}), \quad (2.31)$$

<sup>5</sup> See Appendix A.2 for a derivation of the firing rate for a linear and a quadratic IF model.

where the condition  $u > v_{\text{th}}$  must be true in order for firing events to occur. The firing rate for the QIF model (2.17, 2.18,  $g(v) = v^2$ ) with constant synaptic forcing  $u$  in the limits  $v_{\text{th}} \rightarrow \infty$ ,  $v_{\text{reset}} \rightarrow -\infty$ , takes the form<sup>5</sup>

$$R = \frac{1}{\pi} \sqrt{I+u} H(I+u). \quad (2.32)$$

Thus for *slowly varying* synaptic input  $u(t)$ , a natural leading order choice of firing rate function  $R(t)$  is the one corresponding to constant input  $R$ , such that  $R(t) = f \circ u(t)$  for a firing rate  $f$  composed with  $u$ . In (2.29) this gives rise to the rate-based model

$$u(t) = \int_{-\infty}^{\infty} \eta(s) f(u(t-s)) ds. \quad (2.33)$$

The IF and QIF firing rates are logarithmic and square root in shape, respectively. Three different ways of obtaining rate-based models from spiking models are given in [65]. The derivation shown above is not exact and has relied on the assumption of slow synapses. However, models often incorporate firing rates which are qualitatively similar to the IF and QIF rates. Sigmoidal functions of  $u$  are typically used.

Spiking models return precise information on spike timings, while their rate-based reductions instead give information on the relative firing rate of a neuron. This is illustrated well in Figure 2.8 where the firing rate is shown to be zero when a model neuron is not spiking. As the number of spikes per unit time increases, the output of the firing rate model increases. While rate-based models do not yield precise spike timings, they do an excellent job of capturing the time duration of a burst of spikes.

The importance of individual spikes vs. rates in neural computation is currently an open question in the field [28]. Rate-based descriptions allow for a simplified description of a spiking model; Montbrió, Pazó, and Roxin [150] developed a rate-based model showing that the dynamics of a network of quadratic integrate-and-fire model neurons are exactly described by an appropriate firing rate description [150]. Traditionally, rate-based models have failed to capture spike synchronisation effects, link to biophysical parameters, and describe finite-size fluctuations [190]. The *next generation* of

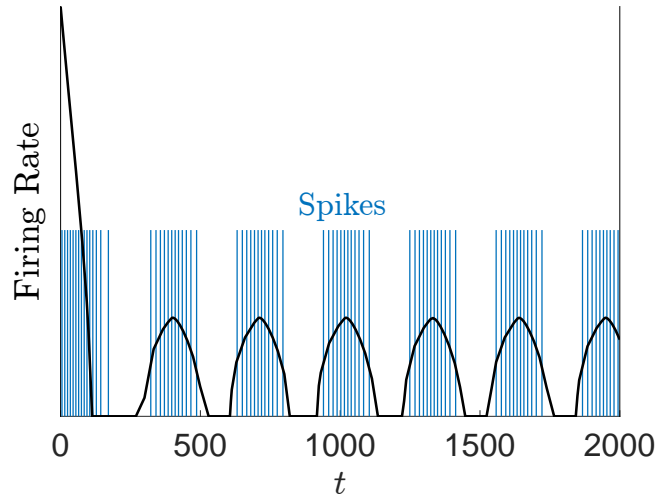


Figure 2.8.: Illustration of the difference in information obtained from a spiking model (blue spikes) and its rate-based reduction (black curve). When many spikes occur in a short period in the spiking model, this is reflected by a higher activity in the rate-based model.

neural field models, beginning with the work in [137, 150], addresses some of these shortcomings [33]. The advantage of rate-based models is they admit a low-dimensional description of a high dimensional (spiking) problem. Individual spikes are washed out in this description, but model simplification allows for more tractable analysis to be carried out. Whether or not rate-based or spiking models are appropriate for study depends on the problem under consideration.

## 2.6 FROM SINGLE NEURONS TO NETWORKS AND SPATIAL FIELDS

So far, we have considered the synaptic dynamics of a *single* post-synaptic neuron. Neurons exist in connected networks and so here, we include a notion of network connectivity into a description of synaptic dynamics. Consider a continuum of neurons with position  $x \in \mathbb{R}$ . Then in general, a framework must provide the capability for a patch of tissue at a location  $x$  to be able to receive input from anywhere else in the domain. There-

fore, the synaptic source,  $\psi$ , is modified by convolving a spike train with a description of network connectivity as

$$\psi(x, t) = w \otimes \sum_{m \in \mathbb{Z}} \delta(t - T^m(x)), \quad (2.34)$$

where the symbol  $\otimes$  represents a spatial convolution, defined as

$$(w \otimes g)(x, t) = \int_{-\infty}^{\infty} w(x - y)g(y, t)dy. \quad (2.35)$$

A useful property of convolutions that is used throughout this thesis is commutativity:  $F \otimes G = G \otimes F$  for arbitrary functions  $F$  and  $G$ .

Equation (2.34) filters spikes occurring across the domain by how they are connected to tissue at  $x$  at a time  $t$ . Here, the connectivity function  $w$  is distance-dependent:  $w = w(x - y)$ . Further, it has been modelled as constant in time. However, in studies of network plasticity, in which changes may occur in the connectivity structure of the brain due to learning – for example, in developing infants [36] – the temporal evolution of the connectivity description is important. The assumption of distance-dependent connectivity may be relaxed too, in which case,  $w = w(x, y, t)$  is a more appropriate description of evolving structural connectivity.

For a source of synaptic activity given by (2.34), the synaptic activity  $u$ , evolves according to  $Qu = \psi$ . Written in full, this is

$$Qu(x, t) = w \otimes \sum_{m \in \mathbb{Z}} \delta(t - T^m(x)). \quad (2.36)$$

Equation (2.36) is in the form of a differential operator acting on  $u$  and is equivalent to the (temporal) integral formulation

$$u(x, t) = \eta * w \otimes \sum_{m \in \mathbb{Z}} \delta(t - T^m(x)), \quad (2.37)$$

where the symbol  $*$  represents a temporal convolution, defined as

$$(\eta * g)(x, t) = \int_{-\infty}^{\infty} \eta(t - s)g(x, s)ds. \quad (2.38)$$

Both differential (2.36) and integral (2.37) formulations are commonly used interchangeably throughout the literature. This spiking model describes the

effect on synaptic activity of idealised spikes, described by delta functions, arriving at a synapse at position  $x$  at times  $T^m$  and causing a post-synaptic response.

As shown in the previous section, spiking models may be reduced to rate-based models if the synaptic response evolves on a slower time-scale than the mean inter-spike interval,  $T^m - T^{m-1}$ . This is typically the case if  $\alpha \ll 1$  in (2.20) and (2.21). Then the spike train may be replaced by a function describing the tissue firing rate [45, 27, 64, 6] as

$$(Qu)(x, t) = (w \otimes f \circ u)(x, t), \quad (2.39)$$

where  $f$  describes the average rate of spikes over a number of mean inter-spike intervals [6]. It is typically a sigmoidal function of  $u$ , generating a feedback loop wherein tissue with high synaptic activity drives more activity to connected tissue. Models of the form (2.39) are referred to as *neural field* models of synaptic activity.

The transition to networks of connected neurons – rather than to continuum fields – is in essence identical to what has been shown above, with the difference that instead of considering a continuum field  $x \in \mathbb{R}$ , a network of spiking neurons  $i \in \{1, \dots, n\}$ , with synaptic activity  $u_i$  is considered. The structural connectivity of a network of connected neurons is described by a weight matrix,  $W_{ij}$ . The synaptic drive to the  $i$ th neuron is given by

$$\psi_i(t) = \sum_{j=1}^n W_{ij} \sum_{m \in \mathbb{Z}} \delta(t - T_j^m) \quad (2.40)$$

and in an analogous manner to Section 2.5 the spike train  $\sum_{m \in \mathbb{Z}} \delta(t - T_i^m)$  may be replaced by a firing rate  $R_i$  for the  $i$ th neuron in the network under the assumption of slow synaptic activity (in the  $i$ th neuron) to give the discrete rate-based model of synaptic drive

$$\psi_i(t) = \sum_{j=1}^n W_{ij} R_j. \quad (2.41)$$

This is fed into the dynamics for  $u$  as

$$Qu_i(t) = \psi_i(t). \quad (2.42)$$

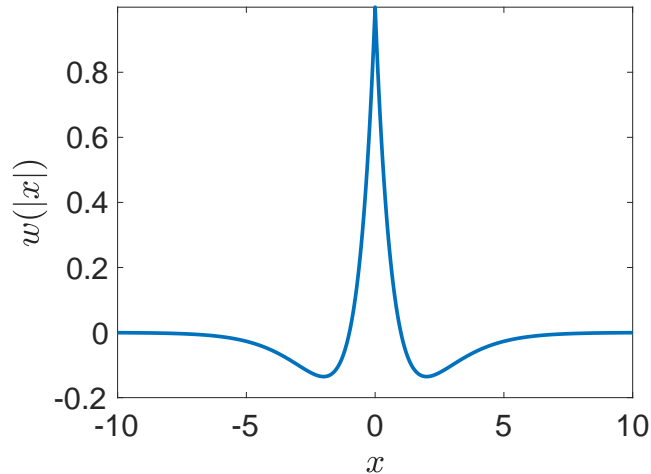


Figure 2.9.: An illustration of the wizard hat connectivity function given by  $w(x) = (1 - |x|)e^{-|x|}$ . Where  $w(x)$  is above zero, connections are excitatory, while below zero, connections are inhibitory.

## 2.7 DEVELOPMENTS: NETWORKS AND NEURAL FIELDS

A seminal work in neural field modelling is that of Wilson and Cowan [228, 229]. They developed a deterministic model for the dynamics of neural populations on the basis that, while local interactions between single neurons is largely a random/stochastic process, on the macroscale, such randomness “gives rise to quite precise long-range interactions.” The idea is similar in spirit to the following: at the macroscale, fluid flow can appear very orderly, yet at the microscale, one observes Brownian motion [228].

Their model is a study of populations of cells, rather than individual neurons. Indeed, there is evidence that “*even within relatively small volumes of cortical tissue, there exist many cells with very nearly identical responses to identical stimuli*” [228, 151]. Their model includes *inhibitory* as well as excitatory populations of neurons, along with refractoriness.

### 2.7.1 The Amari Neural Field Model

Subsequent to the work of Wilson and Cowan, Amari [5] introduced a single-layer neural field with dynamics given by

$$\tau \frac{\partial u}{\partial t} = -u(x, t) + \int_{-\infty}^{\infty} w(x, y) f(u(y, t)) dy + s(x, t), \quad (2.43)$$

where  $u(x, t)$  is the average membrane potential of tissue at  $(x, t)$ . If the connectivity function between neurons from a position  $x$  to a position  $y$  is purely distance-dependent (referred to as a homogeneous field by Amari in [5]), then  $w(x, y) = w(|x - y|)$ . This is assumed to be the case in the following discussion. The shape of  $w(x)$  is important in describing the underlying architecture that is being modelled. In one spatial dimension, a functional form typically chosen for  $w$  to make patterns is the so-called “wizard hat” connectivity given by  $w(x) = (1 - |x|)e^{-|x|}$ . This is an effective model of a mixed population of excitatory and inhibitory interacting neurons. Figure 2.9 illustrates this, where  $w(x)$  takes values either side of zero. Other connectivity functions can of course be chosen, such as the purely inhibitory connectivity used in models of thalamic tissue [148, 176].

A model assumption allowing for a mathematically tractable analysis is that the sigmoidal firing rate function  $f$  takes the form of a Heaviside function:  $f(u) = H(u - h)$ , where  $h$  is a firing threshold. This all-or-nothing response is not required for the formation of the patterns seen in neural fields [5], but rather, it is an aid in constructing patterns and analysing their stability. Such a firing rate description may be obtained by taking the limit as the steepness of a sigmoidal function is continually increased. Amari proceeded to analytically construct a stationary bump solution in the absence of any external stimulus  $s(x, t)$  as follows. Stationary solutions to (2.43) are given by removing any explicit time-dependence as

$$u(x) = \int_{-\infty}^{\infty} w(x - y) H(u(y) - h) dy. \quad (2.44)$$

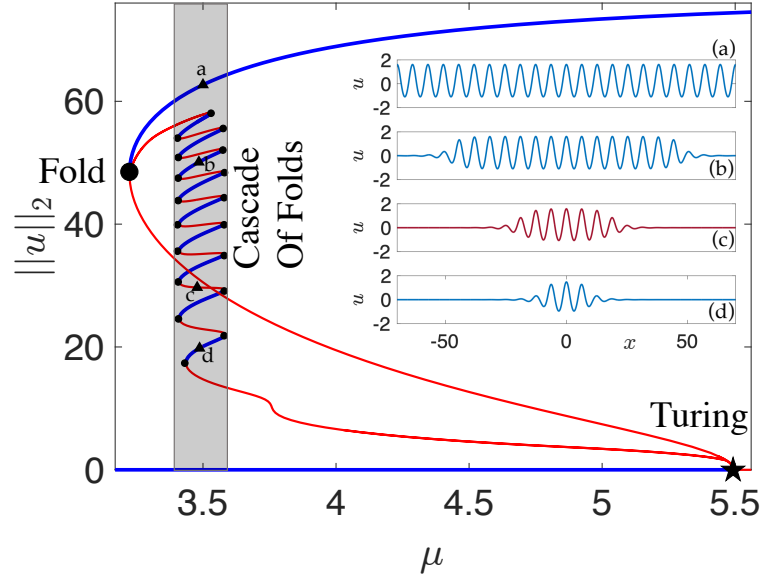


Figure 2.10.: A snaking bifurcation diagram for (2.43) with a sigmoidal firing rate  $f(u; \mu, \theta) = \frac{1}{1+e^{-\mu u+\theta}} - \frac{1}{1+e^{\theta}}$  with steepness  $\mu$  centred at  $\theta$ , and connectivity  $w(|x|) = e^{-bx}(b \sin(x) + \cos(x))$ . The norm of the spatial solution is plotted against the bifurcation parameter  $\mu$ . Insets correspond to the appropriately labelled triangles. Parameter values are  $\theta = 2.5$ , with  $\tau = 1$  and  $s(x, t) = 0$  in (2.43).

Then a simple bump solution is characterised by the condition  $x \in (a_1, a_2)$ ,  $u(x) > h$  for some constant locations  $a_1 < a_2$  (and  $u(x) < h$  outside of this interval). In this way, one obtains

$$u(x) = \int_{a_1}^{a_2} w(x-y)dy. \quad (2.45)$$

The two conditions  $u(a_1) = h$ ,  $u(a_2) = h$  uniquely determine the two unknowns  $a_1, a_2$ .

For smooth sigmoidal firing rate functions, other techniques are available to modellers, including numerical continuation techniques, which allows for the continuation of a solution branch through parameter space. Coupled with a numerical stability routine, such techniques are noteworthy for their ability to provide insight about a model away from the Heaviside limit. We expose this in greater detail in Chapter 3, but we give a flavour of the

insights which continuation techniques yield in Figure 2.10. Solutions to the Amari neural field are *continued* in parameter space, meaning the change in the asymptotic solution profile is tracked as a parameter is varied. The 2-norm of the solution,  $\|\cdot\|_2$ , is a measure of the magnitude of activity and is plotted against the bifurcation parameter. Three different spatially extended solutions are projected into the parameter, norm space: the spatially homogeneous steady state, with  $\|u\|_2 = 0$ , which undergoes a Turing bifurcation at the star ( $\star$ ), and the two additional unstable (signified by the colour red) patterns which bifurcate from this, which are a localised solution (lower red branch) and a spatially periodic solution (upper branch). The unstable spatially periodic bumps increase in activity as  $\mu$  is decreased until a fold point is reached at  $\mu = 3.3$ , denoted by the large black circle ( $\bullet$ ). At this point, the periodic bumps stabilise (the curve is blue beyond the fold point) and continue to grow in activity as  $\mu$  increases.

A *snaking* structure in continuation space exists for the localised solution and can be seen in the grey shaded region of parameter space. Multiple stable (blue) and unstable (red) solutions co-exist via a cascade of fold bifurcations, represented by smaller black circles ( $\circ$ ). Examples of the spatial profiles of patterns along the snaking branch marked by small black triangles ( $\blacktriangle$ ) are shown in the inset. The localised pattern spreads out in space, with more bumps forming as the snaking branch is traversed upwards in increasing norm. The snaking branch terminates by joining to the fold of periodic bumps. This analysis is carried out away from the Heaviside limit, with a sigmoidal firing rate function. In [172], the authors continue steady state patterns analogous to those in Figure 2.10 in two spatial dimensions, with their results “forming a basis for the general study of localised cortical activity”.

The work of Wilson, Cowan, and Amari has had a profound influence on the field of theoretical neuroscience, with neural fields and variants being used as a basis for modelling visual hallucinations [66, 172], the role of the hippocampus in memory function [91], and the onset of epilepsy [196]

to name just a few applications. With the development of computational techniques and efficient ways of implementing these, there is now a large toolbox of analytical and numerical techniques that may be applied to the study of neural systems. The reader is referred to [208, 46] for a review of neural fields from a mathematical point of view.

### 2.7.2 *A Model of Spike Frequency Adaptation*

Spike frequency adaptation (SFA) is the phenomenon in which the firing rate of a neuron decreases when exposed to a continuous stimulus of constant intensity [166, 198]. It is a common, experimentally observed feature of neural dynamics [82]. In 2014, Ermentrout, Foliás, and Kilpatrick [67] studied a model of SFA by considering pattern formation in neural fields with linear adaptation. That is to say, they studied the dynamics of

$$\tau \frac{\partial u}{\partial t} = -u(x, t) + \int_{-\infty}^{\infty} w(x - y) f(u(y, t)) dy - \beta v(x, t) + I(x, t), \quad (2.46a)$$

$$\frac{1}{\alpha} \frac{\partial v}{\partial t} = -v(x, t) + u(x, t), \quad (2.46b)$$

where  $u(x, t)$  denotes synaptic activity as before, and the local negative feedback  $v(x, t)$  models the effects of spike frequency adaptation at rate  $\alpha$  and strength  $\beta$  [19]. Finally, the function  $I(x, t)$  is an external drive to the system; see [235] for an investigation of a spatially localised drive on bumps in a Wilson-Cowan-type model. In the absence of external drive, they derive the amplitude equations describing solutions that emerge at the onset of bifurcation from the homogeneous steady state in one- and two-spatial dimensions. Amplitude equations are derived by carrying out a weakly non-linear analysis about a Turing instability point [160]. In both one- and two-spatial dimensions, there are two ways for the steady state to go unstable: a real eigenvalue crosses the imaginary axis, or a complex conjugate pair of eigenvalues crosses the imaginary axis. Emergent solutions were stationary periodic patterns, standing waves, or travelling waves, with richer

dynamics seen in two spatial dimensions, including spots, stripes, squares, and hexagons, as well as travelling and time-periodic variants of these.

With the inclusion of the external drive, standing bump solutions exist, which destabilise into so-called “sloshers”. Where a breather can be thought of as oscillating “up and down” in time in terms of activity in a space-time plot, sloshers are solutions which appear to oscillate (or “slosh”) to-and-fro (or “left and right”) about the location of drive. Travelling bump solutions destabilise into “sloshing pulse” solutions. These are characterised by a “side-to-side” movement which sits atop a travelling pulse. They have a well-defined wavespeed, and yet cannot be constructed as *stationary* solutions in a co-moving frame (examples of this phenomenon are shown in [67]). This is illustrative of the rich dynamics that are present in neural field-type models.

### 2.7.3 Inhibitory Neural Network Models of Thalamic Tissue

The success of the Hodgkin-Huxley model has paved the way for many biophysical descriptions of single-cell dynamics which are constructed in the same spirit. In 1994, Wang [220] developed a single-cell model capturing the important features displayed by a thalamic relay neuron, namely burst firing upon release from hyperpolarisation, and tonic (periodic) firing when depolarised from rest. Rinzel et al. [178] considered a simplification of Wang’s single-cell model, reducing from six to three relevant ionic currents and applied it to a network of inhibitory connected neurons. In one spatial-dimensional,  $x \in \mathbb{R}$ , the current balance equation in this model is given by the Hodgkin-Huxley-type equation,

$$C_m \frac{\partial V}{\partial t} = -I_L - I_T - I_{\text{syn}}, \quad (2.47)$$

where  $V$  is the membrane potential, and the three relevant currents on the right-hand side are the leak-, T-type  $\text{Ca}^{2+}$ -, and synaptic-currents, respectively. They take the forms  $I_L = g_L(V - V_L)$ ,  $I_T = g_T m_\infty(V) h(V - V_{\text{Ca}})$ , and  $I_{\text{syn}} = g_{\text{syn}} s_{\text{tot}}(x, t) (V(x, t) - V_{\text{syn}})$ . The constants  $g_\mu$ , and  $V_\mu$ ,  $\mu \in$

$\{L, T, \text{syn}\}$  represent an overall conductance strength and the reversal potential for each current, respectively. The variable  $h$  models the de-inactivation of T-type calcium channels, and evolves according to

$$\frac{\partial h}{\partial t} = \phi \frac{h_{\infty}(V) - h}{\tau_h(V)}, \quad (2.48)$$

where the constant  $\phi$  is a scaling for the the voltage-dependent timescale  $\tau_h(V) = \tau_0 + \tau_1 / (1 + \exp((V + 50)/3))$ . The total synaptic activity at  $x$ , is given as

$$s_{\text{tot}}(x, t) = \int_{-\infty}^{\infty} w(x - y) s(y, t) dy,$$

where the total synaptic activity at  $x$  at time  $t$  consists of a weighted sum of synaptic activity elsewhere in the tissue. The tissue connectivity determines this weighting. Rinzel et al. used the connectivity

$$w(x) = A \exp(-x^2/\lambda^2) \left(1 - \gamma \exp(-x^2/\lambda_{\text{gap}}^2)\right), \quad (2.49)$$

where  $A$  is chosen so  $w(x)$  is normalised to 1. The parameters  $\lambda$  determines the spatial scale, while  $\gamma$  determines whether connectivity is on-centre or off-centre (these are defined below). If connectivity is off-centre,  $\lambda_{\text{gap}}$  defines the gap between peaks in the connectivity function. The local synaptic activity  $s(x, t)$ , evolves according to

$$\frac{\partial s}{\partial t} = k_f s_{\infty}(V)(1 - s) - k_r s, \quad (2.50)$$

for saturation and decay rates  $k_f$  and  $k_r$ . The sigmoidal activation functions are given by

$$\begin{aligned} m_{\infty}(V) &= 1/(1 + \exp(-(V + 40)/7.4)), \\ h_{\infty}(V) &= 1/(1 + \exp((V + 70)/4)), \\ s_{\infty}(V) &= 1/(1 + \exp(-(V + 35)/2)), \end{aligned}$$

and are all shown in Figure 2.11 for parameters used in [178].

Figure 2.12 illustrates the on-centre and off-centre coupling used by Rinzel et al. [178] in their study. For on-centre coupling, the synaptic architecture is such that a patch of neuronal tissue receives the majority of input from

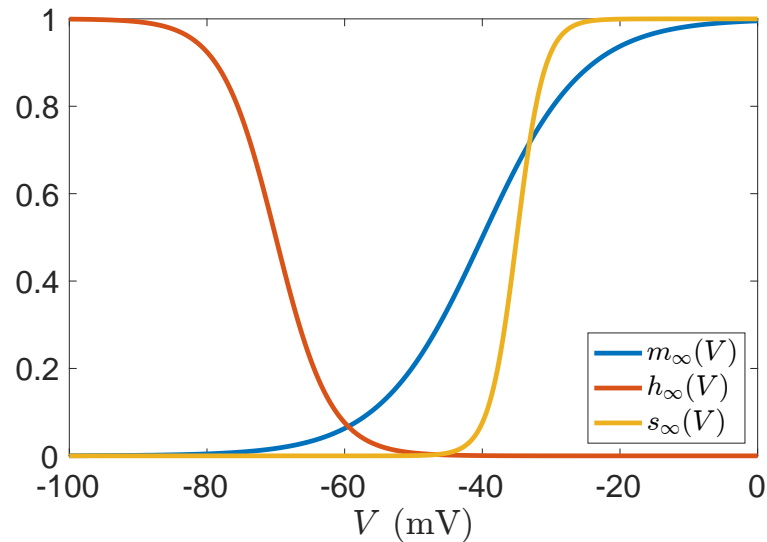


Figure 2.11.: An illustration of the three functions  $m_\infty(V)$  (blue),  $h_\infty(V)$  (orange) and  $s_\infty(V)$  (yellow) in the model (2.47, 2.48, 2.50) for the parameter values in [178].

itself and its nearby neighbours. Interaction strength drops off for tissue further away. For off-centre coupling, interaction strength with tissue in the immediate vicinity is small but grows to some maximum at an intermediate distance. Beyond this, interaction strength again decays away.

In the case of on-centre coupling, *lurching*-type solutions, shown in Figure 2.13, were seen in which activity spreads in a saltatory rather than smooth fashion. A difficulty in studying these waves is that they do not have a well-defined co-moving frame, although their wave-speed appears to be determinable (if not analytically, then certainly numerically by, for example, calculating the slope of the line passing through the outer activity in the space-time plot). Rinzel et al. observed “*highly chaotic fluctuations between spikes, generated completely by deterministic network dynamics*”. Coombes (2005) [45] characterised the lurching speed by considering the temporal period and characteristic length scale of a lurch [44], in a different model to that considered by Rinzel et al. Smooth travelling waves were numerically shown to be a viable solution for off-centre coupling. For the parameters

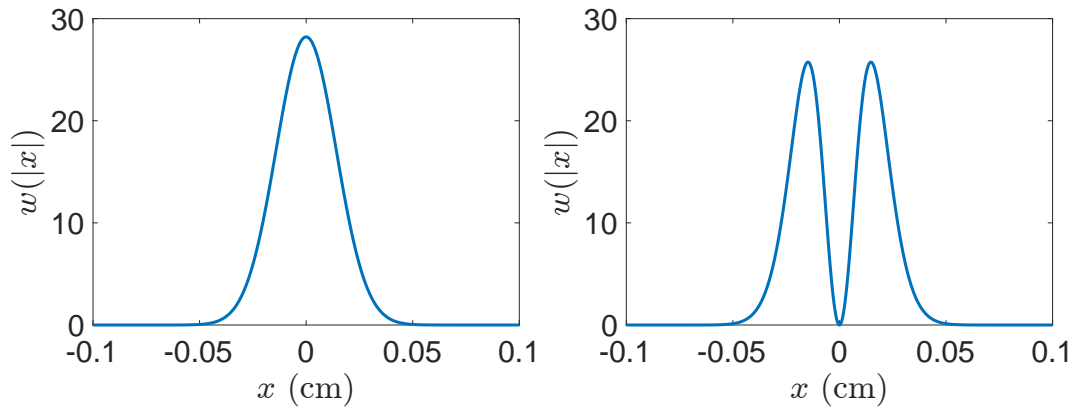


Figure 2.12.: An illustration of on-centre (left) and off-centre (right) coupling as used by Rinzel et al. [178].

used, Rinzel et al. [178] showed that the wave speed was around  $0.6\text{mm s}^{-1}$ .

The inactivation dynamics of the T-type  $\text{Ca}^{2+}$  current generates the PIR events seen in this model. PIR only generates firing events once a sufficient amount of applied inhibition wears off. A consequence of this is that wave speeds are much slower in models that rely upon PIR as a mechanism to generate waves as opposed to excitatory coupling. When connectivity is on-centre, this model incorporates self-inhibition, meaning that if a cell is firing, it receives inhibitory input from itself. Consequently, PIR firing events in this case are brief. Indeed, within a reasonable parameter regime, cells need to receive many bouts of brief inhibitory synaptic input in order for their PIR mechanism to be adequately primed to enable rebound upon release [178]. Let  $\tau_{\text{syn}} = (k_r)^{-1}$  denote the time constant for the decay of synaptic input. The more time a cell spends in the hyperpolarised state, the longer it takes to fire. A result of this is that a lurching wave slows if cells require longer bouts of hyperpolarisation before rebound. However, the rebound will be stronger since a larger proportion of channels will be de-inactivated due to the increased time spent in a hyperpolarised state. Stronger rebound results in more robust PIR patterning. Rinzel et al. noted that if  $\tau_{\text{syn}}$  is too small, then synaptic inhibition becomes too brief to yield PIR firing and in this case the wave cannot persist and disappears. PIR waves leave a train of

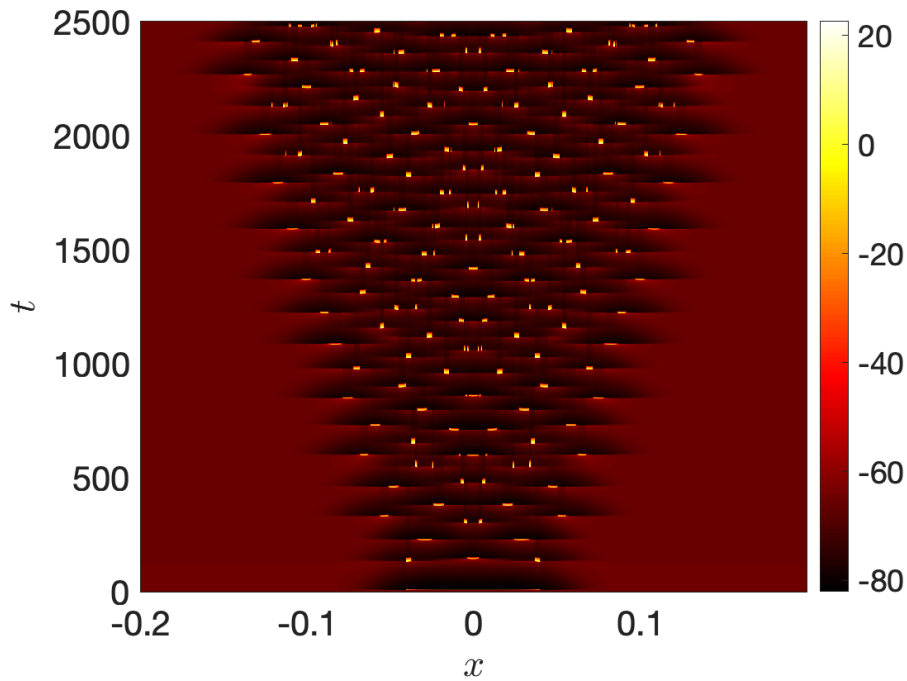


Figure 2.13.: Lurching waves, seen in the model (2.47, 2.48, 2.50) with on-centre connectivity. They travel across the domain in a highly saltatory manner. Parameters are  $\phi = 1.3$ ,  $\lambda = 0.02\text{cm}$ ,  $\lambda_{\text{gap}} = 0.014\text{cm}$ ,  $k_f = 0.5 \text{ ms}^{-1}$ ,  $k_r = 0.025 \text{ ms}^{-1}$ ,  $\gamma = 0$  (on-centre connectivity),  $C_m = 1 \mu\text{F}/\text{cm}^2$ ,  $\tau_0 = 30\text{ms}$ ,  $\tau_1 = 500\text{ms}$ ,  $g_L = 0.4 \text{ mS}/\text{cm}^2$ ,  $g_T = 1.5 \text{ mS}/\text{cm}^2$ ,  $g_{\text{syn}} = 5 \text{ mS}/\text{cm}^2$ ,  $V_L = -70\text{mV}$ ,  $V_{\text{Ca}} = 90\text{mV}$ ,  $V_{\text{syn}} = -85\text{mV}$ .

synaptic inhibition in their wake [178] which can, and often does, promote subsequent rebound events as illustrated in Figure 2.13. Thus instead of a solitary travelling pulse, PIR models often have families of travelling pulses. This phenomenon allows for the formation of highly complicated dynamics from relatively simple initial conditions.

The model described by (2.47, 2.48, 2.50) is a reduction of a two-layer description of the thalamo-cortical relay network found in the brain. Thalamo-cortical cells (TC) and reticular nucleus (RE) cells are connected as shown in Figure 2.14. The TC cells receive inhibitory input from RE cells, priming them for rebound. Upon recovery from hyperpolarisation, the TC cells fire.

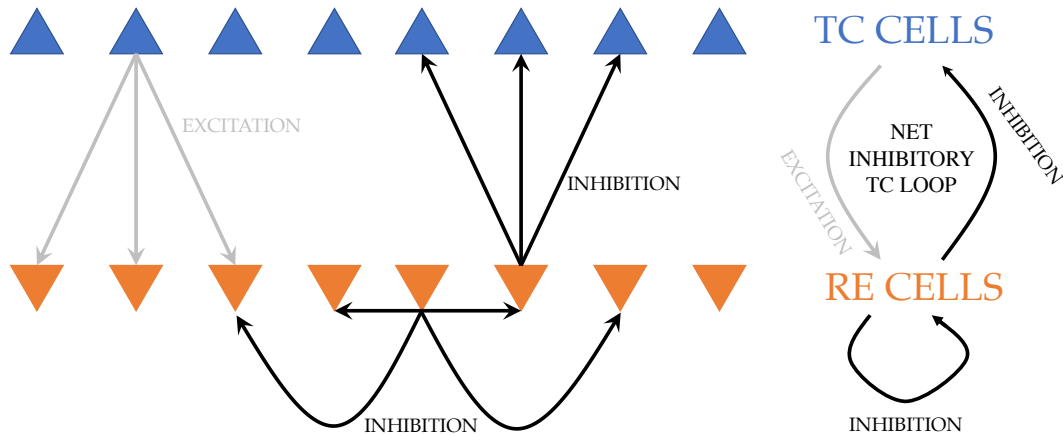


Figure 2.14.: An illustration of a two-layer thalamic network, consisting of inter-connected TC and RE cells, with inhibitory (excitatory) connectivity shown by the black (grey) arrows. The overall inhibitory TC-to-TC loop is shown on the right.

This excites RE cells which fire, sending inhibitory signals to both RE and TC cells. This completes one cycle of activity. The whole process is able to repeat, leading to the generation of periodic activity [44]. The idea behind the *Rinzel-reduction* is for TC cells to indirectly send inhibitory signals to other TC cells via the RE cells. Thus, removing explicit dependence on RE cells, one can, in essence, consider a population of TC cells with inhibitory synaptic self-interactions.

Yew et al. [234] studied the two-population TC and RE circuit in 2001. They used singular perturbation methods to derive formulae for solutions and discover how wave properties, such as speed or shape, depend on parameters. The two-layer model of TC and RE cells were connected as shown in Figure 2.14. Yew et al. demonstrated by direct numerical simulation that smooth and lurching waves exist in the two-layer model. Furthermore, they showed that the model supports the following types of travelling wave: a solitary pulse, a double pulse, a multiple pulse solution, a solitary lurcher, a double lurcher and a lurching wave with periodic lurching activity in its wake. Before considering network dynamics, the authors study single-cell and two-cell dynamics, illustrating the intrinsic single-cell properties and

the very basic network properties. Following this, they find an analytical expression for the smooth wave in the full network model by moving to the co-moving frame.

In 2010, Wasylenko et al. [224] undertook a numerical investigation of lurching waves in a two-population network model akin to that of [234], albeit on a lattice instead of on the continuum. They showed lurching waves in their model to be fixed points of a Poincaré map and carried out a bifurcation analysis by following those fixed points as parameters were varied. In this way, they were able to numerically obtain the bifurcation structure of various lurching solutions to their model. An analytical linear stability analysis of lurching waves is still an open challenge in the field.

## 2.8 STABILITY IN NON-SMOOTH DYNAMICAL SYSTEMS

The models reviewed in the previous section are all set up as smooth, non-linear dynamical systems. This non-linearity is a major obstacle to overcome in an analytical treatment (although not in *every* case). One approach to remedy this is to consider non-smooth, piece-wise linear (PWL) models which caricature the smooth, non-linear ones. For PWL models, linear theory applies away from any non-smoothness. The natural caveat with this approach is that while non-linearity disappears, non-smoothness is introduced which requires a different host of techniques for analysis. The upshot is that non-smoothness typically occurs at locations in phase-space which may be characterised, for example on the hyperplane defining a firing condition, given by  $v = v_{\text{th}}$ .

These locations are referred to as *switching manifolds*. Upon these, the dynamics of the dynamical system changes discontinuously, either in the vector field or in the flow, or in both. Table 1 summarises the main types (1, 2, and 3) of discontinuities that may be found in non-smooth dynamical systems. We add the notion of a type 0 discontinuity which is characterised by a fully smooth dynamical system for completeness.

Type	Vector Field	Solution
0 (Smooth)	Smooth	Smooth
1	Non-smooth, continuous	Smooth
2 (Filippov-type)	Non-smooth, discontinuous	Non-smooth, continuous
3 (Impulsive)	Exposed Delta function	Non-smooth, discontinuous

Table 1.: For the generic dynamical system  $du/dt = F(u)$ ,  $u \in \mathbb{R}^n$ ,  $t > 0$ , the Types of discontinuity in dynamical systems are characterised by the relative non-smoothness of the vector field  $F(u)$  and solution  $u$ .

In 1995, Müller [154] developed a method to determine the linear stability of solutions to non-smooth systems by appropriately characterising the non-smooth jumping events at a switching manifold. This method has been dubbed the *saltation* approach (in Italian, the verb *saltare* means “to jump”). We utilise this approach in Chapter 5, and give the details of a derivation of the saltation operators appropriate to our problem there in Appendix C.2. Here, we give a brief overview of the method.

Consider an arbitrary unperturbed trajectory  $z(t)$ , and a perturbed trajectory  $\tilde{z}(t)$  (see Figure 2.15) to a time-dependent dynamical system

$$\frac{dz}{dt} = F(z), \quad z \in \mathbb{R}^n, \quad (2.51)$$

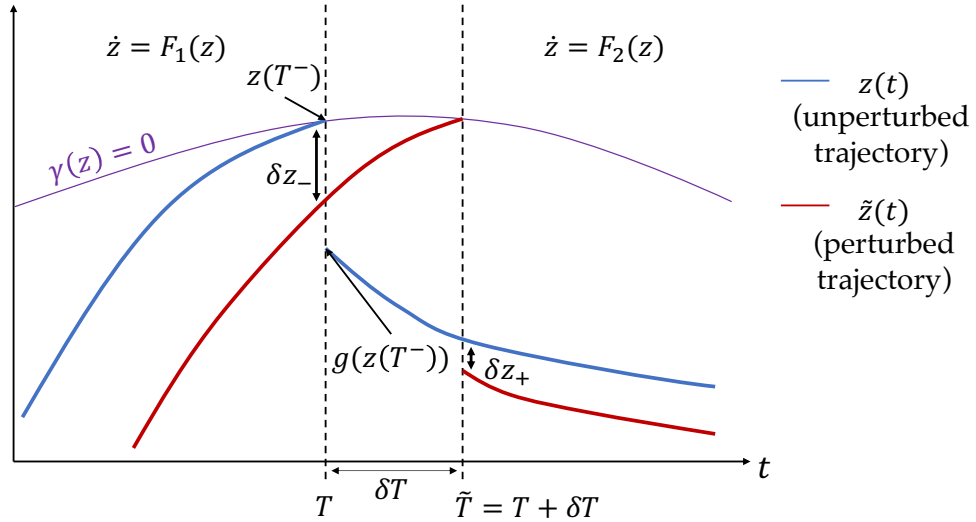


Figure 2.15.: A diagram showing the evolution of a perturbation at a switching event at time  $T$ . The blue (red) line specifies the unperturbed (perturbed) trajectory with switching event occurring at time  $T$  ( $\tilde{T}$ ).

with a switching event in the dynamics at a time  $t = T$  for the unperturbed trajectory, captured by the indicator function  $\gamma(z)$ , via the condition  $\gamma(z(T)) = 0$ . This may be a switch in the vector field, such that

$$F(z) = \begin{cases} F_1(z), & v < a, \\ F_2(z), & v > a, \end{cases}$$

where  $v = a$  is a surface in phase-space where the dynamics switch (here,  $v$  is a component of  $z$  upon which the dynamics switch). In this case,  $\gamma(z) = v - a$ . Or it may be a switch in the solution, such that, where a trajectory hits the switching manifold  $v = a$ , the solution after this moment is discontinuously mapped to the solution just before this moment. If  $T$  denotes the time when the trajectory hits the switching manifold, then  $z(T^+) = g(z(T^-))$ , where the function  $g$  discontinuously maps  $z$  before a switch to its value after a switch. The times  $T^\pm$  are defined by  $T^\pm = \lim_{\epsilon \searrow 0} T \pm \epsilon$ . Collectively, both of these cases are captured in Figure 2.15, where there is a clear discontinuity in the solution (blue line) and its vector field (slope of the blue line) at time  $t = T$ . It is important to note that the switch occurs in phase-space

rather than time. We have introduced the switching time  $T$  simply to help illustrate what happens to trajectories through time.

The perturbation between the two trajectories is defined as  $\delta z(t) = z(t) - \tilde{z}(t)$ . Then the perturbation *after* a switch,  $\delta z_+$ , may be mapped to a perturbation *before* a switch,  $\delta z_-$ , via a *saltation operator*  $K \in \mathbb{R}^{n \times n}$  at time  $t = T$ , such that

$$\delta z_+ = K(T)\delta z_-.$$

Müller showed that the saltation matrix takes the form

$$K(T) = Dg(z(T^-)) - \frac{(Dg(z(T^-))F_1(z(T^-)) - F_2(z(T^+))) \nabla_z \gamma(z(T^-))^T}{\nabla_z \gamma(z(T^-)) \cdot F_1(z(T^-))}. \quad (2.52)$$

This simplifies considerably when applied to a problem. Notice that the numerator of the second term of  $K(T)$  is an *outer product*, generating an appropriately sized  $n \times n$  matrix. For two vectors  $u \in \mathbb{R}^{m \times 1}$  and  $v \in \mathbb{R}^{n \times 1}$ , the outer product,  $(u \otimes_{\text{OP}} v)$ ,<sup>6</sup> is of size  $m \times n$ , and is defined in index notation by  $(u \otimes_{\text{OP}} v)_{ij} = u_i v_j$ , where  $v^T \in \mathbb{R}^{1 \times n}$  denotes the transpose of  $v$ .

Saltation is a useful approach to effectively treat the evolution of perturbations through switching manifolds. It is an invaluable analytical tool in constructing a monodromy matrix in piece-wise models, which is crucial in the linear stability analysis of periodic solutions. Away from switching manifolds in PWL systems, perturbations are propagated forwards via matrix exponentials.<sup>7</sup> The reader will see how this is achieved in Chapter 5. Saltation operators have been used to analytically compute periodic orbit stability in a neuroscience context in [148, 159, 47, 127, 187, 25].

For smooth dynamical systems without switching manifolds, the use of these techniques recovers the smooth theory (in this case they are unneces-

---

<sup>6</sup>The subscript “OP” stands for “Outer Product”, and is given to avoid confusion and to distinguish this symbol from  $\otimes$  representing a spatial convolution.

<sup>7</sup>In theory, the approach can be applied to piece-wise *non-linear* systems, where perturbations are propagated via some non-linear operator instead of matrix exponentials away from switching events. The simplest way to do this is via a numerical approach.

sary). Developing an appropriate non-smooth model which caricatures the underlying biology or the original model well is key in using this approach effectively to gain insights.

## 2.9 EVANS FUNCTION STABILITY OF HETEROGENEOUS SPATIAL PATTERNS

The neural field model with linear adaptation of spike frequency adaptation (2.46) admitted patterns with non-trivial oscillatory dynamics [67]. Simpler solutions such as simple travelling waves and stationary bumps also exist in neural field-type models.

A useful tool in the study of heterogeneous patterns such as these is the *Evans function*. This is used to analyse the linear stability of non-linear waves on unbounded domains [143]. The Evans function is a complex analytic function whose zeroes give the point spectrum of the operator obtained by linearising a system about its travelling wave solution [50]. These zeroes correspond to the eigenvalues of the stability problem and are typically found computationally by finding the intersections of the real and imaginary zero contours in the complex plane. Originally developed for travelling waves, Coombes and Owen (2005) [45] demonstrated that the technique could be adapted to find the eigenvalues of a (stationary) bump solution, and thus provide stability information for a *stationary* class of solutions too. The Evans function technique was first considered by Evans [70, 71, 72, 73] during a stability analysis of Hodgkin-Huxley type equations. Coombes and Owen developed the use of the Evans function for travelling waves in neural field-type integro-differential equations in the case of a Heaviside firing rate function [49].

Here we outline how to determine the Evans function in non-smooth systems. Consider a model with stationary bump solutions, such as the Amari neural field model (2.43) [46]. A stationary bump in an Amari-style neural

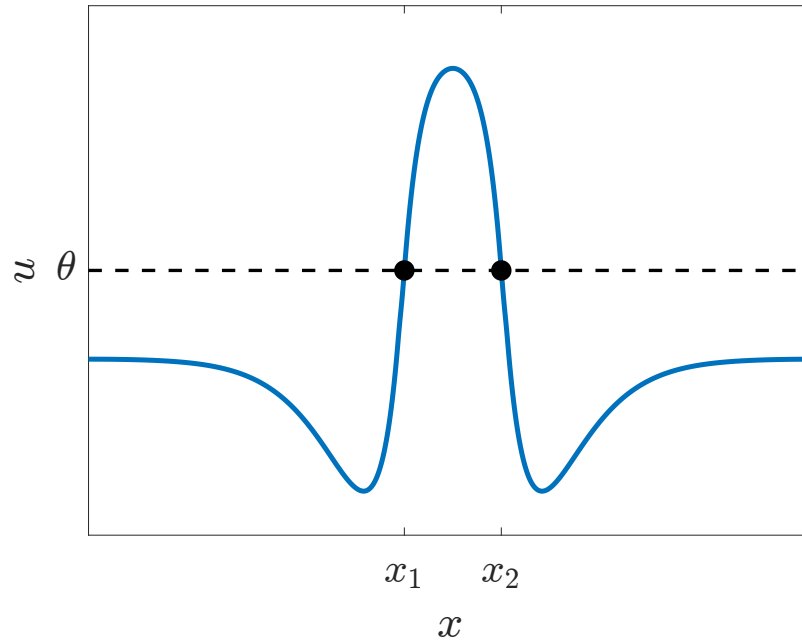


Figure 2.16.: An illustration of a stationary bump (blue curve) parameterised by two threshold crossings,  $x_1$  and  $x_2$  (black dots), at which firing events, given by  $u(x) = \theta$ , occur. The firing threshold  $\theta$  is illustrated by the dashed black line.

field is defined by two locations,  $x_1$  and  $x_2$  (which are both fixed in time), in space for which the firing threshold,  $\theta$ , is crossed (this is illustrated in Figure 2.16).  $x_1$  and  $x_2$  are called *threshold crossings*, and occur at  $u(x) = \theta$ , where the firing rate function  $f(u(x)) = H(u(x) - \theta)$  activates. A complete bump construction identifies  $x_1$  and  $x_2$ , giving a determinable solution profile  $z(x)$ .<sup>8</sup>

To determine the linear bump stability, linearise about it, so that

$$z(x, t) = z(x) + \delta z(x)e^{\lambda t},$$

where  $\delta z(x) \ll 1$  describes spatial variations in the perturbations and  $\lambda$  is an eigenvalue to the stability problem. If  $\text{Re}(\lambda) > 0$ , then solutions are unstable, while if  $\text{Re}(\lambda) = 0$ , a linear instability occurs. Otherwise,

---

<sup>8</sup>The notation  $z$  is useful in generality for multi-component systems. In this scalar neural field example,  $z(x) = u(x)$ .

a solution is linearly stable. A homogeneous linear system in the spatial perturbations at the threshold crossings is then found. It typically takes the form

$$(\Gamma(\lambda) - I_n)\mathbf{x} = \mathbf{0},$$

where  $n$  is the number of distinct threshold crossings (2 in the case of a bump),  $I$  is the identity matrix,  $\mathbf{x}$  is a vector of perturbations<sup>9</sup> at the  $n$  crossing events, and  $\Gamma$  is a complex-valued  $n \times n$  matrix obtained via the above linearisation, containing a description of threshold crossings (concrete illustrations of this are shown in Chapters 4 and 5).

The complex-valued Evans function  $\mathcal{E}$  is generated by demanding that perturbations  $\mathbf{x}$  be *non-trivial* through the equivalent condition  $\mathcal{E}(\lambda) = 0$ , where

$$\mathcal{E}(\lambda) = \det(\Gamma(\lambda) - I_n).$$

The zeroes may be found by decomposing  $\lambda = a + ib$ ,  $a, b \in \mathbb{R}$ , and finding where the zero real and imaginary contours intersect.

In this way, the linear stability of heterogeneous spatially extended solutions may be determined. We utilise the Evans function to obtain bump and wave stability in Chapters 4 and 5 of this thesis.

## 2.10 SUMMARY

The brain is an inherently multi-scale object, working coherently over multiple spatial scales from the microscopically small (proteins, nm) to the macroscopically large (the brain, and the human body, m). The dynamics at the smallest spatial scales contribute to the behaviour observed at the largest spatial scales.

Modellers must therefore decide what is of importance in the problems which are being studied. Is biophysical detail important, or are phenomeno-

---

<sup>9</sup>For the bump solution in Figure 2.16,  $\mathbf{x} = (\delta u(x_1), \delta u(x_2)) \in \mathbb{R}^2$ . These are the perturbation at  $x_1$  and  $x_2$ .

---

logical models – in which underlying biophysical detail comes second to the generation of qualitatively realistic behaviour – acceptable? Figure 2.17 shows a structured hierarchy of spatial scales within the brain, as well as some of the most famous models used at each scale. The Hodgkin-Huxley and Morris-Lecar models incorporate a description of ion channel dynamics at the single-neuron level contributing towards action potential generation, and thus they are dubbed *biophysical* models. The integrate-and-fire (IF) model on the other hand comprises a dynamical system heuristically describing voltage, augmented with firing and reset conditions. There is no explicit biophysical mechanism in the model (although this could be added), nonetheless it captures the salient features of single cell neuronal dynamics: spikes. Although neural fields are phenomenological descriptions of synaptic activity, they offer an effective description of macroscopic brain activity which has been predictive in studies of cortical activity. The study carried out in [140] is illustrative of this, showing agreement in the dynamical response between a neural field model of visual cortex tissue and mesoscopic brain activity across a patch of tissue in the visual cortex, both in response to visual stimuli.

In this thesis, models of different brain regions are studied and developed, using a number of analytical and numerical techniques. We have given an overview and summary of event-driven synaptic modelling, in terms of spikes generating PoSPs, and showed that firing rate models can be motivated by, and heuristically derived from, spiking models. Extending this to include a network of cells or a field describing cortical tissue dynamics, the integro-differential equation framework for neural field models was introduced. The SFA model (2.46) is one of many in this class which demonstrates a plethora of spatio-temporal dynamical activity. The neural field framework can be modified, as demonstrated by Coombes (2003) [44], to effectively model *sub-cortical* structures, in particular, the thalamus. We study an augmented neural field model of thalamic tissue in Chapter 5,

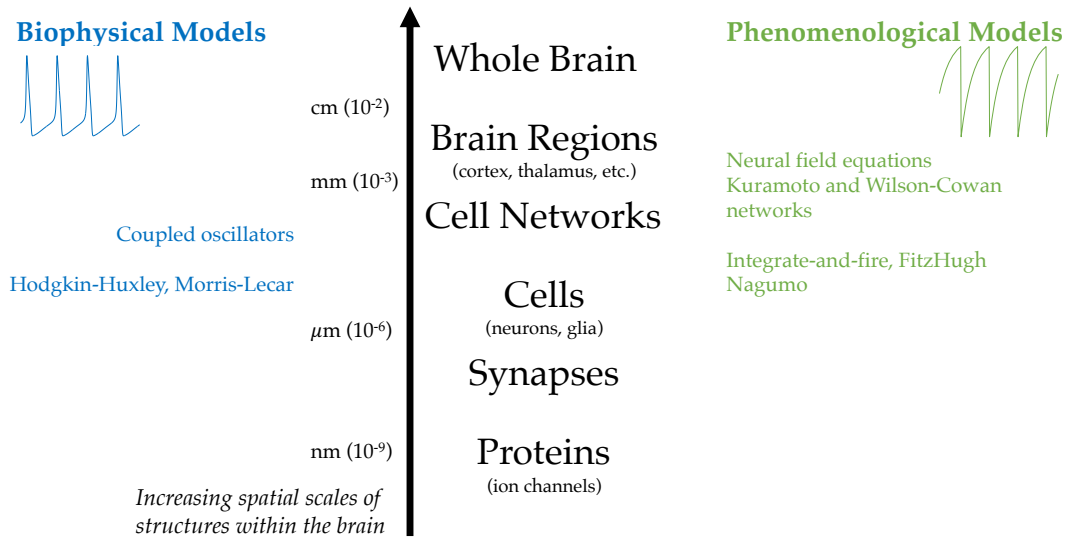


Figure 2.17.: Schematic diagram showing spatially organised scales and structures in the brain and a selection of biophysical and phenomenological models used at appropriate scales.

making use of the Evans function approach to study heterogeneous solution stability for bumps (Chapter 4) and waves (Chapter 5).

In the following chapter, we develop tools to conduct a numerical analysis of models, allowing for the systematic study of various different solution types and patterns to dynamical systems models.

---

 NUMERICAL CONTINUATION METHODOLOGIES
 

---

## 3.1 INTRODUCTION

3.1.1 *Dynamical Systems*

Two useful applied mathematical frameworks that can aid in the understanding of real-world phenomena are *non-linear dynamical systems* and *scientific computation*. These are used hand-in-hand in the modelling of such phenomena. Dynamical systems are often expressed as systems of first-order differential equations of the form

$$\frac{du}{dt} = f(u), \quad u \in \mathbb{R}^n, t > 0, \quad (3.1)$$

for a state variable  $u = u(t)$ , where  $f : \mathbb{R}^n \rightarrow \mathbb{R}^n$  defines a vector field describing how  $u$  evolves in time.

In general, closed form solutions to dynamical systems cannot be found in the majority of cases. An important exception to this is the class of *linear* dynamical systems. In the continuous case, the right-hand side the form  $f(u) = Au$  for some matrix  $A \in \mathbb{R}^{n \times n}$ , which gives rise to a system of linear differential equations in (3.1), with explicit solution given by

$$u(t) = \sum_{i=1}^n \alpha_i v_i e^{\lambda_i t}, \quad (3.2)$$

where  $\lambda_i \in \mathbb{C}$  and  $v_i \in \mathbb{R}^n$  are the eigenvalues and corresponding eigenvectors [102] of the matrix  $A$ , and  $\alpha_i \in \mathbb{R}$  are constants determined by

specifying initial conditions. A solution is *asymptotically stable* if, in the continuous case,  $\text{Re}(\lambda_i) < 0$  for all  $i \in \{1, \dots, n\}$ . This means that trajectories sufficiently close will eventually converge to the solution. A solution is *asymptotically unstable* if it is not asymptotically stable [125]. In the case of discrete dynamical systems, represented by first-order difference equations  $x_{N+1} = f(x_N)$ ,  $N = 0, 1, 2, \dots$ , where  $x_N \in \mathbb{R}^n$  for all  $N$ , linear systems are given by  $f(x_N) = Ax_N$ , and have solution

$$x_N = \sum_{i=1}^n \alpha_i v_i \lambda_i^N. \quad (3.3)$$

Linear, discrete systems are used in the study of the stability of periodic orbits. Their solutions are asymptotically stable if  $|\lambda_i| < 1$  for all  $i \in \{1, \dots, n-1\}$ . For periodic orbits, the trivial eigenvalue satisfies  $\lambda_n = 1$ . In both continuous and discrete cases, solutions are *unstable* if they are not stable. This rich theory for linear systems is often exploited when studying non-linear systems. Typically, one characterises the stability of equilibria in non-linear systems by invoking the Hartman-Grobman theorem [12, 90, 86]. This guarantees that the stability properties of the non-linear system are equivalent to those of the linear system in the vicinity of hyperbolic equilibria; these are equilibria whose eigenvalues do not lie on the critical stability boundaries,  $\text{Re}(\lambda) = 0$  (continuous) and  $|\lambda| = 1$  (discrete). Thus the stability of the linear system is studied to characterise that of the non-linear system.

In general, there are two ways to analyse dynamical systems; via an *analytical* or a *numerical* approach. In the case of the former, one often tries to determine properties of systems in closed form, be they various solution types, or conditions regarding stability, whereas the latter is concerned with determining properties computationally. Consider the example of finding a steady state  $u^*$  satisfying  $f(u^*) = 0$ . For simple systems, this can be done analytically by solving  $f(u) = 0$  to obtain explicit closed form expressions for each component of  $u \in \mathbb{R}^n$ . In general, though, this is not possible, and the steady state(s) are found by computing the root(s) of  $f(u)$  numerically,

using a root-finding algorithm such as Newton's method to converge to the steady state to within a desired tolerance.

### 3.1.2 Space-time Models

A notion of space may be included into (3.1) by considering the system

$$\frac{\partial u}{\partial t} = f(u(x, t)), \quad u \in \mathbb{R}^n, x \in \mathbb{R}, t > 0, \quad (3.4)$$

which may be used to model phenomena which evolve in space and time. Examples include waves and patterns of activity seen in cortical slices, and fluid flow [2]. Spatially extended models of activity are ubiquitous throughout applied mathematics and mathematical biology. The neural field models discussed in Section 2.7 fall under the umbrella of space-time models. Using the method of lines [188, 89], and by specifying appropriate boundary conditions, spatially extended systems may be transformed into systems of ODEs in time (those of the form (3.1)), by considering a spatial mesh  $x_i, i = 1, \dots, n_x$  which approximates space  $x$  well. If space is infinite (as in 3.4), then often periodic boundary conditions are applied to a finite domain. The size of the resultant system is directly related to its spatial resolution,  $n_x$ . A sufficient spatial resolution is often associated with the problem under consideration, but typically requires a large number of ODEs. This number dramatically increases as the number of spatial dimensions under consideration increases. If  $u$  has  $n$  components, then the spatially discretised system consists of  $n \times n_x$  ODEs. Finer meshes are typically better at approximating space, and so  $n_x$  is required to be large enough to sufficiently capture spatial detail.

A number of so-called *invariants* or *special solutions* are admissible as solutions to space-time models. Examples include equilibria, periodic orbits, and waves to name just a few. Their "special" nature arises from their regular behaviour: equilibria stay fixed for all time, periodic orbits repeat

indefinitely in time, and, on a periodic domain, waves are periodic in space *and* time.

In studies of biophysical systems, model parameters often have a physical correspondence to “tunable” quantities. It is of interest to modellers to study how robust patterning is to changes in biophysical parameters. To frame this from a different perspective, do certain states of a biophysical system, for example pathological states, persist for a wide or narrow range of values that can be taken by biophysical quantities, such as intracellular calcium or dopamine concentration? Finding answers to questions like this increases our understanding of the solution structure of dynamical systems, but also may have more clinical benefits further downstream. A point to note here is that to gain useful clinical insights, the model under consideration must be sufficiently detailed; interdisciplinary approaches which actively build up models to more accurately reflect reality should be encouraged for pursuits like this.

### 3.1.3 *Numerical Continuation*

Using numerical integration to repeatedly carry out long-time simulations directed towards finding equilibria or periodic orbits is possible, but is cumbersome and inefficient, especially for the large-dimensional systems that inevitably result from the consideration of space-time models. A more fundamental drawback of this approach is that only stable solutions can be found. Often the knowledge of unstable solutions is useful in determining the boundaries of the basins of attraction for multiple stable solutions, though for large-dimensional systems, this is unlikely. Rather, unstable orbits may be viewed as organising structures in phase space. The method of numerical bifurcation analysis, or numerical continuation, is well-suited to explore dynamical systems from this perspective.

The dependence of ODE systems on parameters can be studied using well-established software packages such as AUTO [59] and MATCONT [56].

These are examples of feature-rich [57] software packages that should be a first port-of-call when studying low-dimensional ODE systems. They are relatively simple to learn how to use, with extensive documentation and tutorials. However, the main drawback with these packages is they are only feasible for low-dimensional dynamical systems. A difficulty arises when studying space-time systems. Numerical bifurcation analysis requires Jacobians of vector fields to be computed for finding solutions via Newton's methods and for stability. Taylor expanding (3.1) about a steady state  $u^*$  as  $u(t) = u^* + \delta u(t)$  (to first order in  $\delta u$ ), we have

$$\frac{d}{dt}\delta u = D_u F(u^*)\delta u + o(\delta u), \quad (3.5)$$

the Jacobian is the matrix of partial derivatives about  $u^*$ , given by  $D_u F(u^*)$ . For generic, large problems, there is no guarantee that Jacobians are sparse (which speeds up the computation of eigenvalues for large systems), and thus it is not feasible to tackle the numerical bifurcation analysis of space-time problems with the packages described above. Instead, matrix-free methods – in which linear systems are solved in such a way that large matrices are not stored, and actions of matrix-vector product operations are utilised instead – may be used for their efficiency [216].

Numerical continuation involves tracking given solutions, be they equilibria, periodic orbits, homoclinic orbits, or bifurcation points, through parameter space. First, let us consider the notion of a *solution branch*. Given some solution  $u_0$  which exists for some parameter  $p_0 \in \mathbb{R}^1$ , if the implicit function theorem is satisfied, there exists a continuous branch of solutions  $u(p)$  in the vicinity of  $p_0$  [122]. Continuation schemes revolve around finding points  $(u_{i+1}, p_{i+1})$ ,  $i = 0, 1, 2, \dots$ , on the solution branch, given a known

---

<sup>1</sup> The system may have multiple parameters (a parameter set), but only one of these ( $p_0$ ) is varied for continuation

solution-parameter pair  $(u_i, p_i)$ . A solution-parameter pair  $(u, p)$  is found by solving the augmented zero-problem  $\tilde{\mathcal{H}}(u, p) = 0$ , where

$$\tilde{\mathcal{H}}(u, p) = \begin{pmatrix} \mathcal{H}(u, p) \\ h(u, p) \end{pmatrix}, \quad (3.6)$$

for  $u \in \mathbb{R}^N, p \in \mathbb{R}$ . Here,  $\tilde{\mathcal{H}} : \mathbb{R}^N \times \mathbb{R} \rightarrow \mathbb{R}^{N+1}$ , defines the zero-problem for the solution-type of interest. For equilibria, the problem  $\mathcal{H}$  is taken to be the vector field of the problem, since equilibria are zeroes of the vector field  $f$  in (3.1). However, for other solution-types, such as travelling waves, an appropriate *interface*, or transformation, must be defined for  $\mathcal{H}$ , such that the solution-type is a zero of an appropriate problem. For example, travelling waves are a solution in an appropriate co-moving frame, so the interface to travelling waves is defined by the transformation to the co-moving frame. Examples of solution-types include the following: equilibria ( $N = n$ ), travelling waves ( $N = n + 1$ ), and periodic orbits ( $N = n + 1$ ). The augmented function  $h : \mathbb{R}^N \times \mathbb{R} \rightarrow \mathbb{R}$  defines a parameter-update condition. Two choices for  $h$  define *parameter* and *pseudo-arclength* continuation, and are described below.

#### 3.1.4 Continuation Schemes

Parameter continuation is the method of obtaining solutions in parameter space via a parametrisation of the solution branch by the continuation parameter,  $p$ . Assuming that a solution,  $(u_0, p_0)$  of  $\tilde{\mathcal{H}}(u, p) = 0$ , is known, the next point on the solution branch,  $u_1$ , is computed for  $p_1 = p_0 + \delta p$ , for a given  $\delta p$ . The next solution,  $u_1$ , can be found by using a root finding algorithm, such as Newton's method, with a suitable initial guess (one method by which this may be found is by time-stepping to a solution).

This is not suitable for systems with strong variations in  $p$ , or for solution branches which fold back on themselves [216]; a consequence of this is that unless an initially chosen solution is unstable, we will not be able to find

the unstable branch of solutions, which is often on the other side of a fold point. In short, poor performance may result from this parametrisation [4].

An alternative parametrisation known as pseudo-arclength continuation (PALC) [117] does not suffer from these issues. In this case, the scalar-valued expression for  $h$  in (3.6) is given by  $h(u, p) = h_u^T(u - u_0) + h_p(p - p_0) - \Delta s$ , where  $(h_u, h_p)$  is the tangent to the solution branch at  $(u_0, p_0)$ , where  $h_u^T$  denotes the transpose of  $h_u$  [216], and  $\Delta s$  is the step-size in the direction of the tangent. An initial guess (“predictor”) is found by extrapolation in the direction given by the tangent at the current solution to the solution branch. A point on the branch is found in the tangent space of the predictor point in the “corrector” step. See Figure 3.1 for an illustration of this. The major advantage of this method is that it can be used to find solutions beyond folds of a solution branch, since the defining PALC system is non-singular at the fold point [122]. Thus, it is a more numerically robust algorithm than parameter continuation.

### 3.1.5 The Predictor-Corrector Step

For all numerical continuation within this thesis, a PALC algorithm is used, where the initial guess for the subsequent point on the solution branch is found using a secant – which passes through two close points on the solution branch – to approximate the derivative, rather than finding the exact derivative via Newton’s method. For large-dimensional systems, Newton’s method is generally expensive and time-consuming, so we use the more efficient method of using a secant to make the “predictor” step. This requires two known solutions,  $(u_0, p_0)$  and  $(u_1, p_1)$ . The second may be found from the first by using standard *parameter continuation* methods. As stated above, this fails close to a fold point, but starting sufficiently far from a fold point allows for the secant continuation to be initialised as so. The PALC algorithm is then used to find subsequent points,  $(u_i, p_i)$ ,  $i \geq 2$ , on the branch, as illustrated in Figure 3.1. Continuation step-size may be adaptive [3], which

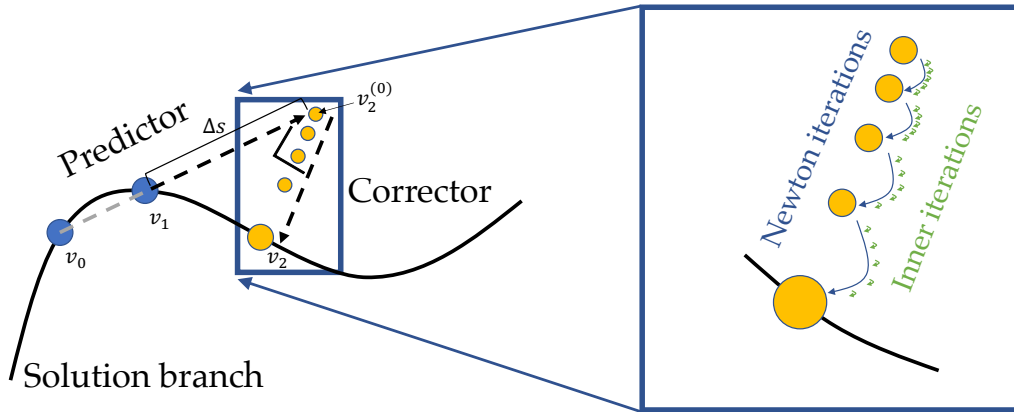


Figure 3.1.: Illustration of the *predictor-corrector* method utilised in the continuation scheme. The predictor uses two previously known solutions to generate an initial guess for the next solution. Convergence is achieved by the corrector, which finds a solution in the tangent space. This is shown in close-up on the right, consisting of the outer Newton iterations, and the inner inner iterations to find the appropriate correction within a given Newton iteration.

can lead to more efficient progress in characterising a solution branch. This is how continuation software developed by Avitabile (2016) [13], which we use and build on, works.

A single continuation step involves solving the system  $F(v) = 0$ , with  $v, F(v) \in \mathbb{R}^N$ . This *zero-problem* consists of finding the state and parameter, and any other quantities of interest that define a solution. These are all contained in the overarching variable,  $v = (u, p)$  in the notation of (3.6). For all of the different solution types considered throughout this chapter, this is encapsulated in Table 2, in the summary of this chapter.

Given two known, consecutive solutions on the solution branch, which, without loss of generality, we label  $v_0$  and  $v_1$ , a suitable *predictor* for  $v_2$ , denoted  $v_2^{(0)}$ , is given by

$$v_2^{(0)} = v_1 + \frac{v_1 - v_0}{\|v_1 - v_0\|_2} \Delta s, \quad (3.7)$$

where  $\Delta s$  is the arc-length of the continuation step, and  $\|\cdot\|_2$  denotes the vector length. For an arbitrary vector  $x = (x_1, x_2, \dots, x_n) \in \mathbb{R}^n$ , this is defined by

$$\|x\|_2 = \sqrt{\sum_{i=1}^n x_i^2}. \quad (3.8)$$

An approximation of a tangent to  $v_1$  is taken in the direction given by the vector  $v_1 - v_0$ . This is illustrated by the dashed grey line in Figure 3.1. The approximated tangent is normalised so the length of the predictor is completely specified by the arc-length  $\Delta s$  (the dashed black line).

The corrector step converges to  $v_2$  (large yellow dot in Figure 3.1), given  $v_2^{(0)}$  (top-most small yellow dot) as a starting point. This is illustrated in the zoom in Figure 3.1. Newton's method may be used for this purpose.

**Theorem 1** (Newton's Method). *Let  $F(v) = 0$  define a system of  $N$  non-linear equations. Furthermore, let  $\{v^{(k)}\}_{k \in \mathbb{N}} \subset \mathbb{R}^N$  be a sequence, and let  $v^* \in \mathbb{R}^N$ . If*

- $F(v) = 0$  has a solution  $v^*$
- $F$  is continuously differentiable in a neighbourhood of  $v^*$
- $D_v F(v^*)$  is nonsingular

*then the Newton iteration*

$$v^{(k+1)} = v^{(k)} + \Delta v^{(k)}, \quad \text{with } D_v F(v^{(k)}) \Delta v^{(k)} = -F(v^{(k)}) \quad (3.9)$$

*converges to the solution  $v^*$  quadratically [53, 216].*

More specifically, a solution  $v$  is said to have numerically converged to the true solution  $v^*$  to within a tolerance  $\epsilon_n$ , if  $\|F(v)\|_2 < \epsilon_n$ , where

$$\|F(v)\|_2, \quad (3.10)$$

is defined as the *residual* (a measure of the error in the solution) of the non-linear system about  $v$ .

See Algorithm 1 for a schematic computational implementation of Newton's method. Typical stopping criteria is for solutions to converge within some specified non-linear tolerance,  $\epsilon_n$ .

---

**Algorithm 1:** An implementation of Newton's method
 

---

```

1 Goal: To numerically find a solution to  $F(x) = 0$ 
2 Input:  $F(\cdot), D_x F(x)(\cdot), x_0$ 
3 Output:  $x$ 
4 Set: NonlinTol, MaxNonlinIterations
5 Set:  $x \leftarrow x_0$ 
6 Set: Residual  $\leftarrow \|F(x_0)\|_2$ 
7 Set: Iterations  $\leftarrow 0$ 
8 while ( $Residual > NonlinTol$ ) & ( $Iterations < MaxNonlinIterations$ ) do
9   Solve the linear system  $DF(x)\Delta x = -F(x)$  for  $\Delta x$ 
10  Update:  $x \leftarrow x + \Delta x$ 
11  Update: Residual  $\leftarrow \|F(x)\|_2$ 
12  Update: Iterations  $\leftarrow Iterations + 1$ 
13 end

```

---

The main advantage of using Newton's method is its fast, quadratic convergence. It does, however, involve solving the Newton linear system

$$D_v F(v^{(k)})\Delta v^{(k)} = -F(v^{(k)}), \quad (3.11)$$

for  $\Delta v^{(k)} \in \mathbb{R}^N$  as shown in Algorithm 1, line 9. This must occur at *each* Newton step (when moving from one yellow dot to the next in Figure 3.1).

For the large systems which result when studying discretised spatial models, the linear system (3.11) may be solved *iteratively* [53] as illustrated by the green arrows in Figure 3.1, to obtain a very good approximation to a true solution. Iterative methods require a suitable *stopping criteria*. This is obtained by considering the residual

$$r_k = D_v F(v^{(k)})\Delta v^{(k)} + F(v^{(k)}), \quad (3.12)$$

of the linear system (3.11), and minimising the *relative* residual, defined by  $\|r_k\|/\|F(v^{(k)})\|$ . This leads to the condition

$$\|D_v F(v^{(k)})\Delta v^{(k)} + F(v^{(k)})\| \leq \eta_k \|F(v^{(k)})\|, \quad (3.13)$$

where the  $\eta_k$  are referred to as the forcing factors. The linear solver solves to within some specified *linear* tolerance. Under the assumption that all  $\{\eta_k\}_{k \in \mathbb{N}}$  are less than one, local convergence is achieved [53].

This use of an iterative method to obtain  $\Delta v^{(k)}$  introduces a source of inexactness, since  $\Delta v^{(k)}$  is found to within a specified tolerance,  $\epsilon_l$ . If this is not small enough, it may affect convergence. There may be other such sources, such as in the evaluation of the function  $F$ , or its Jacobian action. The cumulative effect of this is that the convergence of the inexact Newton's method may suffer. This is especially true for periodic orbits, which may be found as fixed points of a map, computed using a time integration. Therefore, the approximation of a Jacobian action by finite differences is not only slow, but "*dangerous because the error in the time evolution is amplified when it is divided by the step of the difference formula*" [216]. For this reason, exact analytical Jacobian actions are preferred.

The Generalised Minimal Residual (GMRES) method can be used to solve a linear system iteratively. For a nonsingular system  $Ax = b$ , of dimension  $N \gg 1$ , GMRES finds the solution  $x$  to within a given tolerance,  $\epsilon_l$ , by minimising the norm of the residual vector at each inner iteration over a Krylov subspace<sup>2</sup> [181, 225], via a least squares approach [182, 216, 58, 118]. Explicitly, the stopping criteria used by GMRES is [18, 16, 182]

$$\|b - Ax\| / \|b\| < \epsilon_l. \quad (3.14)$$

This is the minimisation of the *relative residual* discussed above. For a more detailed and technical exposition of how this method works, the reader is referred to Saad and Schultz (1986) [182]. Suffice to say, for our purposes it is sufficient to know that the Newton linear system (3.11) may be solved iteratively using the GMRES method to within a specified tolerance,  $\epsilon_l$ . This is implemented in MATLAB (introduced before R2006a) and may be function-called as `gmres`.

---

<sup>2</sup>The  $m$ th-order Krylov subspace generated by  $A \in \mathbb{R}^{n \times n}$  and  $b \in \mathbb{R}^{n \times 1}$  is defined as  $\text{span}\{b, Ab, A^2b, \dots, A^{m-1}b\}$  [181].

If the linear systems (3.11) are solved with suitable tolerances, quadratic convergence of Newton's method can still be achieved. In practice, this typically involves experimentally varying the tolerances  $\epsilon_n$  and  $\epsilon_l$  to find a combination which minimises the *total* computational cost of the whole method [216]. Note that there are two iterative processes occurring. The *outer* Newton iterations to converge to a solution, and the *inner* GMRES iterations needed to solve the linear system (3.11) at each outer iteration. This is illustrated in the zoom of Figure 3.1. The combination of Newton's method with schemes such as GMRES to solve the linear system at each outer iteration are referred to as Newton-Krylov solvers in the literature [118, 119]. Often it is unclear how to balance the number of outer vs. inner iterations in order to obtain the optimal set-up minimising the total computational cost. Typically, the outer tolerance,  $\epsilon_n$ , and the inner tolerance,  $\epsilon_l$ , are related to each other, but it is often an art rather than an exact science in finding optimal values for these, such that continuation does not stall and is sufficiently quick.

### 3.1.6 Summary

To summarise, the continuation routine can be broken down as follows. During each continuation step, a number of Newton iterations are required to converge to the next solution. During each of these outer iterations, a large linear system must be solved, which is done iteratively using GMRES.

The work in this chapter builds on the aforementioned software developed by Avitabile [13] (which is currently able to carry out the continuation of equilibria and simple travelling wave solutions), extending it to continue periodic orbit-type (PO) solutions to spatially extended systems, using the blueprint given in [216] as a basis. We provide a review of the method in [216], and an exposition of the implementation in MATLAB in Section 3.3. The rationale is to study spatially extended periodic-orbits in neural fields,

for which off-the-shelf packages are unavailable, though it is stressed that the methods are applicable beyond neural fields.<sup>3</sup>

The choice to implement the software in MATLAB was made on the basis that many researchers in applied mathematics are familiar with, and use, MATLAB. Of course we would likely obtain greater performance in other languages, such as C++ or perhaps even Python, but it is our opinion that any potential performance gains are eclipsed by implementing in a language familiar to the community; potential users are saved from requiring to learn a new programming language in order to use the software.

Further, we expand on the techniques introduced in [216] to develop novel methods in the stability and continuation of travelling-wave periodic orbit-type (TWPO) solutions. They are characterised by their travelling, repeating units of activity.

### 3.2 EQUILIBRIA AND TRAVELLING WAVES

Equilibria are solutions to dynamical systems characterised by their long-term persistence at steady state. In the words of Kuznetsov [125], “*a system placed at equilibrium remains there forever.*” The word “equilibrium” is typically used in continuous-time systems, while the phrase “fixed point” is used for maps or discrete-time systems. They are the simplest type of dynamical systems solution.

Travelling waves are ubiquitous in the study of biological and physical systems. Members of this generic solution family include fronts, pulses, tango waves [210], spirals, and periodic travelling waves (also known as “wavetrains”). These patterns transfer “information” between different locations in space, and are to be contrasted with standing waves which are confined to a fixed location. Travelling waves with a well-defined wavespeed can be studied and analysed by seeking solutions in an appropriate co-

---

<sup>3</sup>The methods in [216] were developed to tackle problems in fluid dynamics.

moving frame; this technique was introduced by Fisher (1937) [76] and Kolmogorov et al. [121, 211] in a study of the spread of advantageous gene mutations.

From the early 2000s onwards, methods arose that were able to continue travelling solutions to the Navier-Stokes equations [144]. These utilised preconditioners and matrix-free methods to achieve efficiency. The former are used to accelerate convergence to the solution  $x$  of a linear system  $Ax = b$ , by solving the *pre-conditioned* system  $M^{-1}Ax = M^{-1}b$ , which has the same solution as the original linear system [15]. The matrix  $M^{-1}$  is known as the *pre-conditioner*, and is chosen to be a good approximation to  $A^{-1}$ , while also being cheaper to compute [15]. In this case,  $M^{-1}A \approx I$ , where  $I$  is the identity matrix. The latter allows linear systems to be solved in such a way that matrices are not stored, and matrix-vector products are used instead. This is especially useful for large problems, where storage and memory considerations may be prohibitive [29]. They were introduced into the study of neural fields in a study of *localised* rather than travelling patterns by Rankin et al. (2014) [172]; this was the first numerical study of patterns with the *full* integro-differential equation formulation of neural fields. Prior to this, the integral equations were reduced to PDEs via specific choices of connectivity kernels with a suitable Fourier transform, as outlined in [46, 128]. Matrix-free methods allow for a much wider range of connectivity kernels to be considered – not just those allowing the equations to be written in a differential equation form. This includes connectivities with non-smoothness.<sup>4</sup>

The work by Sherratt (2012) [194] notes the importance of travelling wave-train solutions in the study of partial differential equation (PDE) systems. It introduces a software package, WAVETRAN, which is able to continue these solutions and calculate their stability.

---

<sup>4</sup> In neural fields, the connectivity kernel appears under an integral, and so non-impulsive non-smoothness is washed out.

Consider a generic dynamical system in  $(x, t)$ -space,

$$\frac{\partial u}{\partial t} = F(u, p), \quad u = u(x, t), \quad x \in \mathbb{R}, t > 0, \quad (3.15)$$

with a given initial condition  $u(x, 0) = u_0(x)$ . Here,  $u \in \mathbb{R}^n$ , and  $p \in \mathbb{R}$  represents a model parameter. Upon discretisation, the problem of equilibria continuation is given by setting  $\mathcal{H}(u, p) = F(u, p)$  in (3.6), with  $N = n$ . Equilibria satisfy  $u(x, t) = u(x)$  for all  $t$ . Their linear stability can be analysed by considering the evolution of small perturbations (to equilibria) to first order. To do this, substitute  $u(x, t) = u(x) + e^{\lambda t} \delta u(x)$  into (3.15) to obtain

$$\lambda \delta u(x) = D_u F(u, p) \delta u(x), \quad (3.16)$$

which is an eigenvalue-eigenvector problem for the pair  $(\lambda, \delta u)$ . (3.16) can be solved in MATLAB via the function `eigs` if either of the Jacobian matrix  $D_u F(u, p)$  or the action  $D_u F(u, p) \delta u$  are supplied.

In illustration of equilibria continuation, let us consider a Hopfield-style network posed on the periodic plane  $\mathbb{R}^2$ , given as

$$\tau \frac{\partial}{\partial t} s(\mathbf{r}, t) + s(\mathbf{r}, t) = f \left( \int_{\mathbb{R}^2} w(|\mathbf{r} - \mathbf{r}'|) s(\mathbf{r}', t) d\mathbf{r}' + B(\mathbf{r}) \right), \quad (3.17)$$

for  $\mathbf{r} = (x, y) \in \mathbb{R}^2$ , where  $s(\mathbf{r}, t)$  is the synaptic activation of tissue at position  $\mathbf{r}$  at time  $t$ ,  $w(|\mathbf{r} - \mathbf{r}'|)$  is the distance-dependent synaptic connectivity between tissue at  $\mathbf{r}'$  and  $\mathbf{r}$ , and  $f$  is the ‘‘softplus’’ firing rate function,

$$f(s; \mu) = \log(1 + \exp(\mu s)) / \mu, \quad (3.18)$$

which approaches the *Rectified Linear activation (ReLU)* function  $f(s) = s$ ,  $s > 0$ , and 0 otherwise, as  $\mu \rightarrow \infty$ . The synaptic time-constant is represented by  $\tau$ , and  $B(\mathbf{r}) = 1$  for all  $\mathbf{r} \in \mathbb{R}^2$ . The connectivity is given by

$$w(r) = w_0 (a e^{-\gamma r^2} - e^{-\beta r^2}), \quad w_0 = w_{\text{Nor}} \frac{\beta \gamma}{\pi(a\beta - \gamma)}. \quad (3.19)$$

The kernel is normalised to  $w_{\text{Nor}}$ , and  $\beta = 3/\lambda_{\text{net}}^2$  and  $\gamma = 1.05\beta$ , where  $\lambda_{\text{net}}$  is a parameter defining the spatial scale of the connectivity. Burak and Fiete (2009) [30] added a time-dependent drive in this model, with kernel

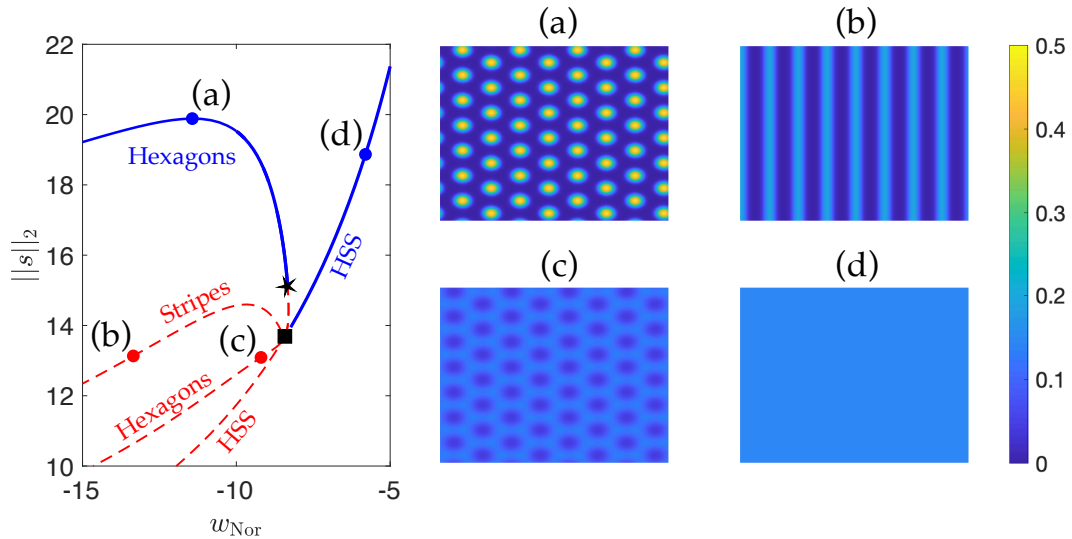


Figure 3.2.: Continuation of qualitatively different equilibria solutions (labelled on diagram) to (3.17), with the solution’s 2-norm plotted against  $w_{\text{Nor}}$  (“HSS” stands for Homogeneous Steady State). Blue and red denote stable and unstable solutions, respectively. A fold bifurcation of hexagons is denoted by a black star (\*), and the instability of the HSS by a black square (■). Solutions represented by the dots (a)-(d) are shown on the right on the plane, all with the same colorbar. Each pattern is on a lattice of  $128^2$  neurons. Parameters are:  $a = 1$ ,  $\lambda_{\text{net}} = 13$ ,  $\tau = 10$ , and  $\mu = 20$ .

anisotropies to generate a first generation model of grid cell dynamics. This is discussed more in the Discussion (Chapter 6) of this thesis, but for our purposes here, it is sufficient to consider a simple Hopfield network without time-dependent drive or anisotropies.

Figure 3.2 shows the results of a 2-D continuation of various equilibria solutions to (3.17), with  $w_{\text{Nor}}$  as the bifurcation parameter. Shown are hexagons, stripes, and the homogeneous steady state in  $(w_{\text{Nor}}, \|\cdot\|_2)$ -space. The homogeneous steady state (lower-most branch) undergoes an instability near  $w_{\text{Nor}} \approx -8$ . As  $w_{\text{Nor}}$  increases beyond this, the homogeneous steady state is the unique stable solution, with an illustration of its spatial structure

on the plane shown in (d). At the instability, three different branches of solution are born in a Turing bifurcation: two branches of unstable hexagons (lower and upper dashed red lines), and a branch of unstable stripes (middle dashed red line), with a pattern from this branch shown by (b). The lower branch of hexagons persists as an unstable solution as  $w_{\text{Nor}}$  decreases, with a point on the solution branch shown by (c). The upper branch of hexagons born at the Turing instability is unstable near the instability point, but turns back on itself in a fold bifurcation, gaining stability in the process. As  $w_{\text{Nor}}$  decreases, the stable pattern is the upper branch of hexagons. Where the stable hexagons exhibit high levels of activity in space, the unstable hexagons have low levels of activity, and vice versa. This can be seen by comparing the spatial activity profiles shown in (a) and (c). Intriguingly, the *stable* hexagons do not form from a Turing instability of the spatially homogeneous steady state, but rather from a *secondary instability* through unstable hexagons.

Standard travelling waves are typically studied in the co-moving frame, defined by  $\zeta = x - ct$ . This is identical to an observer travelling along standard space with wavespeed  $c \in \mathbb{R}$ ; such an observer would see a travelling wave as a stationary solution in their reference frame. In the co-moving frame,

$$\frac{\partial u}{\partial t} = G(u, c, p), \quad G(u, c, p) = c \frac{\partial u}{\partial \zeta} + F(u, p), \quad (3.20)$$

where now  $\zeta$  and  $t$  are understood to be space<sup>5</sup> and time variables *in the co-moving frame*, and  $u \in \mathbb{R}^n$  and  $p \in \mathbb{R}$  is a parameter as before. Let the state vector  $z = (u, c) \in \mathbb{R}^{n+1}$  consist of the wave solution,  $u$ , augmented with its wave speed,  $c$ . This satisfies  $\partial u / \partial t = 0$ : that is, travelling waves satisfy  $G(u, c, p) = 0$ . The problem  $G$  therefore, defines a suitable interface and zero-problem which may be used by a continuation routine, along with

---

<sup>5</sup> The “travelling wave co-ordinate.”

the phase condition  $\mathcal{X}(u, p) = 0$ , to find the travelling wave solution branch. The phase condition, defined by

$$\mathcal{X}(u, p) = u'_{\text{ref}}(u - u_{\text{ref}})^T, \quad u \in \mathbb{R}^n, \quad (3.21)$$

is chosen. Here,  $u_{\text{ref}} \in \mathbb{R}^n$  is a spatial profile given by a reference solution, which is often taken to be the previous solution on the branch, or a sufficiently good initial guess to a true solution. The quantity  $u'_{\text{ref}}$  is the spatial derivative of  $u_{\text{ref}}$ . In the words of Doedel (1981) [61], the orthogonality condition “ensures that  $u \dots$  to be determined occupies a similar position [in phase space] as  $u_{\text{ref}}$ ”. Thus the phase condition “pins” a solution to a particular region of phase space. More specifically, the phase of the next solution to be found is fixed such that the difference between the solution to be found and the reference solution is perpendicular to the tangent vector of the reference solution [122]. We must bear in mind that  $u \in \mathbb{R}^n$ , and so, while the phase condition takes in  $u \in \mathbb{R}^n$  as a function argument, it is scalar-valued.

Then, in the language of (3.6), travelling wave continuation is given by

$$\mathcal{H}(z, p) = \begin{pmatrix} G(z, p) \\ \mathcal{X}(u, p) \end{pmatrix} \in \mathbb{R}^{n+1}. \quad (3.22)$$

Numerical linear wave stability can be found by considering the first  $n$  components of the equation,

$$\lambda \delta z = D_z G(z, p) \delta z, \quad (3.23)$$

with the relevant  $(n + 1) \times (n + 1)$ -sized Jacobian matrix given by

$$D_z G(z, p) = \left( \begin{array}{c|c} D_u G(u, c, p) & D_c G(u, c, p) \\ \hline \mathcal{X}_u(u, p) & \mathcal{X}_c(u, p) \end{array} \right), \quad (3.24)$$

acting on  $\delta z = (\delta u, \delta c)$ . Again, (3.23) is an eigenvalue problem which may be solved numerically using `eigs` in MATLAB. It is important to note that numerical wave stability only finds the point spectrum of the travelling

---

wave solution under consideration. This consists of all isolated eigenvalues with finite multiplicity [186]. The full spectrum of a linearised differential operator for a travelling wave solution may be partitioned into the point spectrum and the essential spectrum [115, 185]. A travelling wave may only be stable if the essential spectrum lies completely in the open left half-plane [185, 170]. See [115] for an excellent overview of analytical wave stability, which involves finding the essential spectrum in addition to the point spectrum. The numerical wave stability in this thesis does not involve computation of the essential spectrum and is backed up by direct numerical simulation to show that changes of stability occur where it is calculated that eigenvalue(s) in the point spectrum cross the stability boundary.

Travelling solutions in space are stationary solutions in the co-moving frame. In linear, or PWL models, these may often be constructed analytically – they are defined by ODEs in  $\zeta$ , in the travelling-wave frame. In theory, these ideas can be extended to more than one spatial dimension by considering a wavespeed vector, with the stipulation that instead of solving ODEs, time-independent spatial PDEs must be solved when seeking stationary solutions in higher dimensions.

### 3.3 SPATIALLY EXTENDED PERIODIC ORBIT CONTINUATION

The previous sections have exposed the high-level methodology with regards to numerical continuation and its application to equilibria and travelling waves. In this section, the focus shifts to spatially-extended *periodic* solutions to space-time models.

#### 3.3.1 A Review of the Problem Formulation

For non-trivial solutions to spatially extended models, computational methods may be used in a complementary analysis along with an analytical study to probe a problem and gain insights. Here, we describe the numerical method we use in the continuation of spatially extended *periodic orbits* as developed by Umbría and Net (2016) [216].

Consider the resultant problem after a continuum space-time problem has been discretised over space, or simply a large system of ODEs. This takes the form

$$\frac{du}{dt} = f(u, p), \quad (u, p) \in \mathcal{U} \subset \mathbb{R}^n \times \mathbb{R}, \quad (3.25)$$

where  $n \gg 1$  is the size of the large-dimensional system of ODEs. The flow

$$\phi(u, t, p), \quad (3.26)$$

is defined as the solution of (3.25) at time  $t$ , with initial condition  $u$  at  $t = 0$ , for a fixed parameter  $p \in \mathbb{R}$ . 3.26 may be thought of as the output of a numerical time-stepper, such as a Runge-Kutta scheme, of (3.25) which *flows* an initial condition  $u$  forward a time  $t$ .

A given trajectory is a periodic orbit solution of (3.25) with period  $T$  if  $\phi(u, T, p) = u$  for all components of  $u$  and  $\phi$ . This is the periodicity condition; it specifies infinitely many periodic orbits, occupying the same phase space, but each with different initial conditions along the orbit. As such, this has a non-unique solution since it is satisfied by many values of  $u$

at any phase along the periodic orbit. Appending a phase condition in time,  $\mathcal{T}(u, p) = 0$ , to the problem selects one of the infinitely many orbits on the cycle [60, 149]. We utilise the Poincaré orthogonality phase condition [61] in time, given by

$$\mathcal{T}(u, p) = f_{\text{ref}}(u - u_{\text{ref}})^T, \quad (3.27)$$

where  $u$  is a solution profile at a fixed time (often considered to be the solution at  $t = 0$ ),  $u_{\text{ref}}$  is a point on a reference solution (at  $t = 0$ ) which is often taken as the previous solution on the branch, or a sufficiently good initial guess to a true solution, and  $f_{\text{ref}}$  is the vector field at  $u_{\text{ref}}$ . Other phase conditions exist, such as the widely used integral phase condition which minimises the distance between successive solutions globally over a period, though the Poincaré condition is sufficient for our purposes. The selection of a unique phase is chosen which closes the system of equations, ensuring there are as many conditions as unknowns. There are  $n + 1$  equations – consisting of  $n$  components of the periodicity condition, and 1 phase condition in time – for  $n + 1$  unknowns –  $n$  components of the solution  $u$ , and 1 period,  $T$ .

Thus, the zero-problem for a spatially extended periodic orbit solution is  $H(u, T, p) = 0$ , where

$$H(u, T, p) = \begin{pmatrix} u - \phi(u, T, p) \\ \mathcal{T}(u, p) \end{pmatrix} \in \mathbb{R}^{n+1}, \quad (3.28)$$

so that  $N = n + 1$  in (3.6). This simultaneously determines  $u$  and the period  $T$ , for a fixed parameter  $p$ ; in other words, (3.28) determines the spatially extended periodic orbit solution for a given parameter set. With  $z = (u, T) \in \mathbb{R}^{n+1}$ , the problem of periodic orbit continuation is given by  $\mathcal{H}(z, p) = H(z, p)$  in (3.6).

In standard periodic orbit continuation, the Jacobian matrix of (3.28) needs to be computed explicitly, which is an  $\mathcal{O}(n^2)$  computation for the Jacobian matrix of size  $(n + 1) \times (n + 1)$ . Instead, the method in [216] requires the *action* of the Jacobian on the perturbed quantities of interest (this is discussed

below). The action is the same size as the problem (3.28) – that is, of size  $(n + 1)$  – and results in a significant increase in computation speed due to dealing with  $\mathcal{O}(n)$  quantities rather than  $\mathcal{O}(n^2)$  quantities. For a number of examples illustrating the computational specification of Jacobian actions, see the GitHub repository here [147].

Suppose a periodic orbit solution  $Z = (u, T, p)$  has been found for a given parameter value. This is a zero of (3.28). For continuation, the Jacobian action of the system (3.28), with respect to the perturbation state vector  $\delta Z = (\delta u, \delta T, \delta p)$  must be determined. Since  $\phi = \phi(u, T, p)$ , then to first order,

$$\begin{aligned} d\phi &= \phi(u + \delta u, T + \delta T, p + \delta p) - \phi(u, T, p), \\ &= D_t\phi(u, T, p)\delta T + D_u\phi(u, T, p)\delta u + D_p\phi(u, T, p)\delta p, \end{aligned} \quad (3.29)$$

and so the Jacobian action of (3.28) on  $\delta Z$  is

$$D_Z H(Z)\delta Z = \begin{pmatrix} \delta u - D_u\phi(u, T, p)\delta u - D_p\phi(u, T, p)\delta p - D_t\phi(u, T, p)\delta T \\ \mathcal{T}_u(u, p)\delta u \end{pmatrix}. \quad (3.30)$$

In order to compute 3.30, we must compute the various terms present. The term  $\mathcal{T}_u(u, p)\delta u$  is analytically computable as

$$\mathcal{T}_u(u, p)\delta u = f_{\text{ref}}\delta u^T. \quad (3.31)$$

Note there is no  $\mathcal{T}_u(u, p)\delta p$  term. The terms involving the Jacobian of the flow are found as follows.

Let  $y(t) = \phi(u, t, p)$  define the flow, or the solution of (3.25), subject to the initial condition  $y(0) = u$ , and fixed parameters  $p$ . Then by (3.25),

$$\frac{dy}{dt} = f(y, p), \quad y(0) = u. \quad (3.32)$$

The terms

$$D_u\phi(u, T, p)\delta u + D_p\phi(u, T, p)\delta p$$

can be obtained as the solution to a set of ODEs coupling the quantities  $y(t)$  and  $y_1(t) = D_u\phi(u, t, p)\delta u + D_p\phi(u, t, p)\delta p$ . With this choice of  $y_1(t)$ , the quantity

$$y_1(T) = D_u\phi(u, T, p)\delta u + D_p\phi(u, T, p)\delta p$$

consists of precisely the terms we are trying to find. A variational problem is solved to find  $y_1(T)$ , as described here. Taking the time derivative of  $y_1(t)$ , we obtain

$$\frac{dy_1}{dt} = D_t D_u\phi(u, t, p)\delta u + D_t D_p\phi(u, t, p)\delta p, \quad (3.33)$$

where the notation  $D_t D_u$  represents the second-order partial derivative  $D_{t,u}$ . By the interchangeability of partial derivatives,

$$\frac{dy_1}{dt} = D_u D_t\phi(u, t, p)\delta u + D_p D_t\phi(u, t, p)\delta p, \quad (3.34)$$

Then noting that  $f(y(t), p) = D_t\phi(u, t, p)$ , and that  $u = \phi(u, 0, p)$ , so that  $y_1(0) = \delta u$ , one obtains

$$\frac{dy_1}{dt} = D_y f(y, p)y_1 + D_p f(y, p)\delta p, \quad y_1(0) = \delta u. \quad (3.35)$$

In summary, integrating the *variational problem*

$$\frac{dy}{dt} = f(y, p), \quad y(0) = u, \quad (3.36a)$$

$$\frac{dy_1}{dt} = D_y f(y, p)y_1 + D_p f(y, p)\delta p, \quad y_1(0) = \delta u, \quad (3.36b)$$

up to a time  $t = T$ , we obtain the desired quantity

$$y_1(T) = D_u\phi(u, T, p)\delta u + D_p\phi(u, T, p)\delta p. \quad (3.37)$$

In this way, all of the terms involved in the computation of the Jacobian action  $D_Z H(Z)\delta Z$  (3.30) are determined. Notice here the lack of matrices in the problem description. The variational problem involves the integration of  $2n$  quantities without requiring the explicit construction of the Jacobian *matrix*. The use of a *suitable* time-stepper is key in utilising the potential of the method. In our tests and usage, a Runge-Kutta (4,5) scheme has been suitable for sufficiently smooth systems.

### 3.3.2 Numerical Stability Routine

Given a spatially extended periodic orbit solution, we numerically determine its stability as follows. Periodic orbit stability is characterised by the existence of Floquet multipliers  $(\lambda_i, i = 1, \dots, n)$ . Of these  $n$  multipliers, one is the *trivial multiplier*,  $\lambda_n = 1$ , which arises due to solution periodicity [21]. If all non-trivial multipliers  $(\lambda_i, i = 1, \dots, n - 1)$  are inside the disc, the orbit is stable. If at least one non-trivial multiplier is outside the unit disc, it is unstable [78, 125]. The three distinct ways eigenvalues can cross the unit disc are shown in Figure 3.3. Instabilities may be of fold of cycles- ( $\lambda = +1$ ), period doubling- ( $\lambda = -1$ ), or Neimark-Sacker-type ( $\lambda = e^{i\theta}, \theta \neq 0, \pi$ ). Recall the periodicity condition defining a periodic orbit

$$u = \phi(u, T, p). \quad (3.38)$$

where  $T$  is the period. Define a Poincaré map  $u_{i+1} = \phi(u_i, T, p)$ , through some transverse section  $\Sigma$  [149] of  $u$ -phase space, and linearise about the

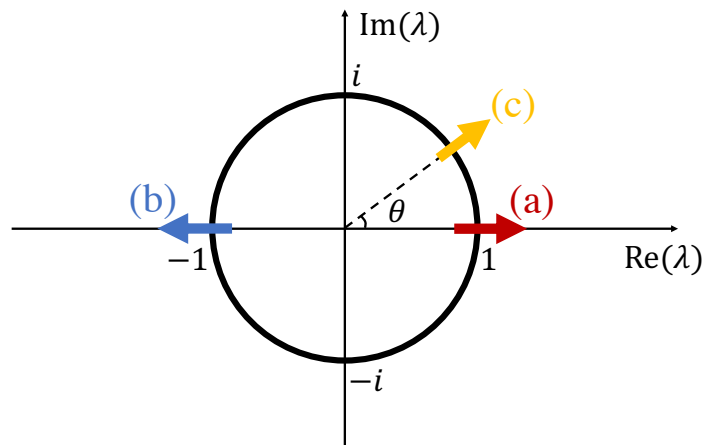


Figure 3.3.: A plot showing the three different qualitative ways an eigenvalue can cross the unit disc resulting in an instability to a periodic orbit: (a) through  $+1$  (red), (b) through  $-1$  (blue), and (c) with non-zero imaginary part (yellow).

periodic orbit solution, which is a fixed point of the map. So,  $u_i = u + \delta u_i$ ,  $u_i \in \mathbb{R}^n$ , where  $i$  is an iteration counter. Then

$$\delta u_{i+1} = D_u \phi(u, T, p) \delta u_i. \quad (3.39)$$

This defines an eigenvalue problem which can be solved by `eigs` in MATLAB to determine the stability of the spatially extended periodic orbit. The quantity  $D_u \phi(u, T, p) \delta u_i$  can be found via the variational problem defined in the previous subsection, with  $\delta T = 0$ , and  $\delta p = 0$ .<sup>6</sup>

### 3.3.3 Computational Implementation

So far, we have determined the necessary zero-problem in order to successfully compute spatially extended periodic orbit solutions; given a sufficiently close initial guess to a true periodic orbit solution, we have the mathematical framework in place to find the true solution. This zero-problem is augmented with a PALC condition as described in Section 3.1, allowing for the continuation of periodic solutions along the solution branch.

The way we set this up computationally is by creating a class in MATLAB for a given model containing the vector field,  $F(u, p)$ , the Jacobian action  $D_u F(u, p) \delta u$ , and the Jacobian action with respect to parameters  $D_p F(u, p) \delta p$ . An instance of this class is created with chosen parameter values, mesh size, and domain length for spatial systems. This is fed into a suitable interface describing the solution-type of interest, for example a spatially-extended periodic orbit, along with a reasonable initial guess. The continuation software then augments the pseudo arc-length condition and carries out the continuation as outlined in Section 3.1.5 and illustrated in Figure 3.1. The flowchart, Figure 3.9 at the end of this chapter illustrates this.

---

<sup>6</sup>Note that we only demand periodicity in  $u$ , and not in  $T$  or  $p$ , which is why  $\delta T$  and  $\delta p$  are set to 0.

### 3.3.4 Convergence Tests

In carrying out periodic orbit continuation using the matrix-free method described in this section, the Jacobian action must be computed exactly. A correct Jacobian action is critical for correct function. As such, we give here a test which may be used to determine if the supplied Jacobian action is correct for a given vector field,  $f$ .

Taylor expanding the right-hand side of (3.25), with  $\epsilon \ll 1$ , about some  $u = u_0$ , we obtain

$$f(u_0 + \epsilon u, p) = f(u_0, p) + D_u f(u_0, p)(\epsilon u) + \mathcal{O}(\epsilon^2). \quad (3.40)$$

**Test 1:** Testing  $D_u f(u, p)\delta u$ . *The error quantity*

$$E(\epsilon) = f(u_0 + \epsilon u, p) - f(u_0, p) - D_u f(u_0, p)(\epsilon u), \quad (3.41)$$

decreases to 0 at  $\mathcal{O}(\epsilon^2)$  as  $\epsilon \rightarrow 0$ .

Thus, a Jacobian action is correctly supplied if and only if  $E(\epsilon) \rightarrow 0$  at  $\mathcal{O}(\epsilon^2)$ .

An identical test can be carried out for the Jacobian action with respect to parameters. Taylor expanding the right-hand side of (3.25) about some  $p = p_0$ , we obtain

$$f(u, p_0 + \epsilon p) = f(u, p_0) + D_p f(u, p_0)(\epsilon p) + \mathcal{O}(\epsilon^2), \quad (3.42)$$

**Test 2:** Testing  $D_p f(u, p)\delta p$ . *The error quantity*

$$E_p(\epsilon) = f(u, p_0 + \epsilon p) - f(u, p_0) - D_p f(u, p_0)(\epsilon p), \quad (3.43)$$

decreases to 0 at  $\mathcal{O}(\epsilon^2)$  as  $\epsilon \rightarrow 0$ .

As a test case, consider the neural field model of spike frequency adaptation (SFA) (2.46), known to exhibit periodic orbit solutions [67]. Figure 3.4 (upper panels) shows these tests for (2.46), demonstrating that  $\mathcal{O}(\epsilon^2)$  convergence of the quantity  $E(\epsilon)$  is achieved as  $\epsilon \rightarrow 0$ . This is shown by the

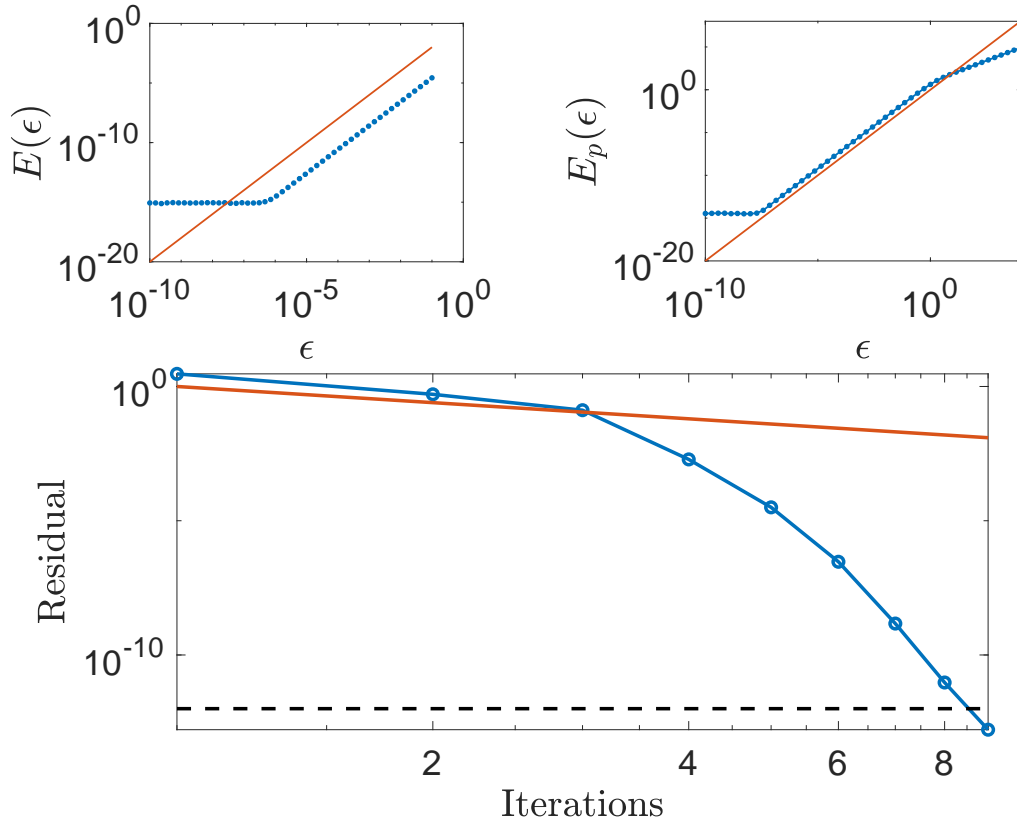


Figure 3.4.: Convergence tests for the SFA model (2.46). Blue dots in the top panels show  $E(\epsilon)$  (left) and  $E_p(\epsilon)$  (right). Blue dots and blue line in the bottom panel shows super-quadratic convergence to a breathing solution. The slope of the orange lines indicate expected  $\mathcal{O}(\epsilon^2)$  convergence on the logarithmic vertical scale in all three panels. The dashed black line denotes the non-linear tolerance,  $\epsilon_n$ , for Newton's method.

matching slopes of the orange (expected error) line and the blue dots (actual error), until machine accuracy is encountered close to  $10^{-15}$ . The quantity,  $E_p(\epsilon)$  passes the test too.

These tests are a necessary check to ensure that the supplied Jacobian action are correct for the vector field  $f$  provided. In the case where the supplied Jacobian action does not match up with the relevant vector field, the slopes will not match; the slope of the points  $E(\epsilon)$  will be shallower than  $\mathcal{O}(\epsilon^2)$ , indicating a sub- $\mathcal{O}(\epsilon^2)$  convergence. The same test is utilised

to show that the Jacobian action (3.30) of the PO problem (3.28) is correctly specified.

Before continuation, a final test is carried out to ensure solutions converge as expected.

**Test 3:** Quadratic Newton convergence to a solution. *A sufficiently close initial guess  $x_0$  to a true solution  $x^*$  of the problem under consideration will exhibit quadratic convergence to  $x^*$ .*

A failure of this test may be a consequence of Tests 1 or 2 not passing, or it may indicate that parameters are poised numerically unfavourably and that numerical stiffness is present in the model. The model (2.46) passes this test for a breathing solution; see the lower panel of Figure 3.4, showing the residual (3.10) at each Newton iteration decreasing beyond what is expected. Quadratic convergence is shown in Figure 3.4: as the number of iterations increases, the convergence occurs more rapidly, as shown by the residual decreasing by larger orders of magnitude. Eventually, the residual falls below the specified tolerance,  $\epsilon_n$  (illustrated by the black dashed line at  $10^{-12}$ ), for the non-linear solver, indicating that the resulting solution has converged to the true solution, to within the specified tolerance.

For the most accurate solution,  $\epsilon_n$  should be close to machine accuracy. For large spatial systems, the smaller  $\epsilon_n$  is, the more iterations are needed per continuation step to converge to a solution, increasing the time taken. This can be significantly costly in cases where each Newton iteration takes a long time. Thus, the required tolerance should be chosen carefully. Often, an overly small tolerance is not required to successfully characterise solutions.

## 3.3.5 Results: Breathers in a Neural Field Model

Figure 3.4 shows that the model (2.46), passes the two tests for  $E(\epsilon)$  and  $E_p(\epsilon)$ , and the convergence test for a breathing solution. Therefore, we are in a position to carry out continuation and have confidence in the results.

Figure 3.5 shows the continuation of a spatially extended, heterogeneous periodic pattern using the methodology developed in this chapter. A stationary breather is continued in the adaptation rate parameter,  $\alpha$ . This bifurcation parameter is plotted against the emergent temporal period of the

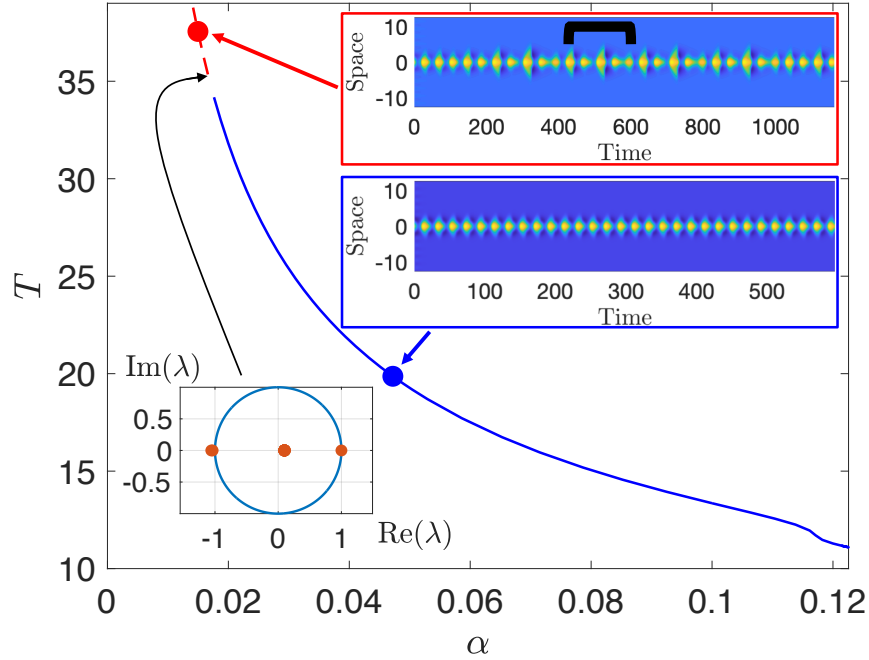


Figure 3.5.: Continuation of a breather in (2.46), in the adaptation rate parameter  $\alpha$  against the temporal period  $T$ , showing a period-doubling-type bifurcation at  $\alpha = 0.017$ . See the main text for more details. Blue (red) lines are stable (unstable) solution branches. The black brace in the top inset illustrates the emergent period of the period-doubled solution. Parameters:  $\beta = 2.75$ ,  $\mu = 10$ ,  $\kappa = 0.375$ ,  $\sigma = 1.2$ ,  $I_0 = 1.9$ , with kernel parameters  $w_E = 1$ ,  $w_I = 0$ ,  $\sigma_E = 1$ , and  $\sigma_I = 2$ . Domain  $(-L_x, L_x)$ , with half-length  $L_x = 4\pi$ , and mesh size  $n_x = 1000$ .

pattern,  $T$ . The branch of stable (blue) breathers persists as  $\alpha$  is decreased, until  $\alpha = 0.017$ , where an eigenvalue leaves the unit disc through  $-1$  (this is shown in the lower-left inset, with eigenvalues represented by orange dots). This is indicative of an instability of period-doubling-type, and is confirmed by direct numerical simulation shown in the upper inset. Two solutions are taken – one from the stable part of the branch, and one from the unstable (red) part of the branch – and perturbed. The time evolution of the resultant patterns is shown in the insets.

A solution on the stable part of the branch, when perturbed, eventually settles back down to its initial unperturbed state. However, solutions on the unstable part of the branch undergo a qualitative change in their dynamics. Rather than settling back down to a standard breather, a more exotic breather is seen, exhibiting a “large-small-large-small-small” repeating unit of sub-breathers over the new period. This is illustrated with the black brace shown in the upper inset.

The predictions of the continuation software agree with direct numerical simulation, with the numerical stability routine predicting the correct type of instability at the correct location on the solution branch. Furthermore, the existence of the trivial eigenvalue at  $+1$  should be noted as a property of periodic orbits as opposed to an instability of  $+1$ -type.

### 3.4 TRAVELLING PERIODIC ORBIT CONTINUATION

#### 3.4.1 *Problem Formulation*

The previous section was concerned with the study of *stationary* spatially-extended periodic orbit solutions. The numerical method does not require any property from a solution other than that it be periodic in time. This covers a wide range of solutions; a few examples are breathers, standing oscillatory waves, such as  $n$ -cycles, and sloshers.

We now turn our attention to a different class of solution: spatially-extended *travelling-wave* temporally-periodic orbits (TWPO). Such solutions appear in a wide variety of contexts. Perhaps the simplest that fit into this category are standard travelling waves, and *travelling wavetrains*. These are stationary in the co-moving frame, and so can be thought to take any temporal period. Examples can be seen throughout biology and in physical systems [148, 120, 68, 138]. However, our main interest is in travelling patterns that exhibit some sort of spatial heterogeneity. In the case where this repeats in time, we obtain TWPO solutions. Examples include saltatory waves with a well-defined wavespeed, travelling breathers [48] seen in neural fields, and lurching waves [224] found in models of thalamic tissue. It should be noted here that travelling breathers are not specific to neural field-type models – they are seen in many multi-component reaction-diffusion equations [197, 146, 145]. Mimura et al. [145] studied them in systems of reaction-diffusion equations by utilising singular perturbation methods and reducing the spatio-temporal description of travelling breathers down to an interface problem described by ODEs. The numerical study of lurching waves in a two-layer, one dimensional lattice model by Wasylenko et al. [224] is currently the most thorough numerical treatment of lurching waves (on a mesh of size  $n_x = 60$ ). The authors utilise continuation techniques to continue different lurching-type patterns by seeking fixed points of a Poincaré map.

The method we describe here is quite general in the sense that it is not limited to globally spatially periodic travelling solutions, but can also be used to continue *localised* solutions which travel, such as the travelling breather solutions in [48]. The only property required of a solution of interest is that it consist of self-similar units that repeat after a temporal period, with a zero or non-zero wavespeed. In the case of a zero wavespeed, travelling periodic solutions reduce to periodic solutions; the problem description reduces to the PO problem given by (3.28).

Simply put, the stationary periodic orbit method given in [216], and reviewed in the previous section, finds solutions  $q(x) = u(x, 0)$  such that  $q(x) = u(x, T)$  for some  $T > 0$ . Here, we extend this method to find solutions which have the same spatial profile after some period  $T$ , up to a spatial shift,  $\xi \in \mathbb{R}$ . Figure 3.6 shows an illustration of this.

Consider a system of coupled partial differential equations, where the state vector  $z(x, t) \in \mathbb{R}^n$ , of the form

$$\frac{\partial}{\partial t} z(x, t) = \mathcal{N}(z(x, t)), \quad x \in \mathbb{R}, t > 0, \quad (3.44)$$

where  $\mathcal{N}$  is an operator (which may be non-local) describing the time evolution of the state variables  $z$ . Further assume that  $z(x, t) = Z(x - ct, t)$ , with  $Z$  being  $T$ -periodic in its second variable (time in the co-moving frame). Notice importantly that we do not restrict ourselves to the case of seeking *time-independent* solutions in the co-moving frame, which correspond to simple travelling waves with no other *intra-period* dynamics.

This generic set-up leads to the consideration of solutions of the general type shown in Figure 3.6; they move with a well-defined wavespeed, but have non-trivial intra-periodic dynamics. We seek solutions which have an identical spatial profile after a temporal period  $T$ , when subject to some spatial shift,  $\xi = cT$ , where  $c$  is the constant wavespeed. For an initial profile  $q(x)$ , and a flow  $\phi$  which maps an initial profile  $q(x)$  to its value at time  $t$ , as  $u(x, t) = \phi(q(x), t, p)$ , a zero-problem defining periodic solutions of the type described here is given by

$$q - S_{-\xi} \phi(q, T, p) = 0, \quad (3.45)$$

where the shift operator  $S$  is defined as

$$(S_{\xi} q)(x) = q(x + \xi). \quad (3.46)$$

Eq. (3.45) flows the solution and then shifts it by a spatial amount  $\xi$ , represented by the action of  $S_{-\xi}$ , at the end of a period. However, an equally valid condition can be considered by flowing the initial profile over a period

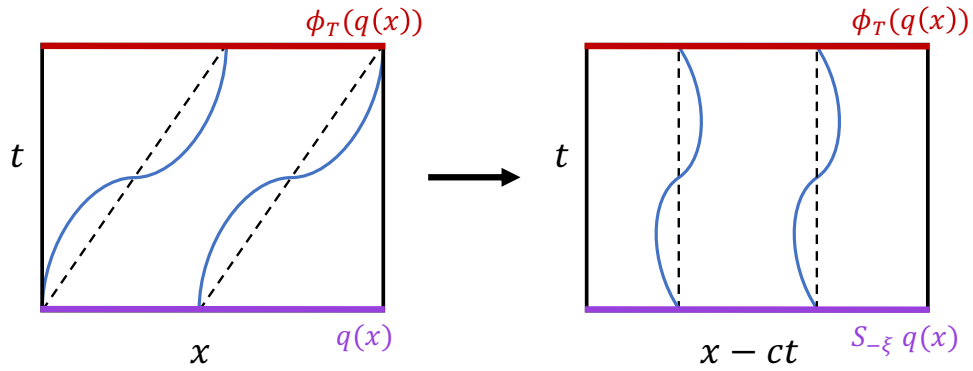


Figure 3.6.: (left) An illustration of the generic solution type our method can continue: a travelling wave which is spatially-heterogeneous over a period. In purple is the profile at some initial time,  $t = 0$ , and in red we highlight the profile after a temporal period  $T$ . (right) The wave profile in the co-moving frame, so that a travelling periodic solution in  $(x, t)$ -space becomes a purely periodic solution in  $(x - ct, t)$ -space. The initial profile,  $S_{-\zeta}q(x)$ , and the final profile,  $\phi_T(q(x))$ , are identical in the co-moving frame, for the correct period  $T$  and shift  $\zeta$ . Black dashed lines in the left-hand pane illustrate the wavespeed, and illustrate the idea that the travelling periodic solution is shifted to become a purely periodic solution in the right-hand pane.

$T$ , and then shifting the *initial* profile by an appropriate  $\zeta$ . This condition is given as

$$S_{-\zeta}q - \phi(q, T, p) = 0, \quad (3.47)$$

and is illustrated in Figure 3.6. We make the choice to shift by  $-\zeta$  to ensure that a positive wavespeed  $c$  corresponds to a positive shift  $\zeta$ .<sup>7</sup>

One of the two periodicity conditions, (3.45) or (3.47), must be chosen to define the zero-problem. Bearing in mind that the method we use requires an analytical Jacobian action that can simply be function evaluated when considering the variational problem (3.36), we make the choice to use (3.47),

<sup>7</sup> A wave moving to the right corresponds to a shift in the positive  $x$ -direction.

so that the shift does not act on the flow. This aids us in determining the Jacobian action below.

In order to solve for  $T$  and  $\xi$ , we require *two* suitable phase conditions to be appended to the periodicity condition: one in space and one in time, since there is translation-invariance in space as well as time for travelling periodic solutions on a homogeneous domain; a solution can be shifted an arbitrary amount in space or time, and it still remains a valid solution. We utilise the phase conditions in space and time, given by  $\mathcal{X}(q, p)$  (3.21) and  $\mathcal{T}(q, p)$  (3.27).

The zero-problem for travelling periodic patterns with spatial heterogeneity over a period can be succinctly given by  $G(q, T, \xi, p) = 0$ , where

$$G(q, T, \xi, p) = \begin{pmatrix} S_{-\xi}q - \phi(q, T, p) \\ \mathcal{T}(q, p) \\ \mathcal{X}(q, p) \end{pmatrix} \in \mathbb{R}^{n+2}, \quad (3.48)$$

where  $N = n + 2$  in (3.6). For a TWPO solution specified by  $V = (q, T, \xi, p)$  to the problem  $G \in \mathbb{R}^{n+2}$ , given by (3.48), the Jacobian action,  $D_V G(V)\delta V$ , on a small perturbation  $\delta V = (\delta q, \delta T, \delta \xi, \delta p)$  about  $V$  must be supplied. The action of the first component of  $D_V G(V)\delta V$  is denoted  $dG_{(q)}$ , and is given by

$$dG_{(q)} = G_{(q)}(q + \delta q, T + \delta T, \xi + \delta \xi, p + \delta p) - G_{(q)}(q, T, \xi, p), \quad (3.49)$$

where  $G_{(q)} = S_{-\xi}q - \phi(q, T, p)$  are the first  $n$  components of  $G$ . Substituting in for  $G_{(q)}$  using (3.48), and Taylor expanding (3.49) to first order in the small quantities, we obtain

$$dG_{(q)} = S_{-\xi}\delta q - S_{-\xi}q'\delta\xi - d\phi \quad (3.50)$$

where  $d\phi = D_q\phi(q, T, p)\delta q + D_T\phi(q, T, p)\delta T + D_p\phi(q, T, p)\delta p$ . The variational problem (3.36) may be used to compute the three terms making up  $d\phi$  as before.

Then the full Jacobian action is specified by

$$D_V G(V) \delta V = \begin{pmatrix} S_{-\xi} \delta q - S_{-\xi} q' \delta \xi - d\phi \\ \mathcal{T}_q(q, p) \delta q \\ \mathcal{X}_q(q, p) \delta q \end{pmatrix} \quad (3.51)$$

where  $\mathcal{T}_q(q, p) \delta q$  is given by (3.31), and

$$\mathcal{X}_q(q, p) \delta q = q'_{\text{ref}} \delta q^T, \quad (3.52)$$

for a reference solution  $q_{\text{ref}}$  and its spatial derivative  $q'_{\text{ref}}$ .

This fully specifies the travelling periodic-orbit problem  $G$  (3.48), and its Jacobian action on a perturbation  $\delta V$ ,  $D_V G(V) \delta V$  (3.51). When  $\xi = 0$ , the problem reduces down to the PO problem (3.28), (3.30). Next, we implement a method which computes the spatial shifts and derivatives present in the problem.

### 3.4.2 Implementation of Shift and Derivative Operators

The means of an *efficient* computation of the shift and derivative are critical in ensuring that computational bottlenecks are minimised. Therefore, we utilise the Fourier shift and derivative properties, with the “*unitary, ordinary frequency*” definition of the Fourier transform defined on the periodic ring  $[-L, L)$  as<sup>8</sup>

$$\mathcal{F}\{f(x)\}(k) = \int_{-L}^L f(x) e^{-2\pi i k x} dx. \quad (3.53)$$

The shift operator  $S_{-\xi}$  acts on a spatial profile  $q(x)$ , shifting it by an arbitrary amount  $\xi$ , as

$$S_{-\xi} q(x) = q(x - \xi), \quad (3.54)$$

which can be computed by utilising the Fourier shift property

$$\mathcal{F}\{q(x - \xi)\}(k) = e^{-2\pi i \xi k} \mathcal{F}\{q(x)\}(k), \quad (3.55)$$

<sup>8</sup>We use the “*unitary, ordinary frequency*” definition of the Fourier transform (with the  $2\pi$  exposed) to keep the notation here as similar as possible to the computational implementation.

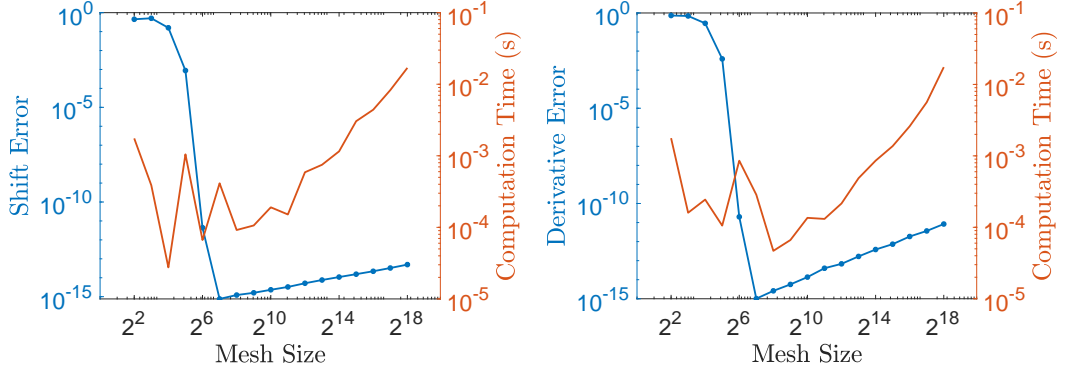


Figure 3.7.: Representative shift error (left) and derivative error (right) in blue as the mesh size is increased. The domain used is  $[-L, L]$ ,  $L = 10$ , with periodic boundary conditions, and the test function is  $f(x) = \exp(-x^2)$ . Also plotted is the representative log-computation time taken to determine shifts and derivatives using Fourier transform methods, in orange.

and Fourier inverting to obtain  $q(x - \xi)$ , as

$$q(x - \xi) = \mathcal{F}^{-1} \left[ e^{-2\pi i \xi k} \mathcal{F}\{q(x)\}(k) \right] (x). \quad (3.56)$$

The derivative operator  $\mathcal{D}$  is implemented in a similar fashion. The operator  $\mathcal{D}$  acts on a profile  $q(x)$  as

$$\mathcal{D}q(x) = q'(x), \quad (3.57)$$

which we compute by utilising the Fourier derivative property that

$$\mathcal{F}\{q'(x)\}(k) = 2\pi i k \mathcal{F}\{q(x)\}(k), \quad (3.58)$$

and then inverting to obtain  $q'(x)$  as

$$q'(x) = \mathcal{F}^{-1} [2\pi i k \mathcal{F}\{q(x)\}(k)] (x). \quad (3.59)$$

In MATLAB, the vector  $k$  takes the form  $k = [0:(nx/2)-1, (-nx/2):-1]'$ , where  $nx$  is the integer mesh size which is some power of two. Using the ordering  $k = [-nx/2:(nx/2)-1]'$  requires the use of the `fftshift` function.

Shown in Figure 3.7 is the error in the shift (left panel) and the derivative (right panel), when computed for a test function using the Fourier shift

and derivative approach, as in (3.56) and (3.59). The test function used is  $f(x) = \exp(-x^2)$ , with a known analytical solution for when it is shifted by some arbitrary amount  $\xi$ ,  $f(x - \xi) = \exp(-(x - \xi)^2)$  or its derivative taken,  $f'(x) = -2x \exp(-x^2)$ . For a domain  $[-L, L]$ ,  $L = 10$  – chosen so that the function comfortably fits inside the domain when it is non-zero, to mirror how an arbitrary pattern may fit on the domain – the error falls sharply as the mesh size is increased beyond  $2^5$ . This behaviour is typical and expected, and is referred to as spectral accuracy [212]. The time taken to compute the shift or derivative is shown in orange. A sweet spot for the mesh size appears to be somewhere between  $2^7$  and  $2^{11}$  mesh points where both the error and the computation time are extremely small. Beyond this, the computation time for both the shift and derivative operations grows exponentially. This behaviour persists, regardless of the test function used. As the domain length  $L$  is increased, the sharp drop in the error occurs at a larger mesh size. This is expected, since more points are required to resolve the mesh for a larger domain. The error rises slightly as the mesh gets larger beyond  $2^{14}$  mesh points. This is due to the accumulation of machine rounding error as the number of arithmetic operations increases [39]; in practice, this is irrelevant since it is not an overly significant rise, and our study takes place with mesh sizes between  $2^7$  and  $2^{11}$ .

While the main advantage of using the Fourier shift and derivative properties lies in its speed, there are a few notable drawbacks. Firstly, this requires a domain to be periodic. While for our purposes, this is acceptable, different boundary conditions may be required for other studies. Another, perhaps more pertinent issue is the requirement by the properties of Fourier analysis that, in order to obtain a *very good* approximation from a finite Fourier series, a solution must not be discontinuous. For solutions which *are* discontinuous, the Gibbs phenomenon [93] is encountered which may ultimately ruin convergence to a solution.

However, the general method of continuation of travelling periodic solutions presented here is still able to converge to these solutions if a dif-

ferent procedure is used to compute shifts and derivatives. The challenge lies in finding such a technique which is also fast and efficient. A simple matrix-vector multiplication of a shift matrix (e.g., a circularly shifted identity matrix) with a state vector is an implementation which would allow the method to find a solution, but this would lead to the types of computational bottlenecks we are keen to avoid. Thus, this is an open challenge moving forward. Are we able to find an *efficient* way to compute shifts which are independent of the mesh size, and derivatives of solutions which contain shocks or discontinuities, to a high degree of accuracy?

### 3.4.3 Convergence Tests

The overarching travelling periodic orbit problem defined by  $G(\cdot)$  (3.48) and  $D_V G(V)(\cdot)$  (3.51) has been constructed, and a method for computing shifts and derivatives has been supplied. We carry out the convergence tests defined in Section (3.3.4) on the problem  $(G(\cdot), D_V G(V)(\cdot))$ . This tests whether the Jacobian action  $DG_V \delta V$  is the correct one corresponding to the problem  $G$  for an arbitrary perturbation  $\delta V$ .

Figure 3.8 shows the characteristic  $\mathcal{O}(\epsilon^2)$  error for  $\epsilon < 10^{-3}$  until it levels off close to machine accuracy. Also shown is the convergence of a travelling periodic solution (right panel). At least quadratic convergence is expected, and this benchmark is shown by the slope of the orange line in log-space. Super quadratic convergence, where the residual “accelerates” towards zero after the second iteration, is seen. This demonstrates the problem is set up correctly, and an initial guess to a travelling periodic solution converges as expected to a true solution. Thus, the method is ready for the continuation of travelling periodic structures. We use the TWPO continuation method in Chapter 4 to continue travelling periodic solutions that exist in the models studied there.

### 3.4.4 Numerical Stability Routine

Here, we derive a scheme to computationally determine linear stability. It uses the same idea as that in Section 3.3.2 for PO-type problems.

Given a general TWPO solution  $V = (q, T, \zeta; p)$  for a fixed parameter set, we determine its numerical stability as follows. Recall that travelling, periodic solutions are determined by

$$S_{-\zeta}q = \phi(q, T, \zeta, p), \quad (3.60)$$

which is illustrated in Figure 3.6. This gives rise to a Poincaré map

$$S_{-\zeta}q_{i+1} = \phi(q_i, T, p), \quad (3.61)$$

through some transverse section  $\Sigma$  [149] of  $q$ -phase space. A rather important consideration is that the section only be taken through  $q$ -phase space, and not  $(q, T, \zeta)$ -phase space, since  $T$  and  $\zeta$  are fixed properties of a given

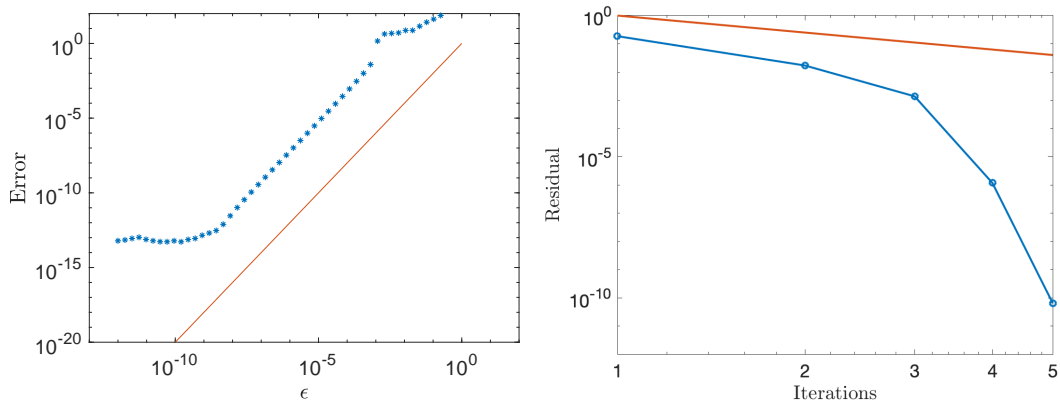


Figure 3.8.: (left) The error in  $E(\epsilon)$  plotted as a function of  $\epsilon$  shown as blue asterisks', for the travelling periodic orbit problem (3.48) and (3.51). The slope of the orange line shows the expected  $\mathcal{O}(\epsilon^2)$  error.  $E(\epsilon)$  follows this closely until a machine or function accuracy is reached at  $E \approx 10^{-15}$ . (right) The residual at each Newton iteration in converging to a true travelling periodic orbit solution. A mesh size  $n_x = 512$  is used.

travelling periodic orbit.<sup>9</sup> Linearise about the travelling periodic orbit solution,  $q_i = q + \delta q_i$ ,  $q_i \in \mathbb{R}^n$ , where  $i$  is an iteration counter. Then

$$S_{-\xi} \delta q_{i+1} = D_q \phi(q, T, p) \delta q_i. \quad (3.62)$$

This defines a *generalised* eigenvalue problem, which are problems of the form

$$Av_i = \lambda_i Bv_i, \quad (3.63)$$

for  $A, B \in \mathbb{R}^{n \times n}$ ,  $v \in \mathbb{R}^n$ . In the case where  $B = I_n$  ( $n \times n$  identity matrix), this reduces down to the standard eigenvalue problem utilised in the PO continuation earlier in this chapter.

The generalised problem (3.62) can be solved by `eigs` in MATLAB to determine the stability of the travelling periodic orbit. The Jacobian action quantity  $D_q \phi(q, T, p) \delta q_i$  can be found via the variational problem defined in Section 3.3.1, with  $\delta T = 0$ ,  $\delta \xi = 0$ , and  $\delta p = 0$ . Note that we only demand periodicity in  $q$  (and not in  $T$ ,  $\xi$ , or  $p$ , which is why  $\delta T$ ,  $\delta \xi$ , and  $\delta p$  are set to zero).

### 3.5 SUMMARY

This chapter has focused on numerical bifurcation analysis in spatially extended systems. Rather different techniques are required when studying the large-dimensional systems that spatial models give rise to, than those implemented in current state-of-the-art software aimed at the analysis of low-dimensional ODE systems, such as AUTO and MATCONT. Iterative schemes currently appear to be the best approach in large-dimensional systems. We briefly reviewed the continuation of equilibria by considering hexagonal patterns in a neural network set on a planar lattice in Section 3.2. Standard travelling wave solutions may be continued by moving to a co-moving frame to obtain an appropriate zero-problem.

---

<sup>9</sup>When flowing a solution, we do not expect that  $T_{\text{end}} = T_{\text{start}} = 0$ , or  $\xi_{\text{end}} = \xi_{\text{start}}$ , since  $T$  and  $\xi$  are properties of the solution.

Solution Type	Quantity of Interest				
	State	Wavespeed	Period	Shift	Parameter
Equilibria	✓	×	×	×	✓
Travelling Wave	✓	✓	×	×	✓
Periodic Orbit	✓	×	✓	×	✓
Travelling Periodic Orbit	✓		✓	✓	✓
Fold-of-Cycles Point	✓✓	×	✓	×	✓
Flip Point	✓✓	×	✓	×	✓
Neimark-Sacker Point	✓✓✓	×	✓	×	✓

Table 2.: (upper): A summary of qualitatively different solutions to space-time models, and the quantities that fully describe such solutions. During continuation, the ticked quantities for each solution-type are emergent quantities. The wavespeed for a travelling periodic orbit is uniquely determined from its period and shift. (lower): Methods to be implemented. Double (triple) ticks in the state column indicate the need to track a corresponding eigenvector (eigenvalue and eigenvector pair) [216].

Spatially-extended periodic orbits have rarely been studied in-depth in a mathematical neuroscience context; the majority of focus up until this point appears to be in fluid dynamics applications [184, 183]. A likely reason for this is the integro-differential nature of the neural field equations. Techniques exist allowing an equivalent PDE representation for choices of connectivity functions whose Fourier transforms have a rational structure [128]. We have developed a continuation suite utilising the methods derived in [216] and elucidated in this chapter at this GitHub repository [147]. One of the many advantages of this suite is that neural field models can be studied in the integro-differential formulation; there is no need to transform the system to PDE system. However, we stress that the suite is not limited to the study of neural field models. The suite builds on the work of [13], going be-

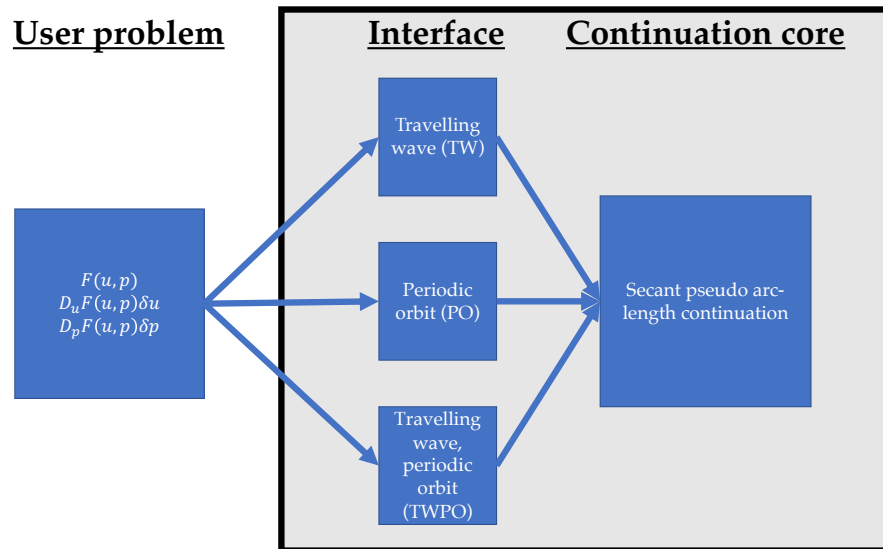


Figure 3.9.: Structure of the periodic orbit continuation code. The interface and continuation core are “hidden” from a user, in the sense that the user is not required to have knowledge about the workings of these two parts. The only demands on the user are to supply their problem in the form shown, and to choose an appropriate interface (which amounts to knowing the solution type of the initial guess).

yond equilibria and travelling waves, allowing for the efficient continuation of periodic solutions. Table 2 summarises the different types of solutions that can be continued using the suite and the emergent quantities that fully characterise each solution-type. We have implemented the methods in [216] to study temporally periodic solutions, and have developed novel methods on top of these to study travelling periodic solutions.

The illustration shown in Figure 3.9 shows a simplified global structure of the spatially-extended periodic orbit continuation software. A problem is specified, containing a description of the vector field  $F$  describing the problem, and Jacobian actions  $D_u F(u, p) \delta u$  and  $D_p F(u, p) \delta p$ . Depending on the solution-type of interest, a relevant interface is chosen – be that travelling wave, periodic orbit, travelling periodic orbit, or the identity interface in the case of equilibria – along with a sufficiently close initial guess to the

solution. From this, solution continuation may proceed. We hope that the development of this suite brings continuation and numerical bifurcation analysis of periodic orbits in spatially-extended systems into the domain of researchers who are not specialists in continuation.

There is scope to include more functionality within the continuation suite. The upper part of Table 2 summarises the current functionality, with future implementations that would allow an even more in-depth study into periodic patterning in space-time models shown in the lower part. Umbría and Net (2016) [216] include methods to track and continue points where bifurcations of periodic orbits occur in two-parameter space. This is a natural way to extend the suite and would allow for two parameter bifurcation diagrams tracking, for example, fold-of-cycles points for spatially extended patterns. Other possible avenues that could be explored are implementing an automatic differentiation scheme to compute the Jacobian actions. This would certainly be beneficial to users, since supplying and testing the Jacobian actions can be quite time consuming for large systems.

With regards to the core continuation scheme, the currently implemented PALC scheme only tracks a single solution branch based on initial data. So-called “deflation” techniques have been developed which allow multiple distinct solutions to differential equations to be found from a single initial guess [75]. This is done by systematically eliminating known solutions from the search-space. Deflated Newton continuation techniques were utilised in [40] to find multiple solution branches to a two-dimensional non-linear Schrödinger equation. Deflation appears to be the next generation of continuation scheme, although it is still in its infancy. Its higher computational cost is also likely a hurdle to overcome in the coming years before it becomes a more mainstream technique. Until then, it is likely that deflated continuation on space-time models will occur via Graphics Processing Unit (GPU) programming [232, 74].

---

## NEURAL FIELDS WITH DYNAMIC FIRING THRESHOLDS

---

### 4.1 INTRODUCTION

Neural tissue consists of a highly complicated network of interconnected cells. This is often modelled using integro-differential equations to describe the synaptic activity of tissue [45] in the cortex of the brain. For slow synaptic interactions, the spike train typically seen to represent action potentials that contribute to inducing a post-synaptic potential can be replaced by a *firing rate* function [45] as outlined in Section 2.5. This is often a sigmoidal function of the synaptic activity such that higher activity in connected tissue feeds higher activity at the point of interest. For synaptic activity  $u$ , the firing rate function is typically of the form  $f = f(u - h)$  where  $h$  is the firing threshold.

In the standard neural field set-up, the firing threshold  $h$  is modelled as being constant [5]. However, there is strong evidence to suggest that the firing threshold is a dynamic quantity which is increased for firing tissue when compared to that of resting tissue. Hill (1936) [94] noted that “*The critical value of [the local membrane potential]  $V$  required for excitation, i.e., the threshold  $U$ , might have been constant and independent of the previous history of the nerve. If the current lasts only for a very short time, this is true. If, however, the current lasts longer, the threshold rises, as is shown by the well-known fact*

that a slowly increasing current has a higher threshold than a quickly increasing one." Hill goes on further to state that "We shall use the term "accommodation" (Nernst, 1908 [158]) to describe the fact that the threshold  $U$  rises when the "local potential"  $V$  is maintained. It is known that the accommodation disappears of itself, i.e.,  $U$  gradually reverts to its original value  $U_0$ , when the nerve is allowed to return to its original resting state."

Further evidence of a dynamic threshold is present in the seminal work of Hodgkin and Huxley [100] who noted the "anodal break excitation" phenomenon in which a hyperpolarised giant squid axon was shown to *fire* upon release from hyperpolarisation, as opposed to simply returning to rest. In some sense then, the hyperpolarisation of tissue changes its firing properties (namely the firing threshold is altered from its resting value). The firing threshold is raised during the refractory period following a neuronal spike when compared to its resting value, hence the difficulty in firing during the refractory period.

In 2005, Coombes and Owen [50] considered a simple phenomenological model of threshold accommodation that took the form

$$u = \eta * w \otimes f(u - h), \quad (4.1a)$$

$$h_t = -(h - h_0) + \kappa g(u - \theta), \quad (4.1b)$$

where the symbols  $*$  and  $\otimes$  represent *temporal* (2.38) and *spatial* (2.35) convolutions, respectively. The function  $f$  is the firing rate function, and  $g$  is a function describing the effects of threshold accommodation. Coombes and Owen took  $f$  and  $g$  to be Heaviside functions, represented by the symbol  $H(\cdot)$ . Explicitly,  $f(u) = H(u)$ , and  $g(u) = H(u)$ . The parameter  $h_0$  is the resting value of the dynamic firing threshold and  $\kappa$  is a parameter that measures the strength of accommodation. The maximal value that can be taken by the threshold is  $h_0 + \kappa$ . The accommodation is itself a threshold process with the accommodation threshold given by  $\theta$ . To briefly summarise, the threshold only increases if  $u$  is sufficiently large ( $u > \theta$ ), and returns to

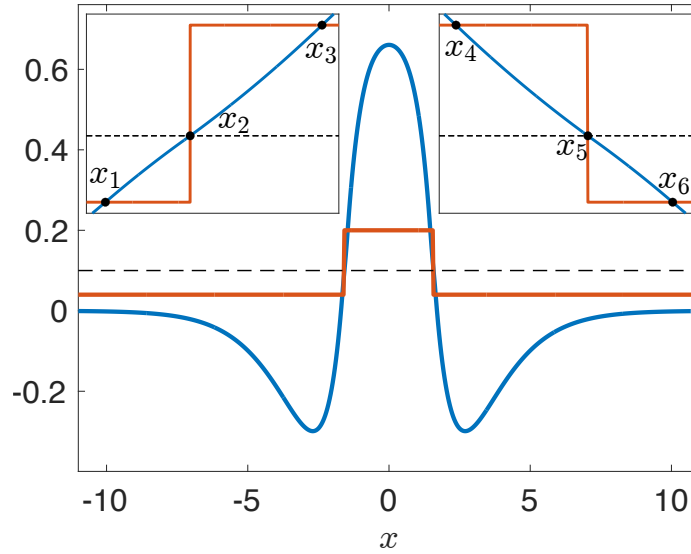


Figure 4.1.: Stationary bump solution to the model (4.1) with  $u(x)$  in blue and  $h(x)$  in orange. The accommodation threshold  $\theta$  is shown as a dashed black line. The solutions are symmetric about  $x = 0$ . The threshold crossings shown in the insets satisfy  $q(x_i) = p(x_i)$  for  $i = 1, 3, 4, 6$ , and  $q(x_i) = \theta$  for  $i = 2, 5$ .

rest otherwise. This is very much in the spirit of Hill's [94] observations summarised above.

It was shown in [50] that the classical wizard hat connectivity

$$w(x) = (1 - |x|)e^{-|x|}, \quad (4.2)$$

shown in Figure 2.9, allows for the existence of spatially localised bumps such as that shown in Figure 4.1. Bumps have been linked to working/short-term memory in the prefrontal cortex [129, 230, 43, 85]. Via a linear stability analysis and using Evans function techniques for stability, they show that the localised bump solution can become unstable in two distinct ways: via a drift instability and a dynamic instability.

A *drift* instability occurs when an eigenvalue, moving in the complex plane, crosses from the left half-plane to the right half-plane along the real line and corresponds to the formation of a travelling pulse.

A *dynamic* instability occurs when a pair of complex conjugate eigenvalues cross from the left half-plane to the right half-plane with non-zero imaginary part and corresponds to the formation of breathers from the instability of the bump. The oscillatory nature of the breather is due to a pair of *complex conjugate* eigenvalues crossing the imaginary axis away from zero.

A similar construction and stability analysis of the solitary travelling pulse showed an instability to a travelling breather; this is a pattern with oscillatory breather-like qualities superimposed on a travelling pulse. For the details of this, see both [50, 48]. Other exotic phenomena were demonstrated via simulation such as the formation of self-replicating bumps, the destruction of two travelling breathers meeting at a collision, and the instability of bumps with dimples (an inflection in a bump) into wandering patterns on the plane.

#### 4.2 A SEMI-SMOOTH DYNAMIC THRESHOLD NEURAL FIELD MODEL

Here we consider a modification of the model considered by Coombes and Owen. It is atypical — and indeed seems unlikely, given the non-smooth nature of the stationary threshold bump solution in space for  $h$  shown in red in Figure 4.1 — of neural tissue to be accurately modelled by such a non-smooth threshold process. Therefore, we alter the threshold dynamics of (4.1), smoothing out the discontinuity in the accommodation dynamics. This is achieved by convolving a smoothing kernel with the function representing the effect of accommodation in the evolution equation for the threshold dynamics. The symmetric smoothing kernel is taken to be isotropic, and is given by

$$w_h(x) = \frac{1}{\sigma\sqrt{\pi}} \exp\left(-x^2/\sigma^2\right), \quad (4.3)$$

where the parameter  $\sigma > 0$  defines the spatial scale of smoothing. We also consider the inclusion of a localised spatial drive  $I(x)$  to the synaptic activity such that the modified model is

$$u = \eta * w \otimes f(u - h) + I, \quad (4.4a)$$

$$h_t = -(h - h_0) + \kappa w_h \otimes g(u - \theta). \quad (4.4b)$$

where the functions  $f$  and  $g$  are sigmoidal functions of the form

$$s(u; \mu) = \frac{1}{1 + \exp(-\mu u)}, \quad \mu > 0, \quad (4.5)$$

where  $\mu$  is a steepness parameter. The sigmoidal function satisfies the property that, as  $\mu \rightarrow \infty$ ,  $s(u; \mu) \rightarrow H(u)$ . In the limit  $\sigma \rightarrow 0$ ,  $w_h(x) \rightarrow \delta(x)$ , whereby (4.4) reduces to the model considered by Coombes and Owen (4.1).

We work in the Heaviside limit ( $\mu \rightarrow \infty$ ) in Sections 4.4 and 4.5, and use the wizard hat connectivity function (4.2) throughout the chapter. This captures the spirit of the model in [50] while also allowing the steady state threshold solution to be spatially continuous, rather than discontinuous, as is the case in [48]. Critically, this gives us the opportunity to use the Evans function approach for linear stability and put stability results for bumps on a clear, non-ambiguous, and formal footing.

## 4.3 TURING ANALYSIS OF THE HOMOGENEOUS STEADY STATE

### 4.3.1 *Constructing the Homogeneous Steady State*

Our analysis of a neural field model of cortical tissue with a dynamic threshold begins with a study of the spatio-temporally homogeneous steady state of (4.4) in the absence of any localised drive. This final condition is equivalent to  $I(x) = 0$ . As shown in Section 2.4, if the post-synaptic response function,  $\eta$ , takes the form of the exponential decay response function given

by (2.20), then (4.1a) can be expressed equivalently as  $Qu = w \otimes f(u - h) + I$ , with  $Q$  given by (2.24). Then (4.4), with the integrals given explicitly, is

$$\frac{1}{\alpha} \frac{\partial}{\partial t} u(x, t) = -u(x, t) + \int_{-\infty}^{\infty} w(y) f(u(x - y, t) - h(x - y, t)) dy, \quad (4.6a)$$

$$\frac{\partial}{\partial t} h(x, t) = -(h(x, t) - h_0) + \kappa \int_{-\infty}^{\infty} w_h(y) g(u(x - y, t) - \theta) dy. \quad (4.6b)$$

where  $f$  and  $g$  are sigmoidal functions as given by (4.5).

Seeking the spatio-temporally homogeneous steady state solution, that is  $u(x, t) = \bar{u}$  and  $h(x, t) = \bar{h}$  for all  $x$  and all  $t > 0$ , (4.6a) reduces to

$$\bar{u} = f(\bar{u} - \bar{h}) \hat{w}(0), \quad (4.7)$$

where

$$\hat{w}(k) = \int_{-\infty}^{\infty} w(y) e^{-iky} dy, \quad (4.8)$$

is the Fourier transform of  $w(x)$ , and  $\hat{w}(0)$  is the normalisation of  $w(x)$ . Since we work with the balanced kernel<sup>1</sup> (4.2),  $\hat{w}(0) = 0$ , leading to the unique solution  $\bar{u} = 0$ . Similarly, (4.6b) becomes  $\bar{h} = h_0 + \kappa g(\bar{u} - \theta) \hat{w}_h(0)$ . For the Gaussian smoothing kernel (4.3),  $\hat{w}_h(0) = 1$ , and so  $\bar{h} = h_0 + \kappa g(-\theta)$ .

Thus, the unique homogeneous state is given by  $(\bar{u}, \bar{h}) = (0, h_0 + \kappa g(-\theta))$ . Note that as  $\mu \rightarrow \infty$ ,  $g(-\theta) \rightarrow H(-\theta) = 0$  for any  $\theta > 0$ , implying that  $\bar{h} = h_0$  in this limit.

#### 4.3.2 Linear Stability of the Homogeneous State

To assess the linear stability of the homogeneous steady state, first linearise about  $(\bar{u}, \bar{h})$  so that

$$u(x, t) = \bar{u} + \delta u(x, t), \quad (4.9a)$$

$$h(x, t) = \bar{h} + \delta h(x, t), \quad (4.9b)$$

---

<sup>1</sup> A “balanced kernel” has the property that the total amount of excitatory and inhibitory connectivity is equal.

and substitute into (4.6) to obtain<sup>2</sup>

$$\begin{aligned} \frac{1}{\alpha} \frac{\partial}{\partial t} \delta u(x, t) &= -\delta u(x, t) \\ &+ f'(\bar{u} - \bar{h}) \int_{-\infty}^{\infty} w(y) \left( \delta u(x - y, t) - \delta h(x - y, t) \right) dy, \end{aligned} \quad (4.10a)$$

$$\frac{\partial}{\partial t} \delta h(x, t) = -\delta h(x, t) + \kappa g'(\bar{u} - \theta) \int_{-\infty}^{\infty} w_h(y) \delta u(x - y, t) dy, \quad (4.10b)$$

Now let us assume spatio-temporally separable perturbations of the form,  $(\delta u(x, t), \delta h(x, t)) = e^{ikx}(\delta u(t), \delta h(t))$ . Then (4.10) reduces to

$$\frac{d}{dt} \delta u(t) = \alpha \left( -\delta u(t) + f'(\bar{u} - \bar{h}) \hat{w}(k) (\delta u(t) - \delta h(t)) \right), \quad (4.11a)$$

$$\frac{d}{dt} \delta h(t) = -\delta h(t) + \kappa g'(\bar{u} - \theta) \hat{w}_h(k) \delta u(t), \quad (4.11b)$$

which can be written in the matrix form

$$\frac{d}{dt} \begin{pmatrix} \delta u \\ \delta h \end{pmatrix} = \mathcal{J}(k) \begin{pmatrix} \delta u \\ \delta h \end{pmatrix}, \quad (4.12)$$

where

$$\mathcal{J}(k) = \begin{pmatrix} \alpha(-1 + \gamma_1 \hat{w}(k)) & -\alpha \gamma_1 \hat{w}(k) \\ \kappa \gamma_2 \hat{w}_h(k) & -1 \end{pmatrix}, \quad (4.13)$$

and  $\gamma_1 = f'(\bar{u} - \bar{h})$  and  $\gamma_2 = g'(\bar{u} - \theta)$  can be treated as parameters that depend on the steady state.

Let the temporal part of the perturbations be  $(\delta u(t), \delta h(t)) = e^{\lambda t}(U, H)$ , where  $U, H$  are constants. Then the eigenvalues,  $\lambda$ , of the linearisation about  $(\bar{u}, \bar{h})$  determine the stability of the homogeneous steady state; they satisfy

$$\lambda^2 + m(k)\lambda + n(k) = 0. \quad (4.14)$$

If  $\text{Re}(\lambda) > 0$  for any  $k$ , the steady state is unstable. The functions  $m$  and  $n$  are given by  $m(k) = -\text{Tr}(\mathcal{J}(k))$  and  $n(k) = \det(\mathcal{J}(k))$ . In full,

$$m(k) = 1 + \alpha - \alpha \gamma_1 \hat{w}(k), \quad (4.15a)$$

$$n(k) = \alpha(1 - \gamma_1 \hat{w}(k) + \kappa \gamma_1 \gamma_2 \hat{w}(k) \hat{w}_h(k)). \quad (4.15b)$$

---

<sup>2</sup> The Taylor expansion  $f(\bar{v} + \delta v) = f(\bar{v}) + f'(\bar{v})\delta v + \mathcal{O}(\delta v^2)$ ,  $\delta v \ll 1$ , has been used here.

For the connectivity (4.2) and smoothing kernel (4.3), the relevant Fourier transforms are

$$\widehat{w}(k) = \frac{4k^2}{(k^2 + 1)^2}, \quad (4.16)$$

and

$$\widehat{w}_h(k) = \exp\left(-\frac{k^2\sigma^2}{4}\right). \quad (4.17)$$

(4.14) gives the implicit dispersion relation  $\mathcal{E}(\lambda, k) = 0$ , where

$$\begin{aligned} \mathcal{E}(\lambda, k) = & \lambda^2 + \lambda(1 + \alpha - \alpha\gamma_1\widehat{w}(k)) \\ & + \alpha - \alpha\gamma_1\widehat{w}(k) + \alpha\kappa\gamma_1\gamma_2\widehat{w}(k)\widehat{w}_h(k). \end{aligned} \quad (4.18)$$

In order to compute the Turing and Turing-Hopf bifurcations of the spatially homogeneous steady state, in the spirit of [32], let  $\lambda = \mu + i\omega$ , where  $\mu, \omega \in \mathbb{R}$ .<sup>3</sup> There are four possible bifurcations of the steady state, all of which occur when eigenvalue(s) cross the imaginary axis,  $\mu = 0$ , in  $(\mu, \omega)$ -space. For  $k = 0$ , the steady ( $\omega = 0$ ) and Hopf ( $\omega \neq 0$ ) bifurcations may occur, while for  $k \neq 0$ , the steady state may undergo Turing ( $\omega = 0$ ) and Turing-Hopf ( $\omega \neq 0$ ) bifurcations.

One may determine the location of bifurcations (other than the steady bifurcation) in parameter space by augmenting the dispersion relation (4.18) with a condition that ensures  $\mu = 0$ . Defining  $\mathcal{M} = \text{Re}(\mathcal{E})|_{\mu=0}$  and  $\mathcal{N} = \text{Im}(\mathcal{E})|_{\mu=0}$ , the implicit function theorem gives the condition

$$\mathcal{M}_k\mathcal{N}_\omega - \mathcal{M}_\omega\mathcal{N}_k = 0, \quad (4.19)$$

which states that the eigenspectrum  $\lambda(k)$  grazes the imaginary axis [217].

A steady bifurcation results in the formation of a *different* homogeneous steady state than the original. It is found by solving  $\mathcal{E}(0, 0) = 0$ . In the case of this model, there is only one homogeneous steady state, and so steady bifurcations do not occur.

---

<sup>3</sup> It should be understood that  $\mu$  used in this context as  $\text{Re}(\lambda)$  is different to the use of  $\mu$  as the sigmoidal steepness parameter in (4.5).

A Hopf bifurcation results in globally synchronous oscillations, where activity across the entirety of space obeys the same dynamics but oscillates periodically in time. It is found by solving  $\mathcal{E}(i\omega, 0) = 0$  for  $\omega$  with  $k = 0$  (bulk oscillations) and a bifurcation parameter. Note that this complex equation yields two equations  $\text{Re}(\mathcal{E}(i\omega, 0)) = 0$ , and  $\text{Im}(\mathcal{E}(i\omega, 0)) = 0$ , for the two unknowns,  $\omega$  and a bifurcation parameter. We can show that for this dynamic threshold model (4.6), the homogeneous steady state never undergoes a Hopf bifurcation to result in bulk oscillations. By solving  $\mathcal{E}(i\omega, 0) = 0$  for  $\omega$ , we obtain the complex quadratic equation in  $\omega$ :  $-\omega^2 + i\omega(1 + \alpha) + \alpha = 0$ . This has complex solutions,  $\omega \in \{i, i\alpha\} \in \mathbb{C}$ . However, when decomposing  $\lambda = \mu + i\omega$ , we made the assumption  $\omega \in \mathbb{R}$ , and so this short calculation shows that an  $\omega \in \mathbb{R}$ , which *would* yield a Hopf bifurcation, does not exist. Therefore, the homogeneous steady state never undergoes a Hopf bifurcation.

A static Turing bifurcation results in the formation of a stationary pattern with a wavenumber given by the non-zero  $k$ . It is found by solving the two conditions  $\mathcal{E}(0, k) = 0$  and (4.19) for  $k = k_c \neq 0$  and a bifurcation parameter.

A dynamic Turing-Hopf bifurcation results in the formation of a pattern with non-trivial spatial *and temporal* structure – a typical example is a periodic wavetrain solution [33]. It is found by solving  $\mathcal{E}(i\omega, k) = 0$  and (4.19) for  $k = k_c \neq 0$ ,  $\omega \neq 0$ , and a bifurcation parameter [34]. Again,  $\mathcal{E}(i\omega, k) = 0$  is a complex equation and thus one must solve the two equations that arise from setting the real and imaginary parts to zero. In total, there are three equations for three unknowns.

In the following section, we determine conditions for static Turing and dynamic Turing-Hopf curves.

### 4.3.3 Static Turing and Turing-Hopf Bifurcation Curves

Let us now compute (4.19) for the  $\mathcal{M}$  and  $\mathcal{N}$  relevant to this problem. Using (4.18),

$$\mathcal{M}(\omega, k) = -\omega^2 + \alpha(1 - \gamma_1 \widehat{w}(k) + \kappa \gamma_1 \gamma_2 \widehat{w}(k) \widehat{w}_h(k)), \quad (4.20a)$$

$$\mathcal{N}(\omega, k) = \omega(1 + \alpha(1 - \gamma_1 \widehat{w}(k))). \quad (4.20b)$$

Differentiating (4.20) with respect to  $\omega$  and  $k$  separately and substituting appropriately into (4.19), we obtain

$$\begin{aligned} \alpha \gamma_1 \left( -\widehat{w}'(k) + \kappa \gamma_2 \frac{d}{dk} (\widehat{w}(k) \widehat{w}_h(k)) \right) (1 + \alpha - \alpha \gamma_1 \widehat{w}(k)) \\ - 2\omega^2 \alpha \gamma_1 \widehat{w}'(k) = 0. \end{aligned} \quad (4.21)$$

Since  $f$  and  $g$  are sigmoidal – and importantly, non-Heaviside – we have that  $\gamma_1, \gamma_2 \neq 0$ . Therefore, to ensure (4.21) holds, we require both  $\widehat{w}'(k) = 0$  and  $\frac{d}{dk} (\widehat{w}(k) \widehat{w}_h(k)) = 0$ . The first condition is true for the wizard hat connectivity (4.2) for non-zero  $k_c = \pm 1$ . The second condition reduces to

$$\frac{\widehat{w}'(k)}{\widehat{w}(k)} = -\frac{\widehat{w}'_h(k)}{\widehat{w}_h(k)} \quad (4.22)$$

and when the first condition is applied, it reduces further to

$$\widehat{w}'_h(k) = 0. \quad (4.23)$$

For the choice of  $w_h(x)$  we use, the only  $k$  satisfying this is  $k = 0$ , and so there is no solution to (4.19) for  $k$  in this case. Consequently, the homogeneous steady state does not undergo Turing or Turing-Hopf instabilities for  $\sigma > 0$ .

However, in the limit that  $\sigma \rightarrow 0$ ,  $w_h(x) \rightarrow \delta(x)$ ,  $\widehat{w}_h(k) \rightarrow 1$  for all  $k$ . In this case,

$$\frac{d}{dk} (\widehat{w}(k) \widehat{w}_h(k)) = \widehat{w}'(k), \quad (4.24)$$

and (4.19) becomes

$$\alpha \gamma_1 \widehat{w}'(k) (-1 + \kappa \gamma_2) (1 + \alpha - \alpha \gamma_1 \widehat{w}(k)) - 2\omega^2 \alpha \gamma_1 \widehat{w}'(k) = 0. \quad (4.25)$$

which yields

$$\widehat{w}'(k) = 0. \quad (4.26)$$

We work in the limit that  $\sigma \rightarrow 0$  for the remainder of this section, in which case the model under consideration is (4.1). For the connectivity (4.2), the Fourier transform is given by (4.16), which has maxima at  $k_c = \pm 1$ . There is also a minimum at  $k = 0$ , however static Turing and dynamic Turing-Hopf bifurcations both require  $k \neq 0$ , hence we only consider the maxima, for which the critical wavenumber satisfies  $|k_c| = 1$ .

We are now in a position to find conditions at which Turing and Turing-Hopf bifurcations from the homogeneous steady state occur. In doing so, we follow a similar methodology as prescribed in [32, 33].

The eigenvalue equation (4.14) has solutions  $\lambda(k) = \lambda_{\pm}(k)$ , where

$$\lambda_{\pm}(k) = \frac{-m(k) \pm \sqrt{m(k)^2 - 4n(k)}}{2}. \quad (4.27)$$

A Turing bifurcation occurs when a purely *real* eigenvalue is crossing the imaginary axis. The scenario is shown by the black dot in Figure 4.2A, which shows that  $\lambda_+(k_c) = 0$ . This occurs when  $n(k_c) = 0$ , since then  $\lambda(k_c) = \{0, -m(k_c)\}$ . This condition on  $n(k_c)$  reduces to

$$\gamma_1 \widehat{w}(k_c) = 1/(1 - \kappa\gamma_2), \quad (4.28)$$

noting that  $\widehat{w}(k_c) = 1$  at  $k_c = \pm 1$ . The non-zero eigenvalue must be negative, since otherwise a bifurcation would already have occurred. Therefore  $\lambda_-(k_c) < 0$ , meaning that  $m(k_c) > 0$ , which reduces to  $1 + \alpha - \alpha/(1 - \kappa\gamma_2) > 0$ . This is a necessary condition that must be satisfied by the parameters in order to ensure a Turing bifurcation occurs.

For a dynamic Turing-Hopf bifurcation, a pair of complex conjugate eigenvalues grazes the imaginary axis. This is shown by the black dots in Figure 4.2B which have  $\lambda(k_c) = \pm i\omega$ ,  $\omega \neq 0$ . This occurs when  $m(k_c) = 0$ , since then  $\lambda(k_c) = \pm \sqrt{-4n(k_c)}/2$ , with the additional condition that  $n(k_c) > 0$ . From the first condition, we obtain the relation

$$\gamma_1 \widehat{w}(k_c) = 1 + 1/\alpha, \quad (4.29)$$

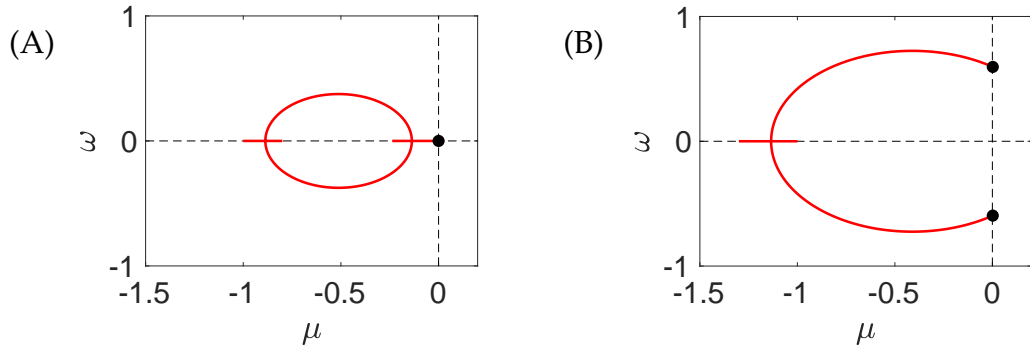


Figure 4.2.: The continuous (in  $k$ ) spectrum  $\lambda(k) = \mu(k) + i\omega(k)$  at a static Turing (A) and a Turing-Hopf bifurcation (B). In (A), the branch of eigenvalues can be seen to just touch the imaginary axis at  $\omega = 0$ . Likewise, in (B) a complex conjugate pair just touches the imaginary axis at  $\omega = \pm 0.5956$ . In both cases, the grazing occurs at  $|k| = k_c = 1$ , as shown by the black dot(s). Parameter values common to both panels are  $h_0 = 0.04$ ,  $\kappa = 0.3$ ,  $\sigma = 0.02$ , and sigmoidal steepness  $\mu = 10$ . In (A):  $\theta = 0.1358$ ,  $\alpha = 0.8$ , and in (B):  $\theta = 0.1$ ,  $\alpha = 1.3$ .

which determines the Turing-Hopf bifurcation curve in  $(\gamma_1, \alpha)$ -space. The additional condition reduces to  $1 + \alpha - \alpha/(1 - \kappa\gamma_2) < 0$ .

The continuous spectrum  $\lambda(k)$  is shown in  $(\mu, \omega)$ -space at a static Turing (A) and a Turing-Hopf (B) bifurcation in Figure 4.2. The spectrum is continuous since it depends on the wavenumber  $k$ ; this figure shows the eigenvalues (4.27) plotted parametrically in  $k$ . An unstable homogeneous steady state (not shown) has its spectrum pushed into the right half-plane, signifying that  $\text{Re}(\lambda) > 0$  for  $k \in (k_1, k_2)$ ,  $k_1 < k_2$ . For a static Turing bifurcation, the spectrum passes through zero, while for a Turing-Hopf bifurcation, the spectrum moves into the right half-plane via a complex conjugate pair of eigenvalues with non-zero imaginary parts.

Figure 4.3 shows the loci of Turing (maroon curve) and Turing-Hopf (light-blue curve) bifurcations in  $(\gamma_1, \alpha)$ -space. These are obtained by plotting (4.28) and (4.29) for appropriate values of  $\alpha$  in each case as discussed above.

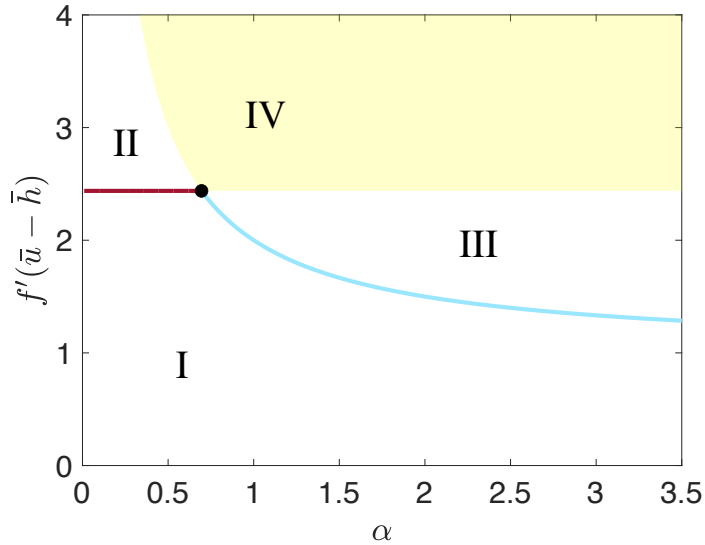


Figure 4.3.: Turing (maroon) and Turing-Hopf (light-blue) curves defined by (4.28) and (4.29) separating parameter space into dynamically distinct regions (I)-(III), along with the pseudo-region (IV) (shaded yellow). Dynamics for  $u(x, t)$  and  $h(x, t)$  in each region are shown in Figures 4.4 and 4.5, respectively. The black dot indicates the locations of a Bogdanov-Takens bifurcation where there is a double zero eigenvalue. Parameters are  $h_0 = 0.04$ ,  $\theta = 0.1$ ,  $\kappa = 0.3$ , with sigmoidal steepness parameter  $\mu = 10$ .

The curves partition parameter space into distinct regions in which different dynamical behaviours emerge upon an instability from the homogeneous steady state. In region I, Figure 4.4a shows that the homogeneous steady state is stable to perturbations, which decay as  $t \rightarrow \infty$ . Moving beyond the static Turing bifurcation, into region II, yields a non-travelling, static Turing pattern as shown in Figure 4.4b. This is a consequence of a real eigenvalue crossing the imaginary axis with corresponding eigenfunction  $e^{ikx}$ . In region III, past the dynamic Turing-Hopf instability, travelling wave-train solutions are produced as shown in Figure 4.4c. When the steady state is both Turing and Turing-Hopf unstable, the two unstable modes compete, yielding more complex spatio-temporal patterning, an example of which is shown in Figure 4.4d, taken from the pseudo-region IV (named as such be-

cause the competing modes may give rise to a number of different complex mixed-mode states). This patterning may be described as some non-trivial *fusion* of a Turing-Hopf travelling wavetrain, and a static Turing pattern. Figure 4.5 shows the solutions for  $h(x, t)$  that correspond to those shown for  $u(x, t)$  in Figure 4.4. It is clear that the dynamical behaviour in  $u$  and  $h$  is very similar, and, qualitatively, is essentially identical. That is, where synaptic activity  $u(x, t)$  is high, then in general, threshold activity  $h(x, t)$  is high. This is as expected, since there is a contribution to the equation for  $u$  in (4.6a) when  $u > h$ . This serves to increase  $u$ , and there is a contribution to the equation for  $h$  in (4.6b) – via the accommodation process – when  $u$  is sufficiently large ( $u > \theta$ ).

When  $1 + \alpha - \alpha/(1 - \kappa\gamma_2) = 0$ , both  $m(k)$  and  $n(k)$  vanish, and the Turing and Turing Hopf curves meet in a Bogdanov-Takens bifurcation in which there is a double zero eigenvalue. This is shown in Figure 4.3 by the black dot and is continued in two-parameter  $(\alpha, \kappa)$ -space in Figure 4.6. It is noteworthy that  $\kappa$  does not grow unbounded as  $\alpha \searrow 0$ , but approaches some finite value  $\kappa \approx 0.5$ .

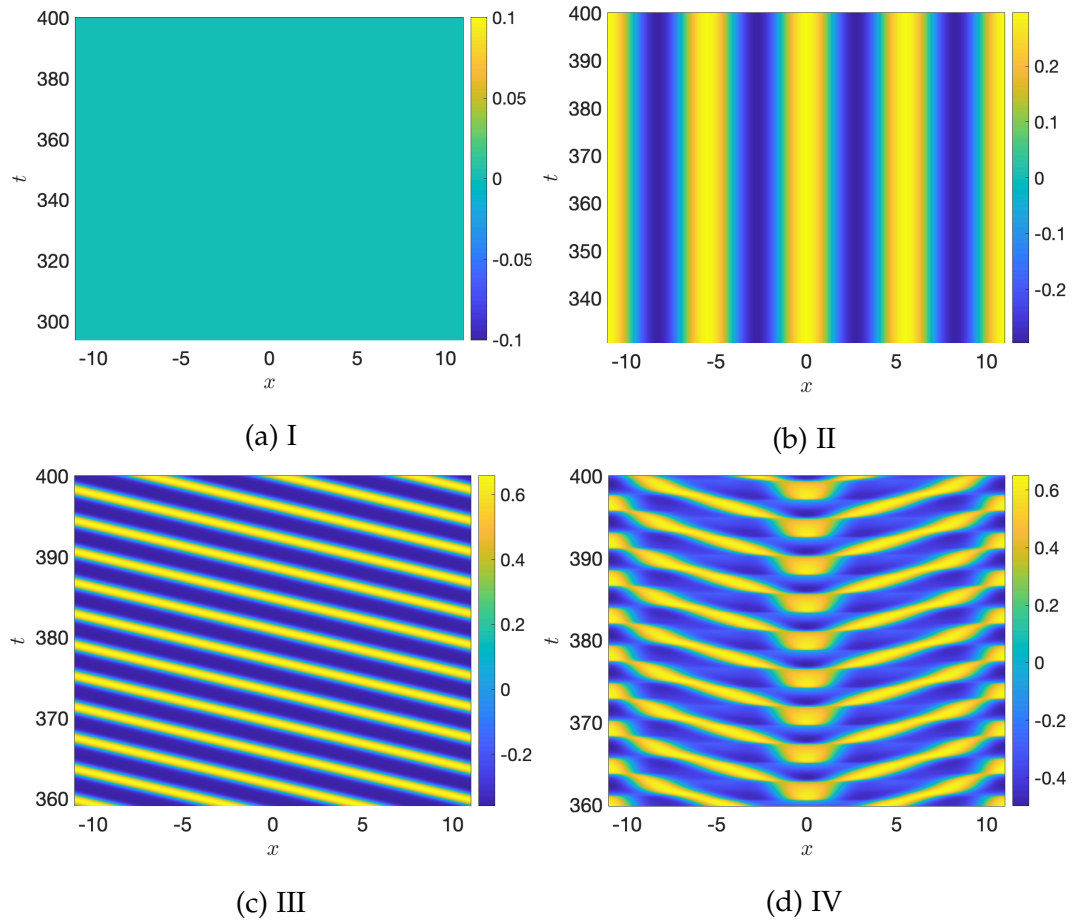


Figure 4.4.: Emergent patterns for  $u(x, t)$  in the four regions I-IV shown in Figure 4.3. In I, the homogeneous steady state is stable, while in regions II-IV, it undergoes an instability into the (II) Turing, (III) Turing-Hopf, and (IV) mixed Turing-Turing-Hopf patterns shown here.

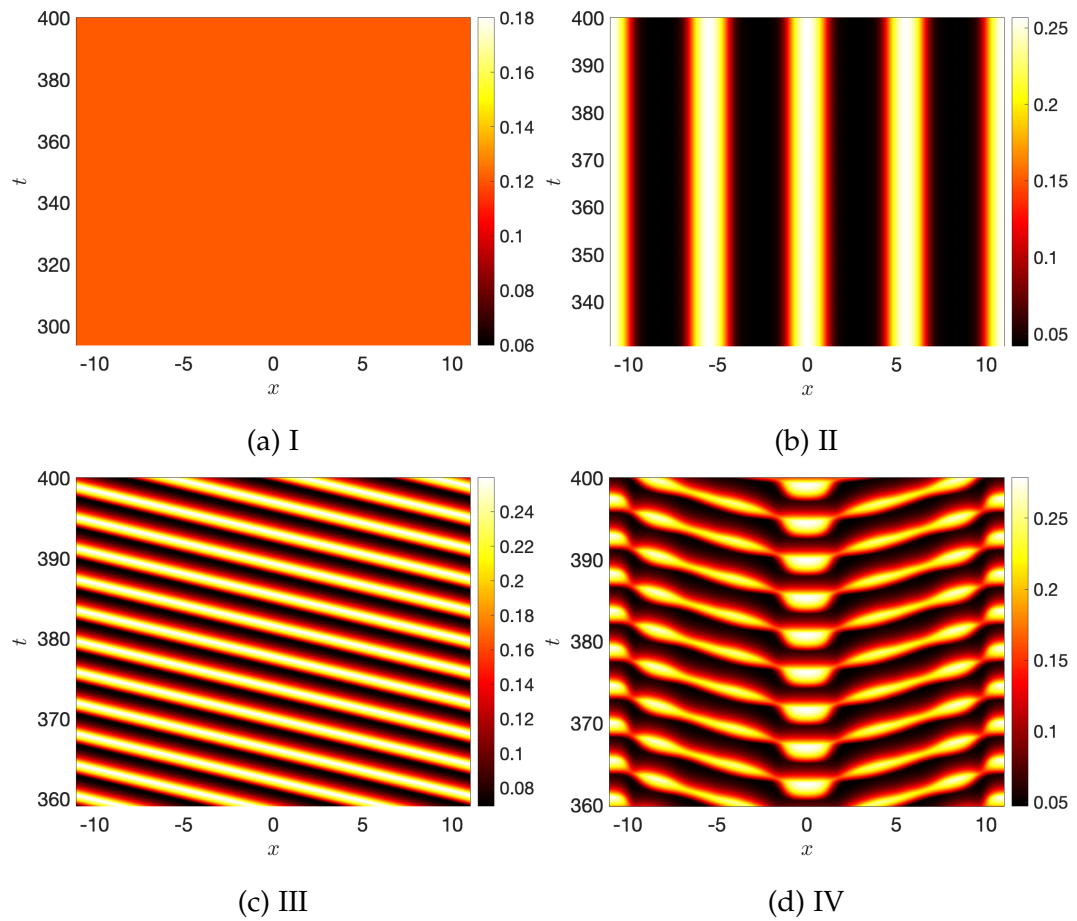


Figure 4.5.: Emergent patterns for  $h(x, t)$  in the four regions I-IV shown in Figure 4.3, with each panel corresponding accordingly with the relevant panel in Figure 4.4. In I, the homogeneous steady state is stable, while in regions II-IV, it undergoes an instability into the (II) Turing, (III) Turing-Hopf, and (IV) mixed Turing-Turing-Hopf patterns shown here.

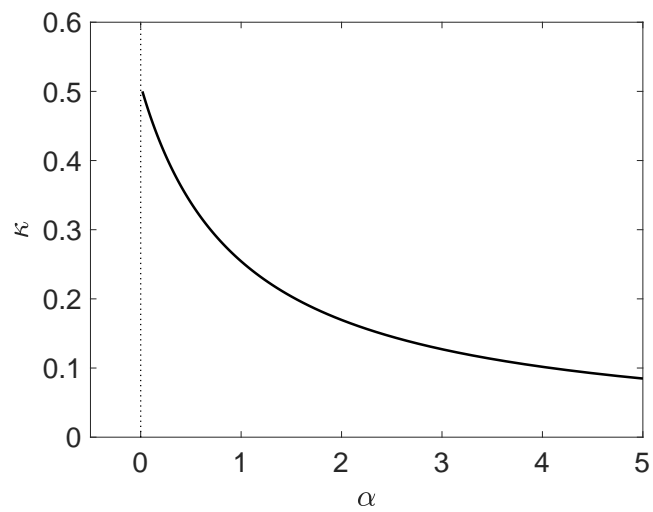


Figure 4.6.: A two parameter bifurcation diagram tracking the co-dimension two Bogdanov-Takens bifurcation point in  $(\alpha, \kappa)$ -space. Other than  $\kappa$ , which is being treated as a second bifurcation parameter here, parameters are as in Figure 4.3.

#### 4.4 CONSTRUCTION OF A LOCALISED BUMP SOLUTION

The previous section showed the construction and stability of the spatially homogeneous steady state as well as various patterned states that emerge as a result of instabilities. Here, we focus on a different class of solution, namely a stationary bump; we construct it and analyse its linear stability for the model with smoothed threshold dynamics (4.4). We do so for the Gaussian smoothing kernel as given by (4.3). The functions  $f$  and  $g$  are now taken to be Heaviside functions.

Seeking time-independent, spatial solutions  $(u, h)(x, t) = (q, p)(x)$  to (4.4), we obtain

$$q(x) = \int_{-\infty}^{\infty} w(x-y)H(q(y) - p(y))dy + I(x), \quad (4.30a)$$

$$p(x) = h_0 + \kappa \int_{-\infty}^{\infty} w_h(x-y)H(q(y) - \theta)dy. \quad (4.30b)$$

A localised bump solution – of the class illustrated in Figure 4.7 – is parameterised by the unknowns  $x_i, i = 1, \dots, 8$ , which indicate the locations of threshold crossing events.<sup>4</sup> The Heaviside functions in each integral allow for the integration domain to be restricted to those subsets of  $\mathbb{R}$  such that the Heaviside function takes the value 1. It can be seen that  $q(x) > \theta$  for  $x \in (x_3, x_6)$ , while  $q(x) > p(x)$  for  $x \in (x_1, x_2) \cup (x_4, x_5) \cup (x_7, x_8)$ . Thus, (4.30) reduces to

$$q(x) = \left( \int_{x_1}^{x_2} + \int_{x_4}^{x_5} + \int_{x_7}^{x_8} \right) w(x-y)dy + I(x), \quad (4.31a)$$

$$p(x) = h_0 + \kappa \int_{x_3}^{x_6} w_h(x-y)dy. \quad (4.31b)$$

---

<sup>4</sup>Other classes of bump solutions no doubt exist which are characterised by different numbers of threshold crossings, but this is the class we focus on since it is most similar to that in [50].

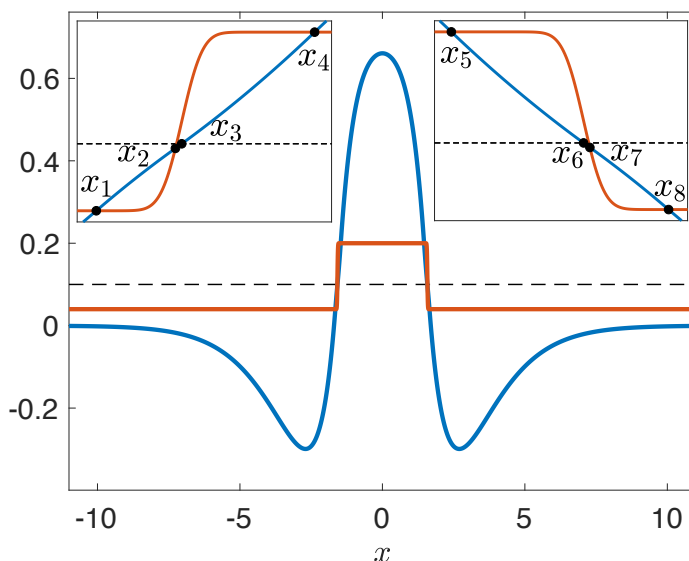


Figure 4.7.: Localised bump solution as solid blue ( $q(x)$ ) and orange ( $h(x)$ ) lines respectively, with  $I(x) = 0$ . Parameter values are  $h_0 = 0.04$ ,  $\theta = 0.1$ ,  $\kappa = 0.16$ ,  $\sigma = 0.02$ . Threshold crossings occur at  $x_1 = -1.65$ ,  $x_2 = -1.583$ ,  $x_3 = -1.5775$ ,  $x_4 = -1.46$ , with  $(x_5, x_6, x_7, x_8) = -(x_4, x_3, x_2, x_1)$  due to the symmetry of the solution. The two insets show an enlargement of the solution near to the threshold crossings  $x_i$ ,  $i = 1, \dots, 8$ . Note the distinct crossing points,  $x_2$  and  $x_3$ , and  $x_6$  and  $x_7$ . See the text for the constraints defining these crossing points. The accommodation threshold  $\theta$  is shown in black (dashed in insets). Compare the smoothed nature of solutions near the crossing events with Figure 4.1.

The eight threshold crossing conditions that determine the eight unknowns  $x_i$ ,  $i = 1, \dots, 8$  are given by

$$\begin{aligned} q(x) &= p(x), & x &= x_i, & i &= 1, 2, 4, 5, 7, 8, \\ q(x) &= \theta, & x &= x_i, & i &= 3, 6. \end{aligned} \tag{4.32}$$

One may calculate the integrals in the expression for  $q(x)$  (4.31a) for a wiz-

ard hat connectivity (4.2) by using the expression for the indefinite integral

$$\begin{aligned} F_1(y; x) &= \int w(x-y) dy \\ &= (y-x)e^{-(y-x)}H(y-x) + (y-x)e^{y-x}H(x-y), \end{aligned} \quad (4.33)$$

Thus, a closed form expression is obtained for  $q(x)$ , defined in terms of the function  $F_1$ , as

$$\begin{aligned} q(x) &= F_1(x_2; x) - F_1(x_1; x) + F_1(x_5; x) - F_1(x_4; x) \\ &\quad + F_1(x_8; x) - F_1(x_7; x) + I(x). \end{aligned} \quad (4.34)$$

To evaluate  $p(x)$  (4.31b), the indefinite integral may be calculated as

$$F_2(y; x) = \int w_h(x-y) dy = -\frac{1}{2} \operatorname{erf}\left(\frac{x-y}{\sigma}\right), \quad (4.35)$$

where  $\operatorname{erf}(x)$  is the Error function defined by

$$\operatorname{erf}(x) = \frac{2}{\sqrt{\pi}} \int_0^x e^{-\xi^2} d\xi, \quad (4.36)$$

and so,

$$\int_{x_3}^{x_6} w_h(x-y) dy = F_2(x_6; x) - F_2(x_3; x), \quad (4.37)$$

giving an explicit expression for  $p(x)$  as

$$p(x) = h_0 + \kappa(F_2(x_6; x) - F_2(x_3; x)), \quad (4.38)$$

in terms of evaluations of the error function, which can simply be computed numerically.

Thus, we have semi-analytical<sup>5</sup> closed form expressions for  $q(x)$  and  $p(x)$ . Along with the conditions (4.32) to determine the eight unknowns  $x_i$ ,  $i = 1, \dots, 8$ , this completes the construction of the spatially localised bump solution. For no spatial drive, or symmetric spatial drive, the solution is symmetric about the origin. This is a consequence of the symmetric connectivity. In this case, the localised bump solution is shown in Figure 4.7, where the close proximity of  $x_2$  and  $x_3$ , and  $x_6$  and  $x_7$ , should be noted.

<sup>5</sup>Semi-analytical in the sense that we must use  $\operatorname{erf}(x)$  in the evaluation of  $p(x)$ .

As  $\sigma$  is increased,  $p(x)$  becomes shallower in the region about the threshold crossings, ultimately resulting in a different class of bump solution with fewer threshold crossings.

#### 4.5 STABILITY OF THE LOCALISED BUMP SOLUTION

To consider the linear stability of the stationary bump, we develop an Evans function approach. This technique has been used in the linear stability analysis of waves on unbounded domains [73, 49]. By considering the bump solution to be a travelling pulse with zero speed, the approach is fruitful in this case. The objective is to find a linear homogeneous system in the perturbations at each event, as outlined in Section 2.9. Here, this will yield an  $8 \times 8$  linear system, since there are eight distinct crossing events in the solution. From this linear system, we shall demand that the perturbations at each event be non-trivial. This constraint will define the Evans function.

To begin, we perturb the time-independent bump solution as

$$u(x, t) = q(x) + \delta u(x, t), \quad h(x, t) = p(x) + \delta h(x, t), \quad (4.39)$$

Then substituting (4.39) into (4.4a), we obtain

$$\begin{aligned} \delta u(x, t) = & \int_0^t ds \eta(s) \int_{-\infty}^{\infty} dy w(x - y) \\ & \times \delta(q(y) - p(y)) [\delta u(y, t - s) - \delta h(y, t - s)]. \end{aligned} \quad (4.40)$$

Now, we make the ansatz that perturbations are spatio-temporally separable, and there is an exponential time-dependence,

$$(\delta u(x, t), \delta h(x, t)) = e^{\lambda t} (\delta u(x), \delta h(x)). \quad (4.41)$$

Then (4.41) is substituted into (4.40) to obtain

$$\frac{\delta u(x)}{\tilde{\eta}(\lambda)} = \int_{-\infty}^{\infty} dy w(x - y) \delta(q(y) - p(y)) [\delta u(y) - \delta h(y)], \quad (4.42)$$

where  $\tilde{\eta}(\lambda) = \int_0^t ds \eta(s) e^{-\lambda s}$  is the Laplace transform of  $\eta(t)$ . To collapse the integral over  $y$  using the delta function, we require knowledge of when

$q(x) = p(x)$ . By (4.32), this occurs for  $x = x_i$ ,  $i = 1, 2, 4, 5, 7, 8$ . Therefore, using a formal property of delta functions (“composition with a function”),

$$\delta(q(x) - p(x)) = \sum_{i=1, i \neq 3, 6}^8 \frac{\delta(x - x_i)}{|q'(x_i) - p'(x_i)|}, \quad (4.43)$$

we obtain

$$\frac{\delta u(x)}{\tilde{\eta}(\lambda)} = \int_{-\infty}^{\infty} dy w(x - y) \sum_{i=1, i \neq 3, 6}^8 \frac{\delta(y - x_i)}{|q'(x_i) - p'(x_i)|} [\delta u(y) - \delta h(y)], \quad (4.44)$$

which, upon collapsing the integral over  $y$  using the delta functions, reduces to

$$\delta u(x) = \sum_{i=1, i \neq 3, 6}^8 g(x, x_i; \lambda) (\delta u(x_i) - \delta h(x_i)), \quad (4.45)$$

where

$$g(x, a; \lambda) = \tilde{\eta}(\lambda) \frac{w(x - a)}{|q'(a) - p'(a)|}. \quad (4.46)$$

It is noted that, in this section,  $g$  refers to the function as defined in (4.46) rather than as the sigmoidal function in (4.4) (which is taken as a Heaviside throughout this section). This expression for  $\delta u(x)$  depends on  $\delta h(x)$  evaluated at crossing points. The goal is to obtain a linear system in either of  $\delta u(x)$  or  $\delta h(x)$ , evaluated at each crossing point. We make the choice here to generate the linear system in  $\delta u(x)$ . With this in mind, we linearise about (4.31b) to obtain

$$\frac{\partial}{\partial t} \delta h(x, t) = -\delta h(x, t) + \kappa \int_{-\infty}^{\infty} dy w_h(x - y) \delta(q(y) - \theta) \delta u(y, t). \quad (4.47)$$

Using that  $\eta_h(t) = e^{-t} H(t)$  is the Green’s function of the linear operator  $\mathcal{L}(t) = 1 + d/dt$ , or alternatively, by making the ansatz (4.41), we have that

$$\delta h(x) = \kappa \tilde{\eta}_h(\lambda) \int_{-\infty}^{\infty} dy w_h(x - y) \delta(q(y) - \theta) \delta u(y), \quad (4.48)$$

where  $\tilde{\eta}_h(\lambda) = \frac{1}{1 + \lambda}$  is the Laplace transform of  $\eta_h(t)$ . Since  $q(x) = \theta$  at  $x = x_3, x_6$ , we again use a formal property of delta functions (“composition with a function”) to obtain

$$\delta h(x) = \kappa \tilde{\eta}_h(\lambda) \int_{-\infty}^{\infty} dy w_h(x - y) \sum_{i=3, 6} \frac{\delta(y - x_i)}{q'(x_i)} \delta u(y). \quad (4.49)$$

Collapsing the integral above using the delta functions, we obtain  $\delta h(x)$  in terms of  $\delta u(x)$  at crossing points as

$$\delta h(x) = f_1(x; \lambda) \delta u(x_3) + f_2(x; \lambda) \delta u(x_6), \quad (4.50)$$

where

$$f_1(x; \lambda) = \kappa \tilde{\eta}_h(\lambda) \frac{w_h(x - x_3)}{|q'(x_3)|}, \quad f_2(x; \lambda) = \kappa \tilde{\eta}_h(\lambda) \frac{w_h(x - x_6)}{|q'(x_6)|}. \quad (4.51)$$

We can now write  $\delta u(x)$  in terms of  $\delta u(x)$  at each crossing event, from which we will be able to obtain a linear system in  $\delta u(x_i)$ ,  $i = 1, \dots, 8$ . First, we have that

$$\delta u(x) = \sum_{i=1}^8 G_i(x) \delta u(x_i), \quad (4.52)$$

where

$$G_i(x) = g(x, x_i), \quad i = 1, 2, 4, 5, 7, 8, \quad (4.53)$$

and

$$G_3(x) = - \left( \sum_{i=1, i \neq 3, 6}^8 g(x, x_i) f_1(x_i) \right), \quad (4.54)$$

and

$$G_6(x) = - \left( \sum_{i=1, i \neq 3, 6}^8 g(x, x_i) f_2(x_i) \right), \quad (4.55)$$

where there is an implicit, but important, dependence on  $\lambda$  in the functions  $g$ ,  $f_1$ ,  $f_2$ , and consequently in  $G_i$ ,  $i = 1 \dots 8$  too, which has been suppressed for notational brevity. By substituting  $x = x_i$ ,  $i = 1, \dots, 8$ , into (4.52), we generate the  $8 \times 8$  linear system

$$\mathbf{x} = \Gamma(\lambda) \mathbf{x}, \quad (4.56)$$

where  $\mathbf{x} = (\delta u(x_1), \delta u(x_2), \delta u(x_3), \delta u(x_4), \delta u(x_5), \delta u(x_6), \delta u(x_7), \delta u(x_8))^T$  is the vector of perturbations at each crossing event and  $\Gamma \in \mathbb{C}^{8 \times 8}$  has elements  $\Gamma_{ij}(\lambda) = G_j(x_i)$ ,  $i, j = 1, \dots, 8$ ,

$$\Gamma(\lambda) = \begin{pmatrix} G_1(x_1) & \dots & G_8(x_1) \\ \vdots & \ddots & \vdots \\ G_1(x_8) & \dots & G_8(x_8) \end{pmatrix}. \quad (4.57)$$

Demanding that perturbations be non-trivial is equivalent to the constraint

$$\det(\Gamma(\lambda) - I_8) = 0, \quad (4.58)$$

where  $I_n$  is the  $n \times n$  identity matrix. Then the relevant Evans function is

$$\mathcal{E}(\lambda) = \det(\Gamma(\lambda) - I_8). \quad (4.59)$$

The eigenvalues of the stability problem are the zeroes of the Evans function. They are found at the intersection of the real and imaginary zero contours of the complex valued Evans function. In practice, they are found by decomposing  $\lambda = a + ib$ ,  $a, b \in \mathbb{R}$ , plotting the zero contours of  $\mathcal{E}(\lambda)$  in  $(a, b)$ -space, and finding their intersections. This can be done either with an algorithm which finds the intersections between two curves, or by noting the points of intersection “by-eye”. For stability, we are interested in eigenvalues close to  $\text{Re}(\lambda) = 0$ .

Figure 4.8 shows a drift instability as  $\alpha$  is varied through  $\alpha = 1.22$ , for  $\kappa = 0.16$ . A single eigenvalue crosses the imaginary axis on the real line. The trivial eigenvalue that exists at  $\lambda = 0$  is a consequence of spatial translation-invariance in the system (this is formalised in Section 4.7). Direct numerical simulation in Figure 4.9 shows that the drift instability destabilises the stationary bump (A) into a travelling pulse (B) as the speed of synaptic transmission increases through  $\alpha = 1.22$ .

Figure 4.10 shows a dynamic instability as  $\alpha$  is varied, for  $\kappa = 0.3$ . A complex conjugate pair of eigenvalues cross the imaginary axis, with simulations showing that the localised bump solution destabilises into a breather, a pattern with oscillatory dynamics, as shown in Figure 4.11. The oscillatory nature of the breather is a consequence of eigenvalues having crossed the imaginary axis with *non-zero* imaginary part, rather than a purely real eigenvalue. These results are entirely consistent with those found in [48].

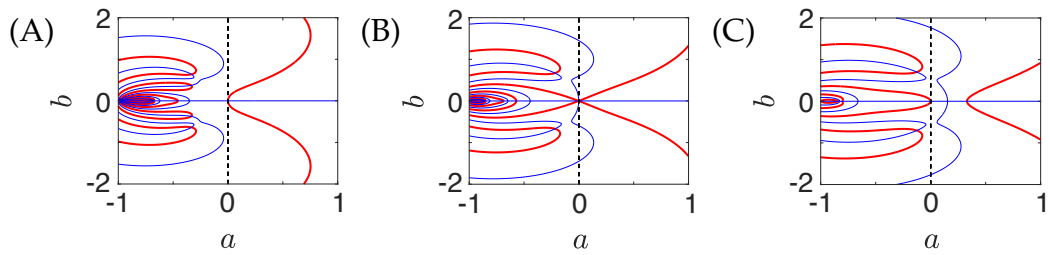


Figure 4.8.: Evans function plots (with  $\kappa = 1.6$ ) of the drift instability as the parameter  $\alpha$  is varied, where  $\lambda = a + ib$ . The red and blue curves signify the zero-contours of  $\text{Re } \mathcal{E}(\lambda)$  and  $\text{Im } \mathcal{E}(\lambda)$  respectively. Intersections of the zero-contours are the zeroes of  $\mathcal{E}(\lambda)$ , and hence are the eigenvalues  $\lambda$  of the stability problem. Note the trivial eigenvalue in all three panels. As  $\alpha$  is varied, a single real eigenvalue crosses the imaginary axis at  $\alpha = \alpha_c \approx 1.22$ . Values of  $\alpha$  are  $\alpha = 1$  (left),  $\alpha = 1.22$  (middle), and  $\alpha = 1.4$  (right). The black dashed line separates the two complex half planes with negative and positive real part, respectively. Parameter values other than  $\alpha$  are  $h_0 = 0.04$ ,  $\theta = 0.1$ ,  $\kappa = 0.16$ ,  $\sigma = 0.02$ .

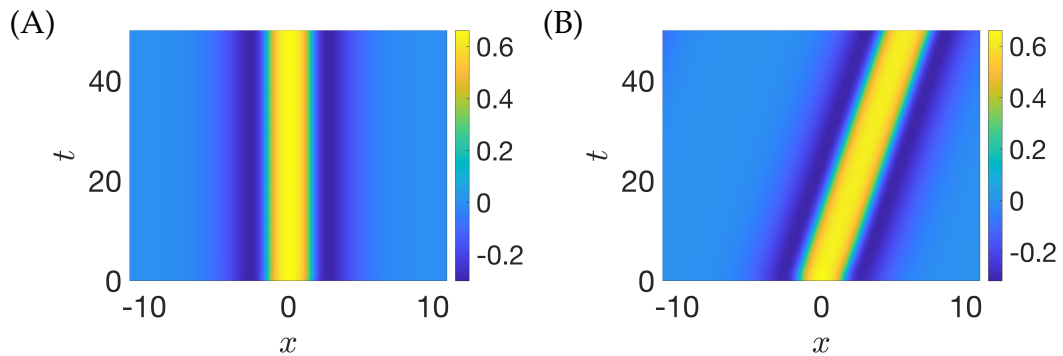


Figure 4.9.: Spatiotemporal plots of  $u(x, t)$  for parameters corresponding to panels 1 and 3 of Figure 4.8 respectively. Panel (A) shows a stable bump solution persisting through time, whereas in panel (B) the bump solution destabilises into a travelling pulse via a drift instability. Parameters are as in Figure 4.8, with  $\alpha = 1$  on the left and  $\alpha = 1.4$  on the right.

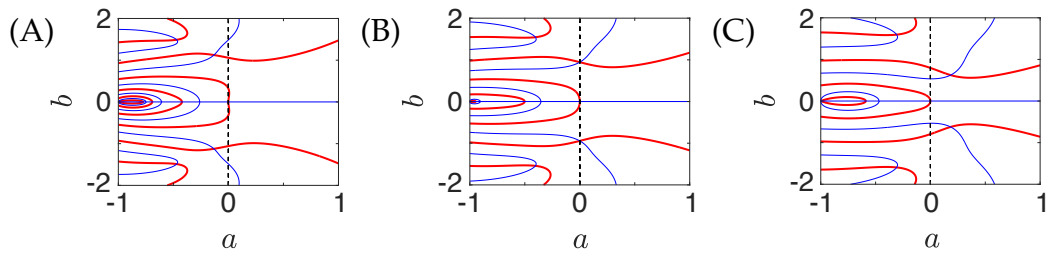


Figure 4.10.: Evans function plots for the localised bump solution at  $\kappa = 0.3$  and all other parameters as in Figure 4.7, as  $\alpha$  is varied, where  $\lambda = a + ib$ . Thick red (thin blue) lines are the real (imaginary) zero contours of  $\mathcal{E}(\lambda)$ . Eigenvalues are given by the intersections of the real and imaginary zero contours. Note the trivial eigenvalue in all three panels. As  $\alpha$  is varied, a complex conjugate pair of eigenvalues crosses the imaginary axis at  $\alpha = \alpha_c \approx 2.13$ . Values of  $\alpha$  are  $\alpha = 1.8$  (left),  $\alpha = 2.13$  (middle), and  $\alpha = 2.5$  (right). Parameters other than  $\alpha$  are  $h_0 = 0.04$ ,  $\theta = 0.1$ ,  $\kappa = 0.3$ , and  $\sigma = 0.02$ .

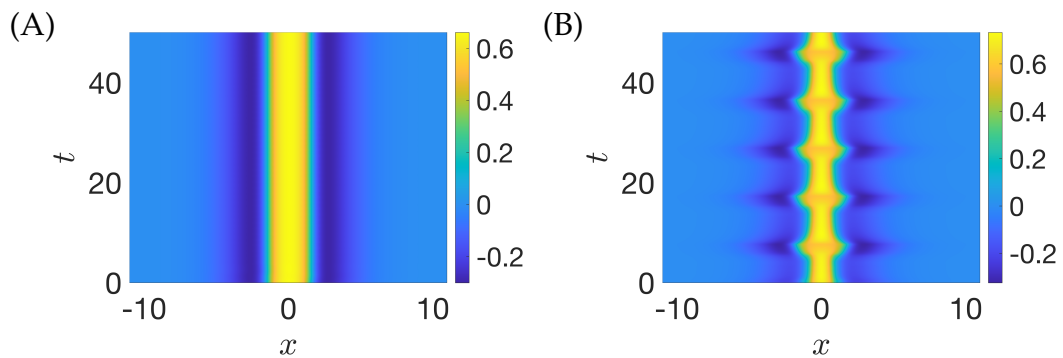


Figure 4.11.: Spatiotemporal plots of  $u(x, t)$  for parameters corresponding to panels 1 and 3 of Figure 4.10 respectively. Panel (A) shows a stable bump solution persisting through time, whereas in panel (B) the bump solution destabilises into a pattern with oscillatory dynamics in time, named a *breather*. Parameters are as in Figure 4.10, with  $\alpha = 1.8$  on the left and  $\alpha = 2.5$  on the right.

## 4.6 EQUILIBRIA AND TRAVELLING WAVE CONTINUATION

The previous sections focused on the analytical construction and linear stability of the spatially homogeneous steady state and a localised bump solution. In this section, we showcase *numerical* continuation, firstly of the stationary bump, and demonstrate the effectiveness of continuation by continuing an as-of-yet unseen pattern: spatially-periodic bumps. Lastly, we consider the continuation of a spatially-heterogeneous, temporally-periodic standing two-cycle pattern. The numerical nature of this section necessitates that  $f$  and  $g$  in the model (4.4) be represented by the sigmoidal function (4.5) with steepness parameter  $\mu$ .

### 4.6.1 Stationary Bump

Figure 4.12 shows the continuation of a stationary bump solution in the accommodation strength,  $\kappa$ . During numerical continuation, the class of bump solution (as characterised by its threshold crossings) may change; more precisely, the number of threshold crossings is not necessarily constant along the solution branch. The numerics are unaffected by this, since the knowledge of threshold crossings is an aid for an analytical construction. A stable branch of solutions persists for the chosen parameter set for  $\kappa < 0.27$ ; for  $\kappa > 0.27$ , the bump solution is unstable. Direct numerical simulation confirms this and informs us that the emergent stable solution is a travelling pulse for  $0.27 < \kappa < 0.3$ , and is the spatially homogeneous steady state for  $\kappa \geq 0.3$ . Of interest is the unstable isola shown for the approximate values of  $\kappa$ ,  $0.25 \leq \kappa \leq 0.26$ . An isola is defined as a closed curve in parameter space [14].

Shown in Figure 4.13 is the shape of the bump solution at the three points labelled (a), (b) and (c) in Figure 4.12. On the main branch, solutions take the general shape of a single “hump” in the main bump as shown in Fig-

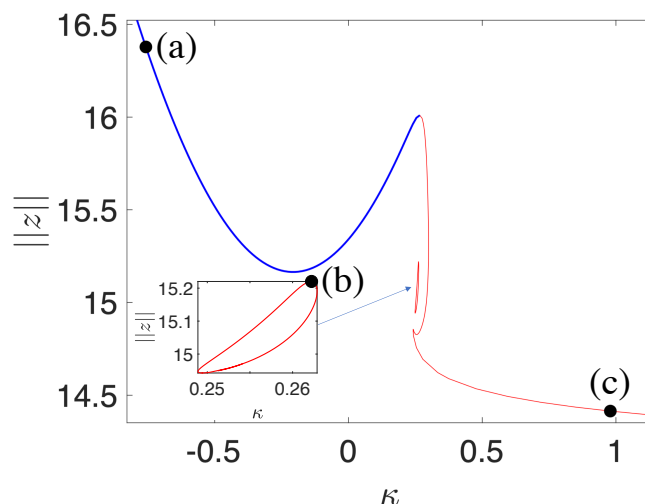


Figure 4.12.: Continuation of a stationary bump in  $\kappa$  with the solution 2-norm plotted on the vertical. Note the existence of an unstable isola of solutions shown in more detail in the inset. Blue (red) curves denote stable (unstable) branches of solutions. Spatial plots of (a), (b), (c) are shown in Figure 4.13. Parameters are:  $h_0 = 0.2$ ,  $\theta = 0.4$ ,  $\alpha = 1.5$ ,  $\sigma = 0.1$ ,  $\mu = 80$ .

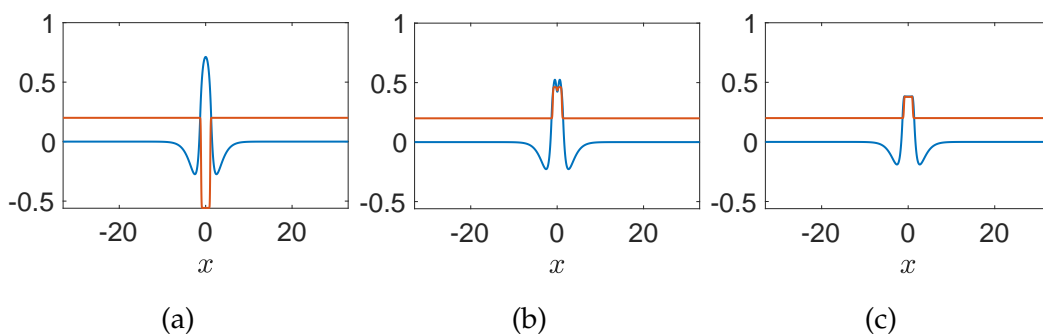


Figure 4.13.: The solutions represented by the black dots in Figure 4.12. The blue and orange lines represent  $u(x)$  and  $h(x)$  respectively. (a) is stable, while (b) and (c) are unstable solutions.

ures 4.13a and 4.13c, whereas on the isola, Figure 4.13b shows that the main bump is composed of two smaller humps. One may expect that as a parameter other than  $\kappa$  is varied, the isola may “join up” with the main branch to create a single uninterrupted branch with no isola present. A method of numerically treating isolas of equilibria is given in [14], where a procedure

is outlined that continues a given isola in a secondary parameter. Due to an isola's nature as a closed branch of solutions, it must contain at least two fold points, and so it is possible to continue each of the fold points in two-parameter space to track regions of existence and the birth/death of the isola [14, 111, 62].

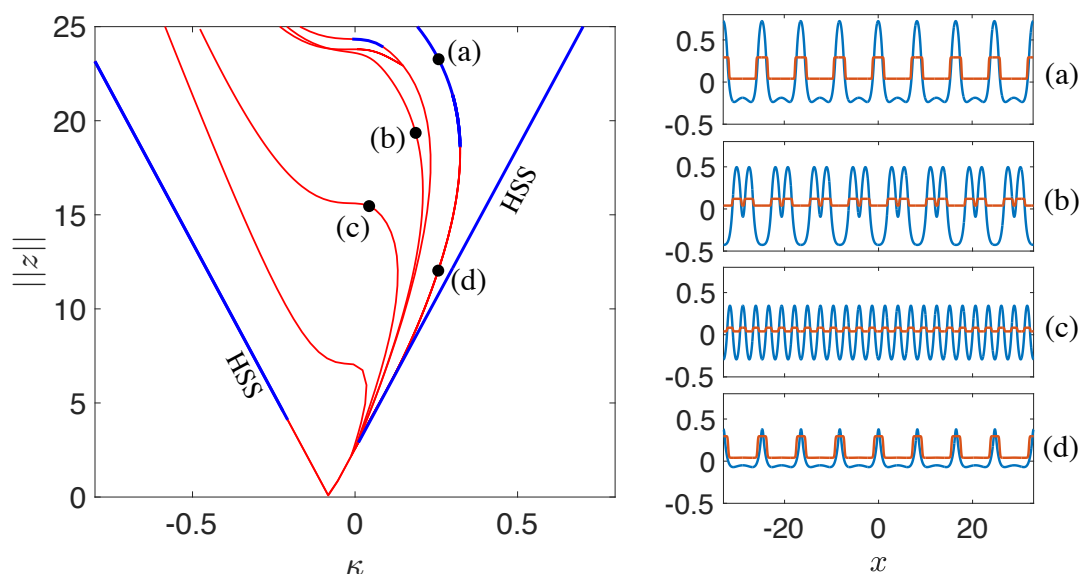


Figure 4.14.: (Left): Continuation of spatially periodic stationary bumps to (4.4) in  $\kappa$  with the solution 2-norm plotted on the vertical. The homogeneous steady state is continued in the same figure (denoted “HSS”) and forms a boundary in  $(\kappa, \|\cdot\|)$ -space in which the various periodic bump solutions exist. Blue curves are stable solutions, while red curves denote unstable solutions. (Right): Plots of  $u(x)$  (blue) and  $h(x)$  (orange) for the four solutions (a)-(d) denoted by the black dots on the continuation diagram. Parameters are:  $h_0 = 0.04$ ,  $\theta = 0.0$ ,  $\alpha = 1.0$ ,  $\sigma = 0.1$ ,  $\mu = 100$ .

### 4.6.2 Stationary Spatially Periodic Bumps

As well as localised bumps, (4.4) supports spatially-periodic bumps. Figure 4.14 shows a continuation of various steady spatially-periodic bump solutions and the homogeneous steady state (HSS). As  $\kappa$  increases through 0, the HSS gains stability.

At the instability point, a variety of branches of unstable spatially-periodic bumps are born that exist within the “v-shaped valley” outlined by the HSS in  $(\kappa, 2\text{-norm})$ -space. Solutions on a few of these unstable branches are shown as (b)-(d). Solution (a) is stable, and this is confirmed via numerical simulation as well as by the numerical stability routine implemented in the continuation. As the norm decreases down a branch, the spatial period decreases (compare, for example (a) with (c)). Solution (b) is a spatially-periodic multi-bump solution. With regards to (a) and (d), the upper branch is stable while the lower branch is unstable.

### 4.6.3 Travelling Pulse

The authors in [48, 50] further constructed the travelling pulse solution to (4.1) by finding the stationary solution in the co-moving wave frame, and analysed its linear stability via an Evans function approach. Where the pulse was seen to go unstable, direct numerical simulation showed the emergence of stable travelling breathers. We explore facets of the travelling pulse solution to (4.4) from a numerical perspective. Figure 4.15 shows the continuation of a travelling pulse solution in the parameter  $h_0$  with wavespeed,  $c$ , shown on the vertical. The existence of the curve demonstrates that travelling waves are solutions to the dynamic threshold model with smoothed dynamics, (4.4). We investigate stability through a combination of direct numerical simulation and a numerical stability routine. In general, an upper branch and a lower branch exist, with the lower being unstable. Both

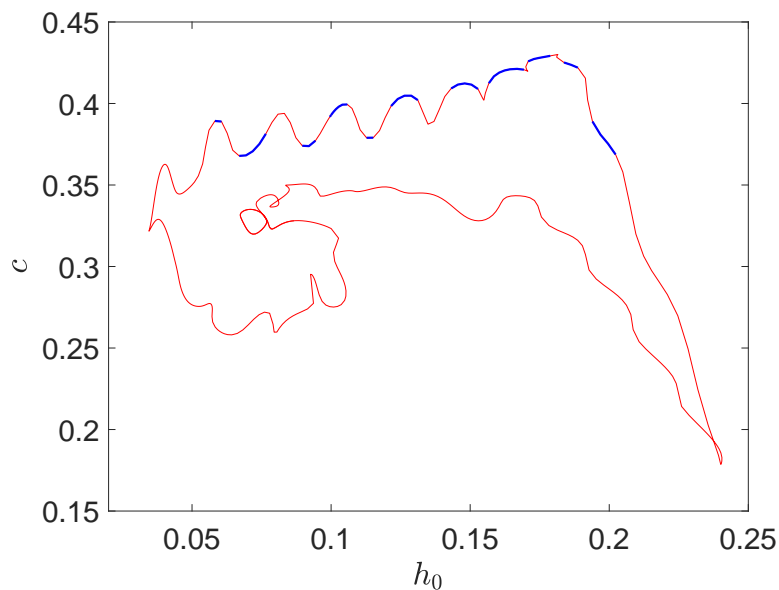


Figure 4.15.: The continuation curve (blue stable, red unstable) for a travelling pulse solution to (4.4) in the parameter  $h_0$ , with the wavespeed  $c$  plotted on the vertical. In general, the upper branch is stable, with the lower branch unstable. Parameter values are  $\theta = 0.4$ ,  $\kappa = 0.4$ ,  $\alpha = 1.5$ ,  $\sigma = 0.1$ , and  $\mu = 80$ .

branches meet at  $h_0 = 0.02$  and  $h_0 = 0.24$ , forming a closed loop of solutions. A stable pulse is shown (by direct numerical simulation) to be the emergent pattern on the upper branch for  $0.05 < h_0 < 0.18$ . The numerical stability routine picks out certain segments of the upper branch as being unstable. A hypothesis we put forward here is that the pulse initially destabilises into some other pattern, which then undergoes a secondary instability to a travelling pulse on these segments. There are a number of different emergent patterns at various points along the lower solution branch including the homogeneous steady state, travelling breathers, standing waves, travelling wavetrains, and the stable pulse on the upper branch. In other words, depending on the parameter value  $h_0$ , a pulse may destabilise into one of any of the solutions here listed. This demonstrates the rich variety of ways in which solutions may go unstable. This may be interpreted as there being a variety of way information transmission can be affected in neural systems.

---

For example, by termination (instability to the homogeneous steady state) or storage (via the generation of standing patterns).

## 4.7 TRANSLATION-INVARIANCE

The persistence of a zero eigenvalue in the Evans function plots Figures 4.8 and 4.10 is a consequence of spatial translation invariance in the system. We show that this is indeed the case by verifying that  $z'(x) = (q'(x), p'(x))$  is an eigenfunction of the operator  $\mathcal{L}$  for the stability problem [115]

$$\mathcal{L}z = \lambda z, \quad (4.60)$$

which is given explicitly by (4.42) and (4.48), with  $\lambda = 0$ .

First, we construct  $z'(x)$  explicitly<sup>6</sup> to obtain

$$q'(x) = \int_{-\infty}^{\infty} w(x-y)\delta(q(y) - p(y)) [q'(y) - p'(y)] dy, \quad (4.61a)$$

$$p'(x) = \int_{-\infty}^{\infty} w_h(x-y)\delta(q(y) - \theta)q'(y) dy. \quad (4.61b)$$

Substituting  $\lambda = 0$  into (4.42) and (4.48), one obtains the equivalent of (4.61), after making the substitution  $\delta z(x) = z'(x)$ . Therefore  $\delta z(x) = z'(x)$  is a solution to the stability problem with  $\lambda = 0$  showing spatial translation invariance of the system. It is clear that the presence of a non-constant spatial drive breaks this translation invariance. Explicitly, (4.61) for  $q'(x)$  becomes

$$q'(x) = \int_{-\infty}^{\infty} w(x-y)\delta(q(y) - p(y)) [q'(y) - p'(y)] dy + I'(x), \quad (4.62)$$

and if  $I(x)$  is non-constant, then  $I'(x) \neq 0$ , breaking translation invariance.

## 4.8 THE INCLUSION OF LOCALISED SPATIAL DRIVE

In Sections 4.4 and 4.5, we considered localised solutions to a neural field equation with a dynamic threshold. Spatial homogeneity was assumed, demonstrated by the persistent zero eigenvalue, and see Section 4.7 for the

---

<sup>6</sup>This is done by taking the derivative with respect to  $x$  of (4.30).

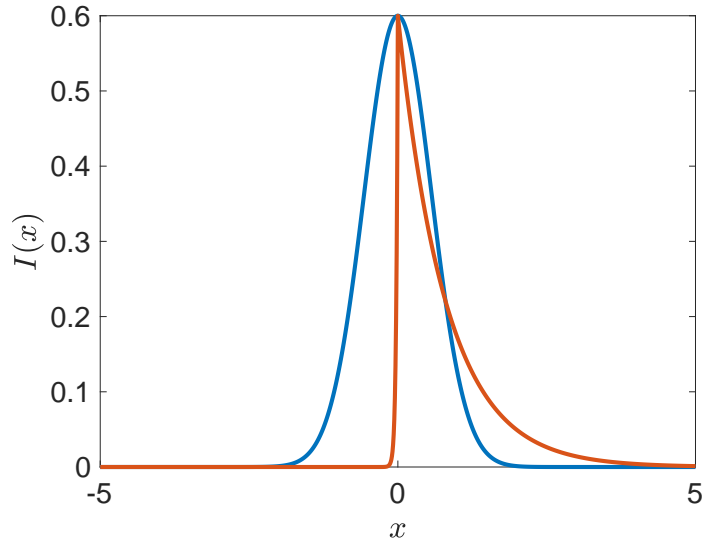


Figure 4.16.: The shape of the the symmetric (4.63) and the asymmetric (4.64) spatial drive, in blue and orange respectively, for  $I_0 = 0.6$  and  $\sigma_I = 0.8$ , and  $d = 30$  in the case of the asymmetric drive. Note the steep descent for  $x < 0$  in this case.

calculation that shows this. Here we consider a non-uniform spatial drive in the dynamics of the synaptic variable. This can be considered as a source of activity, chosen to be centred at the origin.

The spatial drive we consider is localised at the centre of the bump but can be asymmetric. We study two different cases of non-zero drive: symmetric, given by

$$I(x) = I_0 e^{-x^2/\sigma_I^2}, \quad (4.63)$$

and asymmetric, given by

$$I(x) = I_0 \begin{cases} e^{-x/\sigma_I}, & x \geq 0, \\ e^{dx/\sigma_I}, & x < 0, \end{cases} \quad (4.64)$$

with the parameter  $d \neq 1$  to ensure an asymmetry is present. These functions are shown in Figure 4.16. For a non-constant  $I(x)$ , space is no longer homogeneous and so translation invariance is lost. Correspondingly, the stability problem no longer has a persistent zero eigenvalue and therefore the possibility of a drift instability occurring is also lost. The lack of a zero

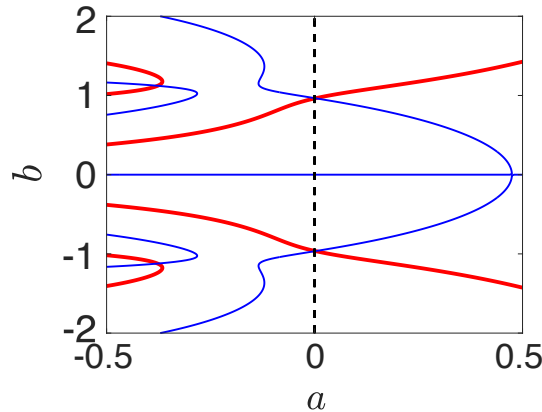


Figure 4.17.: Evans function plot for the localised bump solution with symmetric drive at  $\kappa = 0.3$  and all other parameters as in Figure 4.7. The parameter  $\alpha = \alpha_c \approx 1.86$  at the Hopf-type instability. Thick red (thin blue) lines are the real (imaginary) zero contours of  $\mathcal{E}(\lambda)$ . Eigenvalues are given by the intersections of the real and imaginary contours, and so here we see the onset of instability as a complex conjugate pair of eigenvalues crosses the imaginary axis. Note the absence of the trivial eigenvalue due to translation invariance.

eigenvalue is seen in the Evans function plots Figures 4.17 and 4.19, which both show the onset of a dynamic instability for a symmetric and asymmetric spatial drive respectively.

We show numerically that a symmetric spatial drive of sufficient magnitude changes the nature of the instabilities that occur. The dynamic instabilities shown in the Evans function plots no longer produces breathers, but sloshers as seen in Figures 4.18 and 4.20. These patterns appear to be a hallmark of neural fields with spatial drive; see the work of Folias [80] for a weakly non-linear analysis of a stationary bump that can destabilise into a breather or a slosher. To summarise, in the case of a symmetric spatial drive, symmetric sloshers are seen, as in Figure 4.18 whereas for an asymmetric spatial drive, asymmetric sloshers are seen, as in Figure 4.20, with the relevant Evans plot shown in Figure 4.19.

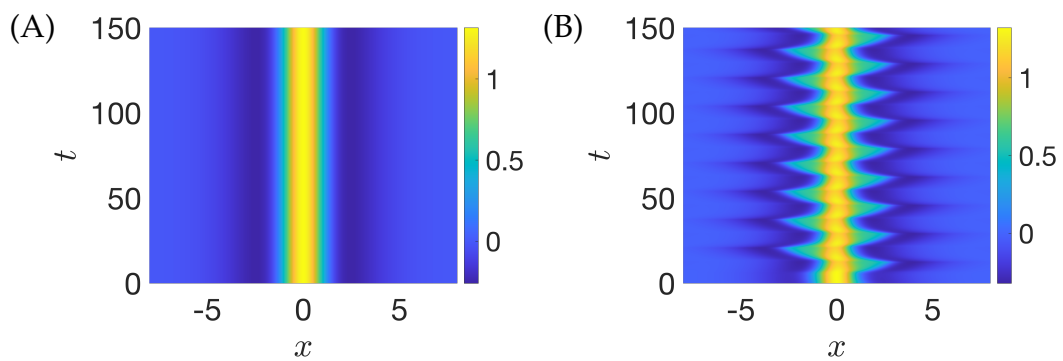


Figure 4.18.: Spatiotemporal plots of  $u(x,t)$  for  $\alpha$  either side of  $\alpha_c \approx 1.86$  which is the bifurcation point as shown in Figure 4.17. Panel (A) shows a stable symmetric bump solution persisting through time, whereas in panel (B) the bump solution destabilises into a pattern with “sloshing” dynamics, aptly named a *sloser*. The spatial drive in this case is symmetric, and results in a symmetric sloser pattern emerging. Parameters are as in Figure 4.17, with  $I_0 = 0.6$ , and  $\sigma_I = 0.8$ . On the left,  $\alpha = 1.8$ , and on the right,  $\alpha = 2.2$ .

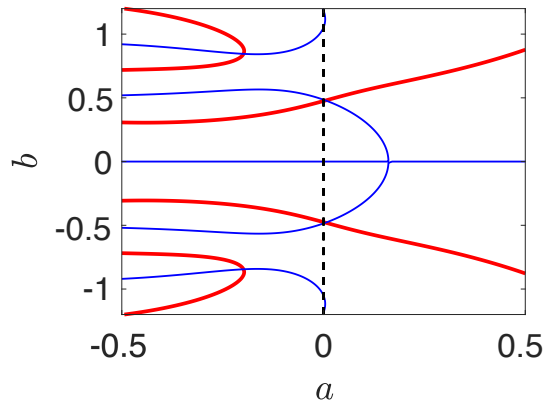


Figure 4.19.: Evans function plots for the localised bump solution with asymmetric spatial drive at  $\alpha = \alpha_c \approx 1.28$ ,  $I_0 = 0.6$  and  $\sigma_I = 0.8$ . All other parameters are as in Figure 4.7. Thick red (thin blue) lines are the real (imaginary) zero contours of  $\mathcal{E}(\lambda)$ . Eigenvalues are given by the intersections of the real and imaginary contours. As  $\alpha$  is varied, a complex conjugate pair of eigenvalues crosses the imaginary axis at  $\alpha = \alpha_c \approx 1.28$ , as shown here. For  $\alpha < \alpha_c$ , all eigenvalues,  $\lambda$ , are such that  $\text{Re}(\lambda) < 0$ . For  $\alpha > \alpha_c$ , a complex conjugate pair of eigenvalues has crossed the imaginary axis resulting in an oscillatory-type solution forming from the bump in this case. See Figure 4.20 for an illustration of this.

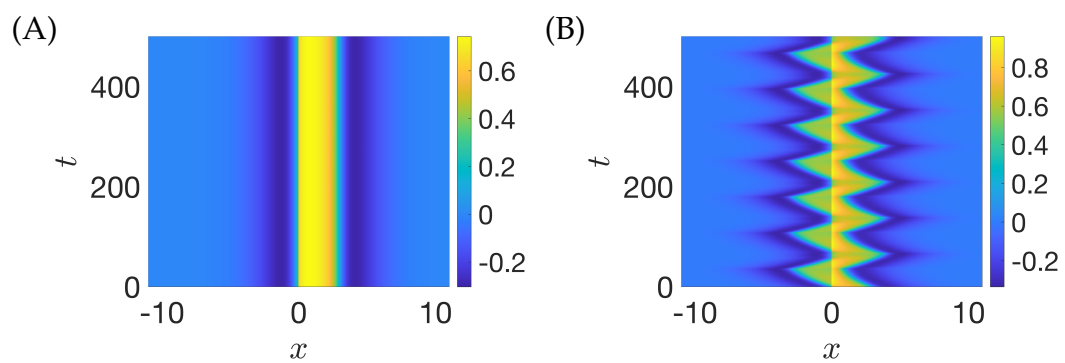


Figure 4.20.: Spatio-temporal plots of  $u(x, t)$  for  $\alpha$  either side of  $\alpha_c \approx 1.28$  in Figure 4.19. Panel (A) shows a stable asymmetric bump solution persisting through time, whereas in panel (B) the bump solution destabilises into an *asymmetric slosher*. The right-hand side of the slosher has higher activity as a consequence of the asymmetry of the spatial drive (see Figure 4.16). Parameters are as in Figure 4.19.

## 4.9 EXOTIC SOLUTIONS

Whether or not more exotic solutions exist can be explored via direct numerical simulation with a variety of initial conditions and parameter sets, as well as by a bifurcation analysis. Figure 4.21 shows a selection of such patterning exhibited by the model. These have been found via direct simulation. Pulse emitter-type solution such as Figure 4.21B have been seen previously in [81] via numerical simulation in a model very similar to (2.46).

The nature of many of the solutions in Figure 4.21 excludes them from analysis via a traditional analytical approach, however a numerical continuation analysis would likely be successful and provide more insight, especially for the travelling breathers (Figure 4.21A) and saltatory waves (Figure 4.21F) which are two of the more *regular* solutions that have been seen. This is done in the next section, using techniques from Chapter 3.

See Table 3 for the parameter values used in simulations to generate the exotic patterns in Figure 4.21. Relatively steep sigmoidal functions (4.5)

Parameter	A	B	C	D	E	F
$h_0$	0.2	0.0	0.04	-0.12	0.04	0.04
$\theta$	0.4	0.1	0.1	0.1	0.34	0.1
$\kappa$	0.4	0.3	0.3	0.25	0.54	0.5
$\alpha$	1.5	2.0	3.0	1.0	1.0	1.0
$\sigma$	0.1	0.1	0.1	0.1	0.01	0.1
$\mu$	80	80	80	80	100	80

Table 3.: Parameter values for which the exotic patterns (A-F) to the model (4.4) in Figure 4.21 were seen to exist, with each column in the table corresponding to each pattern. The value  $\mu$  corresponds to the steepness of the sigmoidal function used as the firing rate function as in (4.5).

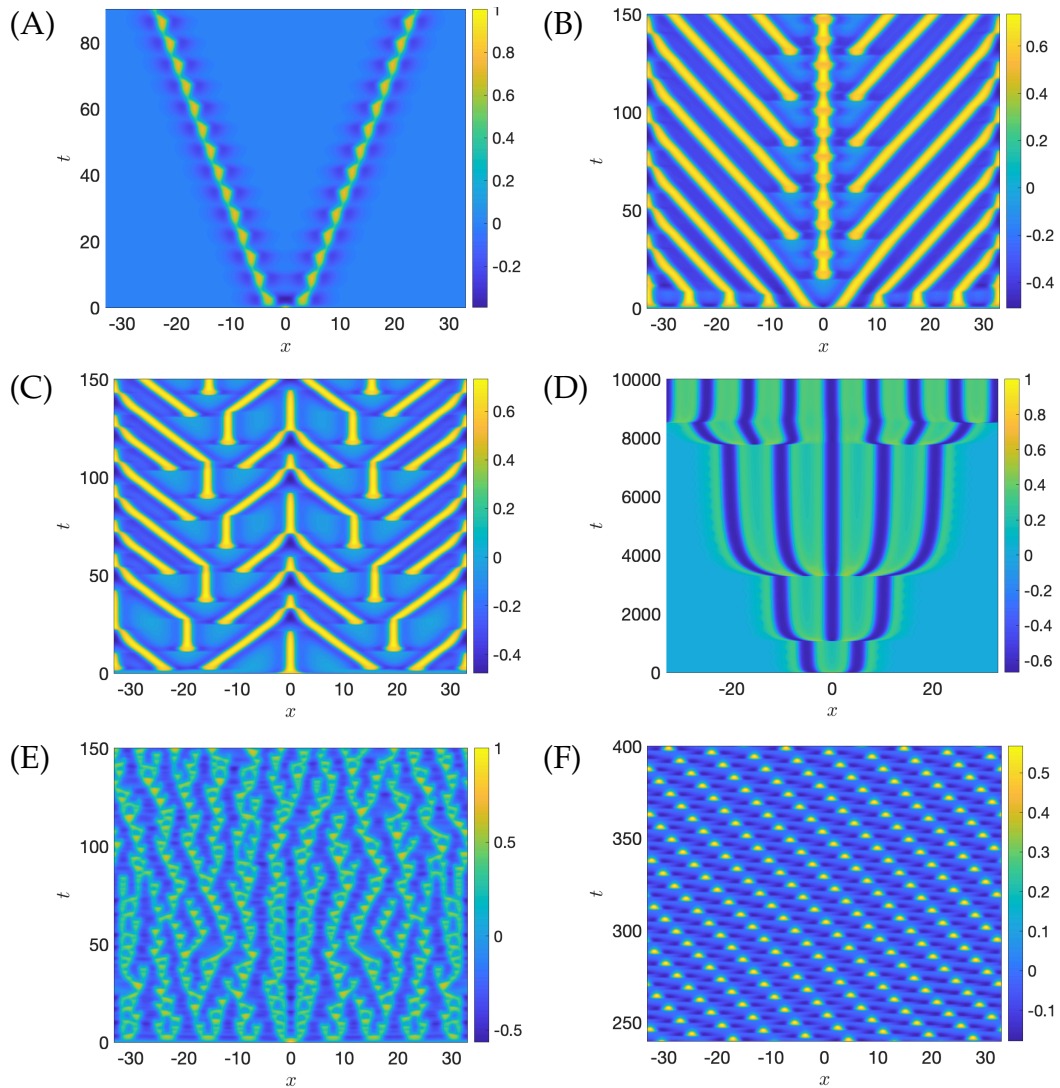


Figure 4.21.: Exotic patterns seen in the dynamic threshold model. (A) travelling breathers, (B) travelling pulses created from a central breather, (C) travelling pulse emitting and annihilating waves, (D) wave/bump creation cascade, (E) chaotic wandering bumps, (F) a saltatory pattern that travels across the domain with a well-defined wavespeed in discrete clumps. These patterns were seen for sigmoidal  $f$  and  $g$ . Parameters used in numerical simulation for each pattern are in Table 3.

were used for the firing rate function  $f$  in these simulations, with  $\mu = 80$ .

Further exploration is required to see if the patterns exist in the Heaviside firing rate limit or indeed in the shallow sigmoidal regime.

#### 4.10 CONTINUATION OF TEMPORALLY PERIODIC STRUCTURES

The travelling breather and saltatory waves in Figure 4.21 are patterns which are periodic in time up to a spatial shift after each temporal period. Thus they fit the necessary criteria to be amenable to a TWPO continuation analysis via the methods developed in Chapter 3.

We begin this section on the continuation of temporally periodic structures with a PO continuation analysis of spatially extended standing wave patterns.

##### 4.10.1 *Standing Waves*

Using techniques from Chapter 3, Figure 4.22 shows an example of the continuation of a spatially-heterogeneous, temporally-periodic solution to (4.4). The pattern under consideration is referred to as a standing two-cycle wave, and is shown for  $u(x, t)$  in the inset at two different points along the solution branch. Plotted is the emergent temporal period,  $T$ , against the continuation parameter  $\alpha$ ; the insets have the same vertical axis scaling for  $t$  to emphasise how drastically the pattern changes along the branch. As the synaptic decay constant  $\alpha$  increases, the period  $T$  decreases resulting in a shorter temporal gap between each successive cycle within a period. This is as one may expect, since a larger  $\alpha$  corresponds to a quicker transfer of synaptic information.

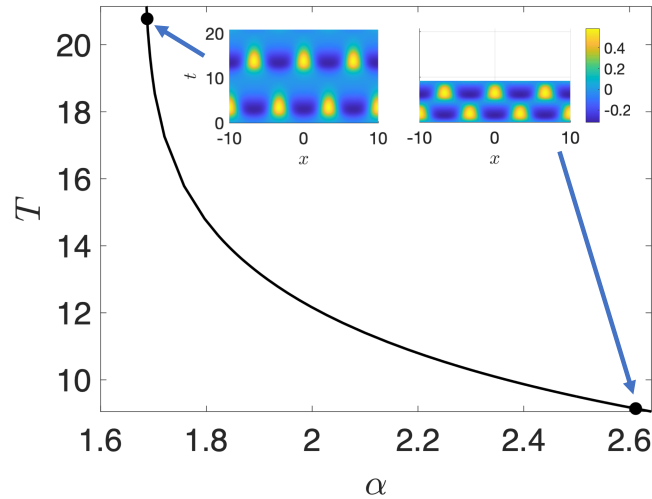


Figure 4.22.: Periodic orbit continuation of a spatially heterogeneous standing wave pattern to (4.4) in  $\alpha$  with the temporal period  $T$  of the pattern plotted on the vertical. The spatio-temporal profile  $u(x, t)$  over a period is shown at two points on the solution branch, denoted by the black dots to highlight how the period and structure of the solution changes along the branch. Parameters are:  $h_0 = 0.1$ ,  $\theta = 0.3$ ,  $\kappa = 0.5$ ,  $\sigma = 1.0$ ,  $\mu = 10$ , with  $I(x) = 0$ .

#### 4.10.2 Saltatory Travelling Periodic Waves

Figure 4.23 shows the bifurcation diagram for the saltatory TWPO solution. This is split over the two panels to adequately present the information obtained from continuation. Recall from Chapter 3 that during a TWPO continuation, there are three “active quantities”, which change at each continuation step: the bifurcation parameter (which is  $\alpha$  in this case), and the two independent quantities which are the temporal period of the pattern  $T$ , and the spatial shift  $\xi$ . The wave-speed of the solution may be computed from these two quantities as  $c = \xi/T$ . Ideally, the norm of the whole spatio-temporal solution should be measured over the entire temporal period, since this returns a consistent value, no matter where the temporal origin is chosen to be (rather than purely the norm of the spatial solution

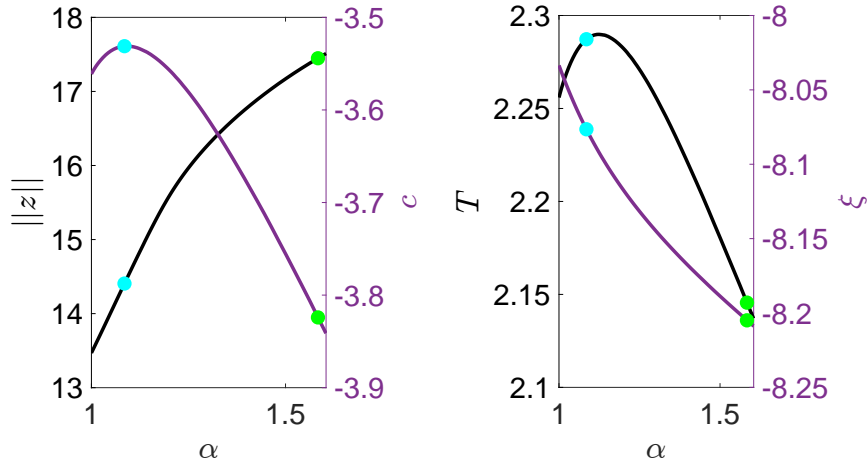


Figure 4.23.: Bifurcation diagram for the saltatory travelling periodic pattern, with multiple solution measures on the vertical. The left-hand panel shows (left axis, black) the norm of the solution  $\|z\|$  and (right axis, purple) the wave-speed  $c$  against  $\alpha$ . The right-hand panel shows (left axis, black) one period of the solution  $T$  and (right axis, purple) one spatial shift  $\zeta$  against  $\alpha$ . Cyan and green dots each correspond to the two spatio-temporal solutions in Figure 4.24. Parameters are as in Table 3, column F. Numerical parameters are  $L_x = 33$  on a periodic domain  $[-L_x, L_x)$  with  $n_x = 2^{12}$  mesh points,  $\epsilon_n = 10^{-5}$ ,  $\epsilon_l = 10^{-4}$ .

at the temporal origin). The left-hand panel shows the projection of the bifurcation diagram into  $(\|\cdot\|, \alpha)$ -space on the left vertical axis (black curve), while the right vertical axis shows  $(c, \alpha)$ -space (purple curve). The right-hand panel projects the bifurcation diagram into  $(T, \alpha)$ -space on the left vertical axis (black curve), and  $(\zeta, \alpha)$ -space on the right vertical axis (purple curve). The cyan dot on each curve represents the same spatio-temporal solution, which is plotted in the top panel of Figure 4.24. The green dots represent a different solution, plotted in the bottom panel of Figure 4.24, with the 200 multipliers with the largest absolute value plotted for each solution on the right.

As  $\alpha$  is increased from 1, the norm of the solution increases over the range of  $\alpha$  plotted. This corresponds to a higher “activity level”, and is

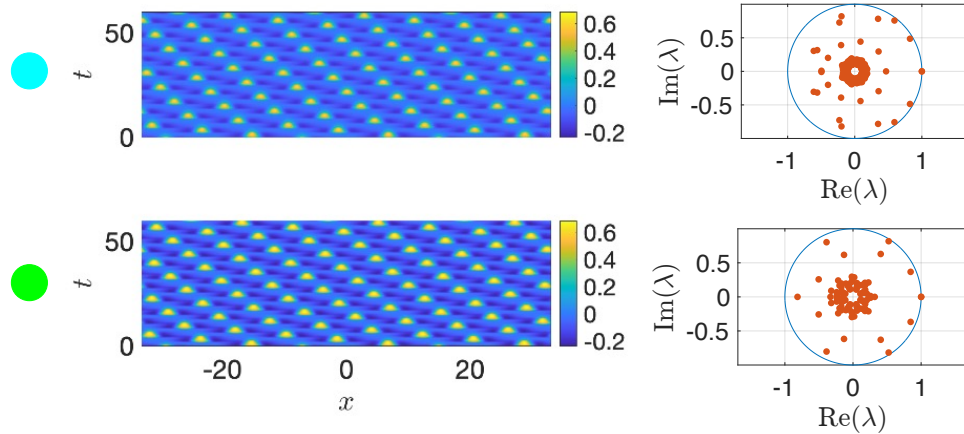


Figure 4.24.: Spatio-temporal plots (left) of the solutions represented by the cyan dot (top row) and green dot (bottom row) in Figure 4.23. The right-hand panels show an ordered selection of the 200 largest numerically computed multipliers in absolute value in orange. The blue circle is the unit disc.

visualised explicitly by comparing the spatio-temporal plots of the solutions corresponding to the cyan and green dots. The magnitude of the speed initially decreases until  $\alpha \simeq 1.1$  (purple curve rises), but increases beyond this, as shown by the purple curve becoming more negative. The sign of the wave-speed is important and corresponds to the direction of travel of the wave. The spatio-temporal plots show the wave moving to the left, hence the wave-speed is negative. A close inspection of the spatio-temporal plots confirms that the magnitude of the wave-speed is greater for the solution corresponding to the green dot, as is shown on the bifurcation diagram.

The black curve in the right-hand panel shows that as  $\alpha$  increases,  $T$  initially rises until  $\alpha \simeq 1.1$ , then decreases. Though this may appear to follow the same pattern as  $c$ , this is not the case exactly, since  $c$  is signed, and is inversely proportional to  $T$ . The purple curve shows  $\zeta$  decreasing as  $\alpha$  is increased. It is important to remember that  $\zeta$  refers to the amount the pattern shifts in space over a single temporal period  $T$ , while the spatio-temporal plots are plotted for  $t \in [0, 9T]$ .

The multipliers for the two solutions represented by the cyan and green dots are plotted in the right-hand panes of Figure 4.24. In each case, the largest eigenvalues (in absolute value) are obtained using Krylov-Schur solvers [204, 123] implemented in MATLAB. All of these multipliers exist inside the unit disc, therefore *all* multipliers are inside the unit disc, meaning the solutions are both stable. The entire branch is predicted to be stable by the numerical stability theory; direct numerical simulation at a number of points along the branch, starting with a perturbed initial condition confirms this to be the case.

#### 4.10.3 Travelling Breathers

Travelling breathers were found by Coombes and Owen in the neural field with a dynamic threshold (4.1) in [48]. As well as existing in neural fields, they appear in systems of multi-component reaction-diffusion equations, with the additional components giving rise to the oscillatory nature of travelling breathing solutions [145, 109]. We utilise the techniques developed in Chapter 3 in order to track the travelling breathers as the synapse parameter  $\alpha$  is varied. This is shown in Figure 4.25, where, as in Figure 4.23, the continuation diagram has been projected into  $(\alpha, \|z\|)$ -,  $(\alpha, c)$ -,  $(\alpha, T)$ -, and  $(\alpha, \xi)$ -space. Here,  $z = (u, h)$  is the state vector of the system. The existence curves are shown in blue and orange, with the colour of each curve corresponding to the axis with the correspondingly coloured labels and ticks. Beginning on the upper branch in  $(\alpha, c)$ -space, as  $\alpha$  is decreased, a fold point is encountered at  $\alpha = 1.345$ . Beyond this,  $\alpha$  begins to increase, while  $c$  continues to decrease, until  $\alpha = 1.6$ , beyond which  $c$  increases slowly. Travelling breathers exist within a narrow window of values for  $\alpha$ .

Two different solutions on the continuation diagram, identified by the cyan and green dots, are selected and plotted in Figure 4.26. The cyan dot is stable, whereas the green dot is unstable, as shown by direct numerical simulation (the lower solution destabilises into a travelling pulse). Simu-

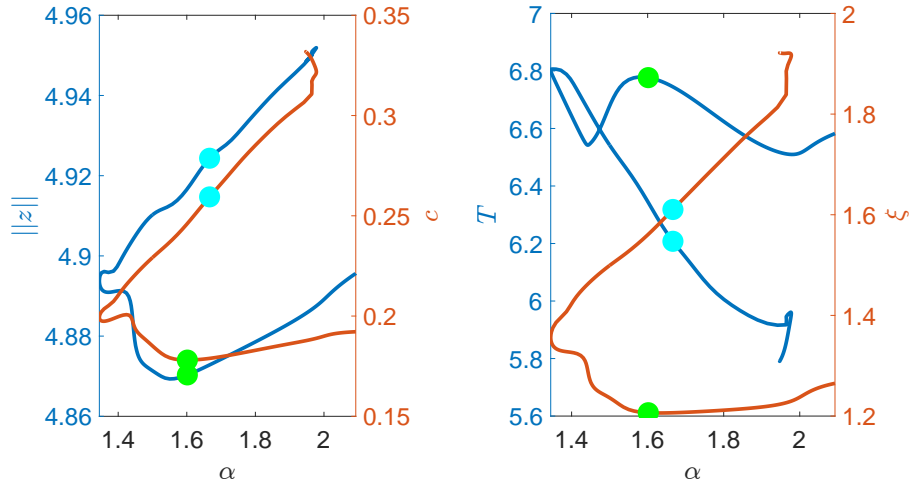


Figure 4.25.: Bifurcation diagram for the travelling breather pattern, with multiple solution measures on the vertical. The left-hand panel shows (left axis, blue) the norm of the solution  $\|z\|$  and (right axis, orange) the wave-speed  $c$  against  $\alpha$ . The right-hand panel shows (left axis, blue) one period of the solution  $T$  and (right axis, orange) one spatial shift  $\xi$  against  $\alpha$ . Cyan and green dots each correspond to the two spatio-temporal solutions in Figure 4.26. Parameters are as in Table 3, column A. Numerical parameters are  $L_x = 24$  on a periodic domain  $[-L_x, L_x)$  with  $n_x = 2^9$  mesh points,  $\epsilon_n = 10^{-6}$ ,  $\epsilon_l = 10^{-5}$ .

lation indicates that the upper branch in  $(\alpha, \|z\|)$ -space is stable, while the lower branch (beyond the fold point at  $\alpha = 1.345$ ) is unstable, with solutions either settling to the corresponding stable solution on the upper branch, to the homogeneous steady state, or to a travelling pulse. This shows the model exhibits multi-stability, where a pulse, a travelling breather, and the homogeneous steady state all co-exist for the same parameter set. The pulse solution emerging at the green dot has a much higher wave speed than the travelling breather.

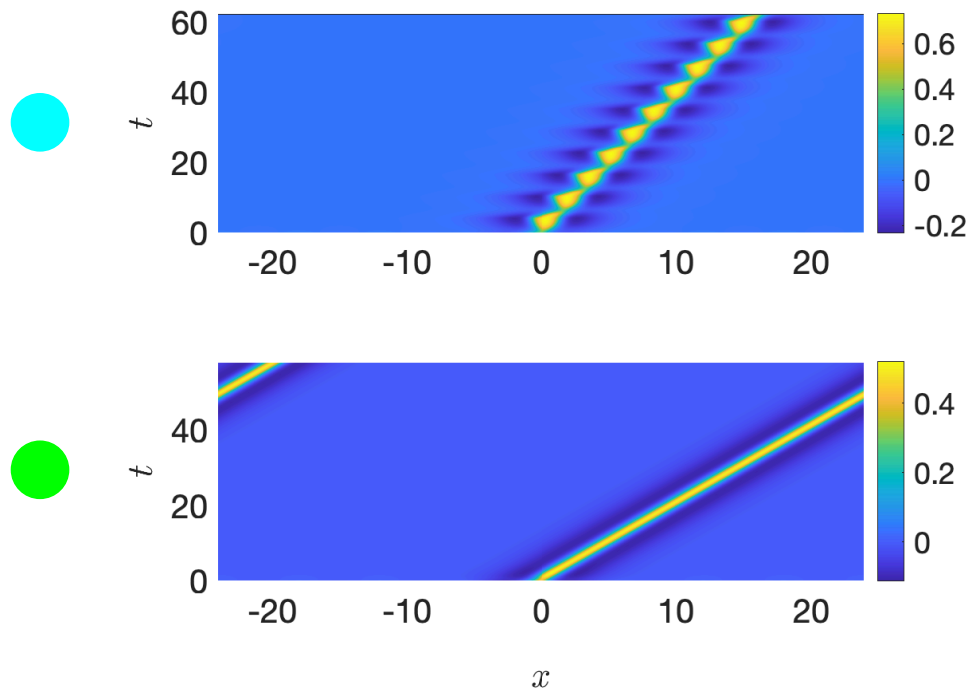


Figure 4.26.: Spatio-temporal plots of the solutions represented by the cyan dot (top row) and green dot (bottom row) in Figure 4.25. The cyan dot is initialised with a stable breather while the green is initialised with an unstable breather which destabilises into a travelling pulse as the emergent pattern.

---

#### 4.11 SUMMARY

Neural fields are typically modelled with a constant threshold, although there are exceptions to this – for example, see [209] which studies neural fields with firing thresholds with noise. In this chapter, we have built upon the work in [50, 48] to shed light on patterning in neural fields incorporating threshold accommodation.

We began with a Turing analysis of the spatially homogeneous steady state in Section 4.3 in which we obtained an implicit dispersion relation between the eigenvalues  $\lambda$  of the stability problem, and the wavenumber of perturbation,  $k$ . We showed that the homogeneous steady state is unable to undergo steady or Hopf bifurcations in this model, and only undergoes static Turing and dynamic Turing-Hopf bifurcations in the case where the functions  $f$  and  $g$  are sigmoidal. Emergent patterns beyond bifurcations were those typically seen in neural field models [67] such as standing Turing patterns and travelling waves. However, in the region of parameter-space beyond both Turing and Turing-Hopf bifurcations, direct numerical simulation showed a mixing of Turing and Turing-Hopf patterns. The synaptic activity  $u$  and dynamic threshold activity  $h$  were qualitatively similar, as expected based on the model equations. This part of the chapter fleshes out the model introduced by Coombes and Owen [50] by analysing the homogeneous steady state in that model.

Since the Turing analysis is a *linear* analysis, we have used it to determine the location and type of bifurcation, and then observed the type of emergent pattern just beyond bifurcation using direct numerical simulations. A weakly non-linear analysis – such as that carried out in [67], where the authors analysed a neural field model incorporating spike frequency adaptation – provides an analytical description of solution behaviour close to the point of bifurcation. However, in our exploration we have favoured techniques from numerical analysis, such as simulation and continuation. From a pattern formation perspective, it is of interest to explore further in two

spatial-dimensions to determine whether or not any more exotic solutions exist. The numerical continuation tools we have developed will be useful in any future numerical analysis on the plane.

In Section 4.4, we focused on a different class of solution, namely the stationary bump solution. Working in the Heaviside firing rate limit allowed for an explicit construction of the bump solution. There are multiple classes of bump solutions supported by the model, but we have focused on the one shown in Figure 4.7. The eight unknowns parameterising the bump solution are found via the eight crossing conditions (4.32) and rely on the knowledge of the integral of a wizard hat connectivity.

In determining the linear stability of the stationary bump, we developed an Evans function approach for stability. Viewing the bump as a stationary wave ensures that the Evans function approach is successful in characterising linear stability. By generating a linear system in the perturbations at the threshold crossings, we were able to determine the complex-valued Evans function whose zeroes are the eigenvalues to the stability problem. In this way, we have been able to put the linear stability of bumps in the neural field model with a dynamic firing threshold on a completely formal footing.

In the absence of any spatially varying drive, there are two possible routes to an instability: the *drift* instability, in which an eigenvalue crosses the imaginary axis through zero, yielding a travelling pulse, and a *dynamic* instability, in which breathers form. With the *inclusion* of a spatially heterogeneous drive, the possibility of a drift instability is lost, and sloshing solutions form at the dynamic instability. An asymmetric spatial drive yields asymmetric sloshing solutions. These types of solutions are ripe for numerical continuation in the drive strength parameter  $I_0$  or the asymmetry parameter  $k$ .

Modelling neural tissue with dynamically varying thresholds is one of a number of routes forward to more realistic cortical modelling. The work in this chapter has elucidated the complex patterning present in such a model

and opens the door towards – and provides routes forward for – further study.

---

THALAMIC NEURAL FIELDS WITH REBOUND  
CURRENTS

---

5.1 INTRODUCTION

In single-neurons, there exist a zoo of ionic currents that can shape the cellular firing response. As reviewed in Chapter 2, Hodgkin and Huxley (1952) [98] demonstrated by a blend of modelling and sophisticated experimentation that the movement of sodium ( $\text{Na}^+$ ) and potassium ( $\text{K}^+$ ) ions into and out of the cell is responsible for the action potential. Ionic currents expressed at the cellular level may be incorporated into models of the membrane potential of single neurons by using extensions of the Hodgkin-Huxley approach, including further gating variables describing the opening and closing of large ensembles of ion channels as follows. A generic number of  $N$  currents  $I_i$ ,  $i \in \{1, \dots, N\}$ , take the form

$$I_i = g_i(V - V_{i,\text{rest}}), \quad g_i = m_i^p h_i^q, \quad p, q \in \mathbb{Z},$$

$$\frac{dX}{dt} = \frac{X_\infty(V) - X}{\tau_X(V)}, \quad X \in \{m_i, h_i\}, \quad i \in \{1, \dots, N\},$$

and are incorporated into a single cell model of membrane potential,  $V$ , as

$$C \frac{dV}{dt} = - \sum_{i=1}^N I_i,$$

each with their own conductances  $g_i$ , and gating dynamics specified by  $m_i$  (activating) and  $h_i$  (inactivating) with their voltage-dependent activation/steady state curves  $X_\infty(V)$  and timescales  $\tau_X(V)$ . The exponents  $p$

and  $q$  describe the number of molecules which must occupy a certain region of the membrane in order for a channel to conduct [100], as reviewed in Chapter 2. The membrane capacitance,  $C$ , and the reversal potential for the  $i$ th ionic species,  $V_{i,\text{rest}}$ , are often modelled as constant, though it has been shown they can vary with age [51].

Where there is a desire to study networks of connected neurons, mean field approaches are often favoured. These often wash out the detailed ionic mechanisms that can sculpt firing patterns, in favour of considering tissue connectivity. This is the basis for many continuum neural field models of the *cortex*, where it is often sufficient to ignore non-linear ionic currents and assume that the firing rate of a population of neurons is a sigmoidal function of synaptic activity only. In this case, it is assumed that neuronal activity only depends on the activity of connected tissue through synaptic currents. See [26, 46, 208] for an overview of this continuum mean field modelling approach.

When the sigmoidal firing rate function is taken to be sufficiently steep so that it may be approximated by a Heaviside function, an abundance of mathematical results for localised patterns and waves can be generated in the neural field framework. To give a flavour of these Heaviside-based results, Amari (1977) [5] was able to construct stationary bumps explicitly, Pinto and Ermentrout (2001) [168] demonstrated the existence of travelling pulse solutions, while Coombes and Owen (2004) [49] developed the Evans function approach to determine the stability of travelling waves in neural field-type systems.

By ignoring any dependence of firing rate mechanisms on intrinsic ionic currents, the standard neural field approach cannot be expected to reproduce *all* biological firing behaviours, in particular those that *rely* on said ionic currents to generate firing events. A case in point is *rebound firing*, or PIR, in which the neuronal response to the release of hyperpolarising inhibition can result in a burst of action potentials [63, 95]. This is a non-

canonical, robust firing mechanism, requiring *hyperpolarisation* rather than depolarisation [107].

As has been discussed briefly in Chapter 2, thalamo-cortical relay (TC) cells are a specific example of a type of neuron which exhibits rebound firing. They are found in the thalamus – the organ often described as the “sensory gateway to the cortex”. When  $\text{Ca}^{2+}$  enters the neuron through T-type  $\text{Ca}^{2+}$  channels in the soma and dendrites [54], a large voltage depolarisation known as a low-threshold  $\text{Ca}^{2+}$  spike (LTS) can occur; the LTS is named due to its occurrence at relatively negative (low) membrane potentials. Due to its ability to generate an LTS, the T-type  $\text{Ca}^{2+}$  current ( $I_T$ ) is sometimes referred to in the literature as the *low-threshold  $\text{Ca}^{2+}$  current* [105]. The LTS occurs over a longer timescale than conventional action potentials mediated by fast  $\text{Na}^+$  and  $\text{K}^+$  currents [222]. As a consequence, these can ride on the crest of an LTS, resulting in a burst firing response, whereby a tight cluster of several action potentials occurs. This is illustrated in Figure 5.1, showing bursts of conventional action potentials when the LTS occurs. The time-scale of the LTS is roughly 30ms, while the conventional action potentials occur over 1-3ms.

Andersen and Eccles (1962) [7] were the first to establish the significance of rebound firing in TC cells, dubbing the phenomenon “post-anodal exaltation”. They conjectured that TC cells were connected reciprocally to other TC cells via inhibitory connections, and that in the late phase of inhibitory PoSPs, thalamic neurons are more excitable than usual. Though it was shown in slice experiments [124] and in vivo [202] that rebound oscillations are due to the mutual interactions between TC and RE cells, the essence of their hypothesis was, nevertheless, correct. Indeed, the model studied by Rinzel et al. [178] is a reduction of the TC-RE network to a single layer of TC cells with inhibitory connections and gives rise to rebound firing. This reduction is outlined in more detail below.

Wang (1994) [220] developed a minimal model of the thalamic relay neuron, incorporating rebound firing through  $I_T$ . This showed non-trivial neu-

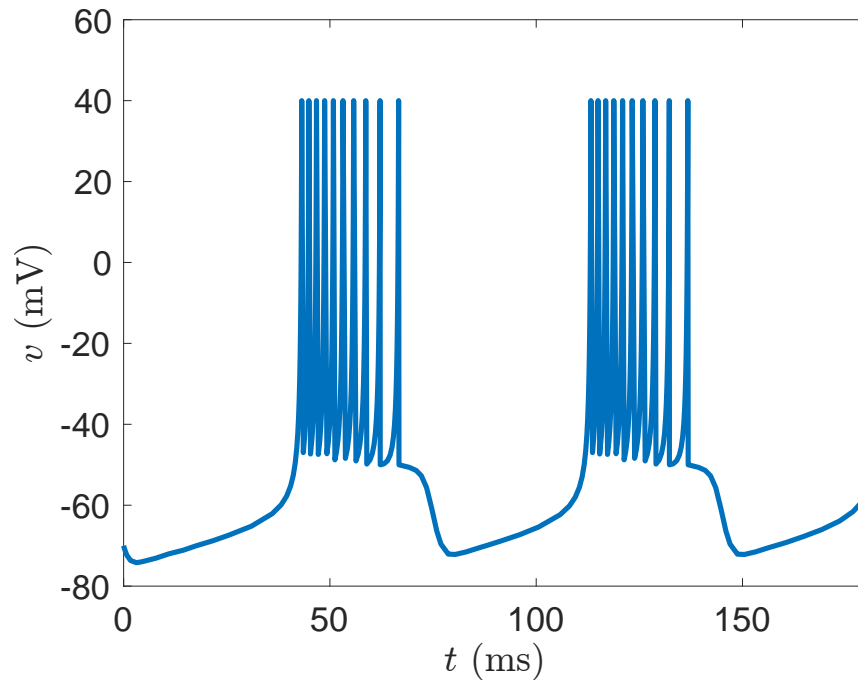


Figure 5.1.: An illustration of two bursts of action potentials riding the crest of the LTS from 40-70ms and 110-140ms with membrane potential in blue. The action potential time-scale (1-3ms) is much shorter than that of the LTS (30ms). This illustration is generated by simulation of the Izhikevich model [110] in a bursting parameter regime.

ronal bursting at the single-cell level. Guckenheimer, Tien, and Willms (2005) [87] treated bursting in the Wang single-neuron model via a fast-slow analysis.

TC cells receive rhythmic, inhibitory signals from cells in the thalamic reticular nucleus (RE) [202, 124]. The properties of the T-type  $\text{Ca}^{2+}$  current in RE cells are different, with the cells requiring *depolarisation* to burst, rather than hyperpolarisation (as is the case for TC cells). Modelling studies have considered closed, *two-layer* circuits where RE cells receive excitatory input from TC cells [234]. Numerical simulation carried out by Rinzel et al. (1998) [178] of connected networks of TC cells, with purely inhibitory synaptic connectivity demonstrates the possibility of information propagation through different types of travelling waves: smoothly propagating

and lurching waves, in which waves propagate in a saltatory fashion. This *one-layer* model is in the spirit of the Andersen-Eccles conjecture discussed above, and is obtained by considering the net effect on TC cells in the two-layer model. The RE loop is modelled indirectly, through considering an overarching TC-to-TC loop; an illustration of this inhibitory TC-to-TC loop is shown on the right of Figure 2.14. In the literature, the network model is reduced to track the envelope of the LTS (as opposed to individual spikes), and smoothly propagating waves may be analysed using singular perturbation methods [234]. However, this approach does not easily allow for the determination of solution stability and bifurcations. Therefore, it is of interest to seek models of sub-cortical tissues – in particular, the thalamus – while enabling us to obtain a better understanding of the mechanisms behind tissue dynamics by retaining analytical tractability. This is especially important given the thalamus acts as an intermediary gateway for motor and sensory signals arriving at the brain before passing to the cortex for processing [193], and is known for its role in the generation of thalamo-cortical rhythms [203].

The integrate-and-fire-or-burst (IFB) model [199, 175] was developed by adding a slow variable to a standard IF single cell model. Smith et al. [199] successfully fitted the model to experimental responses of thalamic neurons and noted that “*its simplicity makes it a candidate for large scale network simulations of thalamic functioning.*” The IFB model was posed on a network of cells by Huertas et al. (2005) [104], who studied thalamic response to visual drive. They demonstrated a rich variety of dynamics including bursting, and phase-locked bursting in the network model.

Bearing in mind that the neural field is an effective model of tissue *connectivity*, it may be augmented with a description capturing the important properties of thalamic tissue, namely rebound firing. This was done in [44] by ensuring the firing rate in the neural field model is a function of some voltage variable which tracks the envelope of bursting spikes, as is the case for the LTS (rather than only synaptic activity) for an IFB model. This is

reviewed in Section 5.2. The approach is sufficiently general to be able to include multiple slow ionic currents and is effective from an analytical standpoint for non-smooth, piecewise linear (PWL) models. A number of techniques from non-smooth dynamical systems theory are available if the sigmoidal gating variable dynamics, such as the steady state curves, and time-scales with respect to voltage, are taken to be PWL functions. In this study, they are taken to be piecewise-constant (PWC) for simplicity and this is sufficient, but it is noted that a sigmoidal function is better approximated by a PWL function. It should be noted that a PWC description of a sigmoid introduces a stronger class of non-smoothness than would be introduced with a PWL description. This is discussed in the Discussion. It is important in any case not to abuse methodologies from smooth dynamical systems theory when considering non-smooth models. Furthermore, one must always bear in mind that approximating a sigmoidal function by a PWC caricature is a first order approximation, and that this may alter dynamics in some cases. We show how network-level stability can be treated by considering *saltation operators*. These were originally derived for ODEs [154], but this approach has been extended here to include non-local spatial interactions. There is no requirement that space be continuous, though that is the state of affairs in this chapter.

In this chapter, we focus on spatially continuous, purely inhibitory non-local neural field models of thalamic tissue that support patterning via PIR. In Section 5.2, we review the augmented thalamic continuum neural field model, introduced in [44], and show how it is constructed to include a slow T-type  $\text{Ca}^{2+}$  current, before moving on to an analysis of the spatially synchronous periodic solution, which is constructed in Section 5.3. Its linear stability is analysed using tools from non-smooth dynamical systems in Section 5.4. This allows us to determine novel routes to patterning by considering the dynamical spatial patterns that emerge at instabilities to synchrony. Notably, this includes an instance of lurching waves, which is discussed in Section 5.5. The linear instability theory we develop is utilised

---

in 2D to determine the types of *planar* patterning in Section 5.6. We use the numerical bifurcation approaches developed for spatially extended periodic orbits in Chapter 3 in a more computational approach in Section 5.7, where by necessity, the smooth, sigmoidal model is treated.

The second half of this chapter is focused on spatially periodic travelling waves. The non-smooth nature of the model allows for an explicit wave construction in Section 5.8 and a calculation of the dispersion relation between the wavespeed and the spatial period of the wavetrain. The non-local input must be carefully treated, and we utilise Fourier analysis to aid in this. Wave stability is the focal point of Section 5.9. For the spatially extended travelling solutions under consideration, we follow a similar Evans function approach as considered for bump stability in Chapter 4. Travelling wave translation-invariance is shown in Section 5.10, before a summary and discussion conclude this chapter in Section 5.11.

## 5.2 THE AUGMENTED NEURAL FIELD MODEL

Since the advent of the neural field model, beginning with the work of Amari [5] and Wilson and Cowan [229], there has been a high level of success in cortical modelling. An example of this is cortical travelling waves; the neural field model successfully models waves of activity seen in vitro [46, 41]. Cortical activity is typically represented by a model that captures the non-local interactions provided by tissue at other locations in space. They are often variants of the form

$$Qu = \psi, \quad \psi = w \otimes f, \quad (5.1)$$

where  $Q$  is a temporal differential operator describing a level of synaptic processing and  $u$  represents synaptic activity. The term  $\psi$  describes a source of activity and consists of the non-local contributions from connected, firing tissue. This is effectively described by the spatial convolution of a connectivity kernel,  $w$ , with a firing rate function,  $f$ , describing firing tissue. The spatial convolution  $\otimes$  is defined by

$$(w \otimes f)(\mathbf{r}, t) = \int_{\Gamma} w(\mathbf{r} - \mathbf{r}') f(\mathbf{r}', t) d\mathbf{r}'. \quad (5.2)$$

where  $\Gamma$  is an integration domain. The standard neural field closes the equations by ensuring the firing rate function  $f$  is a function of  $u$ , so that  $f = f(u)$ . In a study of cortical tissue, this is often a sufficient model.

There is a strong dependence of dynamics on non-linear intrinsic currents which cannot be ignored if we are to consider a *successful* model of thalamic tissue (one which captures features seen experimentally such as the PIR phenomenon).  $I_T$  is incorporated into a neural field-style tissue connectivity as follows. Consider some voltage variable  $v$ , satisfying a Hodgkin-Huxley-type equation to track the currents of interest. The dynamics of  $v$  involve a sum of the relevant currents, which, importantly, includes  $I_T$ . We pose the

model on the continuous plane and consider the dynamics of the voltage envelope variable  $v = v(\mathbf{r}, t)$ ,  $\mathbf{r} = (x, y) \in \mathbb{R}^2$  as

$$C \frac{\partial}{\partial t} v(\mathbf{r}, t) = I_L(\mathbf{r}, t) + I_T(\mathbf{r}, t) + I_{\text{syn}}(\mathbf{r}, t). \quad (5.3)$$

This is the current-balance equation. The constant  $C$  describes the capacitance of neural tissue. The terms on the right-hand side represent the three main currents we include in the model: leak ( $I_L$ ), T-type  $\text{Ca}^{2+}$  ( $I_T$ ), and synaptic ( $I_{\text{syn}}$ ). These three currents are sufficient in capturing the PIR phenomenon.

The leak current takes the standard form  $I_L = -g_L(v - v_L)$ , with constant leak conductance  $g_L$  and leak reversal potential  $v_L$ . It captures the dynamics due to ions not explicitly modelled, such as  $\text{Cl}^-$  ions, and sets the resting potential of the cell.

The T-type  $\text{Ca}^{2+}$  current is given by [220, 178, 199, 44, 104, 148]

$$I_T = -g_T h m_\infty(v) (v - v_T), \quad (5.4)$$

where  $g_T$  and  $v_T$  are the constant conductance and reversal potential respectively, and  $m_\infty(v) = H(v - v_h)$  is the activation function, where  $H(\cdot)$  is the Heaviside step function. The parameter  $v_h$  sets the rebound threshold, at which the T-type  $\text{Ca}^{2+}$  current activates and deactivates. For a model of TC cells,  $v_h < v_L$ , while  $v_h > v_L$  for RE cells. Typical values for  $v_T$  are large and positive (relative to  $v_L$ ), such as 90mV [178] and 120mV [44]. There is an explicit dependence on the inactivating gating variable  $h$  whose dynamics are given by

$$\frac{\partial}{\partial t} h = \frac{h_\infty(v) - h}{\tau_h(v)}, \quad (5.5)$$

where  $h_\infty(v) = H(v_h - v)$ , and  $\tau_h(v) = \tau_h^- H(v - v_h) + \tau_h^+ H(v_h - v)$ . The dynamics of  $h$  can be succinctly described as

$$h \rightarrow \begin{cases} 0 \text{ at a rate } \tau_h^-, & \text{if } v > v_h, \\ 1 \text{ at a rate } \tau_h^+, & \text{otherwise.} \end{cases} \quad (5.6)$$

When  $v < v_h$ ,  $I_T = 0$  due to  $m_\infty(v)$ , and  $h$  saturates to 1. As  $v$  passes through  $v_h$  from below,  $I_T$  activates discontinuously. Although activation

and inactivation functions are typically sigmoidal in shape with respect to voltage [178, 44], we take the piecewise constant caricature here in order to facilitate the subsequent mathematical treatment that takes place throughout this chapter. This caricature is taken for the timescale of  $I_T$  too.

The synaptic current is modelled as  $I_{\text{syn}} = -g_{\text{syn}}u(v - v_{\text{syn}})$  where the conductance scaling,  $g_{\text{syn}}$ , and reversal potential,  $v_{\text{syn}}$ , are constant. The sign of  $v_{\text{syn}}$  relative to the resting potential,  $v_L$ , determines whether or not a synapse is excitatory ( $v_{\text{syn}} > v_L$ ) or inhibitory ( $v_{\text{syn}} < v_L$ ) [44]. We consider a population of inhibitory neurons with the parameter values  $v_L = -65\text{mV}$  and  $v_{\text{syn}} = -200\text{mV}$ , unless stated otherwise. The equations are closed by ensuring the firing rate is a function of the voltage envelope variable,  $v$ , [44] thus augmenting a standard neural field to provide an appropriate description of thalamic tissue. The functional form of  $f(v)$  is

$$f(v) = \frac{1}{\tau_R} H(v - v_{\text{th}}), \quad (5.7)$$

which caricatures a typical sigmoidal firing rate function in the limit of increasing steepness. (5.7) also arises by considering only the absolute refractory period in the firing response (2.31) of the IF model. The parameter  $\tau_R$  represents the absolute refractory period of thalamic tissue, with the maximal firing rate limited to  $1/\tau_R$ . By closing the equations in this way, the source  $\psi$  becomes

$$\psi(\mathbf{r}, t) = \int_{\Gamma} w(|\mathbf{r} - \mathbf{r}'|) f \circ v(\mathbf{r}', t) d\mathbf{r}'. \quad (5.8)$$

The connectivity function  $w$  is radially symmetric, described in polar coordinates with radial distance  $r > 0$  and angle  $\theta \in [0, 2\pi)$  as  $w(r, \theta) = w(r)$ , and takes the form

$$w(r) = w_0 \exp(-r/\sigma) (1 - \gamma \cos(\rho r/\sigma)). \quad (5.9)$$

The parameter  $\gamma$  is a measure of off-centred connectivity and is constrained to lie in the interval  $0 < \gamma \leq 1$ . The oscillatory nature is described by  $\cos(\rho r/\sigma)$ , with larger values of the parameter  $\rho$  corresponding to stronger

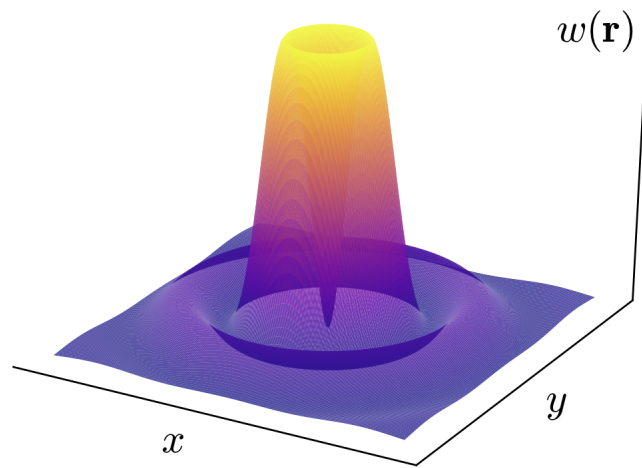


Figure 5.2.: Illustration of the radially symmetric off-centre connectivity kernel  $w(r)$  from (5.9) in 2D. Kernel parameters are as in Table 4 but with  $\rho = 3$ .

oscillatory connectivity. The parameter  $\sigma$  measures the spatial length scale, or *footprint*, of connectivity. The normalisation constant  $w_0$  is chosen to ensure the kernel is normalised to 1. In 1D,

$$w_0 = \frac{\rho^2 + 1}{2\sigma(\rho^2 + 1 - \gamma)}, \quad (5.10)$$

and in 2D,

$$w_0 = \frac{\rho^4 + 2\rho^2 + 1}{2\pi\sigma^2(\rho^4 + (\gamma + 2)\rho^2 - \gamma + 1)}. \quad (5.11)$$

See Appendix C.1 for a derivation of these results. Figure 5.2 illustrates the shape of the connectivity kernel in 2D. Connectivity strength increases as distance between tissue increases until some maximum connectivity at an intermediate distance. Beyond this, connection strength decays. From the discussion in Chapter 2, the post-synaptic response  $\eta$  is taken to be the  $\alpha$ -function (2.21), with the relevant differential operator given as

$$Q = \left(1 + \frac{1}{\alpha} \frac{\partial}{\partial t}\right)^2. \quad (5.12)$$

An equivalent integral representation of the synaptic response given by (5.1) is  $u = \eta * \psi$ , where  $*$  represents a temporal convolution (2.38). With this, the synaptic activity is given by

$$u(\mathbf{r}, t) = \int_0^t \eta(s)\psi(\mathbf{r}, t - s)ds. \quad (5.13)$$

Next, we make simplifying assumptions to remove the non-linearities in the equation for  $v$ . Given the large magnitudes of  $v_T$  and  $v_{\text{syn}}$  (approximately 150mV and 200mV respectively) it is assumed that  $v - v_T \simeq -v_T$  and  $v - v_{\text{syn}} \simeq -v_{\text{syn}}$ . The resultant forms of the relevant currents are

$$I_T = -g_T h H(v - v_h), \text{ and } I_{\text{syn}} = -g_{\text{syn}} u,$$

where the factors  $-v_T$  and  $-v_{\text{syn}}$  have been absorbed into  $g_T$  and  $g_{\text{syn}}$  respectively. These latter parameters no longer represent conductances, but rather scaled, signed strengths of interaction, with units mV mS / cm<sup>2</sup>. From this point onwards, we assume this to be the case. In all that follows, we rewrite the second-order variable  $u$  as two first-order variables with the auxiliary first-order variable

$$r(\mathbf{r}, t) = \left(1 + \frac{1}{\alpha} \frac{\partial}{\partial t}\right) u(\mathbf{r}, t). \quad (5.14)$$

To recapitulate the model in full, we have

$$C \frac{\partial}{\partial t} v(\mathbf{r}, t) = I_L + I_T + I_{\text{syn}}, \quad (5.15a)$$

$$\frac{\partial}{\partial t} u(\mathbf{r}, t) = \alpha(-u(\mathbf{r}, t) + r(\mathbf{r}, t)), \quad (5.15b)$$

$$\frac{\partial}{\partial t} r(\mathbf{r}, t) = \alpha \left( -r(\mathbf{r}, t) + \int_{\mathbb{R}^2} w(\mathbf{r} - \mathbf{r}') f(v(\mathbf{r}', t)) d\mathbf{r}' \right), \quad (5.15c)$$

$$\frac{\partial}{\partial t} h(\mathbf{r}, t) = \frac{h_\infty(v(\mathbf{r}, t)) - h(\mathbf{r}, t)}{\tau_h(v(\mathbf{r}, t))}, \quad (5.15d)$$

With all model ingredients now in place, we briefly describe how the PIR mechanism works in the model. Hyperpolarising input builds a latent current in hyperpolarised tissue ( $h$  increases), which activates when tissue potential passes through the rebound threshold. If tissue is held in a hyperpolarised state for a longer duration, then the effect of the rebound current is stronger. Upon activation of the rebound current, a depolarisation event occurs. If this is large enough, and tissue depolarises beyond the firing threshold, then firing events occur in which signals are sent to connected tissue. For the kernel used, these signal are purely inhibitory, providing a feedback mechanism to propagate rebound patterning across the domain.

Parameter	Value	Description
$g_L$	0.035 mS/cm <sup>2</sup>	Overall leak current conductance strength
$v_L$	-65.0 mV	Leak current reversal potential
$g_T$	8.4 mVmS/cm <sup>2</sup>	Scaled strength of $I_T$ interaction
$\tau_+$	100.0 ms	$I_T$ saturation time constant
$\tau_-$	20.0 ms	$I_T$ decay time constant
$v_{th}$	-35.0 mV	Firing threshold
$v_h$	-70.0 mV	Rebound threshold
$\alpha$	0.1 ms <sup>-1</sup>	Synaptic time constant
$C$	1.0 $\mu$ F/cm <sup>2</sup>	Membrane capacitance
$\tau_R$	5.0 ms	Firing strength scaling constant
$g_{syn}$	200.0 mVmS/cm <sup>2</sup>	Scaled strength of synaptic interaction
$\sigma$	0.02 cm	Length scale of spatial connectivity
$\gamma$	1.0	Measure of off-centre connectivity
$\rho$	2.0	Measure of oscillatory nature in connectivity

Table 4.: Standard parameter values. The upper half contains parameter values obtained from fits with experimental data [199]. The remaining parameter values are specific to the present study. Note that  $g_T$  and  $g_{syn}$  as defined here are not conductances but are compound parameters measuring the strength of currents. See text for details.

Table 4 shows the standard parameter values used in this chapter unless stated otherwise. The upper part contains parameter values obtained from fits to experimental data, while the lower part shows parameters chosen for the current study. In particular note the choice of  $\sigma = 0.02$  cm [178] capturing the small length-scale of thalamic tissue.

### 5.3 CONSTRUCTION OF PERIODIC SPATIAL SYNCHRONY

Neural tissue often exhibits synchronous behaviour [215, 214, 24]; we begin our study of the thalamic neural field model (5.15) with an investigation of synchrony. For convenience, we collect the dynamical variables of the

model in the state vector  $z = (v, u, r, h)$ . The simplest type of synchrony may be given by the homogeneous steady state, where  $z(\mathbf{r}, t) = z_0$  for some constant state vector  $z_0$ , for all  $\mathbf{r} \in \Gamma$ , and all  $t > 0$ . For  $v_h < v_L < v_{th}$ ,  $z_0 = (v_L, 0, 0, 0)$  and is stable to small perturbations by the way the PIR mechanism works. By this, we mean that  $h$  only increases if  $v < v_h$ , and if  $v_L > v_h$ , then a small perturbation will not result in  $v < v_h$ . Therefore, no synaptic activity causing movement away from the homogeneous steady state occurs in this case. A direct stability analysis may be carried for the parameters in Table 4 which shows that all eigenvalues are negative (not shown here), thus indicating the homogeneous steady state is indeed stable.

We begin our analytical treatment of the model (5.15) in earnest by constructing the temporally periodic spatially synchronous solution, given by  $z(x, t) = z(t)$  for all  $x \in \mathbb{R}$ , with the property  $z(t) = z(t + T)$ , for some  $T > 0$ . We choose here to present the following analysis in 1D, however the corresponding 2D analysis is nearly identical, with differences pointed out as and when they occur.

With the spatially-independent ansatz, the full space-time model (5.15), reduces to the non-smooth, piecewise linear system of 4 ODEs given by

$$C \frac{d}{dt} v = -g_L(v - v_L) - g_T h H(v - v_h) - g_{\text{syn}} u, \quad (5.16a)$$

$$\frac{d}{dt} u = \alpha(-u + r), \quad (5.16b)$$

$$\frac{d}{dt} r = \alpha \left( -r + \frac{\bar{w}}{\tau_R} H(v - v_{th}) \right), \quad (5.16c)$$

$$\frac{d}{dt} h = \frac{h_\infty(v) - h}{\tau_h(v)}, \quad (5.16d)$$

where

$$\bar{w} = \int_{-\infty}^{\infty} w(|y|) dy \quad (5.17)$$

is the normalisation of  $w$ . For all figures, we take  $\bar{w} = 1$  but leave it as a general constant in theoretical calculations. Figure 5.3 shows an illustration of the connectivity kernel,  $w(x)$ , in 1D (left panel). Coupling is *off-centre*, in which interaction strength with tissue in the immediate vicinity of the origin is small, grows to some maximum at an intermediate distance, and

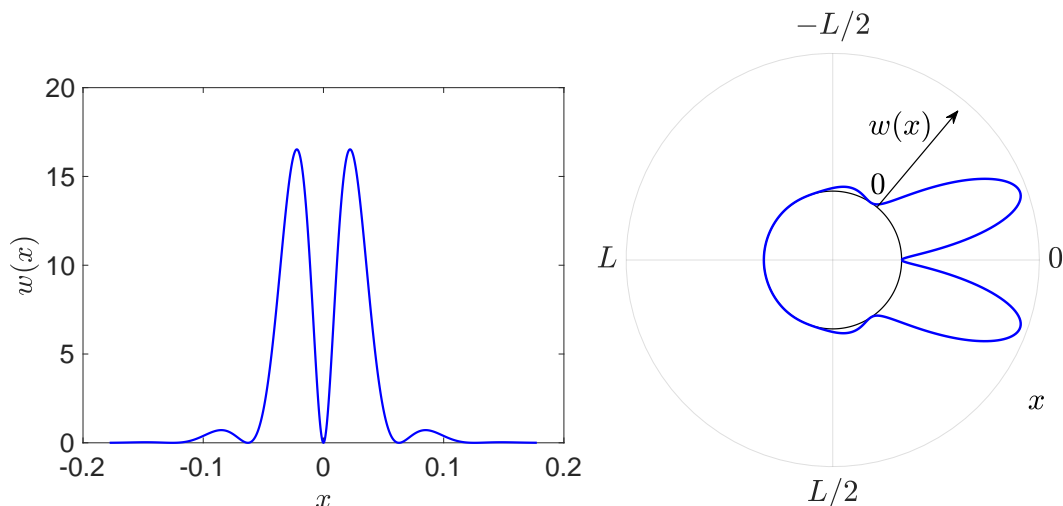


Figure 5.3.: The 1D kernel  $w(x) = w_0 e^{-|x|/\sigma} (1 - \gamma \cos(\rho x/\sigma))$ ,  $x \in \mathbb{R}$  (left), normalised to 1, with  $w_0$  given by 5.10. The periodic extension of  $w(x)$  (blue) on the  $2L$ -periodic ring  $[-L, L]$  is illustrated on the right. Coupling is off-centre with kernel parameters as in Table 4.

decays away for large distances. When posed on a ring with periodic boundary conditions, we define the kernel by periodic extension on the domain  $[-L, L]$ . This is illustrated in Figure 5.3 (right panel) on the  $2L$ -periodic ring, with distance between neurons given outside, and the strength of connectivity for a given distance shown by the relative height of the blue curve at the appropriate angle.

The dynamics of (5.16) changes discontinuously at the two Heaviside-induced switching manifolds  $v = v_h$  and  $v = v_{th}$ . They partition phase space into three distinct regions: (i)  $v < v_h$ , (ii)  $v_h < v < v_{th}$ , (iii)  $v > v_{th}$ . This is a PWL system; away from the switching manifolds, the functions  $f$ ,  $h_\infty$  and  $\tau_h$  are PWC, resulting in a PWL linear model. Thus, away from switching events, (5.16) can be solved to obtain closed form solutions as

follows. Firstly, we explicitly give the equations in each region. In region (i),

$$C \frac{dv}{dt} = -g_L(v - v_L) - g_{\text{syn}}u, \quad (5.18a)$$

$$\frac{du}{dt} = \alpha(-u + r), \quad (5.18b)$$

$$\frac{dr}{dt} = -\alpha r, \quad (5.18c)$$

$$\frac{dh}{dt} = \frac{1-h}{\tau^+}, \quad (5.18d)$$

in region (ii),

$$C \frac{dv}{dt} = -g_L(v - v_L) - g_T h - g_{\text{syn}}u, \quad (5.19a)$$

$$\frac{du}{dt} = \alpha(-u + r), \quad (5.19b)$$

$$\frac{dr}{dt} = -\alpha r, \quad (5.19c)$$

$$\frac{dh}{dt} = -\frac{h}{\tau^-}, \quad (5.19d)$$

and in region (iii),

$$C \frac{dv}{dt} = -g_L(v - v_L) - g_T h - g_{\text{syn}}u, \quad (5.20a)$$

$$\frac{du}{dt} = \alpha(-u + r), \quad (5.20b)$$

$$\frac{dr}{dt} = \alpha \left( -r + \frac{\bar{w}}{\tau_R} \right), \quad (5.20c)$$

$$\frac{dh}{dt} = -\frac{h}{\tau^-}. \quad (5.20d)$$

In each case, the dynamics is linear and so is easily solved for an initial state  $z(0) = (v_h, u_0, r_0, h_0)$  to give an explicit solution  $z(t)$ . By demanding  $T$ -periodicity and continuity of solutions, we find the periodic solution satisfying (5.16). The explicit formula for the solution is rather cumbersome though, and, as such, is not written explicitly here. Instead, the resultant periodic orbit describing spatial synchrony is shown in Figure 5.4. It is characterised by seven unknowns: the times-of-flight  $\Delta_i$ ,  $i = 1, \dots, 4$ , describing the time spent in each partition of phase space, and the three unknowns in the initial state,  $u_0, r_0, h_0$ . These are found by demanding periodicity and

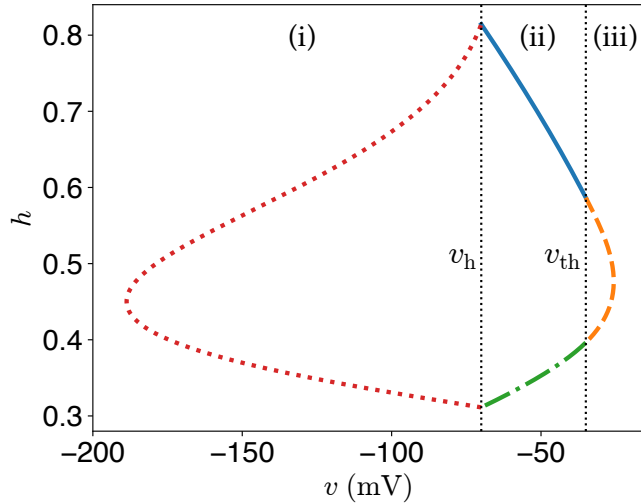


Figure 5.4.: Synchronous period-1 orbit in the  $(v, h)$ -plane. Different colours (line styles) indicate parts of the orbit between switching events. The dotted black lines represent the switching manifolds at  $v_h$  and  $v_{th}$ , with regions (i)-(iii) denoted. Parameter values are as in Table 4.

continuity in the solution. The following seven constraints characterise the sequence of switching events and periodicity of the solution,

$$\begin{aligned}
 v(T_1) &= v_{th}, & u(T_4) &= u_0, \\
 v(T_2) &= v_{th}, & r(T_4) &= r_0, \\
 v(T_3) &= v_h, & h(T_4) &= h_0, \\
 v(T_4) &= v_h,
 \end{aligned} \tag{5.21}$$

where  $T_i$ ,  $i = 1, \dots, 4$ , is the time of the  $i$ th switching event and  $T = T_4$  is the temporal period of the solution. The absolute switching times,  $T_i$ , are related to the times-of-flight,  $\Delta_i$ , by

$$T_i = \sum_{j=1}^i \Delta_j.$$

Solving (5.21) for the seven unknowns  $\Delta_i$ ,  $i = 1, \dots, 4$ ,  $u_0$ ,  $r_0$ , and  $h_0$  completes the construction of the spatially synchronous periodic orbit.

The temporal origin is shown at the beginning of the blue line in Figure 5.4, where  $v(0) = v(T_4) = v_h$ , and corresponds to the state of the system

just after reaching the rebound threshold,  $v = v_h$ , from  $v < v_h$ . At this instant in time,  $h$  is maximal, so the discontinuous activation of the rebound current will have a strong impact on the dynamics of  $v$ . From this point onwards this is seen, and the system evolves in region (ii) from initial conditions  $(v_h, u_0, r_0, h_0)$ . As  $t$  increases, the orbit follows the blue line with  $v$  continuing to increase, while  $h$  decreases. At  $t = T_1$ ,  $v = v_{th}$ , at which point, all tissue fires in synchrony. The dynamics switch to those of region (iii) denoted by the orange line. The dynamics in  $r$  differ from those in region (ii). The addition of a drive in the equation for  $r$  generates synaptic activity. As  $t$  continues to increase,  $v$  reaches its maximum and then begins to decrease (a consequence of  $h$  becoming smaller and  $v$  being much larger than  $v_L$  and  $v_{syn}$ ), until  $v(T_2) = v_{th}$ . Following this, the dynamics switch back to region (ii), with the dynamics in  $r$  reverting back to decay. Due to the finite time-to-peak in the spread of synaptic activity,  $u$  continues to increase for a short time after firing stops.  $v$  continues to decrease until  $v(T_3) = v_h$ , at which point the dynamics enter region (i).  $I_T$  switches off, while  $h$  begins to saturate to one. During this phase,  $v$  is driven towards  $v_{syn}$  due to the action of the elevated  $u$ , before beginning to increase back towards rest, until  $v(T_4) = v_h$ . This completes a full period. Subsequently, the behaviour described here repeats periodically. The orbit is continuous in time. Although jumps exist within the vector field, resulting in non-smoothness in the derivative of the solution, there are no jumps in the solution.

The periodic orbit exhibits bistability with the spatially homogeneous steady state, the latter of which can be shown to be stable via a standard linear stability analysis, for the parameter regime of Figure 5.4. However, given a knowledge of how the rebound mechanism works, the spatially homogeneous steady state,  $z_0 = (v_L, 0, 0, 0)$ , existing in region (ii) ( $v_h < v_L < v_{th}$ ), is clearly stable to small perturbations, since these are not large enough to provide enough hyperpolarisation required to drive the PIR mechanism. This situation may change for a parameter regime where  $v_{th} \simeq v_L \simeq v_h$ .

---

The synchronous periodic orbit solution does not arise via a Hopf bifurcation from a steady state as is typical, but exists as a stand-alone solution due to the PIR mechanism.

## 5.4 LINEAR STABILITY OF PERIODIC SPATIAL SYNCHRONY

### 5.4.1 Local Saltation Approach

We are now in a position to analytically determine the linear stability of the periodic orbit. This is a non-trivial task due to the non-smooth nature of the model. Discontinuities in the vector field induce discontinuities in the perturbations which must be properly treated. This is achieved using saltation operators; these are tools used in non-smooth dynamical systems to map perturbations across discontinuities in solutions or vector fields [154]. The synchronous orbit constructed in the previous section is continuous, with discontinuities present in the vector field; these are referred to as Filippov-type discontinuities in the language of non-smooth dynamical systems [133] (a Type 2 discontinuity in Table 1).

Consider a perturbation  $\delta z(x, t)$  around the synchronous periodic orbit solution  $z(t)$ . Over one period, the periodic orbit trajectory passes through switching manifolds<sup>1</sup> a total of four times. Therefore, four saltation matrices are required to map perturbations across switching events over a single period. The saltation matrices take the form  $K_i \in \mathbb{R}^{4 \times 4}$ ,  $i = 1, \dots, 4$ , and act such that

$$\delta z(x, T_i^+) = K_i \delta z(x, T_i^-),$$

where  $\delta z(x, T_i^\pm) = \lim_{\epsilon \searrow 0} \delta z(x, T_i \pm \epsilon)$  (this is the value of the perturbations *just after* and *just before* the periodic orbit hits a switching manifold).

The model (5.15) has a mixture of local and *non*-local dynamics, therefore we determine the components of  $K_i$ ,  $i = 1, \dots, 4$ , via two separate approaches that are able to deal with each of these types of dynamics. For

---

<sup>1</sup> A switching manifold separates phase space into two regions, with distinct dynamics on either side.

the rows of  $K_i$ ,  $i = 1, \dots, 4$ , pertaining to *local* dynamics,<sup>2</sup> that is  $\delta v(x, T_i^+)$ ,  $\delta u(x, T_i^+)$  and  $\delta h(x, T_i^+)$ , we employ standard approaches from non-smooth dynamical systems [154] as outlined in Section 2.8. Then for the dynamical system  $dz/dt = F(z)$ , the entries for  $\delta v$ ,  $\delta u$  and  $\delta h$  correspond to the first, second and fourth row of

$$K_i = I_4 - \frac{(F_i^- - F_i^+)(\nabla g)^T}{(\nabla g) \cdot F_i^-}, \quad i = 1, \dots, 4, \quad (5.22)$$

where  $F_i^\pm$  denotes the vector field either side of the  $i$ th switching event as  $F_i^\pm = \lim_{\epsilon \searrow 0} F(z(T_i \pm \epsilon))$  (as  $\epsilon$  approaches zero *from above*), and  $I_n$  denotes the  $n \times n$  identity matrix. The indicator function  $g$  characterises the occurrence of switching events at time  $T$  by  $g(z(T)) = 0$  [159]; it parameterises the switching manifolds and is either  $g(z) = v - v_{\text{th}}$  or  $g(z) = v - v_h$ , resulting in  $\nabla g = (1, 0, 0, 0)^T$  in either case. The derivation of the local saltation matrix (5.22) is shown in Appendix C.2.1.

#### 5.4.2 Non-local Saltation Approach

The non-local character of the model enters the saltation matrices in the row corresponding to the mapping of  $\delta r$  across a switching manifold. This is due to the presence of the non-local integral term, summing activity from across the domain, in the evolution equation for  $r$  in (5.15). Starting from the equation for  $r$  in (5.15),

$$\frac{\partial}{\partial t} r(x, t) = \alpha \left( -r(x, t) + \int_{-\infty}^{\infty} w(|y|) f(v(x - y, t)) dy \right), \quad (5.23)$$

we linearise about the steady state  $z(t)$  by letting  $z(x, t) = z(t) + \delta z(x, t)$ , to obtain an evolution equation for  $\delta r$  as

$$\frac{\partial}{\partial t} \delta r(x, t) = \alpha \left( -\delta r(x, t) + f'(v(t)) \int_{-\infty}^{\infty} w(|y|) \delta v(x - y, t) dy \right). \quad (5.24)$$

---

<sup>2</sup>The terms associated with local dynamics are those which affect the evolution of the system at the same point in space. In (5.15), this includes every term except the integral term in the evolution equation for  $r$ .

Making the ansatz  $\delta z(x, t) = e^{ikx} \delta z(t)$ , (5.24) reduces to

$$\frac{d}{dt} \delta r(t) = \alpha \left( -\delta r(t) + f'(v(t)) \delta v(t) \int_{-\infty}^{\infty} w(|y|) e^{-iky} dy \right). \quad (5.25)$$

Here we recognise the form of the Fourier transform

$$\widehat{w}(k) = \int_{-\infty}^{\infty} w(|y|) e^{-iky} dy,$$

and so obtain the evolution equation for  $\delta r$  incorporating a notion of non-locality as

$$\frac{d}{dt} \delta r(t) = \alpha \left( -\delta r(t) + f'(v(t)) \delta v(t) \widehat{w}(k) \right). \quad (5.26)$$

The functional form of  $f(v)$  gives  $f'(v(t)) = \delta(v(t) - v_{\text{th}}) / \tau_R$ . It is noted here that the delta function exists underneath an implicit integral in time given by the derivative on the left-hand side. So, by a formal property of delta-functions (“composition with a function”), (5.26) becomes

$$\frac{d}{dt} \delta r(t) = \alpha \left( -\delta r(t) + \frac{\widehat{w}(k) \delta v(t)}{\tau_R} \sum_{i=1}^2 \frac{\delta(t - T_i)}{|\dot{v}(T_i)|} \right), \quad (5.27)$$

where  $t = T_i$ ,  $i = 1, 2$ , are the times at which  $v(t) = v_{\text{th}}$ . From (5.27), we see that  $\delta r(t)$  changes discontinuously about  $T_i$ ,  $i = 1, 2$ , according to

$$\delta r(T_i^+) = \delta r(T_i^-) + \frac{\alpha \widehat{w}(k)}{\tau_R |\dot{v}(T_i)|} \delta v(T_i^-), \quad i = 1, 2, \quad (5.28)$$

at the switching times  $t = T_i$ ,  $i = 1, 2$ . Thus, the non-local saltation rule is given by (5.28): it relates  $\delta r(t)$  after switching events, at time  $T_i^+$  to the perturbations before switching events, at time  $T_i^-$ , and contains the necessary information to fill in the *non-local* entries in the saltation matrices. These are the prefactors that multiply  $\delta v(T_i^-)$ ,  $i = 1, 2$ . At times  $t = T_i$ ,  $i = 3, 4$ ,  $\delta r(t)$  is continuous as expected, since these switching times correspond to changes in the voltage and rebound dynamics rather than the synaptic and firing dynamics. Explicitly, non-locality is only present in  $K_1$  and  $K_2$ , with the relevant non-local entries given by

$$K_1^{(3,1)} = \frac{\alpha \widehat{w}(k)}{\tau_R |\dot{v}(T_1^-)|}, \quad (5.29a)$$

$$K_2^{(3,1)} = \frac{\alpha \widehat{w}(k)}{\tau_R |\dot{v}(T_2^-)|}, \quad (5.29b)$$

where  $K_i^{(j,k)}$  denotes the  $(j,k)$ th entry of the  $i$ th saltation matrix. Note the explicit dependence of  $K_1$  and  $K_2$  on the wavenumber  $k$ , purely through  $\widehat{w}(k)$ . All other entries to all four saltation matrices,  $K_i$ ,  $i = 1, 2, 3, 4$ , are local, and are found using (5.22). The saltation approach is valid for non-continuous discrete networks too, as shown in [47, 159].

### 5.4.3 Non-smooth Periodic Orbit Stability

The complete saltation matrices are given explicitly as

$$K_1(k) = \begin{pmatrix} 1 & 0 & 0 & 0 \\ 0 & 1 & 0 & 0 \\ \frac{\alpha \widehat{w}(k)}{\tau_R \dot{v}(T_1^-)} & 0 & 1 & 0 \\ 0 & 0 & 0 & 1 \end{pmatrix}, \quad (5.30a)$$

$$K_2(k) = \begin{pmatrix} 1 & 0 & 0 & 0 \\ 0 & 1 & 0 & 0 \\ -\frac{\alpha \widehat{w}(k)}{\tau_R \dot{v}(T_2^-)} & 0 & 1 & 0 \\ 0 & 0 & 0 & 1 \end{pmatrix}, \quad (5.30b)$$

$$K_3 = \begin{pmatrix} 1 + \frac{g_{\Gamma} h(t_3^-)}{C \dot{v}(T_3^-)} & 0 & 0 & 0 \\ 0 & 1 & 0 & 0 \\ 0 & 0 & 1 & 0 \\ \frac{1/\tau^+ - h(T_3^+)/\tau^+ + h(T_3^-)/\tau^-}{\dot{v}(T_3^-)} & 0 & 0 & 1 \end{pmatrix}, \quad (5.30c)$$

$$K_4 = \begin{pmatrix} 1 - \frac{g_{\Gamma} h(T_4^-)}{C \dot{v}(T_4^-)} & 0 & 0 & 0 \\ 0 & 1 & 0 & 0 \\ 0 & 0 & 1 & 0 \\ \frac{-h(0)/\tau^- - 1/\tau^+ + h(T_4^-)/\tau^+}{\dot{v}(T_4^-)} & 0 & 0 & 1 \end{pmatrix}. \quad (5.30d)$$

Between switching events, the dynamics obeyed by the perturbations is linear, and satisfies  $\frac{d}{dt}\delta z(t) = J\delta z(t)$ , where  $J$  is the piecewise constant matrix

$$J = \begin{cases} J_1, & 0^+ \leq t \leq T_1^-, \\ J_2, & T_1^+ \leq t \leq T_2^-, \\ J_3, & T_2^+ \leq t \leq T_3^-, \\ J_4, & T_3^+ \leq t \leq T^-, \end{cases} \quad (5.31)$$

and

$$J_i = \begin{pmatrix} -g_L & -g_{\text{syn}} & 0 & -g_T \\ 0 & -\alpha & \alpha & 0 \\ 0 & 0 & -\alpha & 0 \\ 0 & 0 & 0 & -1/\tau^- \end{pmatrix}, \quad i = 1, \dots, 3, \quad (5.32a)$$

$$J_4 = \begin{pmatrix} -g_L & -g_{\text{syn}} & 0 & 0 \\ 0 & -\alpha & \alpha & 0 \\ 0 & 0 & -\alpha & 0 \\ 0 & 0 & 0 & -1/\tau^+ \end{pmatrix}. \quad (5.32b)$$

All saltation matrices  $K_i$ , all times of flight  $\Delta_i$ , and the in-region vector fields for the perturbations,  $J_i$ ,  $i = 1, \dots, 4$ , describing the evolution of perturbations in each region are known. This is all of the information required to calculate the fundamental matrix (*monodromy matrix*) mapping an initial perturbation to its value after one period. The eigenvalues (multipliers) of the monodromy matrix determine periodic orbit stability. The linear nature of the model away from the switching events means that perturbations may be propagated forwards using matrix exponentials away from the two switching manifolds.

Given some perturbation  $\delta z(t)$  with initial value  $\delta z(0)$ , its value after a period  $T$  is given by  $\delta z(T) = \Psi(k)\delta z(0)$ , where the monodromy matrix is given by

$$\Psi(k) = K_4 \exp(J_4 \Delta_4) K_3 \exp(J_3 \Delta_3) K_2(k) \exp(J_2 \Delta_2) K_1(k) \exp(J_1 \Delta_1). \quad (5.33)$$

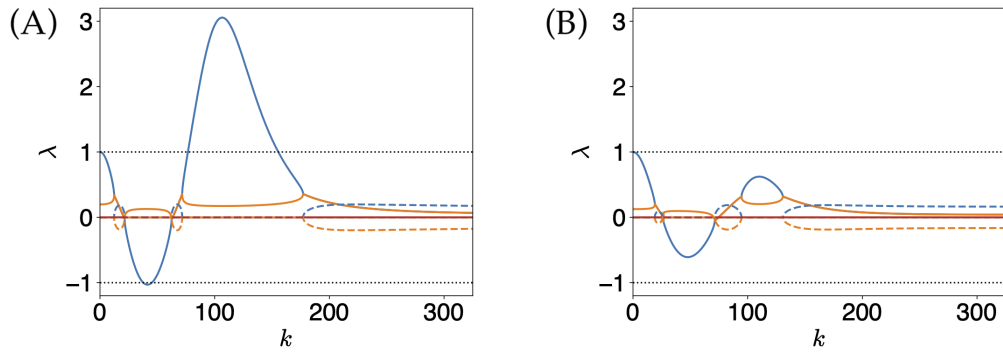


Figure 5.5.: Real (solid lines) and imaginary (dashed lines) parts of the four multipliers of  $\Psi(k)$  as a function of  $k$  in blue, orange, green and red, for two different parameter sets. The green and red eigenvalues are both effectively zero for all  $k$  (the red sits atop the green in these figures). The dotted black line marks the stability boundary at  $|\lambda| = 1$ . Parameter values are as in Table 4 with the exception of the following in (B):  $g_T = 12.6 \text{mVmS/cm}^2$ ,  $\gamma = 0.65$ .

We explicitly note the dependence of  $\Psi$  on  $k$  to highlight that periodic orbit stability is dependent upon the wavenumber of perturbation  $k$ . The saltation matrices  $K_1$  and  $K_2$  are functions of the wavenumber  $k$  through  $\hat{w}(k)$ , hence it is more precise to say that stability is dependent upon tissue connectivity.

The synchronous periodic orbit state is linearly stable if the multipliers,  $\lambda_i$ ,  $i = 1, \dots, 4$ , of  $\Psi(k)$  are contained within the unit disk *for all*  $k$  [125, 78] (excluding the trivial multiplier which exists with certainty for  $k = 0$  only). For spatially homogeneous perturbations ( $k = 0$ ), there is always a multiplier with value  $\lambda = 1$  corresponding to time translation invariance. The orbit can go unstable in three distinct ways as shown in Figure 3.3: (a) a multiplier passes through  $+1$  in a Fold of cycles-type bifurcation, (b) a multiplier passes through  $-1$  in a Flip-type bifurcation, and (c) a multiplier passes through the unit circle at  $e^{i\theta_0}$ ,  $\theta_0 \in [0, 2\pi)$ ,  $\theta_0 \neq 0, \pi$ , in a Neimark-Sacker-type bifurcation [125].

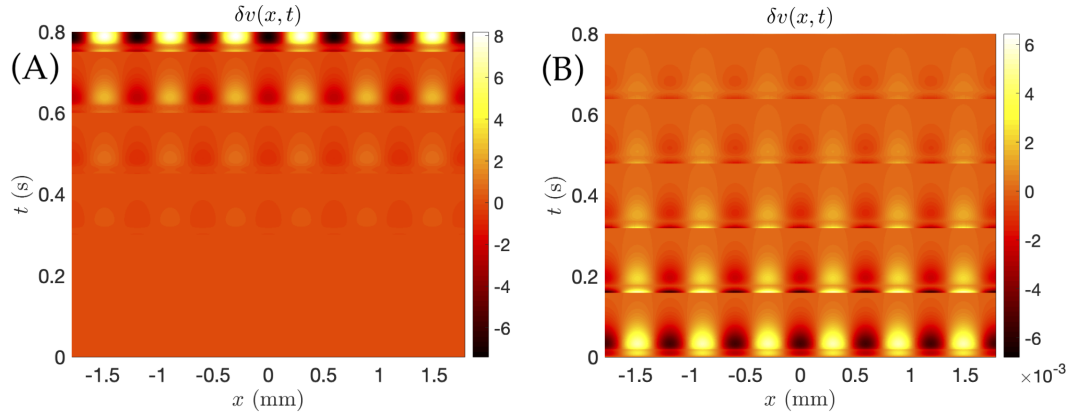


Figure 5.6.: Space-time plot of the perturbation  $\delta v(x, t)$  in mV when synchrony is linearly unstable (A) and stable (B). Parameters values are as in the corresponding panels in Figure 5.5.

In Figure 5.5, we plot the eigenvalues of  $\Psi(k)$  as a function of  $k$  for two different sets of parameter values, as described in the figure caption. In Figure 5.5A, the eigenvalue coloured blue is larger than 1 for a subset of wavenumbers,  $k \in (77, 155)$  (and beyond  $-1$  for  $k \in (38, 45)$ ) indicating that the synchronous solution is linearly unstable in this parameter regime. This is confirmed by direct numerical simulations, shown in Figure 5.6A, where we depict the spatio-temporal evolution of  $\delta v(x, t)$ . Starting simulations from a perturbed synchronous state with a wavenumber of  $k = 106$  and periodic boundary conditions, perturbations grow, as expected, based on the spectrum for this wavenumber. The perturbed pattern eventually destabilises into a standing pattern on top of the global bulk periodic oscillation which is indicative of the type of pattern seen beyond a  $+1$  instability. For the second set of parameter values, we observe in Figure 5.5B that the eigenvalues do not leave the unit disc for any  $k$ . In this case, the theory predicts the orbit is stable to small perturbations. This is illustrated via direct simulation shown in Figure 5.6B with  $k = 106$ , where an initial perturbation around the synchronous state decays to zero. When simulating numerically, these perturbations are scaled to the size of the domain to satisfy periodic boundary conditions.

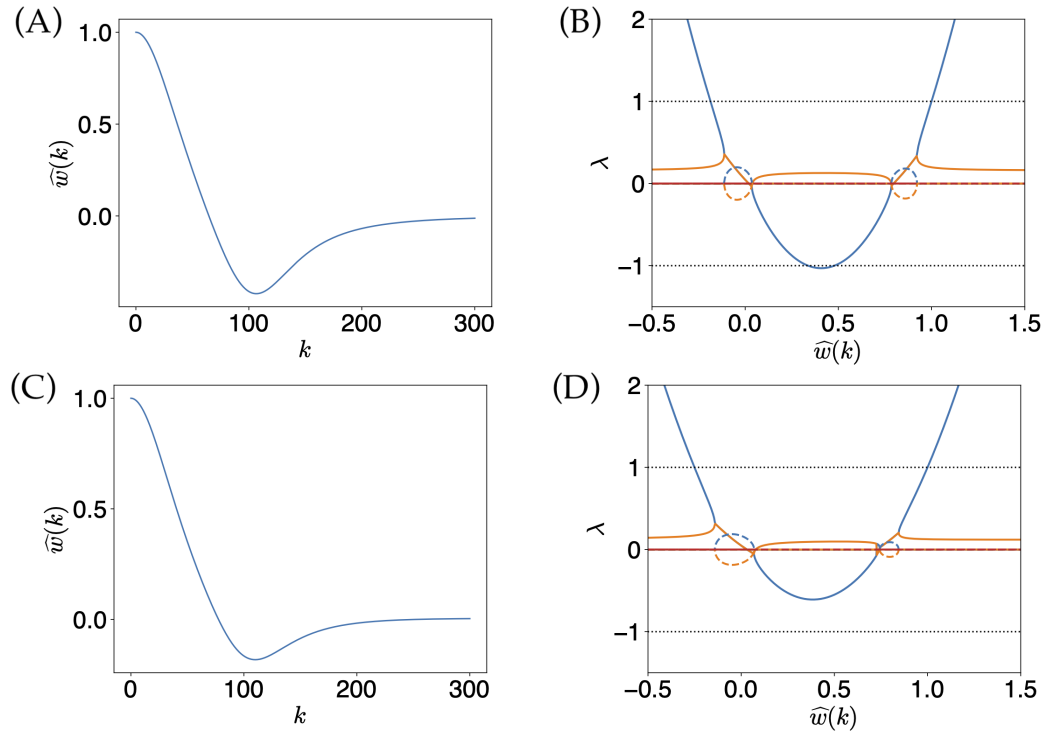


Figure 5.7.: Fourier transform (left) and eigenvalues of  $\Psi(k)$  as a function of  $\hat{w}(k)$  (right). Parameters for the top (bottom) row correspond to those in the left (right) panel of Figure 5.5.

#### 5.4.4 Connectivity-independent Stability

The propagator  $\Psi(k)$  depends on  $k$  through the Fourier transform  $\hat{w}(k)$  of the connectivity kernel, since the saltation matrices  $K_1(k)$  and  $K_2(k)$  depend on  $\hat{w}(k)$ . As a consequence, changing the connectivity,  $w(x)$ , can change the linear stability of the synchronous periodic orbit state. This is illustrated in Figure 5.7, where we plot the eigenvalues of  $\Psi(k)$  as a function of  $\hat{w}(k)$  for the two sets of parameter values in Figure 5.5. The connectivity kernels used are normalised to 1, that is  $\hat{w}(0) = 1$ . As  $k$  increases,  $\hat{w}(k) \rightarrow 0$ , by (5.34) and as shown in Figure 5.7. In the plots of  $\lambda$  vs.  $\hat{w}(k)$ , the excursion taken by the largest eigenvalue must begin at  $\hat{w}(k) = 1$  and end at  $\hat{w}(k) = 0$ . Thus, in this case, if the largest eigenvalue passes outside of the unit disc for  $0 < \hat{w}(k) < 1$ , then the periodic orbit will be unstable for the given

parameter set, regardless of the connectivity function. This is a powerful, *connectivity-independent* characterisation of stability.

If the values of  $\hat{w}(k)$  are such that the corresponding eigenvalues are inside the unit disc, then synchrony is stable. Therefore, given the Fourier transform of a specific kernel, we only need to consult the appropriate plot of  $\lambda_i$ ,  $i = 1, \dots, 4$ , as a function of  $\hat{w}(k)$  to infer linear stability of the synchronous state. As an example, consider the connectivity kernel (5.9) in 1D, with Fourier transform

$$\begin{aligned}\hat{w}(k) &= w_0 \left( a(k; \sigma, 0) - \frac{\gamma}{2} (a(k; \sigma, \rho) + a(k; \sigma, -\rho)) \right), \\ a(k; \sigma, \rho) &= \frac{2\sigma}{1 + (\rho - k\sigma)^2},\end{aligned}\tag{5.34}$$

where the calculation to obtain this is shown in Appendix C.1. For the parameter values as in Figure 5.5A,  $\hat{w}(k) \in (-0.4235, 1)$ , and see Figure 5.7A showing that  $\hat{w}(k)$  is bounded accordingly. We deduce from Figure 5.7B that synchrony is linearly unstable since for  $\hat{w}(k) \in (-0.4235, -0.18)$ , the blue eigenvalue exists outside of the unit disc beyond +1. This agrees with our previous result. On the other hand, the parameter values used in Figure 5.5B, for which synchrony was shown to be linearly stable, lead to the Fourier transform as shown in Figure 5.7C with  $\hat{w}(k) \in (-0.182, 1)$ . Then Figure 5.7D shows synchrony is stable since, for  $\hat{w}(k) \in (-0.182, 1)$ , all eigenvalues are shown to be inside the unit disc.

One point of interest is the small excursion of the blue eigenvalue beyond  $-1$  in Figure 5.7B. For this parameter set, any kernel with  $\gamma = 1$  as in Table 4 will be unstable to a small band of perturbations that pass beyond  $-1$ , since any connectivity satisfying the above properties must be normalised to 1 and decay to 0 as  $k \rightarrow \infty$ . Such a reasonable connectivity will have a smoothly varying Fourier transform, and so we see that to go from  $\hat{w}(k) = 1$  to  $\hat{w}(k) = 0$  smoothly in Figure 5.7B, the blue eigenvalue will always pass through  $-1$  for a small band of wavenumbers. This band can be seen in Figure 5.5A for  $k \in (38, 45)$ .

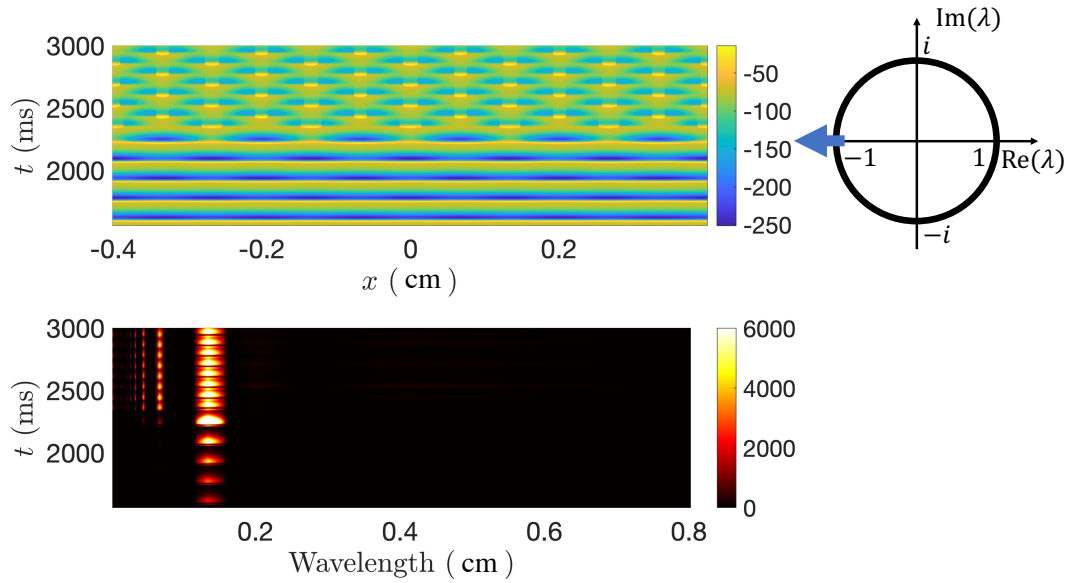


Figure 5.8.: Top: A blinking solution formed from a  $-1$  instability of synchrony ((b) in Figure 3.3). Bottom: The wavelength spectrogram for the solution in the top panel, showing the relative dominance of different spatial wavelengths for each solution through time. Parameters are as in Table 4 with  $\tau_R = 3$ , and the kernel parameter  $\gamma = 0.55$ . The perturbation applied to the initial condition has wavenumber  $k = 47$ .

In the case where an eigenvalue of  $\Psi(k)$  leaves the unit disc along the real axis at  $-1$  in a Flip-type instability, the synchronous solution breaks into standing oscillations in which a point in space fires on every other cycle, and the pattern on one cycle is shifted half a spatial cycle on the next temporal cycle; we denote this solution a “2-cycle”. This is shown in Figure 5.8 (upper panel), along with a spectrogram (lower panel) showing the emergent pattern to have a well-defined wavelength of around 0.18mm on each cycle.

Where an eigenvalue of  $\Psi(k)$  leaves the unit disc through  $+1$  in a Fold-type instability, then a standing pattern emerges which does not exhibit the off-cycle oscillatory behaviour shown by the emergent pattern in the case of a  $-1$  instability. The standing pattern exists on top of the bulk oscilla-

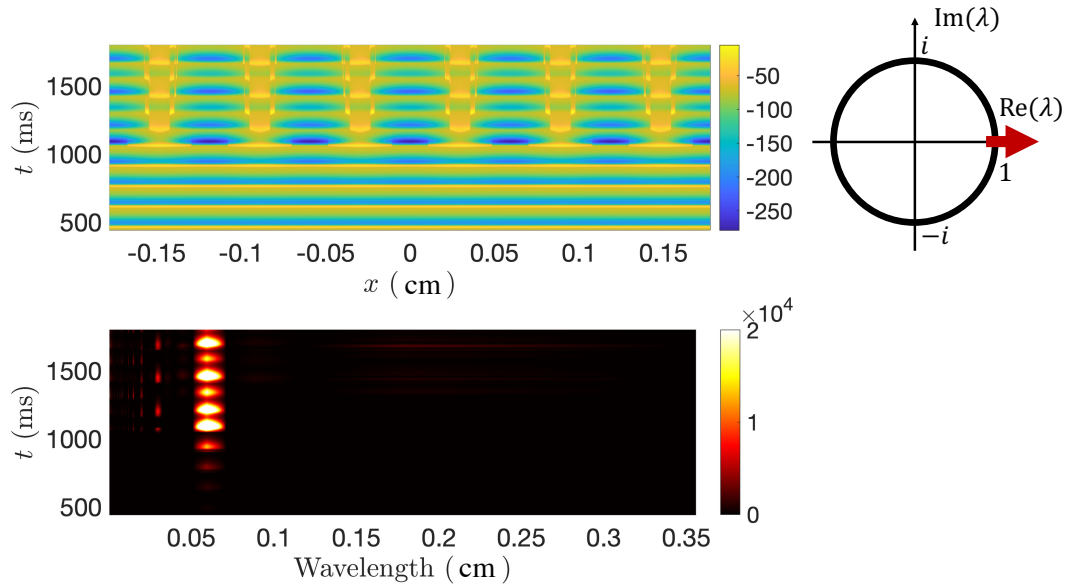


Figure 5.9.: Top: A standing solution formed from a  $+1$  instability of synchrony ((a) in Figure 3.3). Bottom: The wavelength spectrogram for the solution in the top panel, showing the relative dominance of different spatial wavelengths for each solution through time. Parameters are as in Table 4. The perturbation applied to the initial condition has wavenumber  $k = 106$ .

tions. This is shown in Figure 5.9 (upper panel) and is the instability that occurs when perturbing synchrony with a wavenumber from  $k \in (77, 155)$  in Figure 5.5. Indeed, numerical simulation has shown that this emergent standing pattern is not stable, and that it quickly breaks down into other solutions. Although this is not shown explicitly here, it can be inferred from the spectrogram (lower panel), where the power of the dominant wavelength becomes increasingly unsettled as time progresses.

In two spatial dimensions, the linear stability analysis for the synchronous periodic orbit is very similar. The only change when compared to the 1D analysis presented above is that  $\hat{w}(k)$  is replaced by the 2D Fourier transform

$$\hat{w}(\mathbf{k}) = \int_{\mathbb{R}^2} w(\mathbf{r}) e^{i\mathbf{k} \cdot \mathbf{r}} d\mathbf{r}, \quad (5.35)$$

with  $\mathbf{k} \in \mathbb{R}^2$ . For the radially symmetric kernel given by (5.9) we have that

$$\begin{aligned}\widehat{w}(k) &= w_0[g(k; \sigma, 0) - \gamma \operatorname{Re} g(k; \sigma, \rho)], \\ g(k; \sigma, \rho) &= 2\pi \frac{1 - i\rho}{\sigma[k^2 + (1 - i\rho)^2/\sigma^2]^{3/2}},\end{aligned}\tag{5.36}$$

where  $k = |\mathbf{k}|$ . The calculation showing this result is in Appendix C.1, and entails a contour integral to obtain  $g(k; \sigma, \rho)$ .

## 5.5 LURCHING WAVES

We have seen the patterns that emerge from the spatially synchronous periodic orbit when an eigenvalue escapes the unit disc through  $-1$  (period-doubling type) and  $+1$  (fold of cycles type). However, as stated earlier, a third way in which a periodic orbit can become unstable is when an eigenvalue passes through  $e^{i\theta}$ , where  $\theta \neq 0, \pi$  (Neimark-Sacker type) corresponding to a crossing with non-zero imaginary part. Using (5.9) as the connectivity function mimics the shape used by Rinzel et al. in [178], but its symmetrical nature excludes the possibility of obtaining a non-real instability, where eigenvalues cross the unit disc away from  $+1$  and  $-1$ . Therefore, an *asymmetric* connectivity function is now introduced as

$$w(x) = w_0 \begin{cases} e^{-a_1 x/\sigma}, & x > 0, \\ e^{a_2 x/\sigma}, & x \leq 0, \end{cases}\tag{5.37}$$

which has the Fourier transform

$$\widehat{w}(k) = w_0 \left( \frac{1}{a_1/\sigma + ik} - \frac{1}{-a_2/\sigma + ik} \right).\tag{5.38}$$

Both (5.37) and (5.38) are shown in Figure 5.10. The constant  $w_0$  is chosen so that  $w(x)$  is normalised to 1, yielding

$$w_0 = \frac{a_1 a_2}{\sigma(a_1 + a_2)}.\tag{5.39}$$

The propagator  $\Psi(k)$  depends on  $k$  *only* through the Fourier transform,  $\widehat{w}(k)$ , which, for the asymmetric kernel, now has a non-zero imaginary part

as a function of  $k$ , as shown in the right-hand panel of Figure 5.10. As a consequence, the eigenvalues of  $\Psi(k)$  for each  $k$  now have, in general, a non-zero imaginary part, and so Neimark-Sacker-type instabilities may occur. We complete our characterisation of the three types of instabilities that may occur from synchrony by considering the Neimark-Sacker-type instability.

Figure 5.11 shows the excursion of the two largest eigenvalues, to the stability problem for synchrony, in the complex plane. The larger of the two is shown in blue. It can clearly be seen that the eigenvalue crosses the unit disc at  $e^{i\theta}$ ,  $\theta = 0.8593 \dots \approx 7\pi/8$ , away from  $+1$  and  $-1$ . We see a wide range of wavenumbers outside the unit disc for this chosen parameter set. For  $k > 162$ , all eigenvalues are inside the unit disc. Thus the pattern that emerges at the instability, as shown in Figure 5.12 (top panel), is some amalgamation of waves with wavenumbers  $k < 162$ .<sup>3</sup> The emergent pattern is an instance of lurching waves – a hallmark solution of models of thalamic tissue, as first noted by Rinzel et al. (1998) [178]. The spectrogram (lower

<sup>3</sup> These are the wavenumbers such that the largest eigenvalue is outside the unit disc. See Figure 5.11.

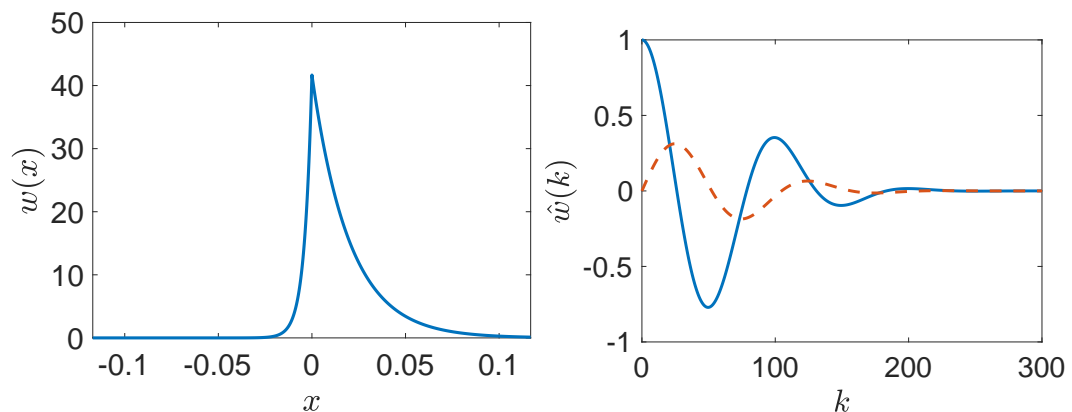


Figure 5.10.: The asymmetric connectivity kernel (5.37) (left) and its complex-valued Fourier transform (5.38) as a function of  $k$  (right) with real and imaginary parts shown in blue and orange respectively. Parameter values are  $\sigma = 0.02$ ,  $a_1 = 1$ ,  $a_2 = 5$ .

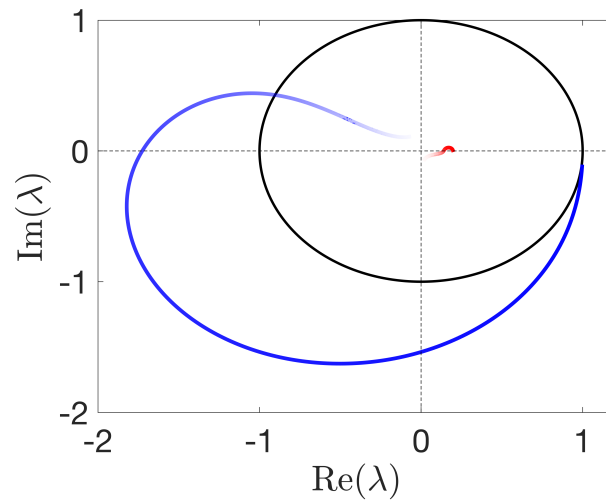


Figure 5.11.: The two non-zero eigenvalues of  $\Psi(k)$  for the asymmetric connectivity (5.37) shown in the complex plane in blue and red plotted parametrically as  $k$  varies from 0 to 600. As  $k$  increases, the transparency of each eigenvalue curve increases. The unit disc is the stability threshold and is shown in black. The largest eigenvalue enters the unit disc as  $k$  increases through  $k = 162$ . Parameters are as in Table 4, with the asymmetric connectivity (5.37), with kernel parameters as in Figure 5.10.

panel) demonstrates the large *wavelength : domain-size* ratio which is present in this pattern.

These waves have a well-defined wavespeed, and yet are not simply stationary solutions in the co-moving frame. Rather, they are *time-periodic* solutions in the co-moving frame. In this sense, structurally, from a wave-like-solutions point-of-view, these are akin to the travelling-wave periodic-orbit patterns discussed towards the end of Chapter 3. Lurching waves have been seen in a variety of different guises since their discovery. Rinzel et al. [178] showed a somewhat unstructured and disorganised pattern which propagated across the domain in a saltatory fashion. Following this, Yew et al. [234] illustrated the existence of highly “blocky” lurching waves, while others considered different clusters of cells firing separately, but with all

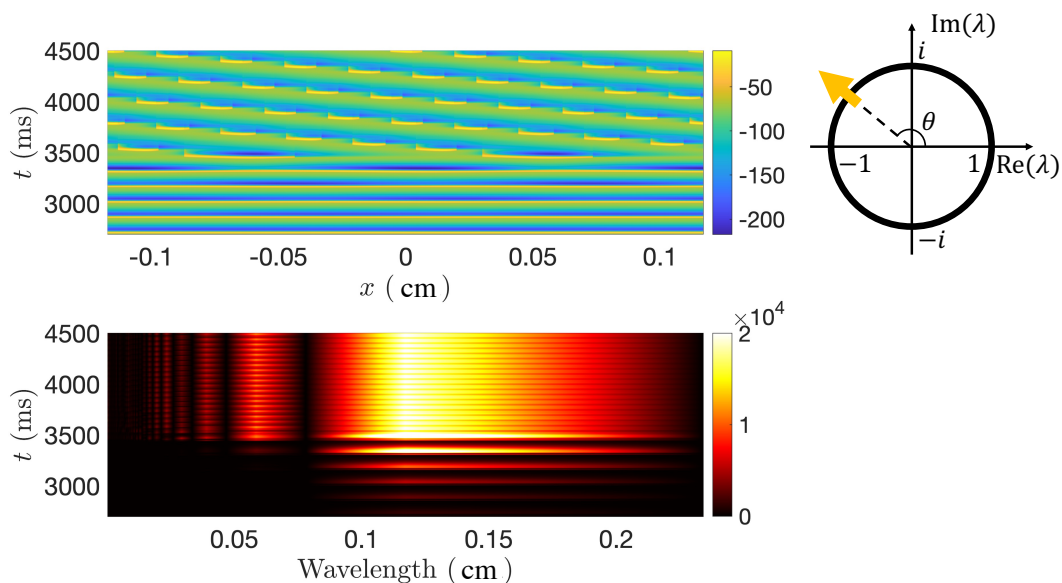


Figure 5.12.: Top: Lurching waves formed from a Neimark-Sacker type instability of synchrony ((c) in Figure 3.3). Bottom: The wavelength spectrogram for the solution in the top panel, showing the relative dominance of different spatial wavelengths for each solution through time. Parameters are as in Table 4, with the asymmetric connectivity (5.37), with kernel parameters as in Figure 5.10. Perturbation wavenumber is  $k = 161$ .

clusters conforming to a well-defined wavespeed [224]. The continuum patterns we have found are in the same spirit as these: oscillating clumps of activity moving with a well defined wavespeed.

This completes our characterisation of the three types of instabilities that may occur from synchrony.

## 5.6 PATTERNING IN TWO DIMENSIONS

As we have seen in 1D, the inclusion of rebound currents can lead to complex spatio-temporal patterns. This is shown to be the case in 2D as well, as

illustrated in Figure 5.13. Starting from a small bump of elevated synaptic activity in the centre of the domain of the form

$$u_0(x, y) = \frac{0.06}{\cosh(x) \cosh(y)},$$

where  $(x, y) \in \mathbb{R}^2$  denotes 2D space, patterns emerge where spatially separated and distinct parts of the domain fire in synchrony via the rebound mechanism. Intriguingly, the patterns generated by the  $I_T$  current here are qualitatively similar to those in [25], which originate from an  $I_h$  current. Patterns arising due to  $I_T$  appear to travel more clearly than those arising due to  $I_h$ . This suggests that generic rebound currents may be capable of producing non-trivial patterns consisting of complex structures.

The linear stability theory for periodic synchrony given in Section 5.4, is valid in 2D; the only change is that the Fourier transform of the connectivity, appearing in the saltation matrices  $K_1$  and  $K_2$ , is the 2D Fourier transform

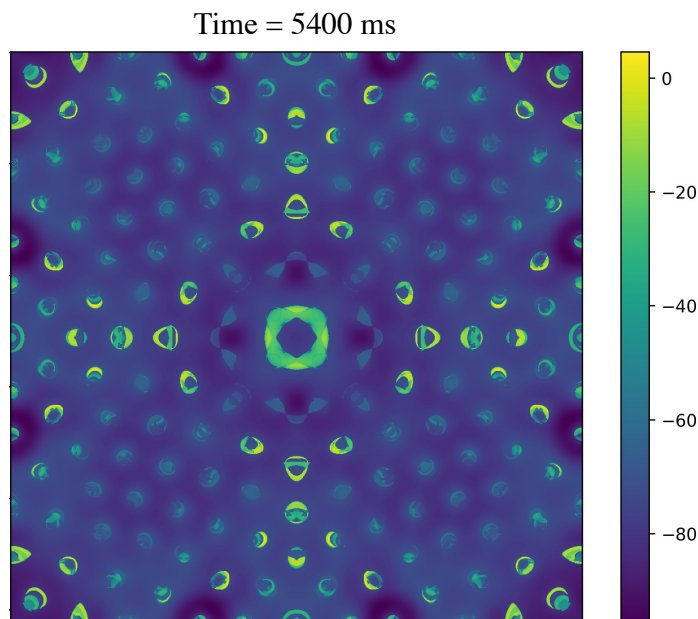


Figure 5.13.: Membrane potential  $v$  in mV on a two-dimensional domain of size  $0.38 \times 0.38 \text{ cm}^2$  with periodic boundary conditions, shown at a fixed time point. Simulations were performed on a grid with  $1024 \times 1024$  spatial points. Parameters are as in Table 4.

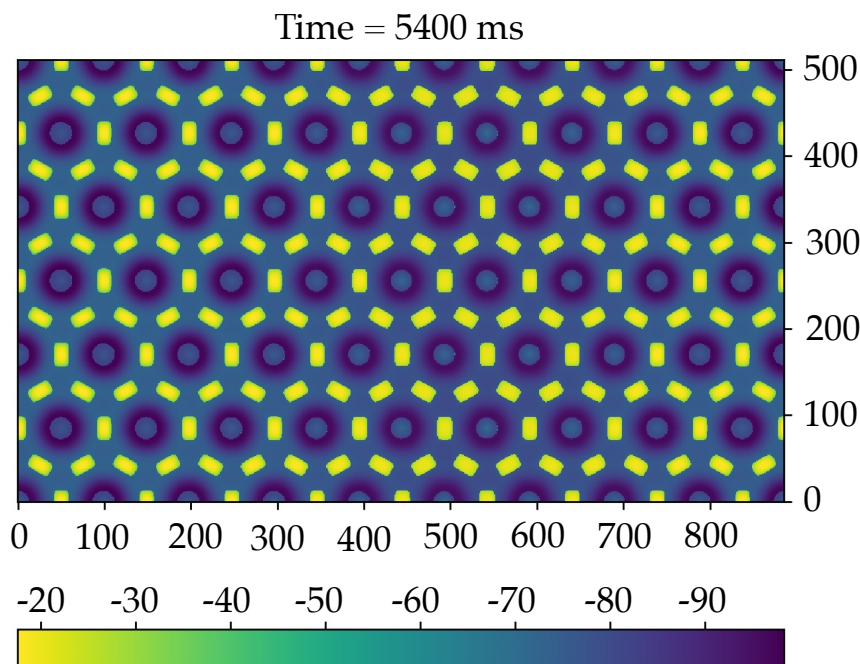


Figure 5.14.: Membrane potential  $v$  in mV at the point of a  $-1$  instability of the synchronous periodic orbit on a two-dimensional domain of size  $0.16 \times 0.27 \text{ cm}^2$  (rotated for illustrative purposes) with periodic boundary conditions. Simulations were performed on a grid with  $512 \times 886$  spatial points. Parameter values are as in Table 4, but with  $g_{\text{syn}} = 188.4 \text{ mVmS/cm}^2$ . Perturbation has wavenumber  $k = 49$ .

(5.35). For the connectivity function (5.9), the 2D Fourier transform is given by (5.36).

Utilising the linear stability theory in 2D, we may find the points of instability to the spatially synchronous periodic orbit, and the emergent patterns that result. Conducting numerical simulations when an eigenvalue crosses the unit disc along the real axis at  $-1$ , we observe a period-doubling-type pattern, shown in Figure 5.14, at the point of instability, much like what is seen in 1D in Figure 5.8. However, unlike in 1D, the planar pattern is transient before undergoing a secondary instability to highly complex spatio-temporal patterning of a similar qualitative nature as shown in Figure 5.13.

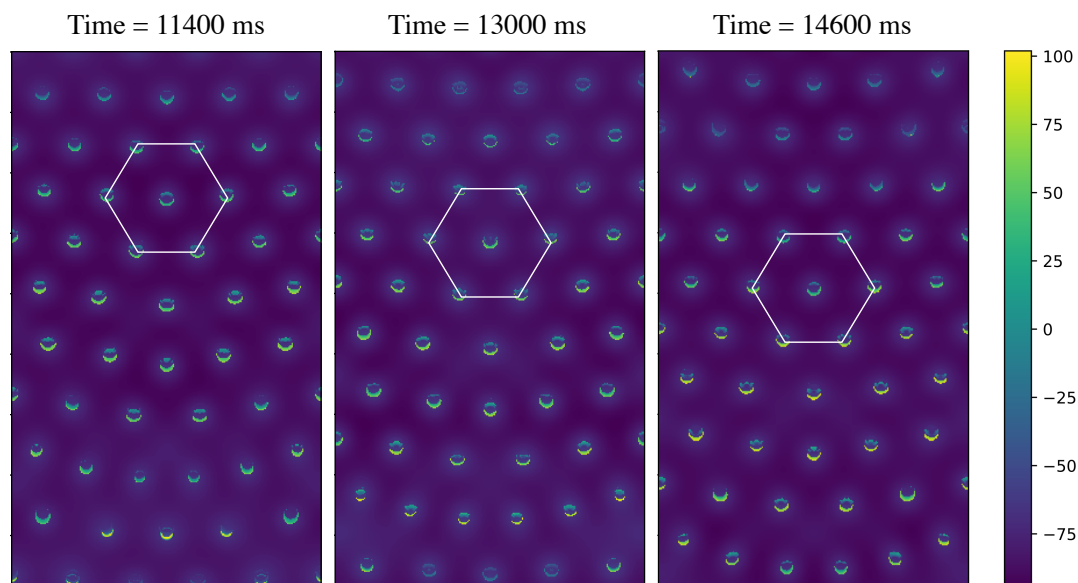


Figure 5.15.: Membrane potential  $v$  in mV on a two-dimensional domain of size  $0.16 \times 0.27 \text{ cm}^2$  with periodic boundary condition for three different time points. The white hexagon connects the same six spots of large membrane depolarisation, illustrating a moving hexagonal pattern. Simulations were performed on a grid with  $512 \times 886$  spatial points. Parameter values are as in Table 4, but with  $\alpha = 0.19$  and  $g_T = 20.3 \text{ mVmS/cm}^2$ .

More structured and regular travelling wave solutions are supported in 2D, as shown in Figure 5.15. These emerge from the perturbation of the synchronous temporally-periodic network state, with parameters poised just beyond a +1 instability. The emergent standing pattern quickly destabilises, much like in 1D. However, unlike in 1D, travelling hexagonal waves form. They travel across the domain as illustrated by the vertical translation of the white hexagon, tracking the same six spots of large membrane depolarisation through time. As the pattern travels, it oscillates. This behaviour is akin to the travelling wave periodic patterns discussed in Chapter 3, and thus is amenable to the continuation analysis detailed there. We have also seen such patterns emerge from a hexagonally patterned initial condition. These patterns do not arise via a Turing mechanism from a spatially homogeneous

---

steady state, but instead via the PIR mechanism elucidated throughout this chapter.

All 2D simulations were carried out in Python using an explicit Runge-Kutta (RK) 2-3 scheme (“RK23”) [23] via the `scipy.integrate.solve_ivp` package of ODE solvers. For the parameters used, the values for the relative tolerance and absolute tolerance of the solver were  $10^{-6}$  and  $10^{-10}$  respectively.

## 5.7 PARAMETER CONTINUATION

As we have seen in the previous sections of this chapter, a blend of linear theory and direct numerical simulation offers a powerful predictive capability in understanding patterning in the model. However, the linear stability is predictive *only about* spatial synchrony. The stability of patterns such as lurching waves, two-cycles, and travelling, oscillating hexagons is, as of yet, unknown. One of the reasons we were able to carry out an analysis of synchrony is due to its simple spatial nature as a dynamic solution – synchrony is governed by ODEs, as shown in (5.16). Here, we carry out a continuation of the ODE solution representing synchrony, and illustrate the similarities and differences with spatially extended synchrony, before using the tools developed in Chapter 3 in the continuation of the more complicated patterns mentioned above.

### 5.7.1 Synchrony

Figure 5.16 shows a periodic orbit continuation carried out for the solution shown in Figure 5.4 to the non-smooth ODE system (5.16). This is done by wrapping the seven conditions (5.21) characterising a periodic orbit inside a PALC routine and continuing the seven unknowns while varying a parameter. The fully non-smooth periodic orbit is then reconstructed using the newly found switching times and initial conditions for the new parameter set. The period  $T$  of the orbit is plotted against the bifurcation parameter  $\alpha$ .

The upper branch is stable until it turns around at a fold point at  $\alpha \approx 0.27$  where an eigenvalue leaves the unit disc at  $+1$ . This is shown by the black circle ( $\bullet$ ). The lower branch is unstable; solutions here occupy a “smaller” portion of phase space than on the stable upper branch, with the unstable orbit partitioning phase space into two basins of attraction for the stable steady state  $z = (v_h, 0, 0, 0)$  and the stable periodic orbit.

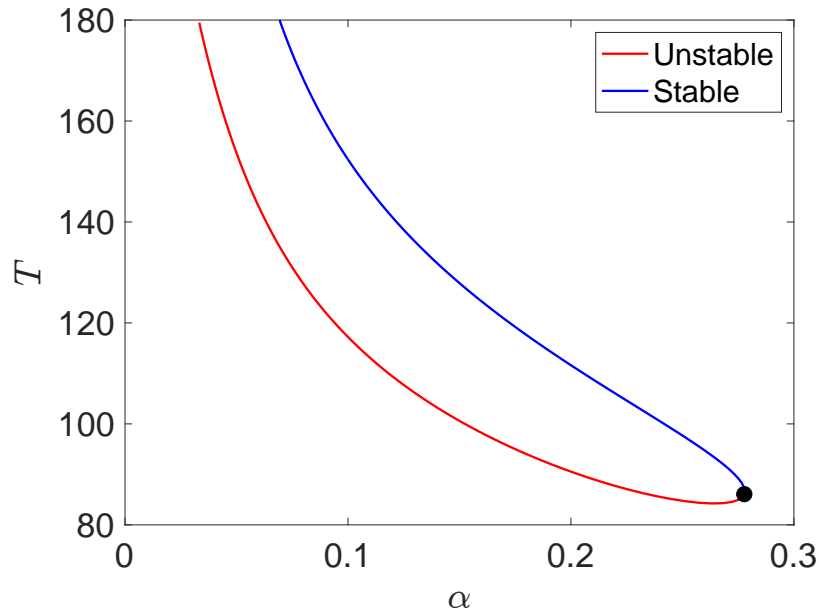


Figure 5.16.: Continuation of the periodic solution shown in Figure 5.4 to the non-smooth ODE system (5.16). The temporal period  $T$  is plotted against the bifurcation parameter  $\alpha$ . The blue and red curves represent stable and unstable periodic orbits, respectively. The black dot represents a fold of cycles bifurcation, where an eigenvalue passes through  $+1$ . Parameters (with the exception of  $\alpha$ ) are as in Table 4.

In essence, Figure 5.16 shows that the period of the stable periodic orbit decreases as the speed of synaptic transmission increases. This is to be expected for quicker synaptic signalling, represented by increasing  $\alpha$ .

The synchronous solution to the spatially extended system (5.15) yields the same existence curve as Figure 5.16 upon continuation in  $(\alpha, T)$ -space, but with different stability properties. This is to be expected – stability of the ODE system is akin to tracking the eigenvalues in Figure 5.5, as a bifurcation parameter is varied, at  $k = 0$  only. The spatially extended system has stability properties determined by the entire range of  $k \in \mathbb{R}$ .

### 5.7.2 Spatially Heterogeneous 2-cycle

The patterns mentioned in the introduction to this section that arise via bifurcations – be they primary bifurcations, or *secondary* bifurcations in the case of the travelling, oscillating hexagons – have a highly non-trivial spatial structure, and as a consequence, difficulties arise when attempting any analysis of the type in Sections 5.3 and 5.4.

Therefore, we utilise the numerical bifurcation approach developed in Chapter 3 for periodic orbit-type solutions. These methods are flexible in the sense that they are indifferent to the spatial heterogeneity in a solution. The only requirement is that the equations governing the model under consideration and any solutions of interest be “sufficiently smooth”. So far, we have considered a PWL, *discontinuous* model which has allowed for the explicit analysis carried out on periodic synchrony. Now however, we consider the case where all Heaviside functions are replaced with steep sigmoidal functions. This affects  $f$ ,  $h_\infty$ ,  $\tau_h$ , and  $I_T$  in the model (5.15).

The sigmoidal function takes the form

$$\mathcal{S}(u; \kappa, \mu) = \frac{1}{1 + \exp(-\mu(u - \kappa))}, \quad \mu > 0, \kappa \in \mathbb{R}, \quad (5.40)$$

where  $\kappa$  and  $\mu$  are parameters determining the sigmoidal shift and steepness, respectively. As  $\mu \rightarrow \infty$ ,  $\mathcal{S}(u; \kappa, \mu) \rightarrow H(u - \kappa)$ .

A balance must be struck between a sufficiently smooth model and a sigmoidal function that is sufficiently steep so as to effectively approximate the non-smooth model. We use  $\mu = 10$ . Although this is not as steep as the value for  $\mu$  used in Chapter 4, it is sufficient here. While this discussion centres on approximating the non-smooth system, it is important to bear in mind that non-smooth model is an idealisation of the non-linear sigmoidal system which is a more accurate reflection of the underlying biology.

We find the sigmoidal model to be in good agreement with the non-smooth model. Where a 1D 2-cycle (as shown in the top panel of Figure 5.8) is predicted at an instability of synchrony in the latter, it appears in

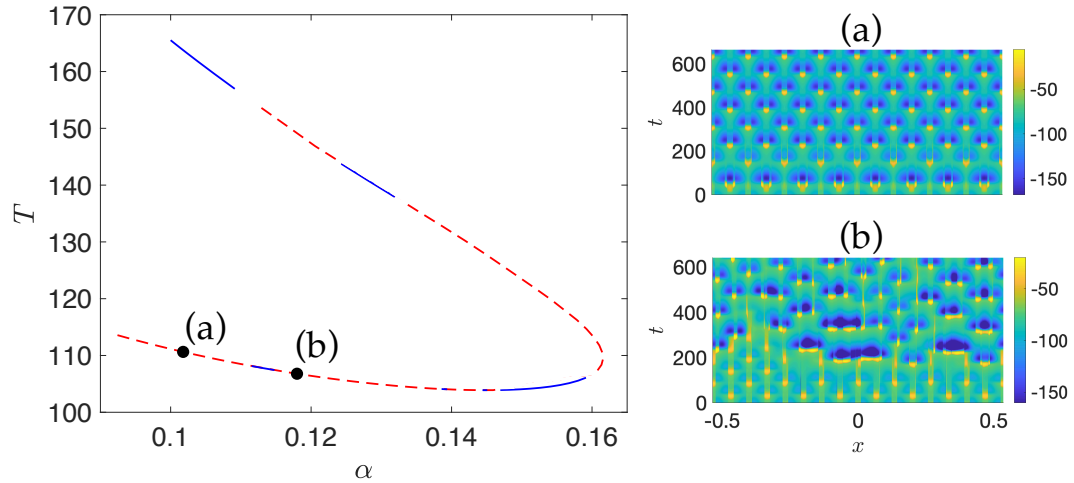


Figure 5.17.: Periodic orbit continuation of the spatially heterogeneous 2-cycle solution,  $T$  vs.  $\alpha$ , to the smooth model (5.15). Blue (solid) and red (dashed) lines are stable and unstable solutions respectively. Parameters are as in Table 4, with  $\tau_R = 3$ ,  $\mu = 10$ , and the kernel parameter  $\gamma = 0.55$ . Continuation parameters:  $\epsilon_n = 10^{-4}$ ,  $\epsilon_l = 10^{-4}$ .

the former. The 2-cycle is a spatially heterogeneous, temporally periodic solution. As such it is amenable to the PO continuation methods in Chapter 3. The results of this are shown in Figure 5.17, showing the relationship between the temporal period  $T$  and the synapse parameter  $\alpha$ . Beginning on the upper branch at  $\alpha = 0.1$ , moving to the right, and following it around onto the lower branch, we see the 2-cycle alternates between stable (blue, solid) and unstable (red, dashed). We time-evolve patterns which are a small perturbation away from (a) and (b) denoted on the lower branch. Both (a) and (b) are predicted by the numerical stability theory to be unstable. This is confirmed via direct numerical simulation, as shown by the two panels on the right. Solution (a) settles to the stable upper branch, with temporal period  $T \simeq 160$ . Whereas the solution on the upper branch directly above (a) is stable, this is not the case for (b): the upper branch is unstable for the same value of  $\alpha$  as (b). Thus, the emergent pattern upon instability of (b) is not the corresponding pattern on the upper branch, but instead is seen to be

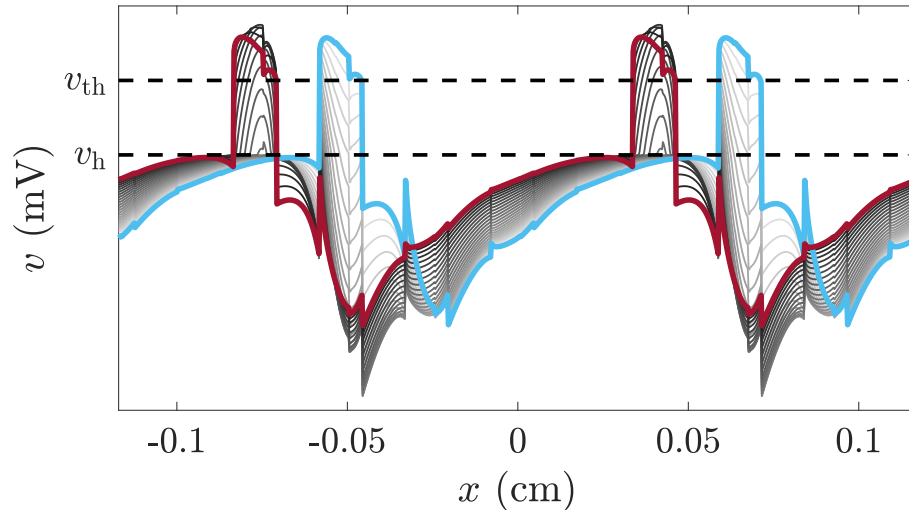


Figure 5.18.: Membrane potential  $v$ , of the lurching wave solution shown in the top panel of Figure 5.12, plotted through time over one temporal period. The initial profile is shown in blue. The wave is shown evolving over a period as the curve goes from light to dark. The dark red curve shows the wave after a temporal period. These temporal snapshots reveal the shock-like, discontinuous nature of the solution in space throughout time.

an exotic, somewhat unstructured pattern which does not settle to a more regular state. In some parts of the domain, patches of activity split up into two, and in others, the firing symmetry in a patch is lost. The dynamics are highly non-trivial, and we have taken a step here in understanding them.

The lurching waves in Figure 5.12 are a travelling, periodic solution which are amenable, in theory, to the TWPO continuation methods in Chapter 3. These exist in the smoothed model too, and are qualitatively identical to those in the non-smooth model. They have a highly non-smooth nature over a temporal period (after which, the profile of the wave is identical, albeit with a spatial shift), as shown in Figure 5.18 – the vertical lines in the solution indicate jumps where the solution is discontinuous (an example is shown at  $x = 0.07$  for the initial, blue profile). The Fourier methods associated with computing shifts and derivatives are unable to function as required and thus, at present, our numerical approach is unable to shed

much light on instabilities of lurching waves. Possible remedies to this are discussed in the Discussion of this thesis.

## 5.8 CONSTRUCTION OF SPATIALLY PERIODIC TRAVELLING WAVES

### 5.8.1 *Synaptic Dynamics*

Travelling waves have been seen in a variety of different models of cortical and sub-cortical tissue as well as *in vitro* and *in vivo* [152]. Notable studies of travelling waves in thalamic models can be found in [178], which considers a biophysical cell-based model, and [234], which uses geometric singular perturbation methods to determine when waves exist in a two-layer model of interacting TC and RE cells.

In the following, we construct spatially periodic waves (also known as a travelling wavetrain) in one spatial dimension and determine the corresponding dispersion relation, relating the wavespeed to their spatial period. Let us denote the co-moving variable by  $\xi = x - ct$ . Recall that, from (5.8) and (5.13) in 1D, the synaptic variable satisfies

$$u(x, t) = \int_{-\infty}^{\infty} dy w(y) \int_0^{\infty} ds \eta(s) f(v(x - y, t - s)). \quad (5.41)$$

Transforming the expression for  $u$ , (5.41), into the co-moving frame, by the spatial shift  $x \rightarrow \xi = x - ct$ , noting the transformation of the spatial coordinate in the *firing rate* function, we obtain

$$u(x - ct, t) = \int_{-\infty}^{\infty} dy w(y) \int_0^{\infty} ds \eta(s) f(v(x - y - c(t - s), t - s)), \quad (5.42)$$

which, in terms of the travelling-wave co-ordinate,  $\xi$ , is

$$u(\xi, t) = \int_{-\infty}^{\infty} dy w(y) \int_0^{\infty} ds \eta(s) f(v(\xi - y + cs, t - s)). \quad (5.43)$$

Travelling wave solutions to (5.3), (5.5), (5.13) in  $(x, t)$ -space are stationary solutions with no explicit time-dependence in  $(\xi, t)$ -space. That is, travelling wave solutions satisfy  $z(\xi, t) = z(\xi)$ . So seeking time-independent solutions to (5.43), we obtain

$$u(\xi) = \int_{-\infty}^{\infty} dy w(y) \int_0^{\infty} ds \eta(s) f(v(\xi - y + cs)), \quad (5.44)$$

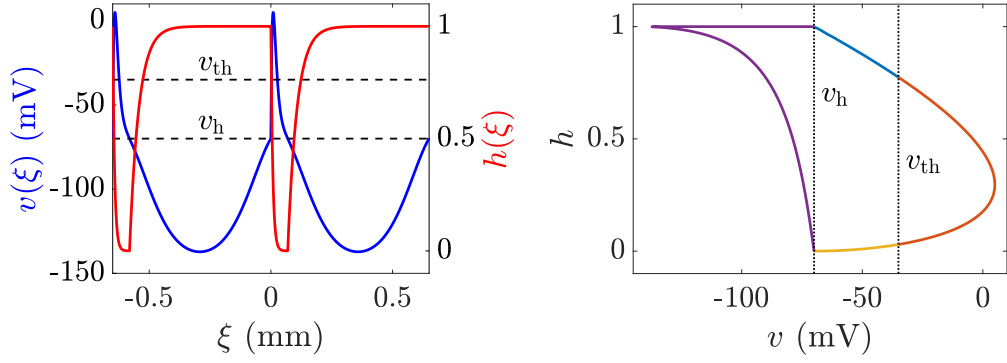


Figure 5.19.: The spatially periodic travelling waves solution (two spatial periods of  $v(\xi)$  (blue) and  $h(\xi)$  (red) in the left panel, while  $(v, h)$ -phase space *through space* over a spatial period, with different colours indicating parts of the orbit between switching events, is shown in the right panel). Over a period,  $[0, \phi]$ , where  $\phi = 0.65\text{mm}$ , switching events  $\xi_i$ ,  $i = 1, \dots, 4$  occur when  $v(\xi)$  crosses the switching manifolds  $v = v_\mu$ ,  $\mu \in \{v_{th}, v_h\}$  in a topologically equivalent manner to Figure 5.4. The dotted black lines represent the switching manifolds at  $v_h$  and  $v_{th}$ , respectively. Parameter values are as in Table 4.

and using the form of  $f$  given by (5.7), (5.44) becomes

$$u(\xi) = \frac{1}{\tau_R} \int_{-\infty}^{\infty} dy w(y) \int_0^{\infty} ds \eta(s) H(v(\xi - y + cs) - v_{th}). \quad (5.45)$$

For  $\xi \in [0, \phi]$ , where  $\phi$  denotes the spatial period of the travelling wave in the co-moving frame,  $v(\xi)$  exhibits an orbit that is topologically identical to the one shown in Figure 5.4, but with the corresponding switching events occurring in the *travelling wave co-ordinate* rather than in time. A plot of  $(v(\xi), h(\xi))$  is shown in the left panel of Figure 5.19 with corresponding phase space shown in the right panel. Hence, we can map the switching times  $T_i$  to switching *events* at  $\xi_i$ ,  $i = 1, \dots, 4$ , in the co-moving frame, where  $\xi_4 = \phi$  is the full spatial period, with  $v(0) = v_h$ .

Explicitly, we construct the travelling wavetrain with the switching conditions  $v(\xi_1) = v_{th}$ ,  $v(\xi_2) = v_{th}$ ,  $v(\xi_3) = v_h$ , and  $v(\phi) = v_h$ , and the periodicity

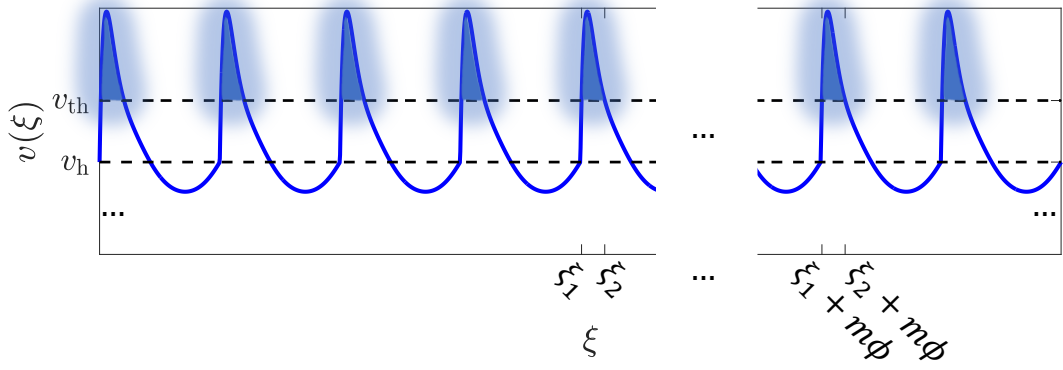


Figure 5.20.: An illustration depicting the spatially periodic travelling waves in the co-moving frame, with the regions providing synaptic input,  $\xi_1 + m\phi < \xi < \xi_2 + m\phi$ ,  $m \in \mathbb{Z}$ , shaded in blue.

conditions  $v(\phi) = v(0)$  and  $h(\phi) = h(0)$ . With this set-up, the Heaviside function in (5.45) only contributes if

$$\xi_1 + m\phi \leq \xi - y + cs \leq \xi_2 + m\phi, \quad m \in \mathbb{Z}. \quad (5.46)$$

as shown in Figure 5.20. This reduces (5.45) to

$$u(\xi) = \frac{1}{\tau_R} \int_0^\infty ds \eta(s) \sum_{m \in \mathbb{Z}} \int_{\xi - \xi_2 + cs - m\phi}^{\xi - \xi_1 + cs - m\phi} dy w(y), \quad (5.47)$$

which, with the substitution  $y' = y - \xi - cs + m\phi$  (and subsequently removing the prime notation) can be rewritten as

$$u(\xi) = \frac{1}{\tau_R} \sum_{m \in \mathbb{Z}} \int_0^\infty ds \eta(s) W(-m\phi + cs + \xi), \quad (5.48)$$

where

$$W(x) = \int_{\xi_1}^{\xi_2} dy w(x - y). \quad (5.49)$$

It is now natural to express the  $\xi$ -periodic function  $u(\xi)$  as a Fourier series, which we obtain as

$$u(\xi) = \sum_{p \in \mathbb{Z}} u_p e^{2\pi i p \xi / \phi}, \quad u_p = \frac{1}{\tau_R \phi} \hat{\eta} \left( \frac{-2\pi c p}{\phi} \right) \hat{W} \left( \frac{2\pi p}{\phi} \right). \quad (5.50)$$

See Appendix C.3 for a derivation of this result. Here,  $\hat{\eta}(k)$  and  $\hat{W}(k)$  denote the Fourier transforms of  $\eta(t)$  and  $W(x)$ , respectively. For  $\eta$  and  $w$  given by (2.21) and (5.9), the aforementioned Fourier transforms are given by

$$\hat{\eta}(k) = \left( \frac{\alpha}{\alpha + ik} \right)^2, \quad (5.51)$$

and

$$\begin{aligned}\widehat{W}(k) &= w_0[b(k, \sigma, 0) - \frac{\gamma}{2}(b(k, \sigma, \rho) + b(k, \sigma, -\rho))], \\ b(k; \sigma, \rho) &= \frac{2\sigma i(e^{-ik\zeta_2} - e^{-ik\zeta_1})}{k(1 + (\rho - k\sigma)^2)},\end{aligned}\tag{5.52}$$

with the result for  $\widehat{W}(k)$  shown in Appendix C.1. This fully specifies the solution  $u(\zeta)$  in the computationally convenient form of a Fourier series. It now remains to construct the  $\phi$ -periodic solutions  $v(\zeta)$  and  $h(\zeta)$ .

### 5.8.2 Rebound Dynamics

Due to the presence of exposed Heaviside functions in the model, the dynamics switch discontinuously when  $v = v_h$ . Over a single spatial period, this occurs at  $\zeta = \zeta_3$  and  $\zeta = \phi$ .

Transforming (5.5) into the co-moving frame, we obtain

$$\left(-c \frac{\partial h}{\partial \zeta} + \frac{\partial h}{\partial t}\right) = \begin{cases} -h/\tau_h^-, & v > v_h, \\ (1-h)/\tau_h^+, & v < v_h. \end{cases}\tag{5.53}$$

Seeking time-independent solutions, that is setting  $\partial h/\partial t = 0$ , to find an equation governing the travelling wave  $z(\zeta)$ , we obtain

$$-c \frac{dh}{d\zeta} = \begin{cases} -h/\tau_h^-, & 0^+ \leq \zeta \leq \zeta_3^-, \\ (1-h)/\tau_h^+, & \zeta_3^+ \leq \zeta \leq \phi^-, \end{cases}\tag{5.54}$$

which is an uncoupled piecewise linear equation. The notation  $\zeta_i^\pm$  is defined by  $\zeta_i^\pm = \lim_{\epsilon \searrow 0} \zeta_i \pm \epsilon$ ,  $i \in \{3, 4\}$ , and denotes space either side of a switching event. With the condition for  $h(\zeta)$  that sets the spatial origin given as  $h(0) = h_0$ , and the continuity condition  $h(\zeta_3^-) = h(\zeta_3^+)$ , this can be solved using integrating factors, which is equivalent to using the Green's functions  $\mathcal{G}_h^\pm(\zeta) = e^{\zeta/(c\tau_h^\pm)}$ , for  $c < 0$  to obtain

$$h(\zeta) = \begin{cases} h_0 \mathcal{G}_h^-(\zeta), & 0^+ \leq \zeta \leq \zeta_3^-, \\ (h_0 \mathcal{G}_h^-(\zeta_3) - 1) \mathcal{G}_h^+(\zeta - \zeta_3) + 1, & \zeta_3^+ \leq \zeta \leq \phi^-. \end{cases}\tag{5.55}$$

The sign of the wave-speed  $c < 0$  ensures that solutions are bounded. This is a consequence of our choice of co-moving frame variable as the space-like  $\zeta = x - ct$  rather than, say, the time-like  $\xi = t - x/c$ , for which  $c > 0$ . A constraint that will determine  $h_0$  is the periodicity condition,  $h(\phi) = h_0$ .

### 5.8.3 Voltage Dynamics

Transforming (5.3) to the co-moving frame, we obtain<sup>4</sup>

$$C \left( -c \frac{\partial v}{\partial \zeta} + \frac{\partial v}{\partial t} \right) = -g_L(v - v_L) - g_T h H(v - v_h) - g_{\text{syn}} u. \quad (5.56)$$

Seeking travelling wave solutions, obtained by setting  $\partial z / \partial t = 0$  in the co-moving frame, the piecewise equation for  $v(\zeta)$  is given by

$$-Cc \frac{dv}{d\zeta} = \begin{cases} -g_L(v - v_L) - g_T h - g_{\text{syn}} u, & 0^+ \leq \zeta \leq \zeta_3^-, \\ -g_L(v - v_L) - g_{\text{syn}} u, & \zeta_3^+ \leq \zeta \leq \phi^-, \end{cases} \quad (5.57)$$

These are first-order linear differential equations in  $v(\zeta)$ , where  $h(\zeta)$  and  $u(\zeta)$  are treated purely as functions of  $\zeta$ . Thus (5.57) can be solved via the Green's function  $\mathcal{G}_v(\zeta) = e^{g_L \zeta / (Cc)}$ , to obtain

$$v(\zeta) = \begin{cases} \mathcal{G}_v(\zeta) v_h + \int_0^\zeta \mathcal{G}_v(\zeta - \zeta') \left( -\frac{g_L v_L}{Cc} + \frac{g_T}{Cc} h(\zeta') + \frac{g_{\text{syn}}}{Cc} u(\zeta') \right) d\zeta', & 0^+ \leq \zeta \leq \zeta_3^-, \\ \mathcal{G}_v(\zeta - \zeta_3) v_h + \int_{\zeta_3}^\zeta \mathcal{G}_v(\zeta - \zeta') \times \left( -\frac{g_L v_L}{Cc} + \frac{g_{\text{syn}}}{Cc} u(\zeta') \right) d\zeta', & \zeta_3^+ \leq \zeta \leq \phi^-. \end{cases} \quad (5.58)$$

We have used the initial condition  $v(0) = v_h$ , and the switching condition  $v(\zeta_3^+) = v_h$ . It is important to note that  $v(\zeta_3^+) = v_h$  has been used in this construction, so the switching event  $v(\zeta_3) = v_h$  is more accurately written as  $v(\zeta_3^-) = v_h$  to clamp  $v$  at  $v_h$  at  $\zeta = \zeta_3^-$ .

---

<sup>4</sup>Observe the notational similarity between the capacitance parameter  $C$ , and the wave speed  $c$ , which is explicitly pointed out to avoid confusion.

#### 5.8.4 The Dispersion Relation

Analogously to Section 5.3 where we had to determine the switching times  $T_i$  and the initial state  $z_0$  to construct the synchronous solution, the spatially periodic wave constructed here according to (5.50), (5.55), (5.58), is parameterised by the switching coordinates  $\xi_i$ ,  $i = 1, 2, 3$ , the period  $\phi$ , the initial value  $h_0$  and the wave speed  $c$ . The six unknowns, and the five switching and periodicity conditions

$$v(\xi_1) = v_{\text{th}}, \quad (5.59a)$$

$$v(\xi_2) = v_{\text{th}}, \quad (5.59b)$$

$$v(\xi_3^-) = v_{\text{h}}, \quad (5.59c)$$

$$v(\phi) = v_{\text{h}}, \quad (5.59d)$$

$$h(\phi) = h_0, \quad (5.59e)$$

define a dispersion relation  $c = c(\phi)$  between the wave speed  $c$  and the spatial period  $\phi$  of the travelling wave.

Figure 5.21 shows the resultant dispersion curve  $c = c(\phi)$  for three different values of  $\alpha$ . We note that  $c < 0$  in these plots which is consistent with the choice of co-moving frame variable used here, as mentioned above. Theoretical predictions  $c = c(\phi)$  are shown by the three lines. As we decrease  $\alpha$  going from the red to the black to the blue line, the emergent wave speed decreases for all  $\phi$ . This is consistent with the interpretation of  $\alpha$  as the reciprocal of the synaptic time scale – decreasing  $\alpha$  increases the time until peak synaptic response, which in turn results in synaptic activity spreading more slowly. The speeds found here are consistent with those found by Rinzel et al. [178], being on the order of  $\text{mms}^{-1}$ . The spatial profile and phase space corresponding to  $\phi = 0.65\text{mm}$  for  $\alpha = 0.1 \text{ms}^{-1}$  are shown in Figure 5.19. With the origin of a spatial period at  $v(0) = v_{\text{h}}$ , the spatially periodic trajectory follows the same qualitative trajectory (shown in the right panel) as that followed by the trajectory describing spatial synchrony. In the final phase over a period (purple line),  $h$  saturate to 1, while the volt-

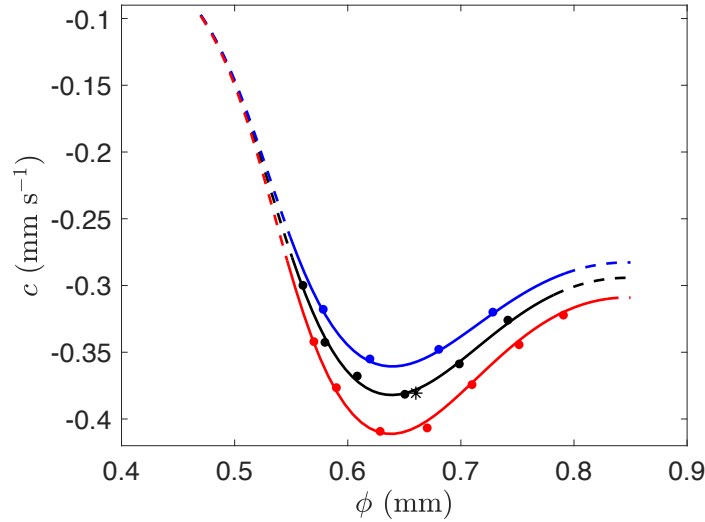


Figure 5.21.: Dispersion curves  $c = c(\phi)$  for periodic travelling waves for three different values of  $\alpha$ :  $0.07 \text{ ms}^{-1}$  (blue),  $0.1 \text{ ms}^{-1}$  (black) and  $0.2 \text{ ms}^{-1}$  (red). Solid lines indicate linearly stable travelling waves, while dashed lines correspond to linearly unstable travelling waves. Dots indicate simulation results, with colour corresponding to the relevant parameter set as defined above. The asterisk represents the emergent wave speed and period of an initially unstable wave with initial period  $\phi = 1.32\text{mm}$ . Parameter values other than  $\alpha$  are as in Table 4.

age variable  $v$  decreases to a minimum before recovering and completing a spatial period. The behaviour described here, and shown in the right panel, should not be confused with a discontinuous reset event. The corresponding behaviour can be seen in the left panel where  $v < v_h$ . The sharp turn in the purple line in phase space occurs as  $v$  recovers from inhibition while  $h$  is already essentially saturated to 1.

In Figure 5.21, the dots represent the emergent wave speed and spatial period from numerical simulations, where initial conditions are a perturbation away from the dispersion curve. These simulation results agree very well with the theoretical predictions. We indicate linear stability of the periodic travelling waves in Figure 5.21 as follows. Linearly stable travelling

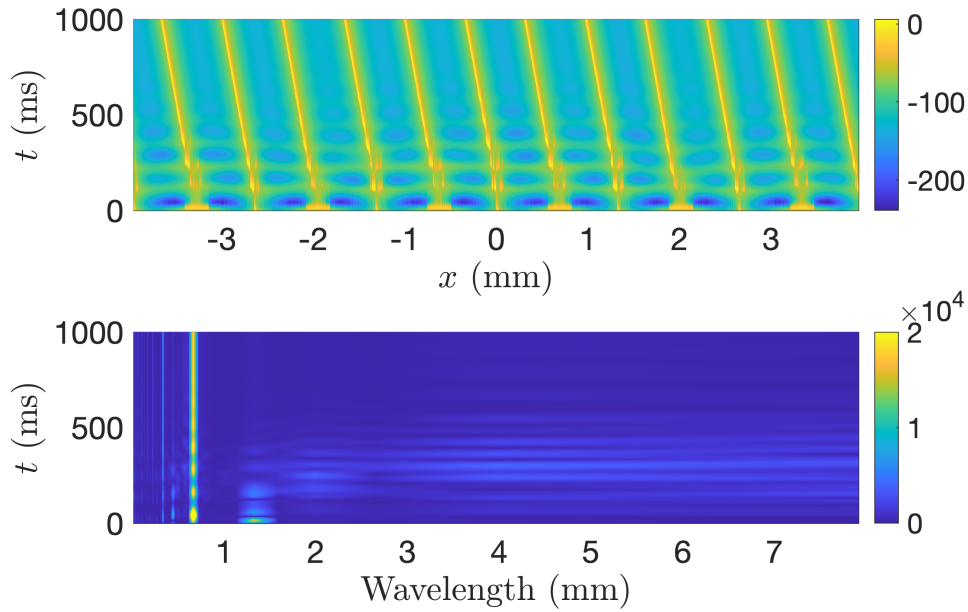


Figure 5.22.: Top: Space-time plot of the  $v$  component in mV of the travelling wave corresponding to the asterisk in Figure 5.21.

Bottom: A spectrogram showing the magnitudes of the wavelengths (reciprocal of spatial frequency) that compose the solution shown in the top panel at each point in time.

waves are denoted by solid lines, while dashed lines refer to linearly unstable travelling waves. This linear wave stability is computed in Section 5.9.

When initiating a numerical simulation with an unstable pattern, the emergent travelling wave is selected from the possible periods in the stable region of Figure 5.21. As an example, the asterisks represents the emergent wave from a simulation initiated with a spatial period of  $\phi = 1.32\text{mm}$ , which is linearly unstable. The emergent wave can clearly be seen to sit on the dispersion curve with a spatial period of  $\phi = 0.66\text{mm}$ . The corresponding space-time plot of the periodic travelling wave denoted by the asterisks is depicted in the top panel of Figure 5.22. In this case, the unstable wave immediately breaks up, with the transient behaviour settling to a wave of spatial period  $\phi_{\text{emergent}} = \phi_{\text{initial}}/2$ . The spectrogram in the lower panel shows the magnitudes of the wavelengths (reciprocal of the spatial frequen-

cies) that compose the solution shown in the upper panel, through time. The dominant wavelength at  $t = 0$  is 1.32mm (as expected since this is the initially unstable solution). The dominant wavelength almost immediately settles to 0.66mm. Faint lines are seen at other wavelengths, for example at 1.32mm and around 0.5mm. These are a consequence of the solution not being purely sinusoidal, and indicate some non-trivial spatial structure. The first of these indicates that wavelengths of 1.32mm are present in the solution over two periods. The second may be characteristic of the generic bump width, shown in the upper panel as the hazy yellow/green colour in the vicinity of the yellow bands representing peaks. The spectrogram is computed by using a discrete Fourier transform at each point in time to obtain the spatial frequencies that make up the solution. The reciprocal of this is then taken to obtain the spatial wavelength, which is the quantity plotted.

## 5.9 STABILITY OF SPATIALLY PERIODIC TRAVELLING WAVES

### 5.9.1 *Synaptic Dynamics*

In the previous section, periodic travelling waves were constructed, and the resultant dispersion curve was plotted in Figure 5.21, upon which, stability was indicated. Those results are based on the following linear stability analysis. Much like in Chapter 4, to analytically compute wave stability, we follow the Evans function approach outlined in Section 2.9. Perturbing about the spatially periodic travelling wave  $z(\xi)$ , in the co-moving frame as

$$z(\xi, t) = z(\xi) + \delta z(\xi, t), \quad (5.60)$$

the aim is to find evolution equations for the *travelling wave part of the perturbations*, and obtain the eigenvalues of the stability problem. Here, this entails constructing an appropriate  $4 \times 4$  linear system in the perturbations

at the four switching events over one spatial period, and demanding that the perturbations *at* said switching events be non-trivial.

We begin by considering perturbations to the synaptic dynamics,  $u(\xi)$ . Substituting the perturbation ansatz (5.60) into the equation for  $u$  in the co-moving frame (5.43), we obtain

$$\begin{aligned} \delta u(\xi, t) &= \int_{-\infty}^{\infty} dy w(y) \int_0^{\infty} ds \eta(s) \\ &\quad \times f'(v(\xi - y + cs)) \delta v(\xi - y + cs, t - s). \end{aligned} \quad (5.61)$$

Making the substitution  $y' = \xi - y + cs$ , we obtain (upon removing prime notation)

$$\delta u(\xi, t) = \int_{-\infty}^{\infty} dy w(\xi - y + cs) \int_0^{\infty} ds \eta(s) f'(v(y)) \delta v(y, t - s). \quad (5.62)$$

where  $f'(v(x)) = \delta(v(x) - v_{\text{th}}) / \tau_R$  underneath the spatial integral. Then based on the points where a trajectory crosses  $v_{\text{th}}$  (see (5.46) and Figure 5.20 for where this occurs) we have the formal “composition with a function” delta function identity that

$$\delta(v(y) - v_{\text{th}}) = \sum_{m \in \mathbb{Z}} \sum_{j=1}^2 \frac{\delta(y - m\phi - \xi_j)}{|v'(m\phi + \xi_j)|}, \quad m \in \mathbb{Z}. \quad (5.63)$$

Utilising (5.63), (5.62) becomes

$$\begin{aligned} \delta u(\xi, t) &= \frac{1}{\tau_R} \int_{-\infty}^{\infty} dy w(\xi - y + cs) \int_0^{\infty} ds \eta(s) \\ &\quad \times \sum_{m \in \mathbb{Z}} \sum_{j=1}^2 \frac{\delta(y - m\phi - \xi_j)}{|v'(\xi_j)|} \delta v(y, t - s), \end{aligned} \quad (5.64)$$

after using that  $z'(\xi)$  is  $\phi$ -periodic – more explicitly, that  $v'(m\phi + \xi) = v'(\xi)$  for all  $\xi \in \mathbb{R}$ , and all  $m \in \mathbb{Z}$ . Collapsing the integral over  $y$  by using the delta function in (5.64), we obtain

$$\begin{aligned} \delta u(\xi, t) &= \frac{1}{\tau_R} \sum_{m \in \mathbb{Z}} \int_0^{\infty} ds \eta(s) \\ &\quad \times \sum_{j=1}^2 w(\xi - \xi_j - m\phi + cs) \frac{\delta v(m\phi + \xi_j, t - s)}{|v'(\xi_j)|}. \end{aligned} \quad (5.65)$$

Let us assume spatio-temporally separable perturbations, that is perturbations of the form

$$\delta z(\xi, t) = e^{\lambda t} \delta z(\xi).$$

This results in

$$\begin{aligned} \delta u(\xi; \lambda) &= \frac{1}{\tau_R} \sum_{m \in \mathbb{Z}} \int_0^\infty ds \eta(s) e^{-\lambda s} \\ &\quad \times \sum_{j=1}^2 w(\xi - \xi_j - m\phi + cs) \frac{\delta v(m\phi + \xi_j)}{|v'(\xi_j)|}. \end{aligned} \quad (5.66)$$

A final assumption we make is that the perturbations are *spatially periodic*, that is  $\delta z(m\phi + \xi) = \delta z(\xi)$  for all  $\xi$ . This reduces (5.66) to

$$\delta u(\xi; \lambda) = \frac{1}{\tau_R} \sum_{m \in \mathbb{Z}} \int_0^\infty ds \eta(s) e^{-\lambda s} \sum_{j=1}^2 w(\xi - \xi_j - m\phi + cs) \frac{\delta v(\xi_j)}{|v'(\xi_j)|}. \quad (5.67)$$

As we did for synaptic activity  $u(\xi)$  in Section 5.8, we express  $\delta u(\xi)$  as a Fourier series, which is computationally useful in constructing the Evans function. The calculation is in the same spirit as that shown in Appendix C.3, but we show it here completely. Rewriting  $w(\xi - \xi_j - m\phi + cs)$  in terms of its Fourier transform as

$$w(\xi - \xi_j - m\phi + cs) = \frac{1}{2\pi} \int_{-\infty}^\infty dk \hat{w}(k) e^{ik(\xi - \xi_j - m\phi + cs)},$$

then (5.67) reduces to

$$\begin{aligned} \delta u(\xi) &= \frac{1}{\tau_R} \int_0^\infty ds \eta(s) e^{-s(\lambda - ick)} \sum_{j=1}^2 \int_{-\infty}^\infty dk \hat{w}(k) e^{ik(\xi - \xi_j)} \\ &\quad \times \left( \frac{1}{2\pi} \sum_{m \in \mathbb{Z}} e^{-ikm\phi} \right) \frac{\delta v(\xi_j)}{|v'(\xi_j)|}. \end{aligned} \quad (5.68)$$

The integral over  $s$  is in the form of a Laplace transform,

$$\tilde{\eta}(\lambda) = \int_0^\infty \eta(s) e^{-\lambda s} ds.$$

Utilising this, and the Dirac comb property,

$$\phi \sum_{m \in \mathbb{Z}} e^{\pm ikm\phi} = 2\pi \sum_{p \in \mathbb{Z}} \delta\left(k - \frac{2\pi p}{\phi}\right),$$

we arrive at

$$\begin{aligned} \delta u(\xi) &= \frac{1}{\tau_R \phi} \sum_{p \in \mathbb{Z}} \tilde{\eta} \left( \lambda - \frac{2\pi i p c}{\phi} \right) \\ &\quad \times \sum_{j=1}^2 \int_{-\infty}^{\infty} dk \hat{w}(k) e^{ik(\xi - \xi_j)} \delta \left( k - \frac{2\pi p}{\phi} \right) \frac{\delta v(\xi_j)}{|v'(\xi_j)|}. \end{aligned} \quad (5.69)$$

Collapsing the integral over  $k$  via the delta function in (5.69) yields the Fourier series representation of  $\delta u(\xi)$  as

$$\delta u(\xi) = \sum_{p \in \mathbb{Z}} \delta u_p e^{2\pi i p \xi / \phi}, \quad \delta u_p = \frac{1}{\tau_R \phi} \hat{w} \left( \frac{2\pi p}{\phi} \right) \sum_{j=1}^2 I_j, \quad (5.70)$$

where

$$I_j = \frac{\delta v(\xi_j)}{|v'(\xi_j)|} \tilde{\eta} \left( \lambda - \frac{2\pi i p c}{\phi} \right) e^{-2\pi i \xi_j / \phi}. \quad (5.71)$$

Over a period  $\phi$ ,  $\delta u(\xi)$  is continuous: there are no discontinuities in the perturbations at  $\xi_i$ ,  $i = 1, 2$ , as was the case at the analogous switching times for *spatial synchrony*. This is a result of the solution being “spatially-dependent” in the co-moving frame: the argument of  $f'$  appearing in (5.61) depends on the spatial integration variable  $y$ . An important consequence of this is that the delta functions that appear in the stability calculation are *inside* the convolution integral; recall that at the analogous point in the analysis for synchrony (5.24), the  $f'$  term had no spatial dependence, leading to exposed delta functions underneath the implicit integral supplied by the time-derivative on the left-hand side. This led to perturbations with jumps.

Since  $\delta u(\xi)$  is continuous over a period, saltation operators are not required at  $\xi_i$ ,  $i = 1, 2$  (as will be shown in the next sub-section,  $\delta v(\xi)$  and  $\delta h(\xi)$  do not exhibit switches in the dynamics at  $\xi_i$ ,  $i = 1, 2$  either).

## 5.9.2 Voltage and Rebound Dynamics

The evolution equations for  $\delta h(\xi, t)$  and  $\delta v(\xi, t)$  can be obtained by substituting the perturbation ansatz (5.60) into (5.53) and (5.56) to obtain the evolution equations for small perturbations as

$$\left(-c \frac{\partial}{\partial \xi} \delta h(\xi, t) + \frac{\partial}{\partial t} \delta h(\xi, t)\right) = \begin{cases} -\delta h(\xi, t) / \tau_h^-, & v > v_h, \\ -\delta h(\xi, t) / \tau_h^+, & v < v_h, \end{cases} \quad (5.72)$$

and

$$C \left(-c \frac{\partial}{\partial \xi} \delta v(\xi, t) + \frac{\partial}{\partial t} \delta v(\xi, t)\right) = \begin{cases} -g_L \delta v(\xi, t) - g_T \delta h(\xi, t) - g_{\text{syn}} \delta u(\xi, t), & v > v_h, \\ -g_L \delta v(\xi, t) - g_{\text{syn}} \delta u(\xi, t), & v < v_h. \end{cases} \quad (5.73)$$

Assuming separable perturbations,  $\delta z(\xi, t) = e^{\lambda t} \delta z(\xi)$ , since all terms are local, the exponential time-dependence is common to all terms, therefore

$$c \frac{d}{d\xi} \delta h(\xi) = \begin{cases} \left(\lambda + \frac{1}{\tau_h^-}\right) \delta h(\xi), & 0^+ \leq \xi \leq \xi_3^-, \\ \left(\lambda + \frac{1}{\tau_h^+}\right) \delta h(\xi), & \xi_3^+ \leq \xi \leq \phi^-, \end{cases} \quad (5.74)$$

and

$$Cc \frac{\partial}{\partial \xi} \delta v(\xi) = \begin{cases} (g_L + C\lambda) \delta v(\xi) + g_T \delta h(\xi) \\ \quad + g_{\text{syn}} \delta u(\xi), & 0^+ \leq \xi \leq \xi_3^-, \\ (g_L + C\lambda) \delta v(\xi) + g_{\text{syn}} \delta u(\xi), & \xi_3^+ \leq \xi \leq \phi^-. \end{cases} \quad (5.75)$$

(5.74) and (5.75) are *linear* equations in their respective perturbations and so are readily solved using the Greens functions  $G_h^\pm(\xi) = e^{(1/\tau_h^\pm + \lambda)\xi/c}$  and  $G_v(\xi) = e^{(g_L + C\lambda)\xi/Cc}$  for  $c < 0$  to obtain

$$\delta h(\xi) = \begin{cases} \delta h(0^+) G_h^-(\xi), & 0^+ \leq \xi \leq \xi_3^-, \\ \delta h(\xi_3^+) G_h^+(\xi - \xi_3), & \xi_3^+ \leq \xi \leq \phi^-, \end{cases} \quad (5.76)$$

and

$$\delta v(\xi) = \begin{cases} \delta v(0^+)G_v(\xi) + \int_0^\infty G_v(\xi - \xi') \\ \quad \times \left( \frac{g_T}{Cc} \delta h(\xi') + \frac{g_{\text{syn}}}{Cc} \delta u(\xi') \right) d\xi', & 0^+ \leq \xi \leq \xi_3^-, \\ \delta v(\xi_3^+)G_v(\xi - \xi_3) + \int_{\xi_3}^\xi G_v(\xi - \xi') \\ \quad \times \frac{g_{\text{syn}}}{Cc} \delta u(\xi') d\xi', & \xi_3^+ \leq \xi \leq \phi^-. \end{cases} \quad (5.77)$$

These solutions for the spatial part (in the travelling wave frame) of the perturbations depend on the variables evaluated at  $\xi = 0^+$  and  $\xi = \xi_3^+$ . This is a consequence of the non-smooth dynamics that arises when  $v(\xi)$  and  $h(\xi)$  cross the switching manifold  $v_h$  at  $\xi = 0$ , and  $\xi = \xi_3$ .

### 5.9.3 A Reduced Saltation Approach

In order to propagate the perturbations through the switching manifolds, we require saltation matrices as in Section 5.4. However, a key difference in the stability of spatially periodic waves is the continuity by  $\delta u(\xi)$  over a spatial period. Recall that when studying the stability of the spatially synchronous periodic orbit, all state variables were discontinuous (for at least one switching time) over a temporal period which necessitated the use of the *full*  $4 \times 4$  saltation matrices. Here however, we may consider *reduced*  $2 \times 2$  saltation matrices such that  $\delta z_r(\xi_i^+) = \mathcal{K}_i \delta z_r(\xi_i^-)$ ,  $i = 0, 3$ , where the reduced state vector is defined as  $z_r(\xi) = (v(\xi), h(\xi))^T$ . This is possible since only  $\delta v(\xi)$  and  $\delta h(\xi)$  are discontinuous over a period (and that the switching condition depends on the value of  $v$  only) for the wavetrains under consideration. By the derivation shown in Appendix C.2.2, the reduced saltation matrices  $\mathcal{K}_i$  are given by

$$\mathcal{K}_i = I_2 - \frac{1}{v'(\xi_i^-)} \begin{pmatrix} v'(\xi_i^-) - v'(\xi_i^+) & 0 \\ h'(\xi_i^-) - h'(\xi_i^+) & 0 \end{pmatrix}, \quad i = 0, 3, \quad (5.78)$$

where the notation  $\zeta_0 = 0$  is used, and  $I_2$  is the  $2 \times 2$  identity matrix. Defining

$$S_g(a) = -\frac{g'(a^-) - g'(a^+)}{v'(a^-)}, \quad (5.79)$$

where  $g \in \{v, h\}$ , and  $a \in \{\zeta_0, \zeta_3\}$ , then

$$\delta h(\zeta_3^+) = \delta h(\zeta_3^-) + S_h(\zeta_3) \delta v(\zeta_3^-), \quad (5.80a)$$

$$\delta v(\zeta_3^+) = (1 + S_v(\zeta_3)) \delta v(\zeta_3^-), \quad (5.80b)$$

both of which “set the space-like initial condition” for  $\delta v(\zeta)$  and  $\delta h(\zeta)$  in  $\zeta_3^+ \leq \zeta \leq \phi^-$ .

Recall that the objective is to obtain a linear system in either  $\delta v(\zeta_i)$  or  $\delta h(\zeta_i)$ ,  $i = 1, \dots, 4$ , from which we can obtain the constraint determining the Evans function. Here, we make the choice to generate this system in  $\delta v(\zeta_i)$ .

Evaluating (5.77) for  $\zeta < \zeta_3$ , one obtains an expression for  $\delta v(\zeta)$  containing  $\delta h(0^+)$ , making any linear system in  $\delta v(\zeta_i)$ ,  $i = 1, \dots, 4$  an *inhomogeneous* system. To remedy this and obtain a *homogeneous* system, we can rewrite  $\delta h(0^+)$  in terms of  $\delta v(\zeta)$  at the switching events by repeated application of the saltation rule as follows. Periodic perturbations (enforced earlier), yield  $\delta h(0^+) = \delta h(0^-)$ . Thus,

$$\delta h(0^+) = S_h(\phi) \delta v(\phi^-) + \delta h(\phi^-) \quad (5.81a)$$

$$= S_h(\phi) \delta v(\phi^-) + G_h^+(\phi - \zeta_3) \delta h(\zeta_3^+) \quad (5.81b)$$

$$= S_h(\phi) \delta v(\phi^-) + G_h^+(\phi - \zeta_3) (S_h(\zeta_3) \delta v(\zeta_3^-) + \delta h(\zeta_3^-)) \quad (5.81c)$$

$$= S_h(\phi) \delta v(\phi^-) + S_h(\zeta_3) G_h^+(\phi - \zeta_3) \delta v(\zeta_3^-) + G_h^+(\phi - \zeta_3) G_h^-(\zeta_3) \delta h(0^+), \quad (5.81d)$$

so that

$$\delta h(0^+) = \frac{S_h(\phi) \delta v(\phi^-) + S_h(\zeta_3) G_h^+(\phi - \zeta_3) \delta v(\zeta_3^-)}{1 - G_h^+(\phi - \zeta_3) G_h^-(\zeta_3)}. \quad (5.82)$$

(5.82) expresses  $\delta h(0^+)$  in terms of  $\delta v(\zeta)$  at  $\zeta = \zeta_3^-, \phi^-$ . The pieces are now in place to generate a linear system from which the Evans function can be generated, and wave stability may be ascertained.

## 5.9.4 The Evans Function

With (5.82), the piecewise expression for  $\delta v(\xi)$ , (5.77), over a period only depends on  $\delta v(\xi_i)$ ,  $i = 1, 2, 3, 4$  (the piecewise expression is not given explicitly here due to the length of the constituent pieces). From this, a linear, homogeneous system can be generated as

$$(\Gamma(\lambda) - I_4)\mathbf{x} = \mathbf{0} \quad (5.83)$$

where

$$\Gamma(\lambda) = \begin{pmatrix} f_1(\xi_1; \lambda) & f_2(\xi_1; \lambda) & f_3(\xi_1; \lambda) & f_4(\xi_1; \lambda) \\ f_1(\xi_2; \lambda) & f_2(\xi_2; \lambda) & f_3(\xi_2; \lambda) & f_4(\xi_2; \lambda) \\ f_1(\xi_3; \lambda) & f_2(\xi_3; \lambda) & f_3(\xi_3; \lambda) & f_4(\xi_3; \lambda) \\ g_1(\phi; \lambda) & g_2(\phi; \lambda) & g_3(\phi; \lambda) & g_4(\phi; \lambda) \end{pmatrix}, \quad (5.84)$$

and  $\mathbf{x} = (\delta v(\xi_1), \delta v(\xi_2), \delta v(\xi_3^-), \delta v(\phi^-))^T$ . The explicit entries of  $\Gamma(\lambda)$  are listed in Appendix C.4.

A non-trivial solution for the perturbations  $\delta v$  at the switching events,  $\mathbf{x}$ , exists if and only if  $\det(\Gamma(\lambda) - I_4) = 0$ . This constraint defines the *Evans function* for this system as

$$\mathcal{E}(\lambda) = \det(\Gamma(\lambda) - I_4), \quad (5.85)$$

which vanishes only for certain values of  $\lambda \in \mathbb{C}$ . To find these, we let  $\lambda = a + ib$ ,  $a, b \in \mathbb{R}$ , and compute the zero-contours of  $\text{Re } \mathcal{E}(\lambda)$  and  $\text{Im } \mathcal{E}(\lambda)$ . The exact zeros to  $\mathcal{E}(\lambda)$  occur where the zero real and imaginary contours intersect. These are the eigenvalues to the stability problem. When all non-trivial eigenvalues are such that  $\text{Re}(\lambda) < 0$ , the wave is stable. Otherwise, it is unstable.

Figure 5.23 shows the zero contours of the Evans function for a linearly stable travelling wave: all eigenvalues are contained in the left-hand side of the complex plane. Upon increasing the spatial period  $\phi$ , a pair of eigenvalues touches the imaginary axis, as seen in Figure 5.24, indicating the onset of an instability. This point is shown in Figure 5.21 by a transition from a

---

black solid to a black dashed line at  $\phi = 0.782\text{mm}$ . For larger values of  $\phi$ , a pair of complex conjugate eigenvalues with positive real parts exist, as shown in Figure 5.25. This indicates a linearly unstable periodic travelling wave. In this way, we are able to delineate the stability boundaries for the dispersion curves,  $c = c(\phi)$ , shown in Figure 5.21.

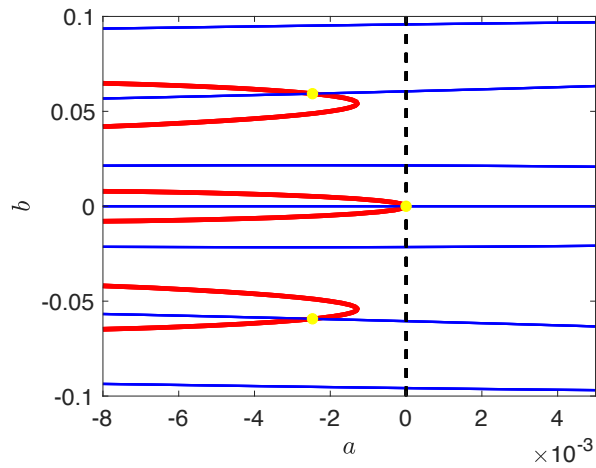


Figure 5.23.: Zero-contours of  $\text{Re } \mathcal{E}(\lambda)$  (thick, red curve) and of  $\text{Im } \mathcal{E}(\lambda)$  (thin, blue curve) for  $\phi = 0.74\text{mm}$  for a linearly stable wave. Intersections of the zero-contours, and hence zeroes of  $\mathcal{E}(\lambda)$ , are shown as yellow dots. The black dashed line separates the two complex half planes with negative and positive real part, respectively. Parameter values as in Table 4.

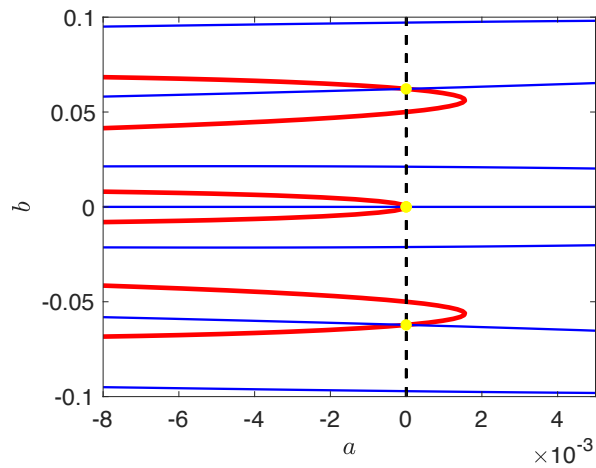


Figure 5.24.: Zero-contours of  $\text{Re } \mathcal{E}(\lambda)$  (thick, red curve) and of  $\text{Im } \mathcal{E}(\lambda)$  (thin, blue curve) for  $\phi = 0.782\text{mm}$  for a wave at a linear instability. Intersections of the zero-contours, and hence zeroes of  $\mathcal{E}(\lambda)$ , are shown as yellow dots. The black dashed line separates the two complex half planes with negative and positive real part, respectively. Parameter values as in Table 4.

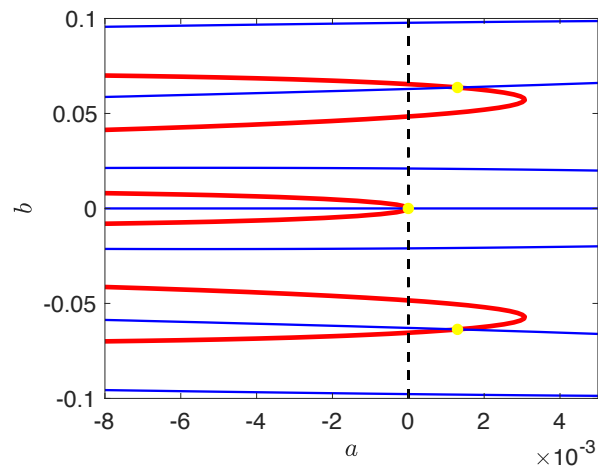


Figure 5.25.: Zero-contours of  $\text{Re } \mathcal{E}(\lambda)$  (thick, red curve) and of  $\text{Im } \mathcal{E}(\lambda)$  (thin, blue curve) for  $\phi = 0.824\text{mm}$  for a linearly unstable wave. Intersections of the zero-contours, and hence zeroes of  $\mathcal{E}(\lambda)$ , are shown as yellow dots. The black dashed line separates the two complex half planes with negative and positive real part, respectively. Parameter values as in Table 4.

### 5.10 TRANSLATION INVARIANCE OF SPATIALLY PERIODIC TRAVELLING WAVES

A zero eigenvalue is shown in all three wave stability plots (Figures 5.23–5.25). This trivial eigenvalue originates from the translational invariance of the underlying equations. Its persistence can be established by showing that  $z'(\xi)$  is an eigenfunction to the stability problem when  $\lambda = 0$  [115].

For the local variables,  $v(\xi)$  and  $h(\xi)$ , this is readily shown by differentiating the travelling wave equations (5.57) and (5.54) with respect to  $\xi$  and comparing with the evolution equations for the spatial parts of the perturbations (5.75) and (5.74), respectively.

In the case of the synaptic variable, first differentiate (5.48) to obtain

$$\frac{du}{d\xi} = \frac{1}{\tau_R} \sum_{m \in \mathbb{Z}} \int_0^\infty ds \eta(s) \times \left( w(|-m\phi + cs + \xi - \xi_1|) - w(|-m\phi + cs + \xi - \xi_2|) \right), \quad (5.86)$$

where we have used that

$$W'(x) = \frac{d}{dx} \int_{\xi_1}^{\xi_2} w(x-y) dy = w(x - \xi_1) - w(x - \xi_2). \quad (5.87)$$

Then setting  $\lambda = 0$  in (5.67), we obtain

$$\delta u(\xi; 0) = \frac{1}{\tau_R} \sum_{m \in \mathbb{Z}} \int_0^\infty ds \eta(s) \sum_{j=1}^2 w(\xi - \xi_j - m\phi + cs) \frac{\delta v(\xi_j)}{|v'(\xi_j)|}. \quad (5.88)$$

Making the substitution  $\delta z(\xi) = z'(\xi)$ , we have

$$\delta u(\xi; 0) = \frac{1}{\tau_R} \sum_{m \in \mathbb{Z}} \int_0^\infty ds \eta(s) \sum_{j=1}^2 w(\xi - \xi_j - m\phi + cs) \frac{v'(\xi_j)}{|v'(\xi_j)|}. \quad (5.89)$$

A critical observation in the demonstration of translation invariance is that  $v'(\xi_1) > 0$  and  $v'(\xi_2) < 0$  by construction. This is illustrated in Figure 5.26, and yields

$$\frac{v'(\xi_1)}{|v'(\xi_1)|} = 1, \quad \frac{v'(\xi_2)}{|v'(\xi_2)|} = -1, \quad (5.90)$$

and so (5.89) reduces to (5.86) as required.

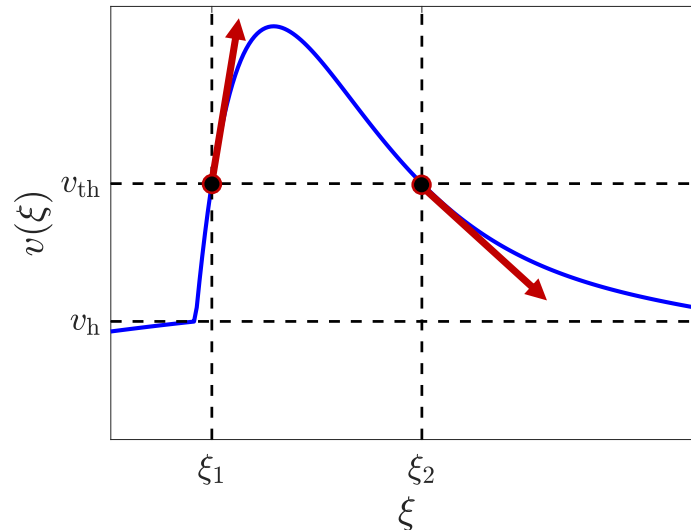


Figure 5.26.: An illustration showing a close-up of the travelling wave solution  $v(\xi)$  depicted in Figure 5.19 near  $\xi_1$  and  $\xi_2$ . Graphically, it is evident that  $v'(\xi_1) > 0$  and  $v'(\xi_2) < 0$ .

Therefore,  $\delta z(\xi) = z'(\xi)$  is a solution to the stability problem for  $\lambda = 0$ , showing the spatial translation invariance of the system, and that the travelling wave orbit is neutrally stable to tangential perturbations.

## 5.11 SUMMARY

Thalamic tissue, and indeed many other subcortical tissues, have, up until now, not enjoyed the same modelling successes as has been seen for the cortex, where neural fields are readily used in understanding the patterning observed. A few examples of cortical patterns are waves of activity that propagate in the primary visual cortex of the awake monkey [153], and the intra-cortical, rhythmic alpha oscillations fluctuating around 10Hz in human brains, recorded via electroencephalograms (EEG) [96]. The Heaviside world perspective adopted by Amari [5], and the growth of non-smooth dynamical systems theory fostered many of the successes of cortical modelling [68, 177, 45, 50]. The domain of the standard neural field is the cortex. Its great advantage is its succinct description of tissue connectivity. In this

---

chapter, we have reviewed the approach in [44] which shows how to extend the standard neural field framework to effectively model *sub-cortical* tissue. The thalamus has been taken as a case-in-point. Non-linear ionic currents expressed at the *cellular* level play a significant role in shaping the firing response at the *tissue* level [55]. By augmenting the neural field description of tissue connectivity with a minimal voltage envelope description of thalamic cell dynamics, we are able to generate a tissue level firing rate model of thalamic tissue. This is done by composing the firing rate function in a standard Amari-style neural field with some non-spiking voltage variable which incorporates a description of gating dynamics for the relevant ionic currents.

The augmented neural field approach is sufficiently general that it is amenable to tissues other than the thalamus where ionic currents play an important role in tissue-level activity – one simply includes the relevant currents and gating dynamics associated with those into the overarching voltage variable. In order to conduct a mathematically tractable analysis as has been done in this chapter, adopting a switch-like perspective for the gating variable dynamics is helpful, though we stress that the non-smoothness introduced must be treated with care, using appropriate non-smooth methodologies [154]. Perhaps more fundamentally, it is important to ensure that the dynamics of the switch-like system is qualitatively similar to that of the full model if the goal is to extract meaningful information about modelled phenomena. For example, one should check whether bifurcations occur at similar locations in parameter space, and that the emergent pattern is qualitatively similar in each case. Here, we have considered a PWL description, and shown that the Amari-style methodology for constructing solutions and analysing their stability is valid for the augmented model.

Crucially, the thalamic model expresses the post-inhibitory rebound phenomenon postulated by Andersen and Eccles (1962) [7] which is a characteristic behaviour of thalamo-cortical cells. Robust, whole tissue synchronous periodic oscillations (the spatially synchronous periodic orbit) are

supported via PIR. These oscillations do not arise via a Hopf bifurcation from a spatially homogeneous steady state as is typically the case in neural fields [33], but exist as a direct consequence of the rebound mechanism. By blending traditional periodic orbit stability methods, in which a monodromy matrix taking perturbations over a period is critical in establishing stability [125], with techniques from non-smooth dynamical systems theory, we have been able to determine the points of instability to the spatially synchronous periodic orbit. We have shown how to construct *new network-level* saltation operators, which take spatial effects into account, to determine the linear stability of the synchronous solution in this case, but the general approach we have taken is more widely applicable. Emergent solutions at the instability of synchrony include those with a spatially periodic component – with a wavelength determined by the anatomical connectivity – superimposed atop of the bulk periodic oscillations; standing 2-cycle oscillations in which a point in space fires on every other cycle, and the pattern on one cycle is shifted by half a spatial cycle on the next temporal cycle; and an instance of lurching waves, in which discrete clumps of activity travel across the domain in a saltatory rather than continuous manner. Direct numerical simulation coupled with a periodic orbit continuation approach further showed that 2-cycles may destabilise into other 2-cycles, or into irregular patterns with disordered dynamics. In short, a number of exotic solutions exist in this simplified model of thalamic circuitry. By considering stationary solutions in a co-moving frame, we have shown how to construct wavetrains in 1D and have utilised saltation operators to construct the Evans function in determining wave stability. Direct numerical simulation shows excellent agreement with the stable branch of the theoretically determined dispersion curve.

The work in this chapter has probed the understanding of patterning from a few different perspectives: an analytical study has been supplemented by direct numerical simulation and a numerical bifurcation analysis. We have shown that the PIR mechanism is able to generate exotic patterning.

Although we have taken a step towards understanding the rich dynamics in neural field models with rebound currents, there is clearly more to do, for example in understanding the secondary bifurcations that lead to travelling, oscillating hexagons on the plane, and the routes to exotic pattern generation. Natural steps forward include a more thorough analysis of planar patterning, as has been done in this chapter for 1D patterns, as well as a continuation of lurching waves, and an analytical construction of lurching waves, since these are a hallmark of systems with  $I_T$  [178]. It is also worth pursuing what mechanisms are *necessary* for lurching waves to form. Here, we have used  $I_T$ , but other rebound currents exist, such as the hyperpolarisation-activated current ( $I_h$ ) which have also been shown to give rise to exotic patterns [25] in networks of cells. Are lurching waves a by-product of  $I_T$  specifically, and appropriate tissue connectivity, or is there a more fundamental pattern generator – that may incorporate rebound currents other than  $I_T$ , for example – at play?

We have considered a closed-loop one-layer model of TC cells, but a more refined, two-layer model of thalamic tissue, and the connectivity between TC and RE cells, as illustrated in Figure 2.14, was studied by Yew et al. (2001) [234]. The switch-like perspective adopted throughout this chapter is well-suited to the study of the two-layer model and would facilitate a similar analysis as has been carried out here, albeit with the extra book-keeping that would come with a two-layer model.

A PWL description is a closer approximation to the fully non-linear sigmoidal description of gating variables and firing rate functions. Indeed, by adopting a PWL approach, it is possible to accommodate window currents that arise when multiple gating variables co-operate in the generation of persistent background currents. Notice that, in the model (5.15) considered in this chapter, the switching manifold  $v_h$  is such that when  $I_T$  is activated,  $h$  is decreasing; a PWL approach allows activation and inactivation curves to overlap, thus generating window currents without detriment to mathe-

---

mathematical tractability. This more generic mixing of gating dynamics may lead to novel dynamics.

---

## DISCUSSION

---

Models of single neuron dynamics have done much to aid in the understanding of neural dynamics. Mechanisms behind action potential generation have been determined by modelling and validated experimentally [100]. The work in this thesis has studied the dynamics that arise in networks of connected neurons. A continuum study has been carried out which has allowed for the use of many continuum dynamical systems techniques for analysis.

To conclude this thesis, we recapitulate the work that has been carried out and the novel findings, before moving on to a discussion of future work that branches off what has been done here.

### 6.1 THESIS RECAPITULATION

A range of topics have been considered in this thesis, but principally, the aim has been to effectively model patterning – and the *mechanisms* behind patterning – in multiple structures within the brain, and to develop new techniques for the analysis of the resulting models.

A review of the relevant neuronal biology and the main analytical techniques used in the bulk of the thesis was given in Chapter 2. The biophysical mechanisms underlying information transmission at a chemical synapse were described, and the development of synaptic models effectively capturing this was reviewed. These are critical in modelling tissue interactions;

the  $\alpha$ -function provides a good description of post-synaptic response and is used in our study of thalamic tissue. The non-canonical PIR mechanism that underlies burst firing plays an important role in generating activity in thalamic tissue. It is an effective mechanism for rhythmogenesis [44, 234] as has been seen in the study of periodic activity in Chapter 5.

Chapter 3 developed numerical techniques for the continuation and stability of spatially extended periodic structures in sufficiently smooth models. Beginning with a description of linear stability in continuous and discrete dynamical systems, we describe how standard continuation algorithms work before reviewing the existing literature for the continuation of equilibria and travelling wave structures. The bulk of this chapter then focuses on using, developing, and testing the methodologies in [216] for the continuation of temporally periodic structures and travelling temporally periodic structures in neural field models. An important novel contribution resulting from this chapter is the development of a continuation software suite incorporating all of the above, which is not restricted to neural-type models.

The focus then shifts away from the development of techniques, and moves towards modelling in Chapter 4. Neural fields have been shown to be effective in modelling cortical activity; we consider an alteration to the standard neural field which incorporates a dynamically varying threshold. Beginning with a linear stability analysis of the spatially homogeneous steady state, we demonstrated that steady and Hopf bifurcations were not present in the model, but that Turing and Turing-Hopf bifurcations were present in the case that the firing rate function and the threshold accommodation functions were both sigmoidal (rather than Heaviside functions). A spatially more complex bump solution was then considered, and an Evans function approach was utilised to determine bump stability. Pulses and breathers were found at the instability of symmetric bumps, while sloshers emerged from asymmetric bumps. The final part of the chapter focuses on the novel continuation of temporally periodic structures such as standing

---

waves, saltatory travelling periodic waves, and travelling breathers using the techniques developed in Chapter 3.

Chapter 5 focuses on modelling in a sub-cortical structure: the thalamus. The model is a neural field describing tissue connectivity augmented to a voltage description of thalamic tissue. The first half of this chapter considers spatial synchrony and the construction of the spatially synchronous periodic orbit and its stability using saltation techniques to correctly characterise jumps in the solution due to vector field discontinuities in the model. Lurching waves appear to be a hallmark feature of thalamic models; we demonstrated that a mechanism for their generation is through a Neimark-Sacker instability of the synchronous periodic orbit. Studies on the plane show a rich variety of patterns that may form. We investigated this via a blend of numerical simulation and the 2D linear stability theory developed for spatial synchrony. Standing and periodic patterns emerging from the instability of synchrony were investigated through continuation. This was a natural approach to gain insight into spatially non-trivial patterns. The second half of the chapter focuses on spatially periodic travelling waves. The dispersion relation between the wave-speed and the spatial period was determined analytically, with excellent agreement between theory and direct simulation. The attention then turned to using saltation methods coupled with an Evans function approach to determine linear stability of the wave-train solution. On the whole, this chapter developed predictive theories which successfully characterised multiple solutions to a model of thalamic tissue. The approach used is sufficiently general for the framework to be applied in models of other sub-cortical tissues too.

## 6.2 FUTURE WORK

This work opens up a number of fruitful paths forward in the analysis of brain dynamics from mathematical perspectives, some of which have been

outlined in the summary sections of each chapter. Here, we briefly recap these and discuss other pieces of work which can branch off from this thesis.

Much of the analysis in this work has relied on PWL caricatures of smooth models. Where smooth sigmoidal functions (5.40) have been present, these have been approximated by a discontinuous Heaviside function. This makes analysis much more straightforward, but comes at the cost of introducing Type 2 discontinuities into the model (see Table 1). Instead of a Heaviside function, a more refined PWL caricature can be considered. Whereas the Heaviside function approximates a sigmoidal function into *two* (discontinuous) linear pieces, the natural next step is to partition the sigmoid into *three* pieces. This is shown in Figure 6.1, with the sigmoidal function shown in black, the Heaviside in blue, and the PWL function shown in dashed orange. The refined PWL curve,  $f_{\text{PWL},3}(u)$ ,<sup>1</sup> is constructed by matching the slope of the central piece to the sigmoid at  $u = \kappa$ . This gives

$$f_{\text{PWL},3}(u) = \begin{cases} 0, & u \leq u_-, \\ \frac{1}{2} + \frac{\mu}{4}(u - \kappa), & u_- < u < u_+, \\ 1, & u \geq u_+. \end{cases} \quad u_{\pm} = \kappa \pm \frac{2}{\mu}. \quad (6.1)$$

It is evident from Figure 6.1 that while the Heaviside function provides a good first order approximation to the sigmoidal function, there are a large portion of values for  $u \in (-1, 1)$  which are not accurately captured. The refined PWL function does a much better job at capturing the changes in the sigmoid and reduces the type of discontinuities from Type 2 to Type 1. Its PWL nature ensures that models using it are amenable to analysis, although it does require tracking non-smooth effects at the two distinct points,  $u = u_{\pm}$ , rather than the Heaviside function, which only requires event tracking at the single point  $u = \kappa$ . This framework can be applied not only to firing rate functions, but to the activation curves and time-scale functions of gating

---

<sup>1</sup>The subscript 3 indicates that the PWL caricature has three linear pieces. Under this notation,  $f_{\text{PWL},2}(u) = H(u - \kappa)$ , and  $f_{\text{PWL},1}(u) = 1/2$ .

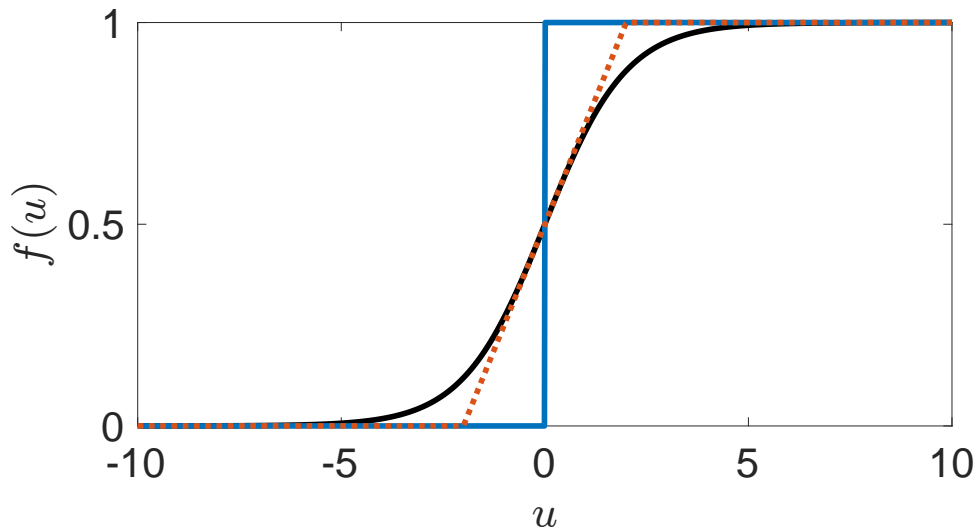


Figure 6.1.: The sigmoid function (5.40) in black, plotted along with two of its PWL caricatures. The two piece caricature,  $H(u - \kappa)$ , is in blue, while the refined three piece caricature, given by (6.1), is in dashed orange. Here,  $\mu = 1$ , and  $\kappa = 0$ .

variables, such as  $h_\infty(v)$  and  $\tau_h(v)$  in (5.5). In the Heaviside framework, gating dynamics are switch-like, with no overlap between activation and inactivation curves; with this refined PWL approach, the opportunity for window currents [131] arises, along with the opportunity for the analysis of any novel dynamics that are sensitive to the existence of window currents. Of course, the PWL caricature can be refined further, however there is no practical benefit in doing so, unless solutions exist in the fully sigmoidal limit which are not captured by  $f_{\text{PWL},3}$ . With further refinement comes more book-keeping during analysis. An appropriate PWL caricature should reflect the original model in its dynamics.

In Chapter 4, the stability of a stationary bump was determined in a neural field with a dynamic firing threshold with smoothed threshold dynamics. The original model considered in [50] is given by (4.1). The *offending term* with regards to bump stability is the exposed Heaviside function  $H(u - \theta)$  in the threshold dynamics.

To see why, consider linearising about a bump solution given by  $q(x)$  and  $p(x)$  with appropriate switching conditions to determine the unknowns parameterising the bump. Note that these may differ from those found in Section 4.4. Suppose for simplicity that the switching conditions are as shown in Figure 4.1 so that  $q(x) = p(x)$ , for  $x = x_i$ ,  $i = 1, 3, 4, 6$ , and  $q(x) = \theta$  for  $x = x_i$ ,  $i = 2, 5$ . Then upon linearising the dynamics for  $u$  and  $h$  about the bump via  $z(x, t) = z(x) + \delta z(x)e^{\lambda t}$  to determine bump stability, we obtain

$$\delta u(x) = \sum_{i=1, i \neq 2, 5}^6 g(x, x_i; \lambda)(\delta u(x_i) - \delta h(x_i)), \quad (6.2)$$

where

$$g(x, a; \lambda) = \tilde{\eta}(\lambda) \frac{w(x - a)}{|q'(a) - p'(a)|}. \quad (6.3)$$

and

$$\delta h(x) = \kappa \tilde{\eta}_h(\lambda) \delta(q(x) - \theta) \delta u(x, t), \quad (6.4)$$

where  $\tilde{\eta}_h = 1/(1 + \lambda)$ . The problem here is that  $\delta h(x) = 0$  for all  $x$  away from the accommodation threshold,  $\theta$ . This includes at  $x = x_i$ ,  $i = 1, 3, 4, 6$ . So there is no contribution to (6.2) from  $\delta h$ . Moreover, at  $x = x_i$ ,  $i = 2, 5$ ,  $\delta h(x)$  takes the functional form of a non-zero delta function, and is therefore undefined. It does not sit underneath an integral (even an implicit one), therefore a direct stability approach using saltation operators is unsuccessful here. Clearly, there *is* a contribution from  $\delta h$ , as shown in [50], and it depends on  $\delta h(x_i)$ ,  $i = 2, 5$ , however the saltation techniques used fail in this case. In a sense, the system is *too non-smooth* for the saltation approach to cope with. In the discussion of types of discontinuities in dynamical systems in Chapter 2,  $\delta h(x)$  above does not fit into the Type 0, 1, 2, or 3 discontinuities shown in Table 1. It is very likely that using a PWL caricature such as (6.1) to approximate the firing rate and/or accommodation functions will deal with this issue effectively, since (6.1) effectively reduces the order of non-smoothness present (see Table 1). The issue detailed above arises from the discontinuous nature of the Heaviside function in the evolution equation for  $h$ . We postulate here that by replacing the discontinuous

Heaviside with a continuous, albeit non-smooth function such as (6.1), we expect the saltation approach to be fruitful.

It is of interest to develop the saltation approach to be able to cope with situations like this. Of course, the situation can be resolved by smoothing the threshold dynamics, as shown in Section 4.5. This is successful because it yields an integral over the exposed delta function in the linearisation. However a direct stability result for such non-smooth systems would develop new analytical techniques in the analysis of non-smooth dynamical systems.

In 2005, Hafting et al. [88] discovered grid cells in the medial entorhinal cortex (MEC) which act to serve as a spatial map in the brain. They showed that grid cells in the dMEC tend to fire at the nodes of a hexagonal lattice. That is, given a single grid cell neuron, if a mammal is to move around in real space, then that single neuron will fire at the nodes of a hexagonal lattice tiling real space. They demonstrated this with experiments measuring firing of single grid cell neurons in rats that were able to traverse a confined space for a sufficiently long time such that the rat crossed multiple places in real space, multiple times. In this way, grid cell firing fields were generated (as in Figure 1 in [88]).

Since this discovery, a number of different models have been suggested as a mechanism for how grid cell activity can emerge. The work by Bonilla-Quintana et al. (2017) [25] is a mathematical study of grid cell firing fields modelled by a spiking network of IF neurons. Hyperpolarisation-activated cyclic-nucleotide-gated (HCN) channels are expressed in cells in the medial entorhinal cortex (MEC). These ion channels give rise to the  $I_h$  rebound current when cells are stimulated by hyperpolarising input. The dynamics of  $I_h$  and  $I_T$  can be contrasted as follows. While inactivation of  $I_T$  may be modulated,  $I_h$  is a non-inactivated current that activates as levels of hyperpolarisation increase [63]. Specifically,  $I_h = -g_h n_h (V - V_h)$ , where

$$\frac{\partial n_h}{\partial t} = \frac{n_{h,\infty}(V) - n_h}{\tau_h(V)}, \quad n_h = n_h(\mathbf{r}, t), \quad \mathbf{r} \in \mathbb{R}^2, t > 0, \quad (6.5)$$

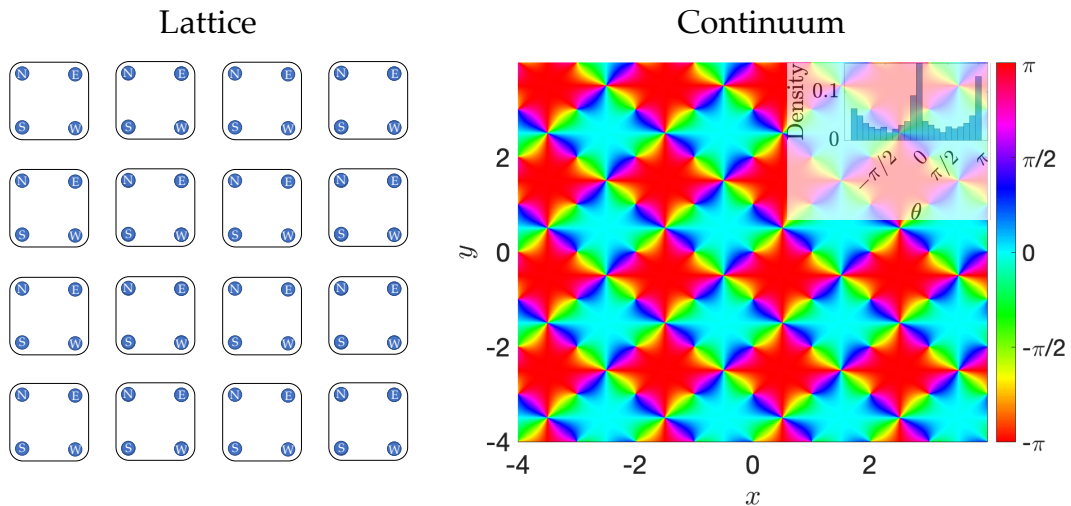


Figure 6.2.: Head direction preference maps on the lattice (left) and the continuum (right). The lattice tiling is as used by Burak and Fiete [30], and consists of repeating  $2 \times 2$  nodes with preferences aligned to the four compass points (N, E, S, W) as illustrated on this  $2^3 \times 2^3$  sized lattice. The continuum tiling is doubly periodic with colour representing the preferred angle,  $\theta$ , at that point in space. The relative density of angles for this HDPM is shown in the semi-transparent histogram in the inset.

which may be contrasted with the form of  $I_T$ , given by (5.4). The work in [25] determines a dispersion relation between the speed of periodic waves and the spatial period, exhibiting a wide range of long wavelength solutions. This is in contrast to the dispersion curve studied in Chapter 5 for the thalamic model shown in Figure 5.21 (showing a relatively small range of wavelengths for stable waves), and supports the hypothesis that  $I_h$  rebound firing modulates the spatial scale of grid cell firing fields in the MEC.

Another main idea are the so-called “continuous attractor” models, as studied in [30]. In these models, “grid cell activity arises from the collective behaviour of a neural network”. The idea is that the network state in the absence of any velocity-dependent drive is steady, whether that be a patterned state (e.g. hexagonal patterning) or a homogeneous state. Upon a response to the velocity of a rat/mammal, the network state is updated accordingly.

A first-order model of grid-cell activity can be constructed by considering a Hopfield network with shifted connectivity and a head-direction preference map (HDPM). The HDPM endows neurons or tissue with a preferred direction such that movement in a particular direction in space induces a larger integrated input from the neurons endowed with a similar head direction [30]. There is currently no experimentally determined HDPM much like there is an orientation preference map in the visual cortex [226]. As such, in a modelling study, there is freedom in how the HDPM is chosen. Burak and Fiete (2009) [30] demonstrated that such a model posed on a lattice driven by the velocity of an agent (e.g., a rat) can drive hexagonal patterns across domains with both periodic and zero-flux boundary conditions. Their HDPM consisted of a  $2 \times 2$  repeated tiling of the domain with a preferred angle  $\phi \in \{0, \pi/2, \pi, 3\pi/2\}$ , corresponding to the four compass points, as shown in the left-hand panel of Figure 6.2. A predictive theory can be developed, indicating which direction(s) are poised to go unstable upon the inclusion of velocity-dependent drive as follows.

Let us re-introduce the Hopfield-style model posed on a finite continuum  $\mathbf{r} = (x, y) \in \mathbb{R}^2$  considered in Chapter 3 (3.17), as<sup>2</sup>

$$\tau \frac{\partial}{\partial t} s(\mathbf{r}, t) = -s(\mathbf{r}, t) + f \left( \iint_{\Omega_p^2} w(\mathbf{r}, \mathbf{r}') s(\mathbf{r}', t) d\mathbf{r}' + B(\mathbf{r}) \right), \quad (6.6)$$

where the domain is the finite periodic plane (torus) given by  $\Omega_p^2 = [-L, L]^2$ ; the subscript  $p$  indicates periodic boundary conditions. The connectivity  $w$  includes a shift  $\epsilon \mathbf{g}$ , so that

$$w(\mathbf{r}, \mathbf{r}') = w(\mathbf{r} - \mathbf{r}' - \epsilon \mathbf{g}(\mathbf{r}')), \quad (6.7)$$

where  $\mathbf{g}$  represents the HDPM, and is specified by

$$\mathbf{g}(\mathbf{r}) = (\cos \phi(\mathbf{r}), \sin \phi(\mathbf{r}))^T, \quad (6.8)$$

where  $\phi(\mathbf{r})$  indicates the preferred angle at position  $\mathbf{r}$ . On the torus, we use a HDPM which is doubly periodic; such maps may be generated by the

<sup>2</sup>In this discussion, vectors are denoted in bold for clarity.

Weierstrass elliptic function [132]. An example is shown in the right-hand panel of Figure 6.2. The parameter  $\epsilon \ll 1$  is small. A first order expansion of  $w$  in  $\epsilon$  yields

$$w(\mathbf{r} - \mathbf{r}' - \epsilon \mathbf{g}(\mathbf{r}')) = w(\mathbf{r} - \mathbf{r}') - \epsilon \nabla w(\mathbf{r} - \mathbf{r}') \cdot \mathbf{g}(\mathbf{r}') + \mathcal{O}(\epsilon^2). \quad (6.9)$$

Finding the steady state  $s(\mathbf{r}, t) = s(\mathbf{r})$ , and expressing it as a perturbation expansion in  $\epsilon$  as  $s(\mathbf{r}) = s_0 + \epsilon s_1(\mathbf{r}) + \mathcal{O}(\epsilon^2)$  gives the conditions determining  $s_0$  and  $s_1(\mathbf{r})$  at  $\mathcal{O}(1)$  and  $\mathcal{O}(\epsilon)$  respectively as

$$0 = -s_0 + f(s_0 \widehat{w}_0 + B), \quad (6.10a)$$

$$\begin{aligned} \{-1 + f'(s_0 \widehat{w}_0 + B) w \circledast\} s_1 &= f'(s_0 \widehat{w}_0 + B) s_0 \\ &\times \iint_{\Omega_p^2} \nabla w(\mathbf{r} - \mathbf{r}') \cdot \mathbf{g}(\mathbf{r}') d\mathbf{r}'. \end{aligned} \quad (6.10b)$$

This specifies the steady state with  $\epsilon \ll 1$  up to  $\mathcal{O}(\epsilon)$ . The symbol  $\circledast$  denotes a spatial convolution *on the finite domain*  $\Omega_p^2$  as

$$(w \circledast s)(\mathbf{r}, t) = \int_{-L}^L \int_{-L}^L w(\mathbf{r} - \mathbf{r}') s(\mathbf{r}', t) d\mathbf{r}'. \quad (6.11)$$

To determine the linear stability of the steady state, perturb about it so that  $s(\mathbf{r}, t) = s(\mathbf{r}) + e^{\lambda t} u(\mathbf{r})$ , resulting in

$$\begin{aligned} (\tau\lambda + 1)u(\mathbf{r}) &= \\ &f' \left( \iint_{\Omega_p^2} (w(\mathbf{r} - \mathbf{r}') - \epsilon \nabla w(\mathbf{r} - \mathbf{r}') \cdot \mathbf{g}(\mathbf{r}')) (s_0 + \epsilon s_1(\mathbf{r}')) d\mathbf{r}' + B \right) \\ &\times \left( w \circledast u - \epsilon \iint_{\Omega_p^2} \nabla w(\mathbf{r} - \mathbf{r}') \cdot \mathbf{g}(\mathbf{r}') u(\mathbf{r}') d\mathbf{r}' \right). \end{aligned} \quad (6.12)$$

Upon the perturbation expansion  $u(\mathbf{r}) = u_0(\mathbf{r}) + \epsilon u_1(\mathbf{r}) + \mathcal{O}(\epsilon^2)$  and  $\lambda = \lambda_0 + \epsilon \lambda_1 + \mathcal{O}(\epsilon^2)$ , we obtain the conditions

$$\mathcal{L}u_0 = 0, \quad (6.13)$$

$$\mathcal{L}u_1 = -\tau\lambda_1 u_0 + \chi(u_0), \quad (6.14)$$

where the operator  $\mathcal{L}$  defined by

$$\mathcal{L}u = (\tau\lambda_0 + 1)u - f'(s_0 \widehat{w}(0) + B)(w \circledast u), \quad (6.15)$$

is self-adjoint,<sup>3</sup> and

$$\begin{aligned} \chi(u_0) = & -f'(s_0\widehat{w}(0) + B) \iint_{\Omega_p^2} \nabla w(\mathbf{r} - \mathbf{r}') \cdot \mathbf{g}(\mathbf{r}') u_0(\mathbf{r}') d\mathbf{r}' \\ & + f''(s_0\widehat{w}(0) + B) \left( w \circledast s_1 - s_0 \iint_{\Omega_p^2} \nabla w(\mathbf{r} - \mathbf{r}') \cdot \mathbf{g}(\mathbf{r}') d\mathbf{r}' \right) \\ & \times (w \circledast u_0). \end{aligned} \quad (6.16)$$

(6.13) determines  $\lambda_0$ , with the corresponding solution  $u_0(\mathbf{r}) = \exp(i\mathbf{k}_j \cdot \mathbf{r})$ , where  $\mathbf{k}_j$  are the wavevectors that fit inside the finite periodic domain. To determine  $\lambda_1$ , we introduce the solvability condition

$$\langle u_0, \mathcal{L}u_1 \rangle = 0, \quad (6.17)$$

which arises via the properties that  $\mathcal{L}$  is self-adjoint and  $\mathcal{L}u_0 = 0$ . The inner product is defined on the torus as

$$\langle u, v \rangle = \int_{-L}^L \int_{-L}^L u^*(\mathbf{r}) v(\mathbf{r}) d\mathbf{r}, \quad (6.18)$$

where  $u^*(\mathbf{r})$  is the complex conjugate of  $u(\mathbf{r})$ . Then  $\lambda_1 = \langle u_0, \chi(u_0) \rangle / \tau$ . The pattern  $s(\mathbf{r})$  destabilises when  $\text{Re}(\lambda_0 + \epsilon\lambda_1) = 0$ . This condition determines the wavevector(s)  $\mathbf{k}$  that become unstable. In the case where  $\epsilon = 0$ , a ring of wavenumbers determined by  $k_c = |\mathbf{k}|$  simultaneously become unstable, however, only a subset of these become unstable when bias is present in the connectivity function. In the case where there is an equal distribution of  $m$  angles  $\phi$  in the HDPM, then  $m$  wavevectors are selected to become unstable. An unequal distribution of angles where one angle dominates, such as that shown in the right-hand panel of Figure 6.2 causes a single wavevector to be selected.

Extending the capability of the continuation suite is a way of bringing modern analytical methods into the domain of mathematical neuroscience. The lurching waves seen at the Neimark-Sacker instability of the synchronous

---

<sup>3</sup> An operator  $\mathcal{L}$  is *self-adjoint* if it satisfies  $\langle \mathcal{L}u, v \rangle = \langle u, \mathcal{L}v \rangle$  for an appropriately defined inner product  $\langle \cdot, \cdot \rangle$ .

periodic orbit in the model of thalamic tissue we studied in Chapter 5 fall into the category of TWPO patterns. Figure 5.18 shows their structure through time. It is clear that there are discontinuous jumps at various points across space, throughout time. This ruins convergence to a true solution when the shift and derivative operators are implemented using a Fourier approach. Implementing a method to carry out the shift and derivative operations in an efficient manner, whilst also catering for solutions with shocks is a route forward to enable the continuation suite to be used for a larger class of solutions.

Tango waves are a relatively newly discovered dynamical phenomena, having first been observed in a diffusive bidomain model of  $\text{Ca}^{2+}$  interactions in both the cell cytoplasm and endoplasmic reticulum (ER) by Li [134] in 2005. The ER is considered to be an intra-cellular store of  $\text{Ca}^{2+}$ . The bidomain model develops upon single domain models (which only consider  $\text{Ca}^{2+}$  concentration in the cell cytoplasm as dynamic), where the ER  $\text{Ca}^{2+}$  concentration is *not* assumed to be finite or dynamic. The interactions between  $\text{Ca}^{2+}$  in the cytoplasm and the ER gives rise to tango waves in the bidomain model. They were named as such by Li due to their characteristic backwards-and-forwards propagation (reminiscent of tango dancers), and were analysed further by Thul et al. [210]. Examples are shown in Figure 4 of [134], and Figures 14 and 15 of [210]. The study by Li (2005) showed that “*the occurrence of tango waves is related to spatial inhomogeneity in the local dynamics.*” Notice that the sloshing solutions to (4.4) with non-trivial spatial inhomogeneity shown in Figure 4.18 have the characteristic “sharpness” associated with tango waves, although the sloshers are a localised pattern.

It is not inconceivable for tango waves to appear in neural field models. A dynamic neural field model with inhomogeneous spatio-temporal input, such as that studied in [231], has the ingredients described above by Li. When considering whether tango waves may be amenable to a continuation analysis, we must determine the appropriate repeating unit. Those tango waves in the right-hand pane of Figure 14 in [210] are not simply amenable

to the TWPO continuation described in Chapter 3, since that assumes that activity within each period is identical, up to a spatial shift. These tango waves appear to have a form of activity which repeats subject to some exponentially increasing scale in time. Developing the continuation suite to analyse highly non-trivial patterns such as these is a fascinating way forward that is certainly worthy of consideration.

In addition to increasing the class of solutions amenable to spatially-extended continuation, [216] includes methods to track fold-of-cycles, period-doubling-type and Neimark-Sacker-type bifurcations. Such techniques will allow a systematic study of patterning by considering how parameter space is partitioned, with different emergent spatial patterns on either side of a two parameter bifurcation curve.

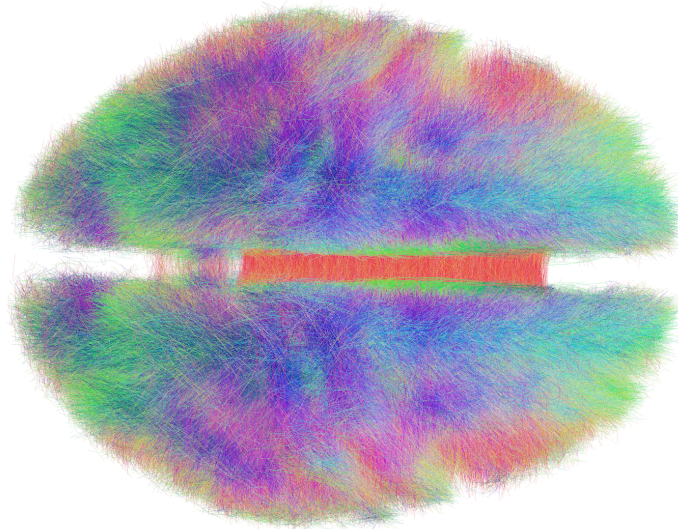


Figure 6.3.: The human connectome, showing the structural connectivity of the anatomical fibres (myelinated axons) in the brain. Each of the RGB colours correspond to fibres traversing the brain in the three different spatial dimensions respectively. This image (original author Andreas Horn) is from Wikimedia Commons and is licensed under the Creative Commons Attribution-ShareAlike 4.0 International License.

---

Furthermore, a natural extension to this modelling study is to consider “more realistic” domains. In this work, we have mostly considered periodic boundary conditions – for fast simulations via the use of fast Fourier transform (FFT) algorithms – or the infinite plane. In both cases, these assumptions simplify analysis. Although domains have been large enough so that boundary effects are nullified, for global patterning this is not the case, and indeed, global patterns depend on the boundary conditions to some extent. A modelling study on a realistic brain mesh, using connectome data, such as that shown in Figure 6.3, is likely to provide more realistic insights, although this comes at the cost of requiring an almost exclusively computational study. Moreover, novel computational techniques would be required to simulate a neural field on a brain mesh with folded surfaces and axonal delays efficiently [167].

# A

---

## APPENDICES: BACKGROUND

---

### A.1 GREEN'S FUNCTIONS FOR SYNAPTIC RESPONSES

Here, we show explicitly that the exponential decay function given by

$$\eta(t) = \alpha e^{-\alpha t} H(t),$$

is the Green's function of the first-order linear differential operator

$$Q = \left(1 + \frac{1}{\alpha} \frac{d}{dt}\right).$$

We begin with consideration of the equation defining a Green's function,  $Qu = \delta$ , where  $\delta(\cdot)$  is a Dirac delta function, with the differential operator given as above. We aim to show that the Green's function is given by the exponential decay function.

With this set-up, about  $t = 0$  we have

$$\left(1 + \frac{1}{\alpha} \frac{d}{dt}\right) \eta(t) = \delta(t), \tag{A.1}$$

which, upon rearranging terms, may be written as

$$\frac{d\eta}{dt} + \alpha\eta(t) = \alpha\delta(t). \tag{A.2}$$

This first-order linear differential equation may be solved using the integrating factor  $\exp(\alpha t)$ . Taking this step-by-step, we first obtain

$$\frac{d}{dt} (\eta(t)e^{\alpha t}) = \alpha e^{\alpha t} \delta(t). \tag{A.3}$$

Integrating this over a small region  $t \in (-\epsilon, \epsilon)$ ,  $\epsilon \ll 1$ , yields

$$\eta(\epsilon)e^{\alpha\epsilon} - \eta(-\epsilon)e^{-\alpha\epsilon} = \alpha. \quad (\text{A.4})$$

By causality,  $\eta(-\epsilon) = 0$ , therefore  $\eta(\epsilon) = \alpha e^{-\alpha\epsilon}$ . This effectively sets the initial condition just after  $t = 0$  when an impulse is received.

For  $t > 0$ ,  $\delta(t) = 0$ , therefore the differential equation reduces to

$$\frac{d\eta}{dt} + \alpha\eta(t) = 0. \quad (\text{A.5})$$

Solving this in  $t > 0$  (integrating over  $t' \in (\epsilon, t)$ ), yields

$$\eta(t) = (\alpha + A)e^{-\alpha t}, \quad (\text{A.6})$$

for some integration constant  $A$  to be determined by the initial condition,  $\eta(\epsilon) = \alpha e^{-\alpha\epsilon}$ . Applying this, the constant  $A = 0$ , yielding the Green's function as

$$\eta(t) = \alpha e^{-\alpha t}, \quad t > 0, \quad (\text{A.7})$$

and  $\eta(t) = 0$  for  $t < 0$  due to causality.

A similar calculation shows that the  $\alpha$ -function

$$\eta(t) = \alpha^2 t e^{-\alpha t} H(t), \quad (\text{A.8})$$

is the Green's function of the *second-order* differential operator

$$Q = \left(1 + \frac{1}{\alpha} \frac{d}{dt}\right)^2. \quad (\text{A.9})$$

Here two initial conditions are required: one setting the value  $\eta(\epsilon)$  and one setting the slope  $\eta'(\epsilon)$ .

## A.2 DERIVING FIRING RATES IN INTEGRATE-AND-FIRE MODELS

### A.2.1 Linear Integrate-and-Fire Model

A linear IF model takes the form

$$\tau_m \frac{dv}{dt} = -v(t) + u(t), \quad (\text{A.10})$$

with the firing and reset conditions at firing times  $t^f$   $u(t^{f-}) = v_{\text{th}}$  and  $u(t^{f+}) = v_{\text{reset}}$ . Now suppose that  $u(t) = U$  is constant, then

$$\tau_m \frac{dv}{dt} = -v(t) + U. \quad (\text{A.11})$$

For the initial condition, we choose the start of a period so that  $v(t_1) = v_{\text{reset}}$ . Now integrating up from  $v(t_1) = v_{\text{reset}}$ , we obtain

$$\int_{v_{\text{reset}}}^v \frac{1}{-v' + U} dv' = \int_{t_1}^t \frac{1}{\tau_m} dt' \quad (\text{A.12})$$

Integrating this and rearranging for  $v(t)$ , we obtain

$$v(t) = U - (U - v_{\text{reset}})e^{-(t-t_1)/\tau_m}. \quad (\text{A.13})$$

If  $v_{\text{th}} > U$ , no spike occurs, since in the absence of a firing event,  $v(t) \rightarrow U$  as  $t \rightarrow \infty$ . However, if  $v_{\text{th}} < U$ , spikes occur with a regular inter-spike interval. If we let  $t_2$  denote the first time after  $t_1$  at which  $u(t) = v_{\text{th}}$ , then the inter-spike interval is given by  $T = t_2 - t_1$ . The threshold condition  $u(t_2) = v_{\text{th}}$  states

$$U - (U - v_{\text{reset}})e^{-(t_2-t_1)/\tau_m} = v_{\text{th}}. \quad (\text{A.14})$$

Solving (A.14) for  $T$ , we obtain

$$T = \tau_m \log \left( \frac{U - v_{\text{reset}}}{U - v_{\text{th}}} \right). \quad (\text{A.15})$$

The total firing period,  $\Delta$  with the inclusion of an absolute refractory period,  $\Delta_{\text{abs}}$ , is  $\Delta = T + \Delta_{\text{abs}}$ . The mean firing rate is the reciprocal of the total firing period ( $R = 1/\Delta$ ), resulting in a firing rate  $R$  of

$$R(U) = \left( \Delta_{\text{abs}} + \tau_m \log \left( \frac{U - v_{\text{reset}}}{U - v_{\text{th}}} \right) \right)^{-1} H(U - v_{\text{th}}), \quad (\text{A.16})$$

for the IF model with constant input  $u(t) = U$ . In the case where  $u(t)$  varies slowly, (A.16) remains a good approximation to the firing rate.

### A.2.2 Quadratic Integrate-and-Fire Model

A QIF model with synaptic input  $u(t)$  takes the form

$$\frac{dv}{dt} = v^2 + I + u(t), \quad (\text{A.17})$$

with the firing and reset conditions as above. If  $u(t) = U$  is constant, then

$$\frac{dv}{dt} = -v^2 + I + U. \quad (\text{A.18})$$

Integrating up from the initial condition  $v(t_1) = v_{\text{reset}}$ , we obtain

$$\int_{v_{\text{reset}}}^v \frac{1}{-v'^2 + I + U} dv' = t - t_1 \quad (\text{A.19})$$

Integrating this, we obtain

$$\tan^{-1} \left( \frac{v(t)}{\sqrt{I+U}} \right) - \tan^{-1} \left( \frac{v_{\text{reset}}}{\sqrt{I+U}} \right) = \sqrt{I+U}(t - t_1). \quad (\text{A.20})$$

Applying the condition that the first firing event after  $t_1$  occurs at time  $t_2$ ,  $v(t_2) = v_{\text{th}}$ , we obtain an expression for the inter-spike period,  $T = t_2 - t_1$  as

$$T = \frac{1}{\sqrt{I+U}} \left( \tan^{-1} \left( \frac{v_{\text{th}}}{\sqrt{I+U}} \right) - \tan^{-1} \left( \frac{v_{\text{reset}}}{\sqrt{I+U}} \right) \right) \quad (\text{A.21})$$

As  $v_{\text{th}} \rightarrow \infty$  and  $v_{\text{reset}} \rightarrow -\infty$ ,

$$T = \frac{\pi}{\sqrt{I+U}}, \quad (\text{A.22})$$

where we have used the asymptotic property  $\tan^{-1}(\xi) \rightarrow \pm\pi/2$  as  $\xi \rightarrow \pm\infty$ .

The firing rate,  $R$  is the reciprocal of the inter-spike period,  $T$ , therefore

$$R = \frac{1}{T} = \frac{\sqrt{I+U}}{\pi} H(I+U), \quad (\text{A.23})$$

for the QIF model with constant synaptic input.

# B

---

## APPENDICES: NEURAL FIELDS WITH DYNAMIC FIRING THRESHOLDS

---

### B.1 FIRST DERIVATIVE OF SOLUTIONS

We require knowledge of  $q'(x)$  and  $p'(x)$  when determining stability. Given that the synaptic part of  $q(x)$  is given by the sum of three integrals with identical integrands but with different limits (4.31a), consider the *generic* integral

$$J(x) = \int_a^b w(x-y)dy. \quad (\text{B.1})$$

Then

$$J'(x) = \frac{d}{dx} \int_a^b w(x-y)dy, \quad (\text{B.2a})$$

$$= \int_a^b \frac{\partial}{\partial x} w(x-y)dy, \quad (\text{B.2b})$$

$$= \int_a^b w'(x-y)dy, \quad (\text{B.2c})$$

$$= \left[ -w(x-y) \right]_{y=a}^b, \quad (\text{B.2d})$$

$$= -w(x-b) + w(x-a). \quad (\text{B.2e})$$

Therefore,

$$\begin{aligned} q'(x) &= w(x-x_1) - w(x-x_2) + w(x-x_4) - w(x-x_5) \\ &\quad + w(x-x_7) - w(x-x_8) + I'(x). \end{aligned} \quad (\text{B.3})$$

For an asymmetric spatial drive  $I(x)$  of the type given by (4.64),  $I'(x)$  is not defined at  $x = 0$ , but  $q'(x)$  is only required at the crossing events  $x =$

$x_i, i = 1, \dots, 8$ , which are never at  $x = 0$ , and so this is a robust expression for  $q'(x)$ .

Similarly, given that  $p(x)$  is given by (4.31b), we have that

$$p'(x) = \kappa \frac{d}{dx} \int_{x_3}^{x_6} w_h(x-y) dy, \quad (\text{B.4a})$$

$$= \kappa \left[ -w_h(x-y) \right]_{y=x_3}^{x_6}, \quad (\text{B.4b})$$

$$= \kappa \left\{ w_h(x-x_3) - w_h(x-x_6) \right\}. \quad (\text{B.4c})$$

# C

---

## APPENDICES: THALAMIC NEURAL FIELDS WITH REBOUND CURRENTS

---

### C.1 FOURIER TRANSFORMS OF CONNECTIVITY FUNCTIONS

In carrying out the linear stability of the spatially synchronous periodic orbit in Section 5.4, it was shown that non-local effects enter into the monodromy matrix via the Fourier transform of the connectivity function. Here, we determine these integral transforms for the connectivity function (5.9) we use in 1D (Section C.1.1) and 2D (Section C.1.3), and the Fourier transform of the integral of the 1D kernel (Section C.1.2) required in the computation of spatially periodic travelling waves in Section 5.8.

#### C.1.1 1D Kernel

Let  $w_0$  be chosen to normalise the kernel (5.9) in 1D

$$w(x) = w_0 e^{-|x|/\sigma} \left( 1 - \gamma \cos\left(\frac{\rho x}{\sigma}\right) \right), \quad x \in \mathbb{R}, \quad (\text{C.1})$$

to 1, that is the kernel normalisation  $\bar{w} = 1$ . Here,  $\sigma$ ,  $\gamma$ , and  $\rho$  are parameters. To normalise,

$$\bar{w} = \int_{-\infty}^{\infty} w(x) dx, \tag{C.2a}$$

$$= 2w_0 \int_0^{\infty} e^{-x/\sigma} (1 - \gamma \cos(\rho x/\sigma)) dx, \tag{C.2b}$$

$$= 2w_0 \sigma \left( \frac{\rho^2 + 1 - \gamma}{\rho^2 + 1} \right), \tag{C.2c}$$

where we have used the property that the integrand is even, and have then rewritten  $\cos(\rho x/\sigma)$  in terms of exponentials (or using a symbolic integration package such as Maple) to evaluate the resulting integral. So for the kernel to be normalised to 1 in 1D, we require that

$$w_0 = \frac{\rho^2 + 1}{2\sigma(\rho^2 + 1 - \gamma)}. \tag{C.3}$$

Let us now calculate the Fourier transform of  $w(x)$  in 1D. This is given by

$$\hat{w}(k) = \int_{-\infty}^{\infty} w(x) e^{ikx} dx \tag{C.4a}$$

$$= w_0 \int_{-\infty}^{\infty} e^{-|x|/\sigma} (1 - \gamma \cos(\rho x/\sigma)) e^{-ikx} dx, \tag{C.4b}$$

$$= w_0 \int_{-\infty}^{\infty} e^{-|x|/\sigma} \left( 1 - \frac{\gamma}{2} (e^{i\rho x/\sigma} + e^{-i\rho x/\sigma}) \right) e^{-ikx} dx, \tag{C.4c}$$

$$= w_0 \left( a(k; \sigma, 0) - \frac{\gamma}{2} (a(k, \sigma, \rho) + a(k, \sigma, -\rho)) \right), \tag{C.4d}$$

where

$$a(k; \sigma, \rho) = \int_{-\infty}^{\infty} e^{-|x|/\sigma} e^{i\rho x/\sigma} e^{-ikx} dx. \tag{C.5}$$

Partitioning the integration domain, we can determine  $a(k; \sigma, \rho)$  as follows

$$a(k; \sigma, \rho) = \int_{-\infty}^0 e^{x/\sigma} e^{i\rho x/\sigma} e^{-ikx} dx + \int_0^{\infty} e^{-x/\sigma} e^{i\rho x/\sigma} e^{-ikx} dx, \tag{C.6a}$$

$$= \left[ \frac{e^{x/\sigma} e^{i\rho x/\sigma} e^{-ikx}}{1/\sigma + i\rho/\sigma - ik} \right]_{x=-\infty}^0 + \left[ \frac{e^{-x/\sigma} e^{i\rho x/\sigma} e^{-ikx}}{-1/\sigma + i\rho/\sigma - ik} \right]_{x=0}^{\infty}, \tag{C.6b}$$

$$= \frac{1}{1/\sigma + i\rho/\sigma - ik} - \frac{1}{-1/\sigma + i\rho/\sigma - ik} \tag{C.6c}$$

$$= -\frac{2}{\sigma} \left( \frac{1}{-1/\sigma^2 - (\rho/\sigma - k)^2} \right), \tag{C.6d}$$

$$= \frac{2\sigma}{1 + (\rho - k\sigma)^2}. \tag{C.6e}$$

In summary, the Fourier transform of  $w(x)$  is

$$\begin{aligned} \widehat{w}(k) &= w_0 \left( a(k; \sigma, 0) - \frac{\gamma}{2} (a(k, \sigma, \rho) + a(k, \sigma, -\rho)) \right), \\ a(k; \sigma, \rho) &= \frac{2\sigma}{1 + (\rho - k\sigma)^2}, \end{aligned} \quad (\text{C.7})$$

and that  $\widehat{w}(0) = \bar{w}$  as expected.

### C.1.2 Integral of 1D Kernel

In constructing spatially periodic travelling waves in Section 5.8, and expressing  $u(\xi)$  as a Fourier series, we are required to evaluate the Fourier transform of  $W(x) = \int_{\xi_1}^{\xi_2} w(x - y) dy$ . To do this, express it as

$$W(x) = \int_{-\xi_2}^{-\xi_1} w(y + x) dy, \quad (\text{C.8})$$

where  $w(x)$  is given by (C.1). Then

$$\widehat{W}(k) = \int_{-\infty}^{\infty} W(x) e^{-ikx} dx, \quad (\text{C.9})$$

$$= \int_{x=-\infty}^{\infty} \int_{y=-\xi_2}^{-\xi_1} w(y + x) e^{-ikx} dy dx, \quad (\text{C.10})$$

$$= w_0 \int_{-\infty}^{\infty} \int_{-\xi_2}^{-\xi_1} e^{-|y+x|/\sigma} (1 - \gamma \cos(\rho(y+x)/\sigma)) e^{-ikx} dy dx. \quad (\text{C.11})$$

Since  $\xi_1$  and  $\xi_2$  are constants, the integral domain is a rectangle with infinite length and finite height. Therefore, the order of integration can be swapped and the cos function written in terms of exponentials to obtain

$$\widehat{W}(k) = w_0 \left( b(k; \sigma, 0) - \frac{\gamma}{2} (b(k; \sigma, \rho) + b(k; \sigma, -\rho)) \right), \quad (\text{C.12})$$

where the function

$$b(k; \sigma, \rho) = \int_{y=-\xi_2}^{-\xi_1} \int_{x=-\infty}^{\infty} e^{-|y+x|/\sigma} e^{i\rho(y+x)/\sigma} e^{-ikx} dx dy. \quad (\text{C.13})$$

The absolute value function is defined by

$$|y + x| = \begin{cases} y + x, & x > -y, \\ -(y + x), & x < -y, \end{cases}$$

so

$$b(k; \sigma, \rho) = \int_{-\xi_2}^{-\xi_1} I_1(y) + I_2(y) dy, \quad (\text{C.14})$$

where

$$I_1(y) = \int_{-\infty}^{-y} e^{(y+x)/\sigma} e^{i\rho(y+x)/\sigma} e^{-ikx} dx, \quad (\text{C.15a})$$

$$= \frac{\sigma e^{iky}}{1 + i(\rho - k\sigma)}, \quad (\text{C.15b})$$

and

$$I_2(y) = \int_{-y}^{\infty} e^{-(y+x)/\sigma} e^{i\rho(y+x)/\sigma} e^{-ikx} dx, \quad (\text{C.16a})$$

$$= \frac{\sigma e^{iky}}{1 - i(\rho - k\sigma)}. \quad (\text{C.16b})$$

Then

$$b(k; \sigma, \rho) = \frac{2\sigma}{1 + (\rho - k\sigma)^2} \int_{-\xi_2}^{-\xi_1} e^{iky} dy, \quad (\text{C.17a})$$

$$= \frac{2\sigma i (e^{-ik\xi_2} - e^{-ik\xi_1})}{k(1 + (\rho - k\sigma)^2)}. \quad (\text{C.17b})$$

In summary, the Fourier transform of  $W(x)$  is

$$\begin{aligned} \widehat{W}(k) &= w_0 \left( b(k; \sigma, 0) - \frac{\gamma}{2} (b(k; \sigma, \rho) + b(k; \sigma, -\rho)) \right), \\ b(k; \sigma, \rho) &= \frac{2\sigma i (e^{-ik\xi_2} - e^{-ik\xi_1})}{k(1 + (\rho - k\sigma)^2)}. \end{aligned} \quad (\text{C.18})$$

### C.1.3 2D Kernel

Let  $w_0$  be chosen to normalise the kernel (5.9) to 1 in 2D, that is  $\bar{w} = 1$ . In polar co-ordinates  $(r, \theta)$ , the radially symmetric kernel is given by

$$w(r) = w_0 e^{-r/\sigma} \left( 1 - \gamma \cos\left(\frac{\rho r}{\sigma}\right) \right), \quad r > 0, \quad (\text{C.19})$$

as in (5.9).

The kernel normalisation is given by

$$\bar{w} = \int_{\mathbb{R}^2} w(|\mathbf{r}'|) d\mathbf{r}' = \int_0^{2\pi} \int_0^\infty w(r) r d\theta dr, \quad (\text{C.20a})$$

$$= w_0 \int_0^{2\pi} \int_0^\infty e^{-r/\sigma} (1 - \gamma \cos(\rho r/\sigma)) r d\theta dr, \quad (\text{C.20b})$$

$$= 2\pi w_0 \int_0^\infty r e^{-r/\sigma} (1 - \gamma \cos(\rho r/\sigma)) dr, \quad (\text{C.20c})$$

$$= 2\pi w_0 \sigma^2 \left( \frac{\rho^4 + (\gamma + 2)\rho^2 - \gamma + 1}{\rho^4 + 2\rho^2 + 1} \right), \quad (\text{C.20d})$$

where the final step can be calculated by rewriting  $\cos(\rho r/\sigma)$  in terms of exponentials, or by using a symbolic integration package such as Maple. Therefore, for the kernel to be normalised to 1 in 2D, we require that

$$w_0 = \frac{\rho^4 + 2\rho^2 + 1}{2\pi\sigma^2 (\rho^4 + (\gamma + 2)\rho^2 - \gamma + 1)}. \quad (\text{C.21})$$

In 2D, the transformation to polar co-ordinates is given by  $d\mathbf{r} = r d\theta dr$ , and  $\mathbf{k} \cdot \mathbf{r} = kr \cos \theta$ , where  $|\mathbf{k}| = k$  and  $|\mathbf{r}| = r$ . Then the 2D Fourier transform is given by

$$\hat{w}(\mathbf{k}) = \int_{\mathbb{R}^2} d\mathbf{r} e^{-i\mathbf{k} \cdot \mathbf{r}} w(|\mathbf{r}|), \quad (\text{C.22a})$$

$$= w_0 \int_{\theta=0}^{2\pi} \int_{r=0}^\infty r e^{-ikr \cos \theta} e^{-r/\sigma} (1 - \gamma \cos(\rho r/\sigma)) dr d\theta, \quad (\text{C.22b})$$

$$= w_0 \int_{\theta=0}^{2\pi} \int_{r=0}^\infty r e^{-ikr \cos \theta} e^{-r/\sigma} \left( 1 - \frac{\gamma}{2} (e^{i\rho r/\sigma} + e^{-i\rho r/\sigma}) \right) dr d\theta, \quad (\text{C.22c})$$

$$= w_0 \left( g(k; \sigma, 0) - \frac{\gamma}{2} (g(k, \sigma, \rho) + g(k, \sigma, -\rho)) \right), \quad (\text{C.22d})$$

where

$$g(k; \sigma, \rho) = \int_0^{2\pi} \int_0^\infty r e^{-\left(\frac{1-i\rho}{\sigma} + ik \cos \theta\right)r} dr d\theta. \quad (\text{C.23})$$

Let  $a = \frac{1 - i\rho}{\sigma}$ . Then

$$g(k; \sigma, \rho) = \int_{\theta=0}^{2\pi} \int_{r=0}^{\infty} r e^{-(a+ik \cos \theta)r} dr d\theta \Big|_{a=\frac{1-i\rho}{\sigma}}, \quad (\text{C.24a})$$

$$= -\frac{\partial}{\partial a} \int_{\theta=0}^{2\pi} \int_{r=0}^{\infty} e^{-(a+ik \cos \theta)r} dr d\theta \Big|_{a=\frac{1-i\rho}{\sigma}}, \quad (\text{C.24b})$$

$$= -\frac{\partial}{\partial a} \int_0^{2\pi} \left[ \frac{-1}{a + ik \cos \theta} e^{-(a+ik \cos \theta)r} \right]_{r=0}^{\infty} d\theta \Big|_{a=\frac{1-i\rho}{\sigma}}, \quad (\text{C.24c})$$

$$= -\frac{\partial}{\partial a} \int_0^{2\pi} \frac{1}{a + ik \cos \theta} d\theta \Big|_{a=\frac{1-i\rho}{\sigma}}. \quad (\text{C.24d})$$

The contour integral

$$I_a = \int_0^{2\pi} \frac{1}{a + ik \cos(\theta)} d\theta, \quad (\text{C.25})$$

appearing in the expression for  $g(k; \sigma, \rho)$  must be evaluated. To do so, we utilise the transformation  $z = e^{i\theta}$ ,  $dz = iz d\theta$ ,  $\cos(\theta) = (z + z^{-1})/2$ . Then

$$I_a = \oint_{\gamma} \frac{1}{a + \frac{ik}{2}(z + z^{-1})} \frac{1}{iz} dz, \quad (\text{C.26})$$

where  $\gamma$  is the contour around the unit disc. Then

$$I_a = -\frac{2}{k} \oint_{\gamma} F(z; a) dz, \quad (\text{C.27})$$

for the integrand defined here as

$$F(z; a) = \frac{1}{z^2 - \frac{2aiz}{k} + 1} = \frac{1}{(z - z_+)(z - z_-)}, \quad (\text{C.28})$$

where the poles of  $F(z)$  are

$$z_{\pm} = i \left( a/k \pm \sqrt{1 + a^2/k^2} \right). \quad (\text{C.29})$$

For the choice  $a = (1 - i\rho)/\sigma$ ,  $\sigma > 0$ , we have  $\text{Re}(a) > 0$  since  $\sigma, k > 0$ . Therefore only  $z_-$  lies inside the contour,<sup>1</sup> so by the Residue theorem, only  $z_-$  yields a non-zero contribution to the contour integral, therefore

$$I_a = -\left(\frac{2}{k}\right) 2\pi i \text{Res}(F, z_-), \quad (\text{C.30})$$

<sup>1</sup> Note that  $z_+ z_- = 1$ , therefore  $|z_+| = 1/|z_-|$ , so if  $z_-$  is inside the unit disc,  $z_+$  is outside it, and vice versa. With  $\sigma, k > 0$ ,  $z_-$  is inside the contour  $\gamma$ .

where  $\text{Res}(F, z_-)$  is the residue of  $F(z)$  at  $z = z_-$ , defined as

$$\text{Res}(F, z_-) = \frac{1}{z_- - z_+} = \frac{1}{-2i\sqrt{1 + a^2/k^2}}. \quad (\text{C.31})$$

Hence, we obtain an expression for  $I_a$  as

$$I_a = \frac{2\pi}{\sqrt{k^2 + a^2}}. \quad (\text{C.32})$$

Returning to the expression for  $g(k; \sigma, \rho)$ ,

$$g(k; \sigma, \rho) = -\frac{\partial}{\partial a} \int_0^{2\pi} \frac{1}{a + ik \cos(\theta)} d\theta \Big|_{a=\frac{1-i\rho}{\sigma}}, \quad (\text{C.33a})$$

$$= \frac{\partial}{\partial a} \left( \frac{2\pi}{k^2 + a^2} \right) \Big|_{a=\frac{1-i\rho}{\sigma}}, \quad (\text{C.33b})$$

$$= 2\pi \frac{a}{(k^2 + a^2)^{3/2}} \Big|_{a=\frac{1-i\rho}{\sigma}}, \quad (\text{C.33c})$$

and so, we obtain

$$g(k, \sigma, \rho) = \frac{2\pi}{\sigma} \frac{1 - i\rho}{(k^2 + \frac{1}{\sigma^2}(1 - i\rho)^2)^{3/2}}. \quad (\text{C.34})$$

In summary, the 2D Fourier transform for the radially symmetric connectivity given by  $w(r)$  is

$$\begin{aligned} \widehat{w}(k) &= w_0 \left( g(k; \sigma, 0) - \frac{\gamma}{2} (g(k; \sigma, \rho) + g(k; \sigma, -\rho)) \right), \\ g(k, \sigma, \rho) &= \frac{2\pi}{\sigma} \frac{1 - i\rho}{(k^2 + \frac{1}{\sigma^2}(1 - i\rho)^2)^{3/2}} \end{aligned} \quad (\text{C.35})$$

where  $k = |\mathbf{k}|$ .

## C.2 DERIVATION OF SALTATION MATRICES

### C.2.1 The Spatially Local Saltation Matrix

Saltation matrices allow for the proper treatment of discontinuous dynamics at switches in non-smooth systems. Here, we derive the saltation matrices

used for mapping perturbations to the synchronous solution across switching manifolds in Section 5.4. A similar derivation is seen in the Appendix of [159]. There are switches in the dynamics of the model (5.15) as the membrane potential variable  $v$  passes through  $v_h$  and  $v_{th}$ . Let us introduce the indicator function  $\gamma(z(t)) = v(t) - \mu$ ,  $\mu \in \{v_h, v_{th}\}$  to track switching events in time. The unperturbed trajectory,  $z(t) = (v(t), u(t), r(t), h(t))$ , is the synchronous periodic orbit. Now consider a perturbed trajectory,  $\tilde{z}(t) = z(t) + \delta z(t)$  where the perturbation is *only* in time, since the perturbations are separable into temporal and spatial parts, and the spatial parts are common to all terms in all equations for the perturbations. The dynamical system satisfied by  $z(t)$  is

$$\frac{dz}{dt} = F(z), \quad (\text{C.36})$$

where  $F$  is PWL. Linearising about the solution  $z(t)$  yields an evolution equation for the perturbations,  $\delta z(t)$ , given by

$$\frac{d}{dt} \delta z(t) = DF(z(t)) \delta z(t), \quad \delta z(0) = \delta z_0, \quad (\text{C.37})$$

where  $DF$  is a PWC matrix (since  $F$  is PWL).

Consider a situation as in Figure C.1 where the vector field  $F$  and/or the solution  $z$  discontinuously changes at a switching time  $t = T$ . More precisely,  $F = F_1(z)$  for  $t < T$  and  $F = F_2(z)$  for  $t > T$ , and the function  $g$  maps solutions across the switching event as  $z(T^+) = g(z(T^-))$ . We want to obtain a relationship between the perturbations before,  $\delta z_-$ , and after,  $\delta z_+$ , a switching event. The following derivation closely follows [154].

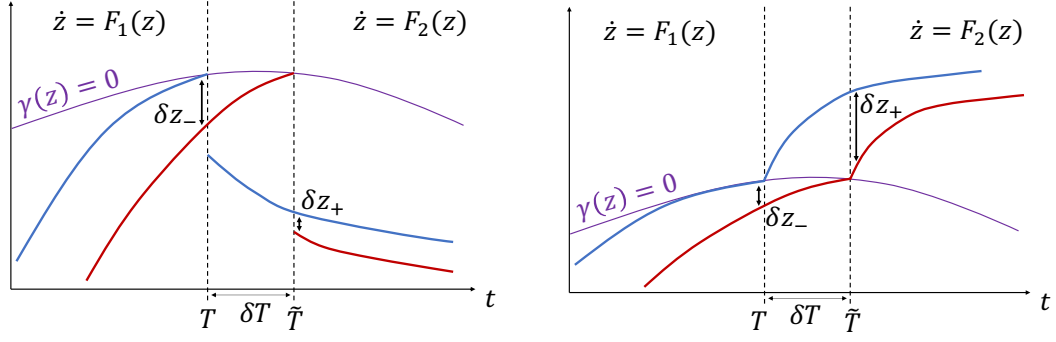


Figure C.1.: Saltation diagrams showing the unperturbed trajectory  $z(t)$  in blue, and the perturbed trajectory  $\tilde{z}(t)$  in red. (left) discontinuity in the vector field and in the solution. (right) discontinuity only in the vector field with continuous solutions.

The unperturbed and perturbed trajectories reach the switching manifold at times  $T$  and  $\tilde{T}$  respectively, so  $\gamma(z(T)) = 0$  and  $\gamma(\tilde{z}(\tilde{T})) = 0$ . By Taylor expanding  $\gamma(\tilde{z}(\tilde{T}))$ , we obtain

$$\gamma(\tilde{z}(\tilde{T})) = \gamma(\tilde{z}(T^- + \delta T)) \quad (\text{C.38a})$$

$$\simeq \gamma(\tilde{z}(T^-) + \dot{\tilde{z}}(T^-)\delta T) \quad (\text{C.38b})$$

$$= \gamma(z(T^-) + \delta z(T^-) + F_1(\tilde{z}(T^-))\delta T) \quad (\text{C.38c})$$

$$= \gamma(z(T^-) + \delta z_- + F_1(z(T^-))\delta T) \quad (\text{C.38d})$$

$$\simeq \gamma(z(T^-)) + \nabla_z \gamma(z(T)) \cdot (\delta z_- + F_1(z(T^-))\delta T) \quad (\text{C.38e})$$

Then since  $\gamma(z(T)) = 0$  and  $\gamma(\tilde{z}(\tilde{T})) = 0$ , we obtain

$$\nabla_z \gamma(z(T)) \cdot (\delta z_- + F_1(z(T^-))\delta T) = 0, \quad (\text{C.39})$$

and so

$$\delta T = -\frac{\nabla_z \gamma(z(T^-)) \cdot \delta z_-}{\nabla_z \gamma(z(T^-)) \cdot F_1(z(T^-))}. \quad (\text{C.40})$$

On each switching manifold, the indicator function is either  $\gamma(z) = v - v_h$ , or  $\gamma(z) = v - v_{th}$ . In either case,  $\nabla_\gamma \gamma(z) = (1, 0, 0, 0)$ , so (C.39) reduces to

$$\delta T = -\frac{\delta v(T^-)}{\dot{v}(T^-)}. \quad (\text{C.41})$$

In constructing the saltation matrix, we must relate perturbations *before* to those *after* a switching event; that is, we must relate  $\delta z_-$  to  $\delta z_+$ . Considering the transition at  $t = \tilde{T}$  in the perturbed trajectory, we obtain

$$\tilde{z}(\tilde{T}^+) = g(\tilde{z}(\tilde{T}^-)), \quad (\text{C.42a})$$

$$= g(\tilde{z}(T^- + \delta T)), \quad (\text{C.42b})$$

$$\simeq g(\tilde{z}(T^-) + \dot{\tilde{z}}(T^-)\delta T), \quad (\text{C.42c})$$

$$= g(z(T^-) + \delta z_- + F_1(\tilde{z}(T^-))\delta T), \quad (\text{C.42d})$$

$$\simeq g(z(T^-) + \delta z_- + F_1(z(T^-))\delta T), \quad (\text{C.42e})$$

$$\simeq g(z(T^-)) + Dg(z(T^-))\left\{\delta z_- + F_1(z(T^-))\delta T\right\}, \quad (\text{C.42f})$$

where,  $F_1(\tilde{z}(T^-))\delta T \simeq F_1(z(T^-))\delta T$  since  $\delta T$  is a small quantity. For the unperturbed trajectory, we obtain

$$z(\tilde{T}^+) = z(T^+ + \delta T), \quad (\text{C.43a})$$

$$= z(T^+) + \dot{z}(T^+)\delta T, \quad (\text{C.43b})$$

$$= g(z(T^-)) + F_2(z(T^+))\delta T. \quad (\text{C.43c})$$

Then the perturbation  $\delta z_+$  is given by

$$\delta z_+ = \tilde{z}(\tilde{T}^+) - z(\tilde{T}^+), \quad (\text{C.44a})$$

$$= Dg(z(T^-))\left\{\delta z_- + F_1(z(T^-))\delta T\right\} - F_2(z(T^+))\delta T, \quad (\text{C.44b})$$

$$= Dg(z(T^-))\delta z_- + \left\{Dg(z(T^-))F_1(z(T^-)) - F_2(z(T^+))\right\}\delta T. \quad (\text{C.44c})$$

Finally, substituting in for  $\delta T$  (C.40), we obtain

$$\delta z_+ = K(T)\delta z_-, \quad (\text{C.45})$$

where

$$K(T) = Dg(z(T^-)) \frac{\left\{Dg(z(T^-))F_1(z(T^-)) - F_2(z(T^+))\right\}\nabla_z\gamma(z(T^-))^T}{\nabla_z\gamma(z(T^-)) \cdot F_1(z(T^-))}. \quad (\text{C.46})$$

For the problem in Section 5.4, solutions are continuous at switching events, so  $g(z) = z$  for  $z = (v, u, r, h)$ , which gives  $Dg = I_4$  where  $I_4$  is the  $4 \times 4$

identity matrix. Switching events occur when  $v$  passes through either of  $v_{\text{th}}$  or  $v_{\text{h}}$ . In either case,  $\gamma(z(t)) = v(t) - \mu$ ,  $\mu \in \{v_{\text{h}}, v_{\text{th}}\}$ , so  $\nabla_z \gamma(z(t)) = (1, 0, 0, 0)^T$  for all  $t$ . Then the form that the local saltation matrix takes at switching times  $T = T_i$ ,  $i = 1, \dots, 4$ , in Section 5.4 of our model is given by

$$K(T) = I_4 - \frac{1}{\dot{v}(T^-)} \begin{pmatrix} \dot{v}(T^-) - \dot{v}(T^+) & 0 & 0 & 0 \\ \dot{u}(T^-) - \dot{u}(T^+) & 0 & 0 & 0 \\ \dot{r}(T^-) - \dot{r}(T^+) & 0 & 0 & 0 \\ \dot{h}(T^-) - \dot{h}(T^+) & 0 & 0 & 0 \end{pmatrix}. \quad (\text{C.47})$$

### c.2.2 Saltation Matrices in the Co-moving Frame

Likewise, saltation matrices allow us to characterise switching in the spatial dynamics of non-smooth systems. In this section, we explicitly derive the general saltation matrix needed for the stability analysis of the travelling wave solution carried out in Section 5.9. Let  $Z(\xi, t) = (v(\xi), h(\xi))$  denote the reduced state vector, where  $\xi$  represents a space-like travelling wave co-ordinate, and introduce the indicator function  $\gamma$  as

$$\gamma(Z(\xi, t)) = v(\xi) - v_{\text{h}},$$

which defines switching events in the travelling wave coordinates satisfying  $\gamma(Z(\xi, t)) = 0$ . Consider the unperturbed trajectory,  $Q(\xi) = (v(\xi), h(\xi))$ , which is the travelling wave solution, and a perturbed trajectory,  $\tilde{Z}(\xi, t) = Q(\xi) + \delta Z(\xi, t)$ , where  $\delta Z$  is small. Now, let the travelling wave spatial co-ordinate at which a switching event occurs be denoted  $\xi = \xi_s(t)$  for the unperturbed trajectory, and  $\xi = \tilde{\xi}_s(t) = \xi_s(t) + \delta \xi_s(t)$  for the perturbed tra-

jectory. Taylor expanding the indicator function for the perturbed trajectory, we obtain

$$\gamma(\tilde{Z}(\tilde{\xi}_s, t)) = \gamma(\tilde{Z}(\xi_s(t) + \delta\xi_s(t), t)), \quad (\text{C.48a})$$

$$= \gamma(Q(\xi_s(t) + \delta\xi_s(t)) + \delta Z(\xi_s(t) + \delta\xi_s(t), t)), \quad (\text{C.48b})$$

$$\simeq \gamma(Q(\xi_s + \delta\xi_s)) + \nabla_Q \gamma(Q(\xi_s + \delta\xi_s)) \cdot \delta Z(\xi_s + \delta\xi_s, t), \quad (\text{C.48c})$$

$$\begin{aligned} &\simeq \gamma(Q(\xi_s)) + \nabla_Q \gamma(Q(\xi_s)) \cdot Q_{\xi}(\xi_s^-) \delta\xi_s \\ &\quad + \nabla_Q \gamma(Q(\xi_s)) \cdot \delta Z(\xi_s, t). \end{aligned} \quad (\text{C.48d})$$

We have introduced the notation  $Q(\xi_s^\pm) = \lim_{\epsilon \searrow 0} Q(\xi_s \pm \epsilon)$  in order to ensure the partial derivative in  $\xi$  is well-defined. Now since  $\gamma(Q(\xi_s)) = 0$  and  $\gamma(\tilde{Z}(\tilde{\xi}_s, t)) = 0$ , (C.48) becomes

$$\nabla_Q \gamma(Q(\xi_s)) \cdot (Q_{\xi}(\xi_s^-) \delta\xi_s + \delta Z(\xi_s, t)) = 0. \quad (\text{C.49})$$

From this, we use the result that  $\nabla_Q \gamma(Q(\xi_s)) = (\partial_v, \partial_h)(v - v_h) = (1, 0)$ , to obtain an expression for the perturbation in the switching co-ordinate ( $\delta\xi_s$ ) in terms of the perturbation of the state vectors as

$$\delta\xi_s(t) = -\frac{\delta v(\xi_s, t)}{v'(\xi_s^-)}. \quad (\text{C.50})$$

We are now in a position to construct the saltation matrix relating perturbations before and after switching events. We consider the deviation,  $\delta Z$ , between the unperturbed and the perturbed trajectories at a switching event,  $\xi = \xi_s$ , as

$$\delta Z(\xi_s^- + \delta\xi_s, t) = \tilde{Z}(\xi_s^- + \delta\xi_s, t) - Q(\xi_s^- + \delta\xi_s), \quad (\text{C.51a})$$

$$\simeq \tilde{Z}(\xi_s^-, t) + \frac{\partial \tilde{Z}}{\partial \xi} \delta\xi_s - Q(\xi_s^-) - \frac{dQ}{d\xi} \delta\xi_s, \quad (\text{C.51b})$$

$$= \delta Z(\xi_s^-, t) + \left( \frac{\partial \tilde{Z}}{\partial \xi} - \frac{dQ}{d\xi} \right) \delta\xi_s. \quad (\text{C.51c})$$

Now, to leading order,  $\frac{\partial \tilde{Z}}{\partial \xi} = \frac{dQ}{d\xi} + o(1)$  (since this term multiples an already small term:  $\delta\xi_s$ ). Then

$$\delta Z(\xi_s^- + \delta\xi_s, t) \simeq \delta Z(\xi_s^-, t) + \left( Q'(\xi_s^-) - Q'(\xi_s^+) \right) \delta\xi_s. \quad (\text{C.52})$$

Substituting (C.50) into (C.52) gives

$$\delta Z(\xi_s^- + \delta \xi_s, t) = \delta Z(\xi_s^-, t) - \frac{\delta v(\xi_s^-, t)}{v'(\xi_s^-)} \left( Q'(\xi_s^-) - Q'(\xi_s^+) \right), \quad (\text{C.53})$$

which can be written in the equivalent, and useful, form as

$$\delta Z(\xi_s^- + \delta \xi_s, t) = \mathcal{K}(\xi_s) \delta Z(\xi_s^-, t), \quad (\text{C.54})$$

where

$$\mathcal{K}(\xi_s) = I_2 - \frac{1}{v'(\xi_s^-)} \begin{pmatrix} v'(\xi_s^-) - v'(\xi_s^+) & 0 \\ h'(\xi_s^-) - h'(\xi_s^+) & 0 \end{pmatrix}, \quad (\text{C.55})$$

is the general form, for our purposes, of the saltation matrix in the co-moving frame.

### C.3 THE FOURIER SERIES REPRESENTATION OF $u(\xi)$

Here, we show how to express spatially periodic solutions in the co-moving frame,  $u(\xi)$ , as a  $\phi$ -periodic Fourier series

$$u(\xi) = \sum_{p \in \mathbb{Z}} u_p e^{2\pi i p \xi / \phi}, \quad (\text{C.56})$$

where the Fourier coefficients  $u_p$  are defined as

$$u_p = \frac{1}{\phi} \int_0^\phi u(\xi) e^{-2\pi i p \xi / \phi} d\xi. \quad (\text{C.57})$$

as required in Section 5.8. This is a computationally useful form that can be used to find existence and stability conditions numerically with analytical expressions. To evaluate (C.57), we make use of the Fourier transform representations of various functions. First note the general form of the *non-unitary, angular frequency* Fourier and inverse Fourier transforms

$$a(k) = \int_{-\infty}^{\infty} a(x) e^{-ikx} dx, \quad (\text{C.58a})$$

$$a(x) = \frac{1}{2\pi} \int_{-\infty}^{\infty} \hat{a}(k) e^{ikx} dk. \quad (\text{C.58b})$$

Beginning from (5.48), rewrite  $\eta$  and  $W$  in terms of their Fourier transforms to obtain

$$u(\xi) = \frac{1}{\tau_R} \sum_{m \in \mathbb{Z}} \int_0^\infty ds \left( \frac{1}{2\pi} \int_{-\infty}^\infty dk_1 \hat{\eta}(k_1) e^{ik_1 s} \right) \times \left( \frac{1}{2\pi} \int_{-\infty}^\infty dk_2 \hat{W}(k_2) e^{ik_2(-m\phi + cs + \xi)} \right), \quad (\text{C.59a})$$

$$= \frac{1}{(2\pi)^2 \tau_R} \sum_{m \in \mathbb{Z}} e^{-ik_2 m \phi} \times \int_0^\infty ds \int_{-\infty}^\infty dk_1 \int_{-\infty}^\infty dk_2 \hat{\eta}(k_1) \hat{W}(k_2) e^{ik_1 s} e^{ik_2(cs + \xi)}. \quad (\text{C.59b})$$

Now, we use the *Dirac comb* relation

$$\phi \sum_{m \in \mathbb{Z}} e^{\pm ikm\phi} = 2\pi \sum_{q \in \mathbb{Z}} \delta\left(k - \frac{2\pi q}{\phi}\right), \quad (\text{C.60})$$

to obtain

$$u(\xi) = \frac{1}{2\pi\tau_R\phi} \sum_{q \in \mathbb{Z}} \int_0^\infty ds \int_{-\infty}^\infty dk_1 \int_{-\infty}^\infty dk_2 \times \delta\left(k_2 - \frac{2\pi q}{\phi}\right) \hat{\eta}(k_1) \hat{W}(k_2) e^{ik_1 s} e^{ik_2(cs + \xi)}, \quad (\text{C.61a})$$

$$= \frac{1}{2\pi\tau_R\phi} \sum_{q \in \mathbb{Z}} \int_0^\infty ds \int_{-\infty}^\infty dk_1 \hat{\eta}(k_1) \hat{W}\left(\frac{2\pi q}{\phi}\right) e^{ik_1 s} e^{i\left(\frac{2\pi q}{\phi}\right)(cs + \xi)}, \quad (\text{C.61b})$$

$$= \frac{1}{2\pi\tau_R\phi} \sum_{q \in \mathbb{Z}} \int_0^\infty ds \int_{-\infty}^\infty dk_1 \times \hat{\eta}(k_1) \hat{W}\left(\frac{2\pi q}{\phi}\right) e^{is(k_1 + 2\pi qc/\phi)} e^{2\pi i q \xi / \phi}. \quad (\text{C.61c})$$

At this point, we substitute this into (C.57) to obtain

$$u_p = \frac{1}{2\pi\tau_R\phi} \frac{1}{\phi} \int_0^\phi d\xi e^{2\pi i \xi (q-p)/\phi} \int_0^\infty ds \int_{-\infty}^\infty dk_1 \times \sum_{q \in \mathbb{Z}} \hat{W}(2\pi q/\phi) \hat{\eta}(k_1) e^{is(k_1 + 2\pi qc/\phi)} \quad (\text{C.62})$$

Now we see the form of a Dirac delta function,

$$\delta(q-p) = \frac{1}{\phi} \int_0^\phi d\xi e^{2\pi i \xi (q-p)/\phi}, \quad (\text{C.63})$$

in the expression (C.62) for  $u_p$ . Substituting in, and collapsing the sum over  $q$ , we obtain

$$u_p = \frac{1}{2\pi\tau_R\phi} \int_0^\infty ds \int_{-\infty}^\infty dk_1 \times \sum_{q \in \mathbb{Z}} \delta(q-p) \widehat{W}(2\pi q/\phi) \widehat{\eta}(k_1) e^{is(k_1+2\pi qc/\phi)}, \quad (\text{C.64a})$$

$$= \frac{1}{2\pi\tau_R\phi} \int_0^\infty ds e^{is(k_1+2\pi pc/\phi)} \int_{-\infty}^\infty dk_1 \widehat{\eta}(k_1) \widehat{W}(2\pi p/\phi). \quad (\text{C.64b})$$

Noticing another delta function,

$$2\pi\delta(k_1 + 2\pi pc/\phi) = \int_{-\infty}^\infty ds e^{is(k_1+2\pi pc/\phi)}, \quad (\text{C.65})$$

we have

$$u_p = \frac{1}{\tau_R\phi} \int_{-\infty}^\infty dk_1 \delta(k_1 + 2\pi pc/\phi) \widehat{\eta}(k_1) \widehat{W}(2\pi p/\phi). \quad (\text{C.66})$$

Finally, collapse the integral over  $k_1$  via the delta function to obtain the Fourier coefficients

$$u_p = \frac{1}{\tau_R\phi} \widehat{\eta}\left(\frac{-2\pi cp}{\phi}\right) \widehat{W}\left(\frac{2\pi p}{\phi}\right), \quad p \in \mathbb{Z}. \quad (\text{C.67})$$

#### C.4 FUNCTIONS FOR EVANS FUNCTION CALCULATION

Here, we give the functions  $f_i(\xi; \lambda)$ ,  $g_i(\xi; \lambda)$ ,  $i = 1, \dots, 4$ , that are the entries of the matrix  $\Gamma(\lambda)$ , (5.84), which is required for computing the Evans function. The conductance parameter  $C$  has been set to 1 here.

$$f_1(\xi) = \frac{g_{\text{syn}}}{c} \frac{1}{|v'(\xi_1^-)|} \sum_{p \in \mathbb{Z}} \bar{I}_{p, \xi_1, \lambda} \left( e^{\frac{2\pi ip\xi}{\phi}} - e^{\left(\frac{g_L + \lambda}{c}\right)\xi} \right), \quad (\text{C.68a})$$

$$f_2(\xi) = \frac{g_{\text{syn}}}{c} \frac{1}{|v'(\xi_2^-)|} \sum_{p \in \mathbb{Z}} \bar{I}_{p, \xi_2, \lambda} \left( e^{\frac{2\pi ip\xi}{\phi}} - e^{\left(\frac{g_L + \lambda}{c}\right)\xi} \right), \quad (\text{C.68b})$$

$$f_3(\xi) = \frac{g_{\text{T}}}{c} f_h(\xi) \left( -\frac{h'(\xi_3^-) - h'(\xi_3^+)}{v'(\xi_3^-)} e^{(\lambda/c + 1/c\tau^+)(\phi - \xi_3)} \right), \quad (\text{C.68c})$$

$$f_4(\xi) = \left( 1 - \frac{v'(\phi^-) - v'(0^+)}{v'(\phi^-)} \right) e^{\left(\frac{g_L + \lambda}{c}\right)\xi} - \frac{g_{\text{T}}}{c} f_h(\xi) \left( \frac{h'(\phi^-) - h'(0^+)}{v'(\phi^-)} \right), \quad (\text{C.68d})$$

where

$$\bar{I}_{p,a,\lambda} = \frac{I_{p,a,\lambda}}{\frac{2\pi ip}{\phi} - \frac{g_{L+\lambda}}{c}}, \quad (\text{C.69a})$$

$$I_{p,a,\lambda} = \frac{1}{\tau_R \phi} \tilde{\eta} \left( \lambda - \frac{2\pi ipc}{\phi} \right) \widehat{w} \left( \frac{2\pi p}{\phi} \right) e^{-\frac{2\pi ipa}{\phi}}, \quad (\text{C.69b})$$

and

$$f_h(\tilde{\zeta}) = \frac{e^{\left(\frac{\lambda}{c} + \frac{1}{c\tau^-}\right)\tilde{\zeta}} - e^{\left(\frac{g_{L+\lambda}}{c}\right)\tilde{\zeta}}}{\left(\frac{\lambda}{c} + \frac{1}{c\tau^-} - \frac{g_{L+\lambda}}{c}\right) \left(1 - e^{\left(\frac{\lambda}{c} + \frac{1}{c\tau^-}\right)\tilde{\zeta}_3} e^{\left(\frac{\lambda}{c} + \frac{1}{c\tau^+}\right)(\phi - \tilde{\zeta}_3)}\right)}, \quad (\text{C.70})$$

and

$$g_1(\tilde{\zeta}) = \frac{g_{\text{syn}}}{c} \frac{1}{|v'(\tilde{\zeta}_1^-)|} \sum_{p \in \mathbb{Z}} \bar{I}_{p,\tilde{\zeta}_1,\lambda} \left( e^{\frac{2\pi ip\tilde{\zeta}}{\phi}} - e^{\frac{2\pi ip\tilde{\zeta}_3}{\phi}} e^{\left(\frac{g_{L+\lambda}}{c}\right)(\tilde{\zeta} - \tilde{\zeta}_3)} \right), \quad (\text{C.71a})$$

$$g_2(\tilde{\zeta}) = \frac{g_{\text{syn}}}{c} \frac{1}{|v'(\tilde{\zeta}_2^-)|} \sum_{p \in \mathbb{Z}} \bar{I}_{p,\tilde{\zeta}_2,\lambda} \left( e^{\frac{2\pi ip\tilde{\zeta}}{\phi}} - e^{\frac{2\pi ip\tilde{\zeta}_3}{\phi}} e^{\left(\frac{g_{L+\lambda}}{c}\right)(\tilde{\zeta} - \tilde{\zeta}_3)} \right), \quad (\text{C.71b})$$

$$g_3(\tilde{\zeta}) = \left( 1 - \frac{v'(\tilde{\zeta}_3^-) - v'(\tilde{\zeta}_3^+)}{v'(\tilde{\zeta}_3^-)} \right) e^{\left(\frac{g_{L+\lambda}}{c}\right)(\tilde{\zeta} - \tilde{\zeta}_3)}, \quad (\text{C.71c})$$

$$g_4(\tilde{\zeta}) = 0. \quad (\text{C.71d})$$

The infinite sums in  $f_1(\tilde{\zeta})$ ,  $f_2(\tilde{\zeta})$ ,  $g_1(\tilde{\zeta})$ ,  $g_2(\tilde{\zeta})$ , are well-behaved as  $p \rightarrow \pm\infty$ , so these can be truncated during computation.

---

## BIBLIOGRAPHY

---

- [1] L. F. Abbott. Lapicque's introduction of the integrate-and-fire model neuron (1907). *Brain Research Bulletin*, 50(5-6):303–304, 1999.
- [2] D. J. Acheson. *Elementary Fluid Dynamics*, 1991.
- [3] E. L. Allgower and K. Georg. *Introduction to Numerical Continuation Methods*. SIAM, 2003.
- [4] E. L. Allgower and K. Georg. *Numerical Continuation Methods: An Introduction*, volume 13. Springer Science & Business Media, 2012.
- [5] S.-I. Amari. Dynamics of Pattern Formation in Lateral-inhibition Type Neural Fields. *Biological Cybernetics*, 27:77–87, 1977.
- [6] D. J. Amit and M. Tsodyks. Quantitative study of attractor neural network retrieving at low spike rates. I. Substrate-spikes, rates and neuronal gain. *Network: Computation in Neural Systems*, 2(3):259, 1991.
- [7] P. Andersen and J. Eccles. Inhibitory phasing of neuronal discharge. *Nature*, 196(4855):645–647, 1962.
- [8] J. D. Angstadt, J. L. Grassmann, K. M. Theriault, and S. M. Levasseur. Mechanisms of postinhibitory rebound and its modulation by serotonin in excitatory swim motor neurons of the medicinal leech. *Journal of Comparative Physiology A*, 191(8):715–732, 2005.
- [9] I. L. Arancibia-Cárcamo, M. C. Ford, L. Cossell, K. Ishida, K. Tohyama, and D. Attwell. Node of Ranvier length as a potential regulator of myelinated axon conduction speed. *eLife*, 6:e23329, 2017.

- 
- [10] C. M. Armstrong. Na channel inactivation from open and closed states. *Proceedings of the National Academy of Sciences*, 103(47):17991–17996, 2006.
- [11] C. M. Armstrong and F. Bezanilla. Currents related to movement of the gating particles of the sodium channels. *Nature*, 242(5398):459–461, 1973.
- [12] D. Arrowsmith and C. Place. The linearization theorem. *Dynamical Systems: Differential Equations, Maps, and Chaotic Behaviour*. London: Chapman & Hall, pages 77–81, 1992.
- [13] D. Avitabile. Numerical computation of coherent structures in spatially-extended systems. In *Second International Conference on Mathematical Neuroscience, Antibes Juan-les-Pins*, 2016.
- [14] D. Avitabile, M. Desroches, and S. Rodrigues. On the numerical continuation of isolas of equilibria. *International Journal of Bifurcation and Chaos*, 22(11):1250277, 2012.
- [15] K. Badcock, B. Richards, and M. Woodgate. Elements of computational fluid dynamics on block structured grids using implicit solvers. *Progress in Aerospace Sciences*, 36(5-6):351–392, 2000.
- [16] A. H. Baker, E. R. Jessup, and T. Manteuffel. A technique for accelerating the convergence of restarted GMRES. *SIAM Journal on Matrix Analysis and Applications*, 26(4):962–984, 2005.
- [17] M. W. Barnett and P. M. Larkman. The action potential. *Practical Neurology*, 7(3):192–197, 2007.
- [18] R. Barrett, M. Berry, T. F. Chan, J. Demmel, J. Donato, J. Dongarra, V. Eijkhout, R. Pozo, C. Romine, and H. Van der Vorst. *Templates for the Solution of Linear Systems: Building Blocks for Iterative Methods*. SIAM, 1994.

- 
- [19] J. Benda and A. V. Herz. A universal model for spike-frequency adaptation. *Neural Computation*, 15(11):2523–2564, 2003.
- [20] R. Betts, D. Johnston, and B. Brown. Nerve fibre velocity and refractory period distributions in nerve trunks. *Journal of Neurology, Neurosurgery & Psychiatry*, 39(7):694–700, 1976.
- [21] W.-J. Beyn, A. Champneys, E. Doedel, W. Govaerts, Y. A. Kuznetsov, and B. Sandstede. Numerical continuation, and computation of normal forms. In *In Handbook of dynamical systems III: Towards applications*. Citeseer, 2001.
- [22] C. Bielza and P. Larrañaga. *Data-driven computational neuroscience: machine learning and statistical models*. Cambridge University Press, 2020.
- [23] P. Bogacki and L. F. Shampine. A 3 (2) pair of Runge-Kutta formulas. *Applied Mathematics Letters*, 2(4):321–325, 1989.
- [24] P. Bonifazi, M. Goldin, M. A. Picardo, I. Jorquera, A. Cattani, G. Bianconi, A. Represa, Y. Ben-Ari, and R. Cossart. GABAergic hub neurons orchestrate synchrony in developing hippocampal networks. *Science*, 326(5958):1419–1424, 2009.
- [25] M. Bonilla-Quintana, K. C. Wedgwood, R. D. O’Dea, and S. Coombes. An analysis of waves underlying grid cell firing in the medial entorhinal cortex. *The Journal of Mathematical Neuroscience*, 7(1):9, 2017.
- [26] P. C. Bressloff. Spatiotemporal dynamics of continuum neural fields. *Journal of Physics A: Mathematical and Theoretical*, 45(3):033001, 2011.
- [27] P. C. Bressloff and S. Coombes. Dynamics of strongly coupled spiking neurons. *Neural Computation*, 12(1):91–129, 2000.
- [28] R. Brette. Philosophy of the spike: rate-based vs. spike-based theories of the brain. *Frontiers in Systems Neuroscience*, 9:151, 2015.

- 
- [29] P. N. Brown and A. C. Hindmarsh. Matrix-free methods for stiff systems of ODE's. *SIAM Journal on Numerical Analysis*, 23(3):610–638, 1986.
- [30] Y. Burak and I. R. Fiete. Accurate path integration in continuous attractor network models of grid cells. *PLoS Comput Biol*, 5(2):e1000291, 2009.
- [31] A. N. Burkitt. A review of the integrate-and-fire neuron model: I. homogeneous synaptic input. *Biological Cybernetics*, 95(1):1–19, 2006.
- [32] Á. Byrne. *Next generation neural activity models: bridging the gap between mesoscopic and microscopic brain scales*. PhD thesis, University of Nottingham, 2017.
- [33] Á. Byrne, D. Avitabile, and S. Coombes. Next-generation neural field model: The evolution of synchrony within patterns and waves. *Physical Review E*, 99(1):012313, 2019.
- [34] A. Byrne, J. Ross, R. Nicks, and S. Coombes. Mean-field models for EEG/MEG: from oscillations to waves. *Brain Topography*, pages 1–18, 2021.
- [35] C. Cang, K. Aranda, and D. Ren. A non-inactivating high-voltage-activated two-pore Na<sup>+</sup> channel that supports ultra-long action potentials and membrane bistability. *Nature Communications*, 5(1):1–9, 2014.
- [36] P. Caroni, F. Donato, and D. Muller. Structural plasticity upon learning: regulation and functions. *Nature Reviews Neuroscience*, 13(7):478–490, 2012.
- [37] W. A. Catterall. Voltage-gated calcium channels. *Cold Spring Harbor Perspectives in Biology*, 3(8):a003947, 2011.

- 
- [38] W. A. Catterall, I. M. Raman, H. P. Robinson, T. J. Sejnowski, and O. Paulsen. The Hodgkin-Huxley heritage: from channels to circuits. *Journal of Neuroscience*, 32(41):14064–14073, 2012.
- [39] T. F. Chan and D. E. Foulser. Effectively well-conditioned linear systems. *SIAM Journal on Scientific and Statistical Computing*, 9(6):963–969, 1988.
- [40] E. Charalampidis, P. Kevrekidis, and P. E. Farrell. Computing stationary solutions of the two-dimensional Gross–Pitaevskii equation with deflated continuation. *Communications in Nonlinear Science and Numerical Simulation*, 54:482–499, 2018.
- [41] R. Chervin, P. Pierce, and B. Connors. Periodicity and directionality in the propagation of epileptiform discharges across neocortex. *Journal of Neurophysiology*, 60(5):1695–1713, 1988.
- [42] C. C. Chow and J. A. White. Spontaneous action potentials due to channel fluctuations. *Biophysical Journal*, 71(6):3013, 1996.
- [43] C. L. Colby, J.-R. Duhamel, and M. E. Goldberg. Oculocentric spatial representation in parietal cortex. *Cerebral Cortex*, 5(5):470–481, 1995.
- [44] S. Coombes. Dynamics of synaptically coupled integrate-and-fire-or-burst neurons. *Physical Review E*, 67(4):041910, 2003.
- [45] S. Coombes. Waves, bumps, and patterns in neural field theories. *Biological Cybernetics*, 93:91–108, 2005.
- [46] S. Coombes, P. beim Graben, R. Potthast, and J. Wright. *Neural fields: Theory and Applications*. Springer, 2014.
- [47] S. Coombes, Y. M. Lai, M. Şayli, and R. Thul. Networks of piecewise linear neural mass models. *European Journal of Applied Mathematics*, 29(5):869–890, 2018.

- 
- [48] S. Coombes and M. Owen. Exotic dynamics in a firing rate model of neural tissue. In *Fluids and Waves: Recent Trends in Applied Analysis: Research Conference, May 11-13, 2006, the University of Memphis, Memphis, TN*, volume 440, page 123. American Mathematical Soc., 2007.
- [49] S. Coombes and M. R. Owen. Evans functions for integral neural field equations with Heaviside firing rate function. *SIAM Journal on Applied Dynamical Systems*, 34:574–600, 2004.
- [50] S. Coombes and M. R. Owen. Bumps, breathers, and waves in a neural network with spike frequency adaptation. *Physical Review Letters*, 94(14):148102, 2005.
- [51] M. Cordero-Erausquin, J. A. Coull, D. Boudreau, M. Rolland, and Y. De Koninck. Differential maturation of GABA action and anion reversal potential in spinal lamina I neurons: impact of chloride extrusion capacity. *Journal of Neuroscience*, 25(42):9613–9623, 2005.
- [52] F. Crick and C. Koch. Towards a neurobiological theory of consciousness. In *Seminars in the Neurosciences*, volume 2, pages 263–275. Saunders Scientific Publications, 1990.
- [53] R. S. Dembo, S. C. Eisenstat, and T. Steihaug. Inexact Newton Methods. *SIAM Journal on Numerical Analysis*, 19(2):400–408, 1982.
- [54] A. Destexhe, M. Neubig, D. Ulrich, and J. Huguenard. Dendritic low-threshold calcium currents in thalamic relay cells. *Journal of Neuroscience*, 18(10):3574–3588, 1998.
- [55] A. Destexhe and T. J. Sejnowski. *Thalamocortical Assemblies: How Ion Channels, Single Neurons and Large-Scale Networks Organize Sleep Oscillations*. Oxford University Press, USA, 2001.
- [56] A. Dhooge, W. Govaerts, and Y. A. Kuznetsov. MATCONT: a MATLAB package for numerical bifurcation analysis of ODEs. *ACM Transactions on Mathematical Software (TOMS)*, 29(2):141–164, 2003.

- 
- [57] A. Dhooge, W. Govaerts, Y. A. Kuznetsov, H. G. E. Meijer, and B. Sautois. New features of the software MatCont for bifurcation analysis of dynamical systems. *Mathematical and Computer Modelling of Dynamical Systems*, 14(2):147–175, 2008.
- [58] H. A. Dijkstra, F. W. Wubs, A. K. Cliffe, E. Doedel, I. F. Dragomirescu, B. Eckhardt, A. Y. Gelfgat, A. L. Hazel, V. Lucarini, A. G. Salinger, et al. Numerical bifurcation methods and their application to fluid dynamics: analysis beyond simulation. *Communications in Computational Physics*, 15(1):1–45, 2014.
- [59] E. Doedel. Software for continuation and bifurcation problems in ordinary differential equations. *Applied Mathematics Report, California Institute of Technology*, 1986.
- [60] E. Doedel, H. B. Keller, and J. P. Kernevez. Numerical analysis and control of bifurcation problems (I): bifurcation in finite dimensions. *International Journal of Bifurcation and Chaos*, 1(03):493–520, 1991.
- [61] E. J. Doedel. AUTO: A program for the automatic bifurcation analysis of autonomous systems. *Congr. Numer*, 30(265-284):25–93, 1981.
- [62] E. J. Doedel, B. E. Oldeman, and C. L. PANDO L. Bifurcation structures in a model of a CO<sub>2</sub> laser with a fast saturable absorber. *International Journal of Bifurcation and Chaos*, 21(01):305–322, 2011.
- [63] J. D. Engbers, D. Anderson, R. Tadayonnejad, W. H. Mehaffey, M. L. Molineux, and R. W. Turner. Distinct roles for IT and IH in controlling the frequency and timing of rebound spike responses. *The Journal of Physiology*, 589(22):5391–5413, 2011.
- [64] B. Ermentrout. Reduction of conductance-based models with slow synapses to neural nets. *Neural Computation*, 6(4):679–695, 1994.
- [65] B. Ermentrout and D. H. Terman. *Mathematical Foundations of Neuroscience*, volume 35. Springer, 2010.

- 
- [66] G. B. Ermentrout and J. D. Cowan. A mathematical theory of visual hallucination patterns. *Biological Cybernetics*, 34(3):137–150, 1979.
- [67] G. B. Ermentrout, S. E. Folias, and Z. P. Kilpatrick. Spatiotemporal pattern formation in neural fields with linear adaptation. In *Neural Fields*, pages 119–151. Springer, 2014.
- [68] G. B. Ermentrout and J. B. McLeod. Existence and uniqueness of travelling waves for a neural network. *Proceedings of the Royal Society of Edinburgh Section A: Mathematics*, 123(3):461–478, 1993.
- [69] A. C. Errington, T. Stohr, and G. Lees. Voltage gated ion channels: targets for anticonvulsant drugs. *Current topics in Medicinal Chemistry*, 5(1):15–30, 2005.
- [70] J. W. Evans. Nerve axon equations: I Linear approximations. *Indiana University Mathematics Journal*, 21(9):877–885, 1972.
- [71] J. W. Evans. Nerve axon equations: II Stability at rest. *Indiana University Mathematics Journal*, 22(1):75–90, 1972.
- [72] J. W. Evans. Nerve axon equations: III Stability of the nerve impulse. *Indiana University Mathematics Journal*, 22(6):577–593, 1972.
- [73] J. W. Evans. Nerve axon equations: IV the stable and the unstable impulse. *Indiana University Mathematics Journal*, 24(12):1169–1190, 1975.
- [74] N. M. Evstigneev. On the convergence acceleration and parallel implementation of continuation in disconnected bifurcation diagrams for large-scale problems. In *International Conference on Parallel Computational Technologies*, pages 122–138. Springer, 2019.
- [75] P. E. Farrell, A. Birkisson, and S. W. Funke. Deflation techniques for finding distinct solutions of nonlinear partial differential equations. *SIAM Journal on Scientific Computing*, 37(4):A2026–A2045, 2015.

- 
- [76] R. A. Fisher. The wave of advance of advantageous genes. *Annals of Eugenics*, 7(4):355–369, 1937.
- [77] R. FitzHugh. Impulses and physiological states in theoretical models of nerve membrane. *Biophysical journal*, 1(6):445–466, 1961.
- [78] G. Floquet. Sur les équations différentielles linéaires à coefficients périodiques. In *Annales scientifiques de l'École normale supérieure*, volume 12, pages 47–88, 1883.
- [79] J. F. Fohlmeister. Voltage gating by molecular subunits of Na<sup>+</sup> and K<sup>+</sup> ion channels: higher-dimensional cubic kinetics, rate constants, and temperature. *Journal of Neurophysiology*, 113(10):3759–3777, 2015.
- [80] S. E. Folias. Nonlinear analysis of breathing pulses in a synaptically coupled neural network. *SIAM Journal on Applied Dynamical Systems*, 10(2):744–787, 2011.
- [81] S. E. Folias and P. C. Bressloff. Stimulus-locked traveling waves and breathers in an excitatory neural network. *SIAM Journal on Applied Mathematics*, 65(6):2067–2092, 2005.
- [82] G. Fuhrmann, H. Markram, and M. Tsodyks. Spike frequency adaptation and neocortical rhythms. *Journal of Neurophysiology*, 88(2):761–770, 2002.
- [83] W. Gerstner, W. M. Kistler, R. Naud, and L. Paninski. *Neuronal dynamics: From single neurons to networks and models of cognition*. Cambridge University Press, 2014.
- [84] G. H. Glover. Overview of functional magnetic resonance imaging. *Neurosurgery Clinics*, 22(2):133–139, 2011.
- [85] P. S. Goldman-Rakic. Cellular basis of working memory. *Neuron*, 14(3):477–485, 1995.

- 
- [86] D. M. Grobman. Homeomorphism of systems of differential equations. *Doklady Akademii Nauk SSSR*, 128(5):880–881, 1959.
- [87] J. Guckenheimer, J. H. Tien, and A. R. Willms. *Bursting: The genesis of rhythm in the nervous system*, chapter Bifurcations in the fast dynamics of neurons: Implications for bursting. World Scientific, Singapore, 2005.
- [88] T. Hafting, M. Fyhn, S. Molden, M.-B. Moser, and E. I. Moser. Microstructure of a spatial map in the entorhinal cortex. *Nature*, 436(7052):801–806, 2005.
- [89] S. Hamdi, W. E. Schiesser, and G. W. Griffiths. Method of lines. *Scholarpedia*, 2(7):2859, 2007. revision #124335.
- [90] P. Hartman. A lemma in the theory of structural stability of differential equations. *Proceedings of the American Mathematical Society*, 11(4):610–620, 1960.
- [91] M. E. Hasselmo. Models of hippocampus. *Scholarpedia*, 6(5):1371, 2011. revision #126866.
- [92] X. He, S. Yan, Y. Hu, P. Niyogi, and H.-J. Zhang. Face recognition using Laplacianfaces. *IEEE Transactions on Pattern Analysis and Machine Intelligence*, 27(3):328–340, 2005.
- [93] E. Hewitt and R. E. Hewitt. The Gibbs-Wilbraham phenomenon: an episode in Fourier analysis. *Archive for History of Exact Sciences*, 21(2):129–160, 1979.
- [94] A. V. Hill. Excitation and accommodation in nerve. *Proceedings of the Royal Society of London. Series B-Biological Sciences*, 119(814):305–355, 1936.
- [95] J. L. Hindmarsh and R. Rose. A model of neuronal bursting using three coupled first order differential equations. *Proceedings of the Royal Society of London. Series B. Biological Sciences*, 221(1222):87–102, 1984.

- 
- [96] R. Hindriks, M. J. van Putten, and G. Deco. Intra-cortical propagation of EEG alpha oscillations. *NeuroImage*, 103:444–453, 2014.
- [97] A. L. Hodgkin and A. F. Huxley. The components of membrane conductance in the giant axon of loligo. *The Journal of Physiology*, 116(4):473, 1952.
- [98] A. L. Hodgkin and A. F. Huxley. Currents carried by sodium and potassium ions through the membrane of the giant axon of loligo. *The Journal of Physiology*, 116(4):449, 1952.
- [99] A. L. Hodgkin and A. F. Huxley. The dual effect of membrane potential on sodium conductance in the giant axon of loligo. *The Journal of Physiology*, 116(4):497, 1952.
- [100] A. L. Hodgkin and A. F. Huxley. A quantitative description of membrane current and its application to conduction and excitation in nerve. *The Journal of Physiology*, 117(4):500, 1952.
- [101] A. L. Hodgkin and B. Katz. The effect of sodium ions on the electrical activity of the giant axon of the squid. *The Journal of Physiology*, 108(1):37, 1949.
- [102] J. H. Hubbard and B. H. West. Linear dynamical systems. In *MacMath 9.0*, pages 121–129. Springer, 1992.
- [103] F. Hucho and C. Weise. Ligand-gated ion channels. *Angewandte Chemie International Edition*, 40(17):3100–3116, 2001.
- [104] M. A. Huertas, J. R. Groff, and G. D. Smith. Feedback Inhibition and Throughput Properties of an Integrate-and-Fire-or-Burst Network Model of Retinogeniculate Transmission. *Journal of Computational Neuroscience*, 19:147–180, 2005.
- [105] J. Huguenard. Low-threshold calcium currents in central nervous system neurons. *Annual Review of Physiology*, 58(1):329–348, 1996.

- 
- [106] J. Huguenard and D. Prince. A novel T-type current underlies prolonged Ca (2+)-dependent burst firing in GABAergic neurons of rat thalamic reticular nucleus. *Journal of Neuroscience*, 12(10):3804–3817, 1992.
- [107] J. R. Huguenard and D. A. McCormick. Thalamic synchrony and dynamic regulation of global forebrain oscillations. *Trends in Neurosciences*, 30(7):350–356, 2007.
- [108] M. Iftinca. Neuronal T-type calcium channels: What’s new? Iftinca: T-type channel regulation. *Journal of Medicine and Life*, 4(2):126, 2011.
- [109] T. Ikeda, H. Ikeda, and M. Mimura. Hopf bifurcation of travelling pulses in some bistable reaction-diffusion systems. *Methods and Applications of Analysis*, 7(1):165–194, 2000.
- [110] E. M. Izhikevich. Simple model of spiking neurons. *IEEE Transactions on neural networks*, 14(6):1569–1572, 2003.
- [111] V. Janovský and P. Plecháč. Computer-aided analysis of imperfect bifurcation diagrams, I. Simple bifurcation point and isola formation centre. *SIAM Journal on Numerical Analysis*, 29(2):498–512, 1992.
- [112] T. Joachims. Optimizing search engines using clickthrough data. In *Proceedings of the eighth ACM SIGKDD International Conference on Knowledge Discovery and Data Mining*, pages 133–142, 2002.
- [113] B. R. Jones and S. H. Thompson. Mechanism of postinhibitory rebound in molluscan neurons. *American Zoologist*, 41(4):1036–1048, 2001.
- [114] E. G. Jones. Golgi, cajal and the neuron doctrine. *Journal of the History of the Neurosciences*, 8(2):170–178, 1999.
- [115] T. Kapitula and K. Promislow. *Spectral and Dynamical Stability of Non-linear Waves*, volume 457. Springer, 2013.

- 
- [116] J. Keener and J. Sneyd. *Mathematical Physiology*. Springer-Verlag, Berlin, Heidelberg, 1998.
- [117] H. B. Keller. Numerical solution of bifurcation and nonlinear eigenvalue problems. *Academic Press, New York*, 1977.
- [118] C. T. Kelley. *Iterative Methods for Linear and Nonlinear Equations*. SIAM, 1995.
- [119] C. T. Kelley. *Solving Nonlinear Equations with Newton's Method*. SIAM, 2003.
- [120] R. R. Kerswell and O. R. Tutty. Recurrence of travelling waves in transitional pipe flow. *Journal of Fluid Mechanics*, 584:69–102, 2007.
- [121] A. Kolmogorov, I. Petrovsky, and N. Piscounov. A study of the diffusion equation with increase in the amount of substance. *Bull. Univ. État Moscou*, 1(1), 1937.
- [122] B. Krauskopf, H. M. Osinga, and J. Galán-Vioque. *Numerical Continuation Methods for Dynamical Systems*, volume 2. Springer, 2007.
- [123] D. Kressner. The Krylov-Schur Algorithm. *Numerical Methods for General and Structured Eigenvalue Problems*, pages 113–130, 2005.
- [124] M. Krosigk von, T. Bal, and D. A. McCormick. Cellular mechanisms of a synchronized oscillation in the thalamus. *Science*, 261(5119):361–364, 1993.
- [125] Y. A. Kuznetsov. *Elements of Applied Bifurcation Theory*, volume 112. Springer Science & Business Media, 2013.
- [126] L. Lacinová. Voltage-dependent calcium channels. *General Physiology and Biophysics*, 24:1–78, 2005.
- [127] Y. M. Lai, R. Thul, and S. Coombes. Analysis of networks where discontinuities and nonsmooth dynamics collide: understanding syn-

- 
- chrony. *The European Physical Journal Special Topics*, 227(10):1251–1265, 2018.
- [128] C. R. Laing. PDE methods for two-dimensional neural fields. In *Neural Fields*, pages 153–173. Springer, 2014.
- [129] C. R. Laing, W. C. Troy, B. Gutkin, and G. B. Ermentrout. Multiple bumps in a neuronal model of working memory. *SIAM Journal on Applied Mathematics*, 63(1):62–97, 2002.
- [130] L. Lapique. Recherches quantitatives sur l’excitation électrique des nerfs traitée comme une polarisation. *Journal of Physiology and Pathology*, 9:620–635, 1907.
- [131] J. Laudanski, C. Sumner, and S. Coombes. Calcium window currents, periodic forcing, and chaos: understanding single neuron response with a discontinuous one-dimensional map. *Physical Review E*, 82(1):011924, 2010.
- [132] D. F. Lawden. *Elliptic Functions and Applications*, volume 80. Springer Science & Business Media, 2013.
- [133] R. I. Leine and H. Nijmeijer. *Dynamics and bifurcations of non-smooth mechanical systems*, volume 18. Springer Science & Business Media, 2013.
- [134] Y.-X. Li. Tango waves in a bidomain model of fertilization calcium waves. *Physica D: Nonlinear Phenomena*, 186(1-2):27–49, 2003.
- [135] R. R. Llinás. The contribution of santiago ramon y cajal to functional neuroscience. *Nature Reviews Neuroscience*, 4(1):77–80, 2003.
- [136] R. R. Llinás and M. Steriade. Bursting of thalamic neurons and states of vigilance. *Journal of Neurophysiology*, 95(6):3297–3308, 2006.

- 
- [137] T. B. Luke, E. Barreto, and P. So. Complete classification of the macroscopic behavior of a heterogeneous network of theta neurons. *Neural Computation*, 25(12):3207–3234, 2013.
- [138] P. K. Maini, D. S. McElwain, and D. Leavesley. Travelling waves in a wound healing assay. *Applied Mathematics Letters*, 17(5):575–580, 2004.
- [139] E. Marban, T. Yamagishi, and G. F. Tomaselli. Structure and function of voltage-gated sodium channels. *The Journal of Physiology*, 508(Pt 3):647, 1998.
- [140] V. Markounikau, C. Igel, A. Grinvald, and D. Jancke. A dynamic neural field model of mesoscopic cortical activity captured with voltage-sensitive dye imaging. *PLoS computational biology*, 6(9):e1000919, 2010.
- [141] B. E. McKay, J. E. McRory, M. L. Molineux, J. Hamid, T. P. Snutch, G. W. Zamponi, and R. W. Turner.  $Ca_v3$  T-type calcium channel isoforms differentially distribute to somatic and dendritic compartments in rat central neurons. *European Journal of Neuroscience*, 24(9):2581–2594, 2006.
- [142] K. Mehrotra, C. K. Mohan, and S. Ranka. *Elements of Artificial Neural Networks*. MIT press, 1997.
- [143] H. G. Meijer and S. Coombes. Travelling waves in models of neural tissue: from localised structures to periodic waves. *EPJ Nonlinear Biomedical Physics*, 2(1):3, 2014.
- [144] I. Mercader, O. Batiste, and A. Alonso. Continuation of travelling-wave solutions of the Navier–Stokes equations. *International Journal for Numerical Methods in Fluids*, 52(7):707–721, 2006.
- [145] M. Mimura, M. Nagayama, H. Ikeda, and T. Ikeda. Dynamics of travelling breathers arising in reaction-diffusion systems—ODE modelling approach. *Hiroshima Mathematical Journal*, 30(2):221–256, 2000.

- 
- [146] A. Minzoni, N. F. Smyth, and A. L. Worthy. Evolution of two-dimensional standing and travelling breather solutions for the sine-Gordon equation. *Physica D: Nonlinear Phenomena*, 189(3-4):167–187, 2004.
- [147] S. Modhara and D. Avitabile. Periodic orbit continuation in spatially extended systems: applications to neuroscience repository, <https://github.com/danieleavitabile/rebound-periodic-orbit-continuation>. 2022.
- [148] S. Modhara, Y. M. Lai, R. Thul, and S. Coombes. Neural Fields with Rebound Currents: Novel Routes to Patterning. *SIAM Journal on Applied Dynamical Systems*, 20(3):1596–1620, 2021.
- [149] J. Moehlis, K. Josic, and E. T. Shea-Brown. Periodic orbit. *Scholarpedia*, 1(7):1358, 2006. revision #153208.
- [150] E. Montbrió, D. Pazó, and A. Roxin. Macroscopic description for networks of spiking neurons. *Physical Review X*, 5(2):021028, 2015.
- [151] V. B. Mountcastle. Modality and topographic properties of single neurons of cat's somatic sensory cortex. *Journal of Neurophysiology*, 20(4):408–434, 1957.
- [152] L. Muller and A. Destexhe. Propagating waves in thalamus, cortex and the thalamocortical system: experiments and models. *Journal of Physiology-Paris*, 106(5-6):222–238, 2012.
- [153] L. Muller, A. Reynaud, F. Chavane, and A. Destexhe. The stimulus-evoked population response in visual cortex of awake monkey is a propagating wave. *Nature Communications*, 5:3675, 2014.
- [154] P. C. Müller. Calculation of Lyapunov exponents for dynamic systems with discontinuities. *Chaos, Solitons & Fractals*, 5(9):1671–1681, 1995.

- 
- [155] E. Neher, B. Sakmann, and J. H. Steinbach. The extracellular patch clamp: a method for resolving currents through individual open channels in biological membranes. *Pflügers Archiv*, 375(2):219–228, 1978.
- [156] D. L. Nelson, A. L. Lehninger, and M. M. Cox. *Lehninger Principles of Biochemistry*. Macmillan, 2008.
- [157] M. E. Nelson. Electrophysiological models. *Databasing the brain: from data to knowledge*, pages 285–301, 2004.
- [158] W. Nernst. Zur theorie des elektrischen reizes. *Archiv für die gesamte Physiologie des Menschen und der Tiere*, 122(7):275–314, 1908.
- [159] R. Nicks, L. Chambon, and S. Coombes. Clusters in nonsmooth oscillator networks. *Physical Review E*, 97(3):032213, 2018.
- [160] R. Nicks, A. Cocks, D. Avitabile, A. Johnston, and S. Coombes. Understanding sensory induced hallucinations: From neural fields to amplitude equations. *SIAM Journal on Applied Dynamical Systems*, 20(4):1683–1714, 2021.
- [161] E. Niedermeyer and F. L. da Silva. *Electroencephalography: Basic Principles, Clinical Applications, and Related Fields*. Lippincott Williams & Wilkins, 2005.
- [162] S. Noachtar and J. Rémi. The role of EEG in epilepsy: a critical review. *Epilepsy & Behavior*, 15(1):22–33, 2009.
- [163] G. Parkin. Valence, oxidation number, and formal charge: three related but fundamentally different concepts. *Journal of Chemical Education*, 83(5):791, 2006.
- [164] E. Perez-Reyes. Molecular physiology of low-voltage-activated T-type calcium channels. *Physiological Reviews*, 83(1):117–161, 2003.

- 
- [165] D. H. Perkel and B. Mulloney. Motor pattern production in reciprocally inhibitory neurons exhibiting postinhibitory rebound. *Science*, 185(4146):181–183, 1974.
- [166] S. P. Peron and F. Gabbiani. Role of spike-frequency adaptation in shaping neuronal response to dynamic stimuli. *Biological Cybernetics*, 100(6):505–520, 2009.
- [167] S. Petros. *The Numerical Solution of Neural Field Models Posed on Realistic Cortical Domains*. PhD thesis, University of Nottingham, 2022.
- [168] D. J. Pinto and G. B. Ermentrout. Spatially structured activity in synaptically coupled neuronal networks: I Travelling fronts and pulses. *SIAM*, 62:206–225, 2001.
- [169] D. Purves, G. J. Augustine, D. Fitzpatrick, W. Hall, A. LaMantia, J. McNamara, and L. White. Neuroscience, 2008. *De Boeck, Sinauer, Sunderland, Mass*, 15:16, 2014.
- [170] J. D. Rademacher, B. Sandstede, and A. Scheel. Computing absolute and essential spectra using continuation. *Physica D: Nonlinear Phenomena*, 229(2):166–183, 2007.
- [171] I. M. Raman, A. E. Gustafson, and D. Padgett. Ionic currents and spontaneous firing in neurons isolated from the cerebellar nuclei. *Journal of Neuroscience*, 20(24):9004–9016, 2000.
- [172] J. Rankin, D. Avitabile, J. Baladron, G. Faye, and D. J. Lloyd. Continuation of localized coherent structures in nonlocal neural field equations. *SIAM Journal on Scientific Computing*, 36(1):B70–B93, 2014.
- [173] R. L. Rasmusson, M. J. Morales, S. Wang, S. Liu, D. L. Campbell, M. V. Brahmajothi, and H. C. Strauss. Inactivation of voltage-gated cardiac K<sup>+</sup> channels. *Circulation Research*, 82(7):739–750, 1998.
- [174] P. Rinck. *Magnetic Resonance in Medicine*. Wiley-Blackwell, 2001.

- 
- [175] J. Rinzel. Models in neurobiology. In *Nonlinear Phenomena in Physics and Biology*, pages 345–367. Springer, 1981.
- [176] J. Rinzel and G. Ermentrout. *Methods in Neuronal Modeling: From Ions to Networks*, chapter Analysis of neural excitability and oscillations, pages 251–292. The MIT Press, Cambridge, Massachusetts, 2nd edition, 1998.
- [177] J. Rinzel and G. B. Ermentrout. Analysis of neural excitability and oscillations. *Methods in Neuronal Modeling*, 2:251–292, 1998.
- [178] J. Rinzel, D. Terman, X.-J. Wang, and B. Ermentrout. Propagating activity patterns in large-scale inhibitory neuronal networks. *Science*, 279:1351–1355, 1998.
- [179] M. F. Rossier. T-type calcium channel: a privileged gate for calcium entry and control of adrenal steroidogenesis. *Frontiers in Endocrinology*, 7:43, 2016.
- [180] S. Rudolph, W. G. Regehr, et al. Active dendrites and differential distribution of calcium channels enable functional compartmentalization of golgi cells. *Journal of Neuroscience*, 35(47):15492–15504, 2015.
- [181] Y. Saad. Krylov subspace methods for solving large unsymmetric linear systems. *Mathematics of Computation*, 37(155):105–126, 1981.
- [182] Y. Saad and M. H. Schultz. Gmres: A generalized minimal residual algorithm for solving nonsymmetric linear systems. *SIAM Journal on Scientific and Statistical Computing*, 7(3):856–869, 1986.
- [183] J. Sánchez and M. Net. On the multiple shooting continuation of periodic orbits by Newton–Krylov methods. *International Journal of Bifurcation and Chaos*, 20(01):43–61, 2010.
- [184] J. Sánchez, M. Net, B. Garcia-Archilla, and C. Simó. Newton–Krylov continuation of periodic orbits for Navier–Stokes flows. *Journal of Computational Physics*, 201(1):13–33, 2004.

- 
- [185] B. Sandstede. Stability of Travelling Waves. In *Handbook of Dynamical Systems*, volume 2, pages 983–1055. Elsevier, 2002.
- [186] B. Sandstede and A. Scheel. Absolute and convective instabilities of waves on unbounded and large bounded domains. *Physica D: Nonlinear Phenomena*, 145(3-4):233–277, 2000.
- [187] M. Şayli, Y. M. Lai, R. Thul, and S. Coombes. Synchrony in networks of Franklin bells. *IMA Journal of Applied Mathematics*, 84(5):1001–1021, 2019.
- [188] W. E. Schiesser. *The Numerical Method of Lines: Integration of Partial Differential Equations*. Elsevier, 2012.
- [189] S. M. Schuetze. The discovery of the action potential. *Trends in Neurosciences*, 6:164–168, 1983.
- [190] T. Schwalger and A. V. Chizhov. Mind the last spike—firing rate models for mesoscopic populations of spiking neurons. *Current Opinion in Neurobiology*, 58:155–166, 2019.
- [191] T. J. Sejnowski, C. Koch, and P. S. Churchland. Computational Neuroscience. *Science*, 241(4871):1299–1306, 1988.
- [192] G. M. Shepherd. *Foundations of the neuron doctrine*. Oxford University Press, 2015.
- [193] S. M. Sherman and R. W. Guillery. *Functional Connections of Cortical Areas: A New View from the Thalamus*. MIT Press, 2013.
- [194] J. A. Sherratt. Numerical continuation methods for studying periodic travelling wave (wavetrain) solutions of partial differential equations. *Applied Mathematics and Computation*, 218(9):4684–4694, 2012.
- [195] E. Shlizerman and P. Holmes. Neural dynamics, bifurcations, and firing rates in a quadratic integrate-and-fire model with a recovery

- variable. I: Deterministic behavior. *Neural Computation*, 24(8):2078–2118, 2012.
- [196] V. Shusterman and W. C. Troy. From baseline to epileptiform activity: a path to synchronized rhythmicity in large-scale neural networks. *Physical Review E*, 77(6):061911, 2008.
- [197] Y. Sire and G. James. Travelling breathers in Klein–Gordon chains. *Comptes Rendus Mathématique*, 338(8):661–666, 2004.
- [198] G. D. Smith, C. L. Cox, M. S. Sherman, and J. Rinzel. A firing-rate model of spike-frequency adaptation in sinusoidally-driven thalamocortical relay neurons. *Thalamus & Related Systems*, 1(2):135–156, 2001.
- [199] G. D. Smith, C. L. Cox, S. M. Sherman, and J. Rinzel. Fourier analysis of sinusoidally driven thalamocortical relay neurons and a minimal integrate-and-fire-or-burst model. *Journal of Neurophysiology*, 83:588–610, 2000.
- [200] O. Sokolova, L. Kolmakova-Partensky, and N. Grigorieff. Three-dimensional structure of a voltage-gated potassium channel at 2.5 nm resolution. *Structure*, 9(3):215–220, 2001.
- [201] I. Soltesz and K. Staley. *Computational Neuroscience in Epilepsy*. Academic Press, 2011.
- [202] M. Steriade, M. Deschenes, L. Domich, and C. Mulle. Abolition of spindle oscillations in thalamic neurons disconnected from nucleus reticularis thalami. *Journal of Neurophysiology*, 54(6):1473–1497, 1985.
- [203] M. Steriade, E. G. Jones, and R. R. L inas. *Thalamic Oscillations and Signalling*. Wiley, New York, 1990.
- [204] G. W. Stewart. A Krylov–Schur algorithm for large eigenproblems. *SIAM Journal on Matrix Analysis and Applications*, 23(3):601–614, 2002.

- 
- [205] J. Stilgoe. Machine learning, social learning and the governance of self-driving cars. *Social Studies of Science*, 48(1):25–56, 2018.
- [206] E. M. Talley, L. L. Cribbs, J.-H. Lee, A. Daud, E. Perez-Reyes, and D. A. Bayliss. Differential distribution of three members of a gene family encoding low voltage-activated (T-type) calcium channels. *Journal of Neuroscience*, 19(6):1895–1911, 1999.
- [207] Y. Tang, J. R. Nyengaard, D. M. De Groot, and H. J. G. Gundersen. Total regional and global number of synapses in the human brain neocortex. *Synapse*, 41(3):258–273, 2001.
- [208] J. R. Terry, W. Woldman, A. D. Peterson, and B. J. Cook. Neural field models: A mathematical overview and unifying framework. *Mathematical Neuroscience and Applications*, 2, 2022.
- [209] R. Thul, S. Coombes, and C. R. Laing. Neural field models with threshold noise. *The Journal of Mathematical Neuroscience*, 6(1):1–26, 2016.
- [210] R. Thul, G. Smith, and S. Coombes. A bidomain threshold model of propagating calcium waves. *Journal of Mathematical Biology*, 56(4):435–463, 2008.
- [211] V. Tikhomirov. A study of the diffusion equation with increase in the amount of substance, and its application to a biological problem. In *Selected works of AN Kolmogorov*, pages 242–270. Springer, 1991.
- [212] L. N. Trefethen. *Spectral Methods in MATLAB*. SIAM, 2000.
- [213] J. S. Trimmer and K. J. Rhodes. Localization of voltage-gated ion channels in mammalian brain. *Annu. Rev. Physiol.*, 66:477–519, 2004.
- [214] P. Uhlhaas, G. Pipa, B. Lima, L. Melloni, S. Neuenschwander, D. Nikolić, and W. Singer. Neural synchrony in cortical networks: history, concept and current status. *Frontiers in Integrative Neuroscience*, 3:17, 2009.

- 
- [215] P. J. Uhlhaas and W. Singer. Neural synchrony in brain disorders: relevance for cognitive dysfunctions and pathophysiology. *Neuron*, 52(1):155–168, 2006.
- [216] J. S. Umbría and M. Net. Numerical continuation methods for large-scale dissipative dynamical systems. *The European Physical Journal Special Topics*, 225(13):2465–2486, 2016.
- [217] N. A. Venkov, S. Coombes, and P. C. Matthews. Dynamic instabilities in scalar neural field equations with space-dependent delays. *Physica D: Nonlinear Phenomena*, 232(1):1–15, 2007.
- [218] M. von Krosigk, T. Bal, and D. A. McCormick. Cellular mechanisms of a synchronized oscillation in the thalamus. *Science*, 261(5119):361–364, 1993.
- [219] T. Wang, L. Yin, X. Zou, Y. Shu, M. J. Rasch, and S. Wu. A phenomenological synapse model for asynchronous neurotransmitter release. *Frontiers in Computational Neuroscience*, 9:153, 2016.
- [220] X.-J. Wang. Multiple dynamical modes of thalamic relay neurons: rhythmic bursting and intermittent phase-locking. *Neuroscience*, 59(1):21–31, 1994.
- [221] X.-J. Wang and J. Rinzel. Alternating and synchronous rhythms in reciprocally inhibitory model neurons. *Neural Computation*, 4(1):84–97, 1992.
- [222] X.-J. Wang, J. Rinzel, and M. A. Rogawski. A model of the T-type calcium current and the low-threshold spike in thalamic neurons. *Journal of Neurophysiology*, 66(3):839–850, 1991.
- [223] N. Ward, M. Brown, A. Thompson, and R. Frackowiak. Neural correlates of motor recovery after stroke: a longitudinal fMRI study. *Brain*, 126(11):2476–2496, 2003.

- 
- [224] T. M. Wasylenko, J. E. Cisternas, C. R. Laing, and I. G. Kevrekidis. Bifurcations of lurching waves in a thalamic neuronal network. *Biological Cybernetics*, 103(6):447–462, 2010.
- [225] D. S. Watkins. *The matrix eigenvalue problem: GR and Krylov subspace methods*. SIAM, 2007.
- [226] M. Weliky, W. H. Bosking, and D. Fitzpatrick. A systematic map of direction preference in primary visual cortex. *Nature*, 379(6567):725–728, 1996.
- [227] J. West and M. Bhattacharya. Intelligent financial fraud detection: a comprehensive review. *Computers & Security*, 57:47–66, 2016.
- [228] H. R. Wilson and J. D. Cowan. Excitatory and inhibitory interactions in localized populations of model neurons. *Biophysical Journal*, 12(1):1–24, 1972.
- [229] H. R. Wilson and J. D. Cowan. A mathematical theory of the functional dynamics of cortical and thalamic nervous tissue. *Kybernetik*, 13(2):55–80, 1973.
- [230] K. Wimmer, D. Q. Nykamp, C. Constantinidis, and A. Compte. Bump attractor dynamics in prefrontal cortex explains behavioral precision in spatial working memory. *Nature Neuroscience*, 17(3):431–439, 2014.
- [231] W. Wojtak, S. Coombes, D. Avitabile, E. Bicho, and W. Erlhagen. A dynamic neural field model of continuous input integration. *Biological Cybernetics*, 115(5):451–471, 2021.
- [232] I. Yamazaki, S. Tomov, and J. Dongarra. Deflation strategies to improve the convergence of communication-avoiding gmres. In *2014 5th Workshop on Latest Advances in Scalable Algorithms for Large-Scale Systems*, pages 39–46. IEEE, 2014.

- 
- [233] G. Yellen. The voltage-gated potassium channels and their relatives. *Nature*, 419(6902):35–42, 2002.
- [234] A. C. Yew, D. Terman, and G. B. Ermentrout. Propagating activity patterns in thalamic neuronal networks. *SIAM Journal on Applied Mathematics*, 61:1578–1604, 2001.
- [235] M. Yousaf, J. Wyller, T. Tetzlaff, and G. T. Einevoll. Effect of localized input on bump solutions in a two-population neural-field model. *Nonlinear Analysis: Real World Applications*, 14(2):997–1025, 2013.
- [236] F. H. Yu and W. A. Catterall. Overview of the voltage-gated sodium channel family. *Genome Biology*, 4(3):1–7, 2003.
- [237] X. Zhan, C. Cox, and S. M. Sherman. Dendritic depolarization efficiently attenuates low-threshold calcium spikes in thalamic relay cells. *Journal of Neuroscience*, 20(10):3909–3914, 2000.